Operando Visualization and Interfacial Engineering of Li Metal Anodes

by

Eric Kazyak

A dissertation submitted in partial fulfillment
of the requirements for the degree of
Doctor of Philosophy
(Mechanical Engineering)
in the University of Michigan
2020

Doctoral Committee:

Assistant Professor Neil P. Dasgupta, Chair
Associate Professor Jeff Sakamoto
Professor Donald J. Siegel
Professor Katsuyo Thornton

Eric Kazyak

kazyak@umich.edu

ORCID iD: 0000-0001-5099-3985

This dissertation is dedicated to my family and friends. Without these people by my side along the way, I would not have made it to the finish line. I would especially like to thank my wife Krista, for her constant love and support, and for putting up with all of my antics and idiosyncrasies. I would also like to thank my Mom and Dad. They instilled in me from an early age a passion for learning new things and for making a difference, for which I am grateful beyond words.

ACKNOWLEDGEMENTS

First and foremost, I would like to express my sincere gratitude to my advisor, Neil. The incalculable hours spent together working on various projects, proposals, and papers have led to great personal growth over the years. We have come a long way in the last 5+ years, growing the group from 3 to over 20 people. I am so thankful that I chose to study here at the University of Michigan under your guidance - it has been a great ride, and I look forward to continuing our work together.

I would also like to thank each of my committee members for their thoughtful insights and suggestions that have helped me along the way. This includes both for the papers that we have published together and as members of my committee.

In particular, Jeff and the members of his group (Travis Thompson, Asma Sharafi, and Regina Garcia-Mendez) have been amazing collaborators over the years, leading to many deep and insightful conversations and experiments. Without their expertise and help, much of the work included in this dissertation would not have been possible.

I would also like to thank everyone in my lab group for their help along the way. There are so many people that have helped with the completion of this work, and provided innumerable helpful conversations and insights. They also made my time at Michigan far more enjoyable than I could have hoped. In particular, Kevin and Michael, who worked alongside me as we began working on batteries, and became great friends along the way. Will for coming to my rescue to answer Matlab and Latex questions. Andrew, Adrian, Yuxin, Mark, and Jose, for the many hours spent in battery subgroup and in lab, coming up with ideas, figuring out what the data means, and just hanging out.

Of course, this work would not have been possible without financial support provided by several funding sources over the years. First, the National Science Foundation for awarding me a Graduate Research Fellowship under Grant No. (DGE 1256260). The Joint Center for Energy Storage Research, an Energy Innovation Hub funded by the U.S. Department of Energy, Office of Science, Basic Energy Sciences for funding the work in chapters 3 and 4. The U.S. Department of Energy's Advanced Research Projects Agency-Energy (ARPA-E) for funding the work covered in Chapters 5, 6, 7, and 8 under Award Number DE-AR-

0000653. Finally, the University of Michigan Rackham Graduate School for enabling me to travel and present this work at conferences via Rackham Conference Travel Grants.

In addition, much of the data included in this thesis was collected using equipment at shared user facilities. These include the Michigan Center for Materials Characterization, the Environmental Molecular Sciences Laboratory at Pacific Northwest National Laboratory, and the Advanced Photon Source at Argonne National Laboratory.

This work has resulted in several publications, from which much of the content included herein is adapted. These are the references for those publications:

1. Kazyak, E.; Wood, K. N.; Dasgupta, N. P. Improved Cycle Life and Stability of Lithium Metal Anodes through Ultrathin Atomic Layer Deposition Surface Treatments. *Chem. Mater.* 2015, 27 (18), 64576462.

2. Wood, K. N.; Kazyak, E.; Chadwick, A. F.; Chen, K.-H.; Zhang, J.-G.; Thornton, K.; Dasgupta, N. P. Dendrites and Pits: Untangling the Complex Behavior of Lithium Metal Anodes through *Operando* Video Microscopy. *ACS Cent. Sci.* 2016, 2, 790801.

3. Sharafi, A.; Kazyak, E.; Davis, A. L.; Yu, S.; Thompson, T.; Siegel, D. J.; Dasgupta, N. P.; Sakamoto, J. Surface Chemistry Mechanism of Ultra-Low Interfacial Resistance in the Solid-State Electrolyte $Li_7La_3Zr_2O_{12}$. *Chem. Mater.* 2017, 29 (18), 79617968.

4. E. Kazyak, R. Garcia-Mendez, W. S. LePage, A. Sharafi, A. L. Davis, Adrian J. Sanchez, K.-H. Chen, J. Sakamoto, N. P. Dasgupta, Li Penetration in Solid Electrolytes: Direct Observation of Morphology, Propagation, and Reversibility via *Operando* Video Microscopy [*Submitted*]

5. Kazyak, E.; Chen, K.-H.; Wood, K. N.; Davis, A. L.; Thompson, T.; Bielinski, A. R.; Sanchez, A. J.; Wang, X.; Wang, C.; Sakamoto, J.; et al. Atomic Layer Deposition of the Solid Electrolyte Garnet $Li_7La_3Zr_2O_{12}$. *Chem. Mater.* 2017, 29 (8), 37853792.

6. Kazyak, E.; Chen, K. H.; Davis, A. L.; Yu, S.; Sanchez, A. J.; Lasso, J.; Bielinski, A. R.; Thompson, T.; Sakamoto, J.; Siegel, D. J.; et al. Atomic Layer Deposition and First Principles Modeling of Glassy Li_3BO_3-Li_2CO_3 Electrolytes for Solid-State Li Metal Batteries. *J. Mater. Chem. A* 2018, 6 (40), 1942519437.

Preface

One of the primary contributions of this dissertation is the development of a technique that I call *operando* video microscopy. This technique synchronizes optical video microscopy with the electrochemical response of the system. By view this data as a time-synchronized video, deep insights can be gained into the coupling between morphology evolution and the electrochemical performance. As a result, much of the data in chapters 4 and 6 is best viewed in video form. Some of these videos are included, but many more are available online in the individual papers, and these will be referred to throughout as well. Flash player must be enabled in order to play them, if it is not enabled, the videos will appear as blank spaces. With flash player enabled, the videos should play when clicked. In the likely event that flash player becomes totally obsolete, or if you just don't want to install it, please find the videos for each chapter in their respective publications.

TABLE OF CONTENTS

Dedication . . . . . **ii**

Acknowledgements . . . . . **iii**

Preface . . . . . **v**

List of Figures . . . . . **ix**

List of Tables . . . . . **xix**

List of Abbreviations . . . . . **xx**

Abstract . . . . . **xxiii**

Chapter

1 Introduction **1**

1.1 Better Batteries for a Better Society 1
1.2 Outline 4
1.3 Individual and Group Research Statement 6

2 Background **9**

2.1 Basics of Lithium Batteries 10
2.1.1 Thermodynamics 10
2.1.2 Kinetics 13
2.1.3 Practical Considerations 16
2.2 Li Metal Batteries 18
2.3 Basics of Solid Electrolytes 20
2.4 Basics of Atomic Layer Deposition 23
2.4.1 ALD Process Development 30

3 Atomic Layer Deposition for Protective Coatings on Li Metal **35**

3.1 Results and Discussion 37
3.2 Conclusions 45
3.3 Materials and Methods 46
3.3.1 Film Deposition 46
3.3.2 Cell Fabrication 47
3.3.3 Electrochemical Testing 47

4 *Operando* Visualization in Liquid Electrolytes 48

4.1 Visualization Cell Approach and Observations 49
4.1.1 Approach 49
4.1.2 Experimental Observations 53
4.2 Numerical Model 58
4.3 Results and Discussion 59
4.3.1 Visualization Cell Interpretation: General Framework 60
4.3.2 Visualization Cell Interpretation 66
4.3.3 Effect of Electrolyte on Electrode Performance and Voltage Profiles 71
4.4 Conclusions 77
4.5 Materials and Methods 79
4.5.1 Material Handling 79
4.5.2 Visualization Cells 79
4.5.3 Three-electrode Measurements 80
4.5.4 Coin Cells 80

5 Surface Chemistry of $Li_7La_3Zr_2O_{12}$ (LLZO) 81

5.1 Results and Discussion 83
5.1.1 Surface Chemical Analysis 83
5.1.2 Contact Angle Measurements and Calculations 86
5.1.3 Electrochemical Characterization 89
5.2 Conclusions 92
5.3 Materials and Methods 93
5.3.1 LLZO Specimen Preparation 93
5.3.2 Surface Conditioning 93
5.3.3 Surface Chemistry Characterization 94
5.3.4 Contact Angle Measurements 94
5.3.5 Electrochemical Measurements 95

6 *Operando* Visualization in Solid Electrolytes 97

6.1 Results and Discussion 101
6.1.1 Through-plane *Operando* Visualization 101
6.1.2 The In-Plane Visualization Platform 104
6.1.3 Experimental Validation of the In-Plane Visualization Platform . 107
6.1.4 Li Penetration Morphologies 109
6.1.5 Reversibility and Cycling 117
6.1.6 Li-Filled Crack Growth Analysis 122
6.1.7 Deep Discharge and Void Formation 127
6.1.8 Demonstration in a Sulfide Solid-State Electrolyte 132
6.2 Conclusions 134
6.3 Materials and Methods 135
6.3.1 Electrolyte Synthesis 135
6.3.2 Electrode Fabrication 136
6.3.3 Optical Imaging 136
6.3.4 Electrochemical Measurements 137

6.3.5 Image Processing . . . 137
6.3.6 Electron Microscopy . . . 138
6.3.7 3-D Reconstruction . . . 138

7 Atomic Layer Deposition of $Li_7La_3Zr_2O_{12}$ Solid Electrolyte Materials . . . 139

7.1 Results and Discussion . . . 142
7.2 Conclusions . . . 157
7.3 Materials and Methods . . . 157
7.3.1 Film Deposition . . . 157
7.3.2 Film Characterization . . . 159

8 Atomic Layer Deposition of Lithium Borate Solid Electrolytes . . . 161

8.1 Results and Discussion . . . 162
8.1.1 Process Development . . . 162
8.1.2 Film Characterization . . . 163
8.1.3 Ionic Conductivity . . . 167
8.1.4 Electrochemical Stability . . . 171
8.1.5 Full Cell Fabrication and Cycling . . . 175
8.2 Conclusions . . . 177
8.3 Materials and Methods . . . 178
8.3.1 Film Deposition . . . 178
8.3.2 Film Characterization . . . 179
8.3.3 Computational Modeling . . . 180
8.3.4 Electrochemical Characterization . . . 180

9 Conclusions and Future Work . . . 183

9.1 Conclusions . . . 183
9.2 Future Work . . . 185

Bibliography . . . 188

LIST OF FIGURES

FIGURE

1.1 Estimated U.S. Energy consumption by source and sector for 2018. 2
1.2 Estimated carbon dioxide emission intensity by sector from 1975-2016. 3

2.1 Energy barrier diagram of a reaction before (a) and after (b) dynamic equilibrium has been reached, and with an overpotential of η(c). 14
2.2 Energy barrier diagram at equilibrium (A) and with an overpotential of η(B). . 15
2.3 Schematic representation of the stability window for electrolytes in 4 cases, i) reductively unstable at the negative electrode, ii) reductively unstable with SEI passivation, iii) stable at both positive and negative electrodes, and iv) oxidatively unstable at the positive electrode. The unoccupied (blue) and occupied (orange) energy levels are general representations and could be considered as the lowest unoccupied molecular orbital (LUMO) and highest occupied molecular orbital (HOMO) in an organic liquid or as the conduction band minimum (CBM) and the valence band maximum (VBM) in an SSE. 18
2.4 Plot of the number of records on Web of Science for each publication year for the search "Lithium metal anode", as of 11/20/2019. 19
2.5 Plot of the ionic conductivity of ALD SSE materials vs. the year of publication. A typical value for an organic liquid electrolyte is provided for reference. 22
2.6 Schematic representation of ALD process with TMA and water. 24
2.7 Schematic representation of how film thickness is a function of the number of ALD cycles for ideal, delayed, and accelerated nucleation behavior. 26
2.8 Schematic representation of how film growth per cycle (GPC) varies as a function of precursor dose time (a), and purge time (b). 27
2.9 Schematic representation of the temperature dependence of growth rate for ALD processes that may exhibit condensation, incomplete reactions, precursor decomposition, and/or desorption. It should be noted that not all ALD processes exhibit a typical ALD window. 29
2.10 Cross-sectional SEM images of ALD ZnO films on *Morpho* nanostructures. . . 30
2.11 Schematic representation of measurements needed to calculate the conformality of an ALD film in a trench of an arbitrary aspect ratio. 31

3.1 Galvanostatic testing of Li symmetric cells at 1 mA cm^{-2}. After an initial reduction in overpotential losses, stable behavior is observed until sudden failure. Failure time is observed to vary as a function of ALD coating thickness. Percentage improvement is relative to control. 37

3.2 (a) Constant current charge/discharge voltage profiles for Li symmetric cells showing the effects of ALD coatings on overpotential losses at 1 mA cm^{-2}. Each half cycle represents 0.25 mAh cm^{-2}. In this plot, the dotted lines represent the point of failure for each cell. For the control sample, this was 711 cycles for the 20x; this point was at 1259 cycles. All cells were tested to failure. EIS measurements taken after 0, 300, and 700 cycles are shown in the insets. (b) Zoom in on stable voltage overpotential regime. (c) Zoom in after failure of control and 30x samples, showing erratic voltage behavior while the 20x sample remains stable. 39
3.3 Schematic of interface locations in cell, correlated with the relevant features in a sample EIS spectra. 40
3.4 SEM images showing the morphological changes between the control Li electrode (a, c, e, g) and the 20x Al_2O_3 sample (b, d, f, h). Images were taken after both cells exhibited failure, ca. 1,280 cycles. 42
3.5 Schematic of the morphology evolution of the ALD film upon compression during coin cell assembly (a-b). SEM image (c) and EDS map of Al K-edge showing the cracks depicted in the schematic. 45

4.1 Video 4.2 still frames for a cell cycled at 5 mA cm^{-2} (two-electrode measurement). EL-b morphology and corresponding voltage trace are shown at times (a) before cycling; (b) after first half-cycle (deposition at EL-b); (c) at cell polarization minimum (dissolution at EL-b); (d) at cell polarization maximum; pitting not yet evident; (e) morphology at end of half-cycle; pitting observed (examples highlighted in yellow circles); (f) morphology at end of third half-cycle (deposition at EL-b); new dendrites are deposited in the pits which formed at the end of the previous half-cycle (yellow circles). 51
4.2 Synchronized morphology and voltage changes for 1 M $LiPF_6$ in EC/DMC cycled at 5 mA cm^{-2}. 52
4.3 Schematic of synchronized electrochemistry/video microscopy concept. 53
4.4 Schematic of cell design used for *operando* video microscopy. The Li electrodes are shown in maize, the polyether ether ketone (PEEK) electrode holders are shown in blue, and the o-ring is shown in red/orange. 54
4.5 Voltage profile for visualization cell with a separator cycled in $LiPF_6$ cycled for over 100 cycles. The characteristic peaking behavior is obvious for each half cycle. The corresponding video is shown in Video 4.6. 56
4.6 *Operando* video of Li/Li symmetric cell with a celgard separator above the working electrode during cycling 100 times. 57
4.7 Voltage profile of a Li-Li symmetric cell where the first six half cycles were cycled for 7.5 min. Subsequent half cycles were cycled for longer periods of time. In a) the longer cycle was a sequence of cycling at either 1 mA cm^{-2} or 5 mA cm^{-2} for 15 s followed by a rest period of 30 s. For a more detailed view see b). This sequence was carried out until the amount of time under galvanostatic conditions was 45 min. In c) the cell was cycled at 2 cm^2; the first 4 half cycle were 7.5 min and the subsequent 2 half cycles were for 45 min. 58
4.8 Comparison of voltage traces for various geometries, as labeled in each panel. . 59

4.9 (a) Numerical modeling results of cell polarization showing agreement with experimental data. (b) Simulated area fraction associated with the kinetically fast reaction (θ_{fast}) on each electrode during cycling. When θ_{fast} at the dissolving electrode reaches zero, a maximum in cell voltage occurs. 60
4.10 (a) A schematic representation of reaction pathways for the cathode, anode, and electrolyte. The overpotential at each electrode is a function of the total current, which is equal to a sum of current contributions from each reaction pathway at that electrode. The magnitude of current that passes through each pathway is dependent on the impedance associated with that pathway. The dominant pathway for current at each electrode is associated with the processes with the lowest impedance (Z_p), which has the largest influence on the electrode overpotential. A schematic representation of the regions associated with the area fraction of each process, θ_p, is shown for the cathode (b) and for the anode (c). The impedance of each process is inversely proportional to θ_p and ΔG_p, as discussed in section 4.3.1. 62
4.11 Schematic representation of difference in activation barriers between a) the anodic (electrodissolution) processes of Li removal from either dendrites (labeled by den) or the bulk (labeled by bulk) and b) the cathodic (electrodeposition) processes involving nucleation (labeled by nuc) and growth (labeled by grow). 64
4.12 Three-electrode measurements showing the cell polarization contributions from each electrode. Here EL-b is the working electrode (WE) and EL-a is the counter electrode (CE). For visual aid, CE has been multiplied by -1 such that the total cell polarization = CE + WE. Voltage is vs Li/Li^+. 66
4.13 Schematic representation of experimental observations in section 4.1.2. The upper electrode is EL-a, and the lower electrode is EL-b. (a) Before cycling. (b) End of first half-cycle: pits form at EL-a (anode), and dendrites grow on EL-b (cathode). 67
4.14 Changes in cell polarization (top) are correlated with a schematic representation of morphology (middle; color-coded to match the appropriate reaction pathway as described in Figure 4.10) and energy barrier diagrams (bottom). In the energy barrier diagram the difference between the solid and dashed lines is for the equilibrium and bias conditions, respectively. The energy barrier diagrams display dominant reaction pathways at each electrode. This is shown at four points in the voltage trace: (a) Beginning of half-cycle: dendrite nucleation is the kinetically slow process. (b) Cell polarization minimum: dendrites present on both electrodes, kinetically fast reaction pathways. (c) Cell polarization maximum: active Li removed from dendrites; electrodissolution transitions to kinetically slow bulk dissolution. (d) Second decrease in cell polarization: pitting becomes the kinetically slow process. 69
4.15 An experimental two-electrode voltage trace showing the dominant reaction pathways at each electrode as a function of time. Shaded regions indicate dominant pathways at the anode (above profile) and cathode (below profile). Unshaded areas represent regions of transition between pathways. 72

4.16 Voltage traces for coin cells cycled in $LiPF_6$ at current densities of 0.5, 0.75, 1, 2, 5, 10 mA cm^{-2}. 73
4.17 Comparison of three very different electrolyte systems ($LiPF_6$, LiFSI, and LiTFSI). (a) Visualization cell images after 900 s of deposition at 5 mA cm^{-2}. A clear difference in dendrite size, nucleation density, and surface coverage is observed. (b) Cell discharge curves at 1 mA cm^{-2} showing remaining capacity after 20 cycles (theoretical capacity 3860 mAh g^{-1}). This performance can be linked to peak position in panel c, where voltage traces for each electrolyte system are shown. 74
4.18 Voltage traces for the different electrolytes studied in this work. Due to the small cell polarization for the LITFSI, a magnified portion of the voltage profile is shown to the right. 75
4.19 Time-dependent EIS measurements for the LiPF6, LiFSI and LiTFSI electrolyte systems. a) Growth of impedance as a function of time for the different electrolyte systems b) EIS spectra after 30 s of contact with fresh Li c) a magnified view of the EIS spectra shown in b). The other graphics show a schematic representation of how ether-based electrolytes decrease the energy barriers of d) nucleation and e) dissolution from the bulk. 76
4.20 Schematic depicting the modified version of the aCE method proposed by Aurbach et al. a) Initial setup of the cell. Starting from this point, the cells were cycled at 1 mA cm^{-2} such that 3.6 C cm^{-2} of charged were passed during each of the galvanostatic half cycles. b) During the final cycle all of the Li was dissolved from one electrode and plated onto the other. The amount of Li lost to SEI formation or through dead/detachment of Li can then be calculated and divided by the number of cycles to determine an aCE value. 77

5.1 XPS analysis of LLZO before and after HT at 400 and 500 °C. (a) C:(La+Zr) atomic ratio as a function of HT temperature; (b) O 1s and (c) C 1s core levels; (d) percentage of total composition of different oxygen species on the LLZO surface as a function of HT temperature after WP. 85
5.2 XPS analysis of LLZO showing the O 1s core level of sample after DP (DP-Control) and after DP and HT at 400 °C (DP-400 °C). 86
5.3 Contact angle measurements of molten metallic Li on (a) Li_2CO_3, (b) DP-LLZO, (c) WP-LLZO, (d) WP-LLZO after HT at 500 °C. 87
5.4 Time-series images showing molten Li droplet bouncing off of a lithium carbonate pellet (A-D), rolling off of a DP LLZO pellet (E-H), and adhering to the WP+HT LLZO surface even when fully inverted (I-L). 88
5.5 (a) Schematic of the all-solid-state Li-LLZO-Li cell, (b) equivalent circuit used for modeling the EIS data, (c) representative Nyquist plot of the Li-LLZO-Li cell (for LLZO heated to 500 °C), as-assembled and after preconditioning at 175 °C. Markers indicate experimental data and dotted lines represent from the equivalent circuit model simulation using the circuit shown in panel b, (d) the Li-LLZO interfacial resistance after preconditioning at 175 °C versus the HT temperature. N = 3 for each HT condition. Error bars represent standard deviations. 90

5.6 (a) DC cycling of Li-LLZO-Li cells (LLZO HT to 500 °C after WP) at RT, stepping the current density from 0.01 to 1 mA cm^{-2}, (b) the CCD versus Li-LLZO interfacial resistance comparing the results of this study with other studies available in the literature, (c) Nyquist plots of a Li-LLZO-Li cell after each 20 cycles for cell cycled 100 times, (d) galvanostatic cycling of Li-LLZO-Li cell at 0.2 mA cm^{-2} for 100 cycles at 0.4 mAh cm^{-2}. The blue dotted line shows the times at which EIS was collected and is shown in panel c. 91

6.1 *Operando* video of TP cell cycling. Time-synchronized voltage trace with cross-sectional optical microscopy of Li/LLZO/Li cell during galvanostatic plating of 0.5 mA cm^{-2} under stack pressure. Flash player must be enabled for playback. 102

6.2 Through-plane cycling in LLZO with *operando* cross-sectional visualization. Images, schematic, and electrochemical data from *operando* TP Li/LLZO/Li cell (a) schematic showing cell geometry, (b) Voltage response of cell during galvanostatic plating at 0.5 mA cm^{-2}, (c) post-mortem image of active area of electrode interface that was plated to, (d-g) Image series from TP visualization cell. 103

6.3 (a) Applied current density and measured cell polarization as current is increased in the TP cell. (b) Optical image of active area of cell after the Li electrode was removed and the interface was gently sanded to reveal the base of the Li filaments. (c) EIS before cycling and after short-circuit. 104

6.4 Demonstration of in-plane visualization platform. (a) Schematic representation of in-plane cell geometry and experimental setup, (b,c) Images of in-plane Li/LLZO/Li cell before and after Li penetration and short-circuit, (d) voltage response of cell during stepped current, with zoom-in shown in (e), (f) Nyquist plots of in-plane cell before and after cycling until short-circuit, and (g) image showing pellet with multiple in-plane cells deposited on the surface. 105

6.5 Measurement of CCD with in-plane cell architecture. *Operando* video microscopy of CCD test on in-plane Li/LLZO/Li cell with time-synchronized voltage response during the current steps. For each current step, 0.25 mAh cm^{-2} of Li was plated in each direction. 106

6.6 Nyquist plot of in-plane cell with as-deposited Li metal electrodes (prior to annealing) with inset of the equivalent circuit model used to fit the EIS data collected throughout the manuscript. 108

6.7 Highest safe current density and cell polarization for each of the in-plane cells with annealed Li electrodes. 109

6.8 Different types or morphologies of Li penetration. Optical images, SEM images, and schematics of straight Li penetration type (a-c), branching type (d-f), spalling type (g-i), diffuse type (j-l). Contrast and brightness adjustments were made to the entire image in (a,j) to make features more evident in in-situ optical images. 110

6.9 Cross-sectional analysis of branching-type Li filament. Post-mortem characterization of Li penetration morphology with scanning electron and optical microscopy. Secondary (a,d) and backscattered (e) electron images of LLZO cross-section through branching-type Li filament at location shown in the optical images shown in (b). Optical image of same area of cross-section shown in (c). 112
6.10 3-D reconstruction of crack bifurcation in LLZO at an impurity. FIB-SEM images of cross-section slices through branching type Li penetration (left) with resulting 3-D reconstruction (right) showing Li penetration in gray and impurities in yellow. 113
6.11 Presence/absence plot for branching-type Li filaments, and the current density at which nucleation occurred for each of the in-plane cells tested. 114
6.12 Cross-sectional analysis of spalling-type Li filament. Secondary (a,c,e) and backscattered (b) electron images of FIB cross-sections through spalling-type Li filaments. Top-down (d) and cross-sectional (f) optical images of the same feature shown in (c). 115
6.13 Video of diffuse type Li penetration. *Operando* video microscopy of CCD test on in-plane Li/LLZO/Li cell with time-synchronized voltage response during the current steps. The Li electrodes in this cell were not annealed prior to testing. Back-lighting was used, making Li penetration features appear as silhouettes. Contrast and brightness adjustments were made to the entire images to make features more evident in the video. 116
6.14 Optical images of the same branching type Li filament with different lighting, as labelled in the panels. CP stand for cross-polarization. 117
6.15 Reversibility and cyclability of Li filaments First cycle. (a) Optical image of in-plane Li/LLZO/Li cell at end of first half-cycle at 75 mA cm^{-2}, (b) corresponding voltage trace, (c) image during second half-cycle before Li is exhausted from filament structures on the left, (d) corresponding voltage trace, (e) image at point in second half-cycle when filament structures are exhausted of Li (disappear from view), (f) corresponding voltage trace, (g) image from end of second half cycle, (h) corresponding voltage trace. 118
6.16 Reversibility and cyclability of Li filaments: Subsequent cycles. (a) Voltage profile of in-plane Li/LLZO/Li cell during galvanostatic cycling at 5 mA cm^{-2} and 10 mA cm^{-2} with points in time labelled corresponding to the *operando* optical images in (b-l). 121
6.17 Analysis of Li propagation rate. (a-c) Schematic representation of Li propagation and relaxation inside of a crack, (d) representative *operando* optical image of a Li-filled crack with areas analyzed in (f) and Figure 6.20 labelled, (e) Plot of crack growth over time during a representative set of current pulses, with a hyperbolic tangent fit of the curve that was used to track crack position, (f) plot of pixel brightness vs. position along a line across the crack tip for frames during and after a current pulse, (g) plot of crack growth rate vs. applied current. 123

6.18 (a) Representative frame from *operando* imaging during pulsed crack growth experiment with lines overlaid where pixel brightness values were extracted. (b) Extracted pixel brightness values after normalization, along with the hyperbolic tangent fit that was used to track crack-tip position over time. 124
6.19 Pulsed current with filament growth measurements. *Operando* video microscopy with time-synchronized voltage response and corresponding measurements of filament growth during short stepped current pulses. 125
6.20 Electron and optical microscopy images of straight type crack propagation. (a,b) SEM images of Li that has been extruded out of the crack where it intersects the surface of the LLZO pellet. (c,d) *Operando* optical images of straight type Li penetration. 126
6.21 High-magnification video of straight-type Li filament propagation. *Operando* video microscopy of an in-plane Li/LLZO/Li cell showing propagation of the Li filament through an LLZO grain, and Li being extruded out of the crack at the surface. 127
6.22 Analysis of in-plane Li/LLZO/Li cell behavior during extended galvanostatic plating. (a-c) *Operando* optical images at different points in time during Li plating, (d) voltage response to the 4 mA cm^{-2} current pulses with inset showing voltage decay after the current pulses for selected pulses, (e) Area-specific resistance (based on the initial electrode areas) of interface, bulk, and total from EIS after each current pulse. (f) Interface capacitance and apparent electrode area after each current pulse. (g) Schematics of void formation at high current densities. (h) Optical images of anode after each current pulse, processed using thresholding and outlier removal in imageJ so that white area represents metallic Li. 129
6.23 Cross-sectional SEM images of FIB-cut Li/LLZO interfaces. (a) after stripping, and (b) after plating. 131
6.24 Demonstration of in-plane visualization architecture in glassy LPS. (a,b) *Operando* optical images of in-plane Li/LPS/Li cell before and after Li penetration. (c) Electrochemical data from cycling of the same cell, with insets (d,e) showing zoom-in on a cycles before and during Li filament nucleation. . . 133

7.1 Schematic representation of an ALD supercycle composed of constituent binary ALD processes (top) and plot of film mass uptake (left, measured by QCM) and chamber pressure (right) vs time (bottom). Each binary process shown (A, B, C) has a mass increase associated with the metal-organic precursor pulse. 143
7.2 Pulse length saturation curves for (a) LaFAMD, (b) TDMAZ, and (c) LiO^tBu with ozone measured by *in situ* QCM, assuming bulk density. 143
7.3 (a) XPS survey scan of an as-deposited ALD LLZO film (inset compares ideal and actual compositions) and (b) plot of Li content (no. of Li atoms/total no. of cations) vs the proportion of total subcycles that is Li. 144

7.4 *In situ* QCM data showing the uptake in mass during the binary processes for LaFAMD/O_3 (a), LiO^{t}Bu/O_3 (b), and TDMAZ/O_3 (c). The mass uptakes during one repeat unit of the supercycle for the LLZO ALD process showing that each process results in growth when combined (d). Wide view of LLZO ALD process showing linear growth over many supercycles. 145
7.5 Plot showing decrease in La:Zr ration as a function of Li pulse proportion in ALD Supercycle as measured by ICP-OES (a). Plot of average La_2O_3 mass uptake during subcycles immediately following various base materials (b). La nucleation is dramatically suppressed when the previous subcycle was LiO^{t}Bu-O_3 and significantly increased when the previous subcycle was TDMAZ-O_3. 146
7.6 (a) SEM image showing as-deposited ALD LLZO film on a Si substrate, (b) SEM image showing the ALD film from the top of a Si trench shown in (c), (d) SEM image showing the ALD coating at the bottom of a Si trench, (e) TEM image showing the ultrathin conformal coating at the tip of a ZnO nanowire, and (f) TEM image showing a sharp film/wire interface, with electron diffraction (inset) showing the amorphous nature of film. 147
7.7 Synchrotron grazing incidence XRD pattern of as-deposited 100 nm LLZO showing amorphous nature of the film. 148
7.8 EIS spectra showing Nyquist plots for a range of temperatures on the IDEs (a) with zoom in on low-impedance region shown in (b). Markers are experimental data and solid lines are fitted curves using equivalent circuit model shown in (c). (d) Ion-beam milled cross-sectional SEM image of ALD film on IDE structure. (e) Arrhenius plot for both TP and in-plane measurements along with the calculated activation energies for each. Conductivities of the films could only be directly measured down to 100 °C due to high impedance. 149
7.9 XRD patterns with peaks assigned to appropriate phases for four annealing conditions: (I) 600 °C rapid thermal annealing with a 10 min hold in a O_2 atmosphere, (II) 600 °C muffle furnace annealing for 1 h in a Ar atmosphere, (III) 900% excess Li film, with 555 °C sealed furnace annealing for 30 min in a He atmosphere with $LiMnO_2$ present as the Li source while the sample was at 555 °C, and (IV) 400% excess Li film, with 540 °C sealed furnace annealing for 30 min in a He atmosphere with $LiMnO_2$ present as the Li source. 151
7.10 (a) Temperature profile measured during *in situ* annealing experiment. Colored triangles correspond to the points in time when the XRD patterns shown in (b) were collected. Lines shown on the top and bottom axes are powder standards for t-LLZO and c-LLZO, respectively (ICSD 246816 and 261302). 152
7.11 Area Detector data from ALD film annealed*in situ* in He environment at 555 °C with $LiMnO_2$ as a Li source to prevent Li loss. The spottiness of many of the peaks indicates a relatively small number of grains sampled, and means that peak ratios may not be statistically meaningful to determine preferential texture within the ALD film. The horizontal axis of the area detector is linear in 2θ, but not in d, so the plot above does not match perfectly, but the intensity and order of the peaks does match. 154

7.12 SEM micrographs showing high-magnification (a) and wide-view (b) ALD film morphology under annealing condition IV in Figure 7.9. Falso color is used to highlight the faceted feature in both (a) and (b). 155
7.13 (a-f) Low magnification optical images showing evolution of film microstructure after annealing at different temperatures. Phase segregation and clear crystalline grains appear starting at 600 °C, with islands forming. These islands remain up to 900 °C, with smaller grains appearing in both 800 °C and 900 °C. These smaller grains can be seen in the SEM images shown in (g, k-m), and in the EDS maps shown in (h-j), which show that the smaller grains are aluminum and lanthanum rich, and zirconium deficient. This matches with the perovskite $LaAlO_3$ impurity observed in XRD patterns observed under those conditions. In addition the film is no longer dense and pinhole free, but rather a porous matrix of interconnected particles as seen in (m). 156

8.1 Characterization of ALD film growth with *in situ* QCM (a and c) and spectroscopic ellipsometry (b and d) showing (a) saturation of growth rate with increasing TIB pulse time, (b) linearly increasing film thickness with number of supercycles, (c) dramatically enhanced growth of the LBCO ALD process compared to the binary boron oxide process, and (d) consistent growth rate across a range of deposition temperatures. 163
8.2 SEM images of etched Si trenches with ALD ZnO (to reduce charging and increase contrast) and LBCO showing conformality. Full trench shown in (a) with locations along height of trench highlighted and shown in (be) with measured thicknesses. 164
8.3 (a) XPS survey scan for 200 °C deposition temperature with insets showing calculated compositions for each as-deposited film at the three deposition temperatures. (b) XPS O 1s core scan showing changes in oxygen bonding environment with deposition temperature. (c) Plot of the ratio of boron to carbon and (d) the ratio of NBO to BO with deposition temperature. All data shown are after 15 min. of sputtering with Ar ions to remove surface layers. 165
8.4 XPS C 1s (A), B 1s (B), and Li 1s (C) core scans for the three deposition temperatures. The C 1s cores were used to determine the relative amount of Li_2CO_3 in the film for deconvolution of the Li_2CO_3 and BO in the O 1s core scans shown in Figure 8.3. 166
8.5 Image and schematic (A) and SEM image and equations (B) detailing how the Pt IDEs were used to measure ionic conductivity in an in-plane cell architecture, along with the equivalent circuit models used to fit the EIS spectra (C,D) 168

8.6 (a) Arrhenius plot for IDE sample with 44 nm film deposited at 260 °C, showing irreversible increase in conductivity upon annealing in Ar glovebox. (b) Plot showing ionic conductivity as a function of deposition temperature. (c) Arrhenius plot for each of the measurement configurations for the 95 nm film deposited at 200 °C. Nyquist plots for 95 nm film deposited at 200 °C for 30, 35, and 40 °C for (d) Pt IDE and (e) TP Li vs. Au. Experimental data are shown by the point markers and the equivalent circuit fits are shown by the dotted lines. (f) Plot showing the thickness dependence of the ionic conductivity for films deposited at 200 °C, two data points are shown for each thickness, but most fall on top of each other and are not visible. 169
8.7 XRD of as-deposited LBCO film at 200 °C on glass substrate with no visible diffraction peaks, indicating an amorphous or glassy structure. 170
8.8 Plot showing reported ionic conductivity values for ALD films since the first report in 2013. Labels correspond with Table 8.1. 171
8.9 Plot of the ASR vs. film thickness showing ionic conductivity iso-lines, with several common and state-of-the-art SSE materials plotted for context. 172
8.10 (a) EIS over time after deposition of a Li metal electrode. (b) Ionic conductivity of an IDE exposed to air and then re-annealed. (c) SPEIS results showing plot of ionic and electronic conductivity as a function of applied potential along with the ionic transference number. (d) CV scan at 0.1 mV s^{-1} showing stability of LBCO in voltage window between 0 and 3.8 volts. (e) Same cell as (b) swept to -0.05 volts showing Li plating and stripping at the blocking stainless steel electrode. 174
8.11 UV-vis spectroscopy of 100 nm 200 °C as-deposited LBCO ALD film on a quartz substrate. Relative transmittance above 90% throughout the measured range is an indication of a large optical bandgap, consistent with the values predicted by DFT calculations. 175
8.12 (a) SEM image of FIB cross-section of full cell stack used in electrochemical measurements. (b) Charge and discharge curves at different rates for full cells, with schematic inset of cell architecture. (c) Discharge capacity at varying rates corresponding for crystalline and amorphous ALD V_2O_5 cathode films (d) plot of discharge capacity and coulombic efficiency for cell cycled at 10C. . 176
8.13 Schematic description of SPEIS method that was used to measure ionic and electronic conductivities as a function of applied potential in a SS vs. Li blocking/non-blocking cell. A DC bias is applied, after sufficient time for the resulting current to stabilize, an average value is taken in the stable region to determine electronic conductivity. Subsequent EIS is performed about the bias potential to extract ionic conductivity from a fitted Nyquist plot. This procedure continues for a range of applied potentials. 182

LIST OF TABLES

TABLE

3.1 Table of XPS survey spectra quantification showing the presence of aluminum before and after Li plating/stripping treatment.[a]180 s Ar Sputter to remove adventitious film. [b]Galvanostatically plated to 8.5 mAh cm^{-2}. [c]Plated/stripped at 1 mA cm^{-2} 43

7.1 For each precursor used, the source temperature, pulse and purge times, growth rate, and number of subcycles in each supercycle. *Carrier gas flow rate increased to 20 SCCM during purge step. 158

8.1 Table of reported SSEs deposited by ALD and their properties, corresponding with the ionic conductivity values plotted in Figure 8.8. 173

LIST OF ABBREVIATIONS

Li lithium

EIS electrochemical impedance spectroscopy

CE Coulombic efficiency

SEM scanning electron microscopy

TEM transmission electron microscopy

XPS x-ray photoelectron spectroscopy

SEI solid electrolyte interphase

ALD atomic layer deposition

LLZO $Li_7La_3Zr_2O_{12}$

LIB lithium-ion battery

LMSSB lithium metal solid-state battery

CVD chemical vapor deposition

TMA trimethylaluminum

EDS energy dispersive x-ray spectroscopy

EDL electrical double layer

CT charge transfer

EV electric vehicle

EC ethylene carbonate

EMC ethylmethyl carbonate

DMC dimethyl carbonate

3-D three-dimensional

aCE average Coulombic efficiency

SSE solid-state electrolyte

LiPON lithium phosphorous oxynitride

SSB solid-state battery

QCM quartz crystal microbalance

LiOtBu lithium tert-butoxide

LaFAMD Tris(N,N'-di-i-propylformamidinato)lanthanum

TDMAZ Tetrakis(dimethylamido)zirconium

Al-LLZO Al-doped LLZO

ICP-OES inductively coupled plasma optical emission spectroscopy

HRTEM high-resolution transmission electron microscopy

IDE interdigitated electrode

c-LLZO cubic garnet phase LLZO

t-LLZO tetragonal garnet LLZO

ICSD inorganic crystal structure database

LBCO Li_3BO_3-Li_2CO_3

AIMD *ab initio* molecular dynamics

DFT density functional theory

TIB triisopropylborate

UHV ultra-high vacuum

NBO non-bridging oxygen

BO bridging oxygen

TP through-plane

ASR area-specific resistance

LBO lithium borate

SPEIS staircase potentiostatic electrochemical impedance spectroscopy

CV cyclic voltammetry

UV ultraviolet

FIB focused ion beam

UHP ultra-high purity

DC direct current

VTIP vanadium oxytriisopropoxide

DP dry polishing

WP Wet polishing

HT heat treatment

CCD critical current density

RIHP rapid induction hot-press

CPE contant-phase element

LPS Li_2S-P_2S_5

XRD x-ray diffraction

RT room temperature

SCCM standard cubic centimeters per minute

BSE back-scattered electron

AFM atomic force microscopy

SSB solid-state battery

ABSTRACT

The grand challenge of climate change has created an enormous need for superior battery technologies that deliver higher energy/power densities at low cost without sacrificing safety and cycle life. Such batteries would enable widespread vehicle electrification, increased use of renewable energy sources, and dramatic improvements for myriad other energy storage applications. One of the most promising approaches to offer a step-increase in energy density, lithium (Li) metal anodes, boast 10x higher specific capacity than graphite anodes. Unfortunately, implementation has been limited by capacity fade and safety concerns that stem from interfacial instability and morphology evolution during cycling.

The primary goal of this thesis is to better understand the interfaces and interphases between Li metal electrodes and electrolytes, and thus enable enhanced performance through interfacial engineering. The work has two primary thrusts: 1) characterization of liquid and solid-state electrolyte (SSE) interfaces with Li metal to observe, correlate, and understand coupled electro-chemo-mechanical phenomena; and 2) development of atomic layer deposition (ALD) films for use as SSEs, interfacial coatings, and interlayers.

In thrust one, *operando* video microscopy is developed to characterize the dynamic changes occurring at Li metal interfaces and correlate them with their electrochemical signatures. This technique is used to develop a comprehensive model of reaction pathways on Li metal electrodes. This model explains how transitions between these reaction pathways, driven by spatially varying kinetics and morphology evolution on the electrode surface, give rise to distinct electrochemical signatures.

To better understand the Li/electrolyte interface in lithium metal solid-state bat-

tery (LMSSB)s, the correlation between surface chemistry, wettability, and interfacial impedance of LLZO SSEs is explored with x-ray photoelectron spectroscopy (XPS) and sessile drop tests. This demonstrates the coupled behavior at the Li/SSE interface and that careful control of surface chemistry can enable higher rate capability. *Operando* video microscopy is adapted to SSE systems. Four distinct morphologies of Li penetration are identified in SSEs, and studied under a range of plating and stripping conditions. The voltage signatures of Li penetration in SSEs are compared with those of liquid electrolytes, to better understand the reaction pathways at the Li/SSE interface. The rate of propagation of Li penetration is quantified as a function of applied current to gain insight into the coupled electro-chemo-mechanical behavior of the system. Void formation in the Li electrode at the Li/SSE interface is observed during deep discharge, demonstrating the importance of morphology evolution during both plating and stripping.

In thrust two, ALD of Al_2O_3 is used to improve the homogeneity of Li flux across the electrode/electrolyte interface. Cycle life and deep discharge performance are doubled. Subsequently, ALD processes are developed for two SSEs, Al-doped LLZO and glassy Li_3BO_3-Li_2CO_3 (LBCO). Challenges with low ionic conductivity and post-annealing of the LLZO films are overcome with the LBCO films, which do not require crystallization to obtain high ionic conductivities. ALD LBCO films demonstrated to have approximately 6x higher ionic conductivity ($2.2*10^{-6}$ S cm^{-1}) than other reported ALD films. The films also have good electrochemical stability at both high and low potentials, and are incorporated into a Li metal battery with high Coulombic efficiency and good cycle life.

In summary, this thesis furthered the understanding and performance of Li metal anodes through the development and use of novel methods of characterization and means of interfacial modification. The implications of this work could aid in the development of next-generation Li metal batteries.

CHAPTER 1

Introduction

1.1 Better Batteries for a Better Society

The United Nations Population Division predicts that by 2050 the global population will reach nearly 10 billion.[1] The rapid growth in population over the past two centuries was made possible by the abundant and inexpensive energy resources provided by fossil fuels. Coal, and more recently oil and natural gas, fueled the industrial revolution, and the technological advances that have followed.[2] Unfortunately, these resources are not only finite and therefore unsustainable, but the combustion products (most notably CO_2) have altered the global climate.[3] These changes, which are ongoing at an increasing rate, pose significant threats to human and natural systems on an alarming scale now and in the future.[4,5] Transitioning away from the use of fossil fuels as quickly as possible is therefore the defining challenge of our time.

Though this is a global challenge, it is illustrative to look at the United States as an example of how energy is consumed and where that energy comes from. In 2018, approximately 80% of energy in the U.S. comes from fossil fuels (Figure 1.1).[6] Renewable energy sources are a growing, but still relatively small (11%) component of the overall portfolio. From these primary energy sources, a little over 1/3 is used to produce electricity, which is then used predominantly by the residential and commercial sectors. The largest of the use sectors, transportation, only uses a very small amount of electricity, and over 90% of

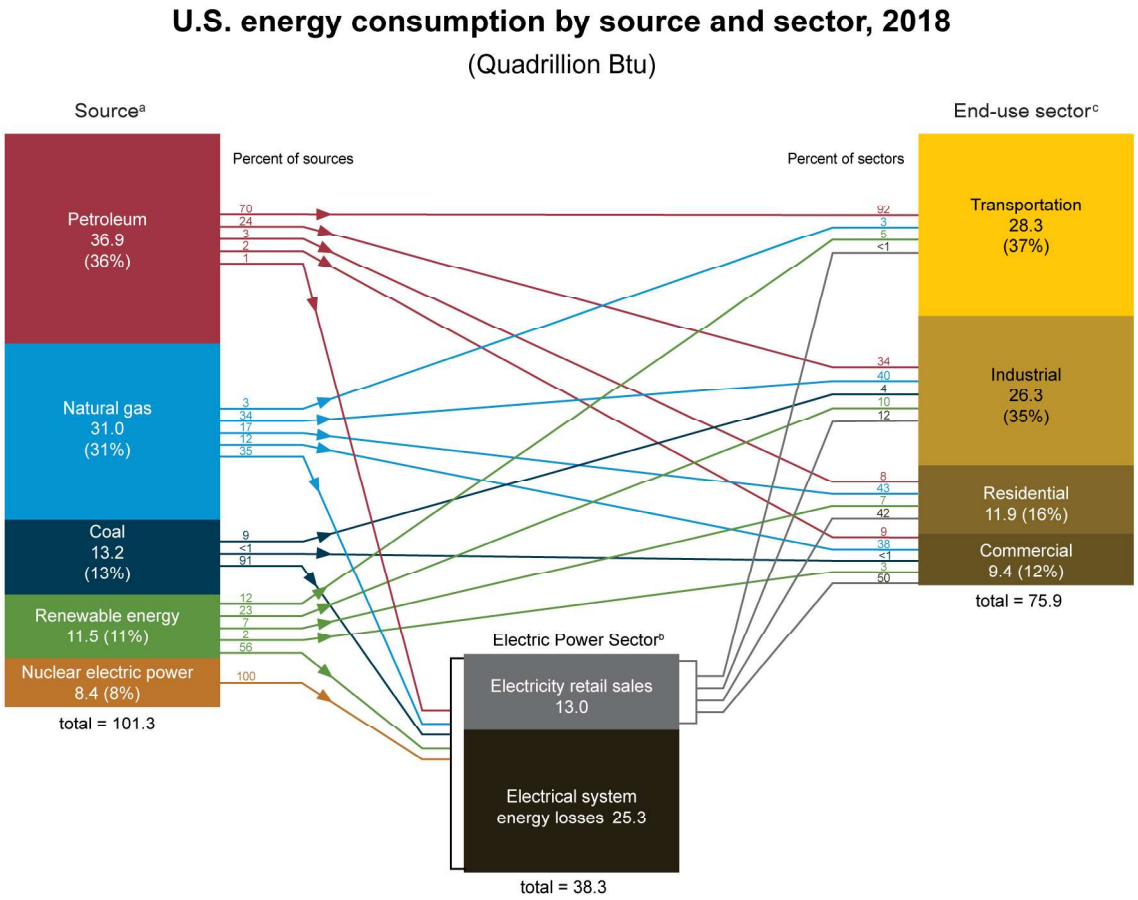

Figure 1.1: *Estimated U.S. Energy consumption by source and sector for 2018.*[6]

the energy consumed comes from petroleum. Though the use of renewable energy sources (Wind, Solar, etc.) is growing, these sources are dominantly used to produce electricity. As the transportation system is currently dominated by liquid fuels, the increasing prevalence of renewable sources has had little effect on the greenhouse gas emissions due to transportation. As shown in Figure 1.2, while the industrial, residential, and commercial sectors have all trended downward over the past several decades, transportation, has remained consistently high.

Electrification of the transportation sector could have a substantial impact on global CO_2 emissions, enabling the use of renewable energy sources for transportation.[8] Great strides have been made in the commercialization of electric vehicle (EV)s over the past decade, but the primary limiting factor remains the ability to safely and efficiently store the

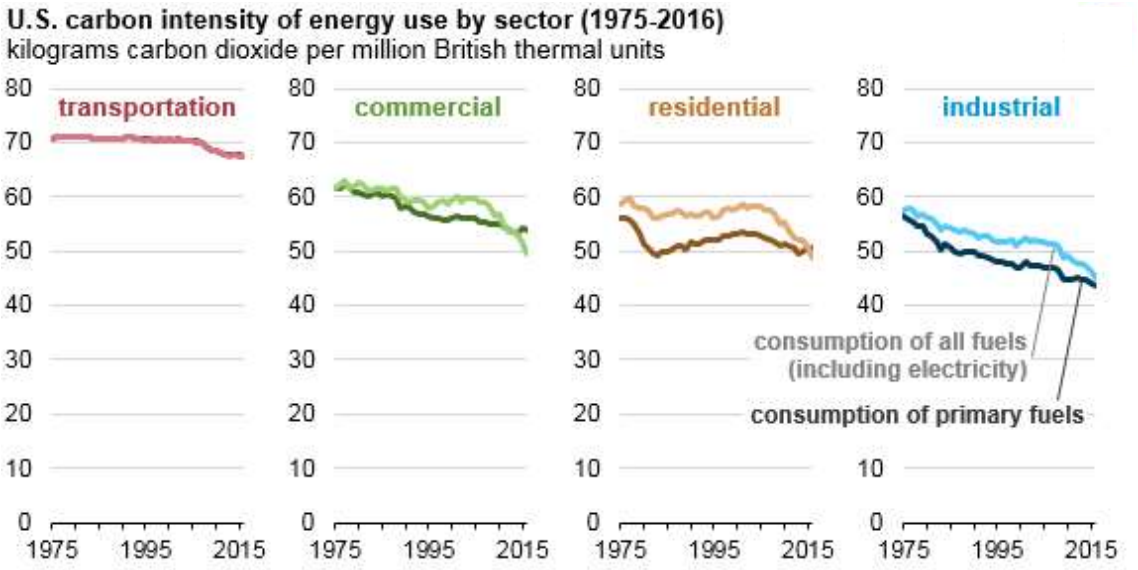

Figure 1.2: *Estimated carbon dioxide emission intensity by sector from 1975-2016.*[7]

electrical energy within a small volume at low cost.[9]

Improvements in battery technology over the past several decades have enabled transformative changes to the way we live, travel, work, play, and communicate. From grid-scale storage to EVs to medical devices, the ability to efficiently store electrical energy and use it on-demand plays a key role in myriad applications.[10,11] Though battery technology has improved dramatically, battery performance and cost remain the main challenges to widespread vehicle electrification.[12]

One attractive option to enable high energy density batteries is to use metallic Li as the negative electrode.[13] This would provide a dramatic (~10x) increase in the specific capacity of the electrode, but also introduces a range of practical challenges. The extreme reactivity and volume changes associated with Li metal anodes cause low efficiency, poor cycle life, and significant safety concerns. Strategies to understand and overcome these challenges are described in further detail in chapter 2 and will be the focus of this dissertation.

1.2 Outline

With the overarching goal of enabling Li metal anodes through improved understanding and control of interfacial properties, this thesis first explores Li metal anodes in liquid electrolytes. Subsequently, the focus shifts to understanding the coupled electro-chemo-mechanical phenomena in bulk SSEs. Finally, it details the development of ALD processes for SSE materials with the goal of enabling high performance interfaces.

Chapter 2 will provide background on some of the most relevant concepts and methods that will be utilized throughout the remainder of the thesis. This will provide a foundation upon which the rest will build. These topics will include the basics of Li batteries, the advantages and challenges of Li metal anodes, SSEs, and ALD.

Chapter 3 will explore the use of ultrathin (1-10 nm) Al_2O_3 layers to suppress dendrite formation upon cycling of Li metal symmetric cells. The optimized coating doubles the lifetime of the anode before failure both under galvanostatic deep discharge conditions and cyclic plating/stripping of symmetric Li-Li cells. The improved performance is attributed to improved electrode morphology resulting from homogeneous Li-ion flux across the electrode/electrolyte interface.

Chapter 4 presents a comprehensive understanding of the voltage variations observed during Li metal cycling, which is directly correlated to morphology evolution through the use of *operando* video microscopy. A custom-designed visualization cell was developed to enable *operando* synchronized observation of Li metal electrode morphology and electrochemical behavior during cycling. A mechanistic understanding of the complex behavior of these electrodes is gained through correlation with continuum-scale modeling, which provides insight into the dominant surface kinetics. More specifically, this chapter explores: (1) when dendrite nucleation occurs, (2) how those dendrites evolve as a function of time, (3) when surface pitting occurs during Li electrodissolution, (4) how kinetic parameters dictate overpotential as the electrode morphology evolves, and (5) how this understanding can be applied to evaluate electrode performance in a variety of electrolytes. The results

provide detailed insight into the interplay between morphology and the dominant electrochemical processes occurring on the Li electrode surface through an improved understanding of changes in cell voltage, which represents a powerful new platform for analysis.

Chapter 5 examines the impact of surface chemistry on the interfacial resistance between the $Li_7La_3Zr_2O_{12}$ SSE and a metallic Li electrode. Control of surface chemistry allows the interfacial resistance to be reduced to 2 Ω cm^2, lower than that of liquid electrolytes. A mechanistic understanding of the origins of ultra-low resistance is provided by quantitatively evaluating the linkages between interfacial chemistry, Li wettability, and electrochemical performance. A combination of Li contact angle measurements, XPS, first-principles calculations, and impedance spectroscopy show that the presence of common LLZO surface contaminants, Li_2CO_3 and LiOH, result in poor wettability by Li and high interfacial resistance. On the basis of this mechanism, a simple procedure for removing these surface layers is demonstrated, which results in a dramatic increase in Li wetting and the elimination of nearly all interfacial resistance. The low interfacial resistance is maintained over one-hundred cycles and suggests a straightforward pathway to achieving high energy and power density solid-state battery (SSB)s.

Chapter 6 explores the coupled electrochemical-morphological-mechanical evolution of Li metal-LLZO interfaces. Quantitative analysis of synchronized electrochemistry with *operando* video microscopy reveals new insights into the nature of Li propagation in SSEs. Several different filament morphologies are identified, demonstrating that a singular mechanism is insufficient to describe the complexity of Li propagation pathways. The dynamic evolution of the structures is characterized, which elucidates the relationship between current density and propagation velocity, as well as the reversibility of plated Li before short-circuit occurs. Under deep-discharge, void formation and dewetting are directly observed, which are directly related to evolving overpotentials during stripping. Finally, similar Li penetration behavior is observed in glassy Li_3PS_4, indicating the relevance of the new insights to SSEs more generally.

Chapter 7 details the development of a thermal ALD process for the pentenary oxide, aluminum doped LLZO. The ability to tune composition within the amorphous as-deposited film is shown and studied using *in situ* quartz crystal microbalance (QCM) measurements and XPS. Postannealing using a variety of substrates and gas environments was performed, and the formation of the cubic phase was observed at temperatures as low as 555°C, significantly lower than what is required for bulk processing. Additionally, challenges associated with achieving a dense garnet phase due to substrate reactivity, morphology changes, and Li loss under the necessary high-temperature annealing are quantified via *in situ* synchrotron x-ray diffraction (XRD).

Chapter 8 details the development of an ALD process for synthesis of amorphous lithium borate-carbonate LBCO films. These films exhibit ionic conductivities up to 2.2×10^{-6} S.cm^{-1}, six times greater than previously reported for any ALD SSE. The high conductivity, coupled with a wide band gap and electrochemical stability window, leads to a total area-specific resistance (ASR) of <5 Ω cm^2 for a 100 nm thick electrolyte and an ionic transference number >0.9999 from 0-6 volts vs. Li metal. The LBCO ALD SSE exhibits stability upon exposure to air, and in contact with both Li metal anodes and cathode materials. Thin-film full cells containing Li metal electrodes exhibit high Coulombic efficiency for over 150 cycles with no capacity fading. These characteristics make glassy LBCO a promising new material for LMSSBs.

Chapter 9 concludes this thesis by summarizing the main contributions to the field and presenting opportunities for future work building upon the discussions from the individual chapters.

1.3 Individual and Group Research Statement

The research presented in this thesis was very collaborative in nature and represents the efforts of not only myself, but many others. It would not have been possible without the

work of my collaborators and coauthors. A brief summary of contributions to these works is below.

Chapter 3 was adapted from Kazyak, et al. 2015.[14] Development and characterization of the ALD process was carried out by Eric Kazyak. Fabrication and testing of the cells, electron microscopy, data analysis, and writing were carried out by Eric Kazyak and Kevin Wood. XPS data was collected and analyzed by Eric Kazyak. Neil P. Dasgupta assisted with revising the manuscript and provided guidance and support.

Chapter 4 was adapted from Wood, et al. 2016.[15] Eric Kazyak designed and built the visualization cell used for the work, and developed the procedure for assembling the cell to achieve reproducible results. Kevin N. Wood, Kuan-Hung Chen, and Eric Kazyak assembled the cells which are shown in the manuscript. Kevin Wood and Eric Kazyak analyzed the results and developed the analytical model. Ji-Guang Zhang provided the ether-based electrolytes. The numerical model was developed and implemented by Alexander Chadwick and Katsuyo Thornton. Neil P. Dasgupta and Katsuyo Thornton provided guidance and support.

Chapter 5 was adapted from Sharafi et al. 2017.[16] Asma Sharafi and Jeff Sakamoto developed the surface treatment process to achieve low interfacial impedance. Eric Kazyak performed the XPS analysis. Eric Kazyak and Andrew L. Davis designed and built the sessile drop testing setup for molten Li, and performed the measurements. Asma Sharafi prepared all samples and assembled/tested the symmetric cells. Seungho Yu and Donald J. Siegel designed and carried out the computational modeling.

Chapter 6 was adapted from Kazyak et al. 2019.[17] Eric Kazyak designed and built the testing setup for the in-plane cell testing. Asma Sharafi, Regina Garcia-Mendez, and Catherine Haslam prepared the LLZO pellets. Eric Kazyak collected and processed the *operando* video microscopy data. William S. LePage assisted with the crack growth analysis code and data analysis. Eric Kazyak performed the focused ion beam (FIB) and scanning electron microscopy (SEM) imaging and three-dimensional (3-D) reconstruc-

tions. Adrian J. Sanchez, Eric Kazyak and Andrew L. Davis performed the COMSOL modelling. Jeff Sakamoto and Neil P. Dasgupta provided guidance and support.

Chapter 7 was adapted from Kazyak, et al. 2017.[18] Eric Kazyak performed all of the ALD process development and characterization. Ashley R. Bielinski and Eric Kazyak performed the *in situ* synchrotron XRD measurements at beamline 33-BM-C at the Advanced Photon source under the guidance of the beamline scientist Dr. Evgenia Karapetrova. Kuan-Hung Chen and Kevin Wood provided ideas for tuning the process conditions to achieve the desired phase. Jeff Sakamoto and Travis Thompson provided insight into the LLZO material and how to make/characterize it. Travis Thompson assisted with analysis and fitting of the XRD data. Xiang Wang and Chongmin Wang performed the transmission electron microscopy (TEM) characterization. Andrew Davis assisted with annealing of the ALD films and with running and analyzing the QCM experiments. Eric Kazyak performed the XPS, inductively coupled plasma optical emission spectroscopy (ICP-OES), and SEM analysis. Neil P. Dasgupta provided insights, guidance, and support.

Chapter 8 was adapted from Kazyak et al. 2018.[19] Eric Kazyak developed the ALD process and prepared all LBCO samples. Kuan-Hung Chen and Andrew L. Davis assisted with film characterization and electrochemical testing. Adrian J. Sanchez and Jose Lasso designed and built the specialized holder for patterning Li evaporation for through-plane (TP) cell fabrication. Ashley R. Bielinski prepared the V_2O_5 films for full cells. Seungho Yu and Donald J. Siegel performed the density functional theory (DFT) and *ab initio* molecular dynamics (AIMD) calculations. Travis Thompson, Jeff Sakamoto, Neil P. Dasgupta, and Eric Kazyak came up with the idea to make lithium borate materials by ALD, and provided guidance for the electrochemical characterization of the film for use as an SSE. Eric Kazyak performed the SEM, XPS, QCM, and electrochemical measurements.

CHAPTER 2

Background

Since the first battery was demonstrated over 200 years ago by Alessandro Volta, improvements to the technology have enabled dramatic transformations to the way that we use electrical energy.[20] One of the most transformative of those developments was the invention of the lithium-ion battery (LIB).[20] While I was writing this thesis, three of the scientists who made major contributions to the development of LIBs were awarded the Nobel Prize in Chemistry, demonstrating the impact that this had on society.[21]

M. Stanley Whittingham first demonstrated the that *intercalation* of Li between layers of titanium disulfide could be the basis of a new battery system.[22] Li-ions were inserted between the layers of a crystalline host material. This mechanism enables rapid and reversible cycling of rechargeable batteries. Though his positive electrode material worked well, the Li metal used as the negative electrode was too reactive and unstable to be commercially viable.

John B. Goodenough then developed an improved positive electrode material, Li_xCoO_2 (LCO), which had a higher potential vs. Li, enabling more energy to be stored.[23] The cells were still limited by the negative electrode until Akira Yoshino demonstrated an intercalation host material that could be used as the negative electrode.[24] He demonstrated that a layered carbon material (graphite) could intercalate a relatively large number of Li^+ ions between its layers, and that they could also be easily removed during recharging. These two materials, LCO and graphite, were used in the first commercially available LIBs intro-

duced in 1991 by Sony, and are still used today.[25] Along the way LIBs have revolutionized laptops, phones, medical devices, and increasingly EVs.[20]

Further advances in battery technology could have similarly transformative impacts on society in the near future.[20] Enabling those advances for the betterment of society is the overarching motivation for this work. Before delving into the details of the work conducted for this thesis, this chapter will briefly cover some of the most important concepts for understanding the work to follow.

2.1 Basics of Lithium Batteries

All rechargeable batteries allow the conversion of electrical energy into chemical energy, and (some fraction of) that energy can then be converted back into electrical energy when it is needed. This section will briefly cover the thermodynamics that underlie the storage of energy within a battery, and that determine the voltage and capacity. Next, the components that make up practical Li-ion batteries will be introduced. Finally, the deviations from ideal behavior that occur when a battery is cycled, and the implications, will be discussed. The content of this section was primarily based on information and equations from Huggins' Advanced Batteries,[26] O'Hayre's Fuel Cell Fundamentals,[27] and Kittel's Introduction to Solid State Physics.[28]

2.1.1 Thermodynamics

In order to power any device, the two terminals (positive and negative) of a battery must be at different potentials. The difference between the two potentials, or the voltage, is the driving force that propels electrons through a circuit in order to do useful work. The different potentials arise due to the difference in the energy levels of electrons in the two electrodes.[26] In any material, the electrons can occupy a range of quantized energy states.[28] The energy level at which there is a 50% probability of occupation is called the Fermi

level.[28] The difference in the Fermi level (ΔE_F) of the two materials determines the open circuit voltage of the battery:[26]

$$V_{oc}F = -\Delta E_F = \mu_{e-}^{A} - \mu_{e-}^{C} \tag{2.1}$$

where F is Faraday's constant and μ_{e-}^{A} and μ_{e-}^{C} are the chemical potentials of electrons in the anode and cathode, respectively. The chemical potential is the incremental change in the Gibb's free energy G of the system if one more of a species is added (assuming constant temperature and pressure):[27]

$$\mu_i = \left(\frac{\partial G}{\partial N_i}\right)_{T,P} \tag{2.2}$$

The chemical potential of a species in a material can be expressed in relation to the chemical potential of that species in its standard state (μ_i°) and the activity (a_i)), which is the effective concentration of the species:[27]

$$\mu_i = \mu_i^{\circ} + RT \ln a_i \tag{2.3}$$

If the activity is close to unity, the species i will behave like the standard chemically pure phase. As the activity, or effective concentration decreases, the chemical potential also decreases, changing the potential of the electrode. This relationship can be expressed as the Nernst equation, which is one of the most useful thermodynamics equations for electrochemical systems:[27]

$$V_{OC} = \frac{-RT}{z_i F} \ln \frac{a_i^{+}}{a_i^{-}} \tag{2.4}$$

where a_i^{+} and a_i^{-} are the activity of species i in the positive and negative electrodes, respectively. This is a fundamental relationship that applies not only in batteries, but in any electrochemical system.[29]

In order for electrons to be freed from the anode, and to move to the cathode, chemical half-reactions (oxidation and reduction) must occur at the respective electrodes. Therefore, the difference in chemical potential can also be thought of as the driving force for the net chemical reaction that is occurring. In any chemical reaction, the difference in the Gibb's free energy of the reactants and the products describes whether a reaction will occur spontaneously.[30] Put simply, whether a reaction is like a ball rolling up or down a hill. If the products have lower energy than the reactants, the reaction will tend to occur spontaneously (like a ball rolling downhill), and the degree of difference between the energy levels determines the amount of driving force (like the height of the hill). This can be expressed as:[26]

$$\Delta G_{rxn} = -zFV_{OC} \tag{2.5}$$

where z is the charge number of the species involved in the reaction (1 for Li^+). Despite the fact that in a battery the half reactions are occurring at the two separate electrodes, the driving force for the overall reaction is the same.

In order to harness this voltage, electrons must be forced through the external circuit. To accomplish this, the two electrodes are separated by an electrolyte/separator which conducts ions, but not electrons. As the electrode materials are not always good electronic conductors, they are typically supported on metal current collectors that are connected with the external circuit.

In order to be a rechargeable, the reactions that occur at each electrode must be easily reversed. To drive the reaction in the "uphill" direction, a voltage is applied to recharge the cell, which "tilts" the energy surface and drives the reactions in the opposite direction as what occurred spontaneously during discharge.[27] As mentioned above, one of the key breakthroughs that has enabled Li-ion batteries is the development of materials that can intercalate, or host, Li^+ ions between layers of their crystal structure.[21] As no major phase transformations need to occur in order for this to occur, and the ions can move into and out of the layers relatively easily, this process can be readily reversed during recharging.[31]

The capacity of these materials, or the amount of charge that can be stored in the electrode, is determined by the number of available sites that can be filled and vacated during cycling. For graphite electrodes, one Li atom can be hosted for every 6 carbon atoms, forming LiC_6.[32,33] So the vast majority of the mass and volume in the electrodes is the host material, rather than the Li itself. This is the primary motivation to transition to Li metal anodes, where all of the mass of the electrode is storing energy. Li metal anodes will be discussed in further detail in Section 2.2.

2.1.2 Kinetics

The thermodynamics described above dictate the open-circuit conditions of the cell, but any useful system will operate at some non-zero current. This means that the actual performance of the cell will deviate from open-circuit conditions. This deviation can be described by kinetics and mass transport *losses*. At the highest level, these losses represent energy from the cell that is sacrificed in order to drive the finite current, analogous to friction or air resistance for the ball rolling down the hill.

During any chemical reaction, including discharging a battery, the reactants must rearrange into the products. Even for a spontaneous reaction, where the endpoint is energetically favorable, there are states in between which are less energetically favorable than even the reactants. The free energy of the system at various states between the reactants and products can be described by an *activation barrier*. As shown by $\Delta G^{\ddagger}$ in Figure 2.1, this is the energy difference between the reactants and the highest energy state during the reaction.[27]

At any temperature above absolute zero, the thermal energy in the system means that at any given time, there is some probability that a reactant species has enough energy to overcome this activation barrier.[27] As charge-transfer is occurring, this means that charge is moving. The rate at which charge is flowing is called current (I). Typically in electrochemical systems it is more useful to make comparisons with current normalized by area,

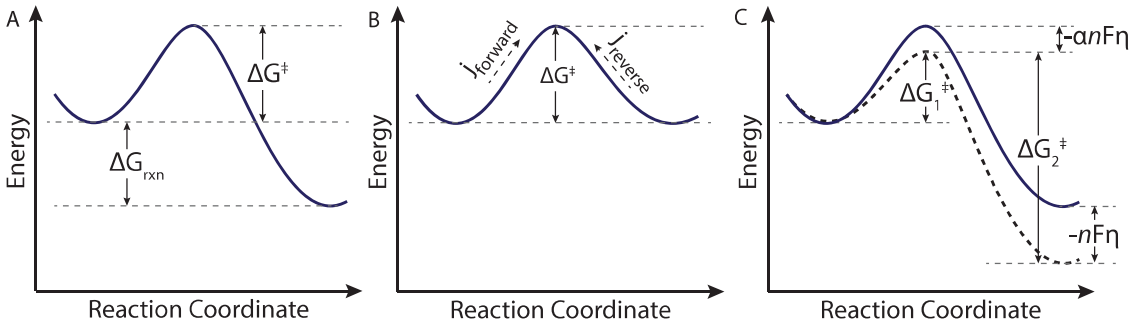

Figure 2.1: *Energy barrier diagram of a reaction before (a) and after (b) dynamic equilibrium has been reached, and with an overpotential of η(c).*

or current density (j).

The current density of the forward reaction (reactants to products) can be expressed in terms of the concentration of the reactants (c_R^*), and rate of decay of reactants into products (f_1):[27]

$$j_{forward} = nFc_R^* f_1 e^{\frac{-\Delta G^\ddagger}{RT}} \tag{2.6}$$

In a battery under open circuit conditions, no electrons can flow from one electrode to the other. Thus, as the forward reaction occurs, an electric field will build up at electrode/electrolyte interface.[26] This electric field will alter the energy diagram shown in Figure 2.1a until the system reaches a dynamic equilibrium, when there is no *net* current (Figure 2.1b). At this point, the rate of the reverse reaction must equal the forward reaction. This current density is called the *exchange current density*, j_0. Since $j_0 = j_{forward} = j_{reverse}$ at equilibrium, Equation 2.6 also describes the exchange current density.

When a battery is charged or discharged and current begins to flow from one electrode to the other, the system is no longer in equilibrium. In order to drive the current during discharge, some of the open circuit voltage must be sacrificed to overcome the activation barriers. This is called the activation overpotential, η_{act}, and the effect is again to alter the energy diagram, but this time so that the forward reaction is more favored than the reverse

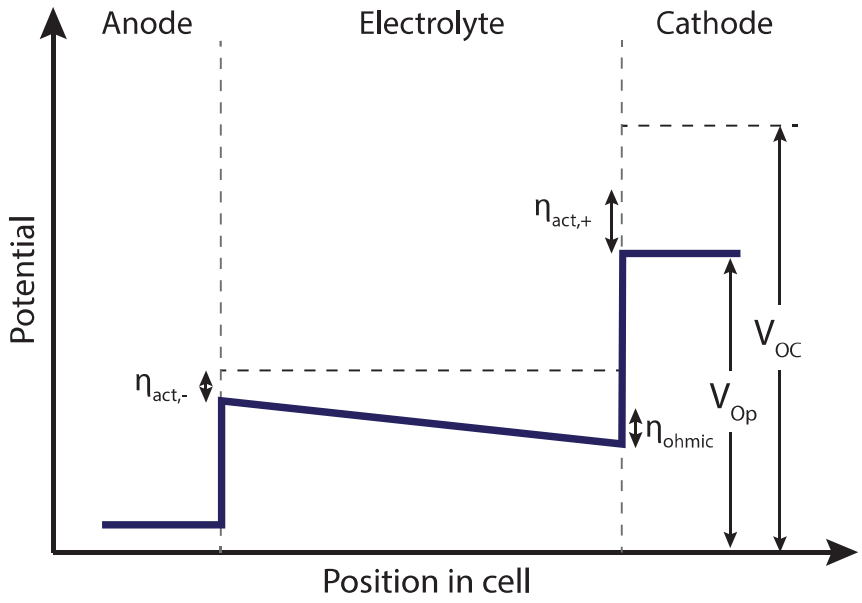

Figure 2.2: *Energy barrier diagram at equilibrium (A) and with an overpotential of η(B).*

(Figure 2.1c). The symmetry of how the overpotential changes the forward and reverse activation barriers is described by α. The net current that flows (and that can be used to do useful work) exponentially increases as a function of how much voltage is sacrificed to drive the current:

$$j_{net} = j_0 \left[\exp\left(\frac{\eta_{act}}{RT}\right) - \exp\left(\frac{-(1-\alpha)nF\eta_{act}}{RT}\right) \right] \tag{2.7}$$

This is called the Butler-Volmer equation, and is very useful to describe the relationship between current and voltage in electrochemical systems.[34] There are overpotentials at both the anode/electrolyte interface and the cathode/electrolyte interface, as shown in Figure 2.2.

In addition, there are losses due to the transport of ions through the electrolyte by conduction, diffusion, and convection, which are denoted η_{ohmic}. These losses create gradients in electric potential, concentration, and pressure, respectively, which each contribute to the flux of ions across the cell. The operating voltage of the cell is then determined by the sum of all of the overpotentials subtracted from the thermodynamic or open-circuit voltage:

$$V_{Op} = V_{OC} - \eta_{act} - \eta_{ohmic} \tag{2.8}$$

In addition to the voltage drop, the concentration gradients that form during cycling of a battery can play an important role. Equation 2.7 does not account for this, but it can be extended to account for changes in the reactant and/or product concentrations as follows:

$$j_{net} = j_0^0 \left[\frac{c_R^*}{c_R^{0*}} \exp\left(\frac{\alpha n F \eta_{act}}{RT} \right) - \frac{c_P^*}{c_P^{0*}} \exp\left(\frac{-(1-\alpha) n F \eta_{act}}{RT} \right) \right] \tag{2.9}$$

This becomes a very important consideration in batteries when discharging or charging quickly. Not only do the ohmic losses required to drive ions across the electrolyte more quickly increase, but the kinetic losses at the interfaces become larger as the concentration of the product (Li^+) increases at the anode and the concentration of the reactant (Li^+) decreases at the cathode. In addition, the equilibrium potential drops due to the change in the activity of the reactants and products (Equation 2.4).

2.1.3 Practical Considerations

To reduce these losses and enable fast charging and discharging, control of the properties of the materials in the cell are critical.[35] For instance, to reduce activation losses, the electrodes are comprised of small particles, rather than monoliths. This creates a large amount of surface area for the half-reactions to occur, thereby decreasing the local current density and requiring less overpotential. The porosity between particles allows the liquid electrolyte to permeate down into the electrode, providing good ionic conduction throughout the electrode. A binder is used to hold the particles together, and a conductive additive is used to aid electronic conduction between particles.

The distance between the two electrodes determines the minimum distance that ions must be transported through the electrolyte. Thus, along with the electrolyte properties, it will govern the ohmic losses and the severity of the concentration gradient that forms.

Therefore, this distance, which is defined by the thickness of the separator, is minimized. However, if the separator is too thin, then any imperfection in the materials, or the manufacturing, or stresses that arise during cycling, may allow the electrodes to touch each other. When this occurs, the electrons can pass directly between the two electrodes, and the cell can discharge extremely quickly. This leads to heating of the cell, which can have catastrophic consequences due to the flammability of the electrolyte.[36]

To this point, it has been assumed that all of the components of the battery are *compatible*. That is, they do not react with each other in undesirable ways when they come into contact. This is not the case in Li-based batteries.[37] While the high voltage (>3 volts) is advantageous for energy density and power output, this also presents practical challenges. The electrolyte is exposed to both the anode and the cathode, and thus should be stable at a wide range of potentials.

The range of potentials within which the electrolyte is neither oxidized or reduced is often called the *stability window*,[38] and is shown in Figure 2.3. If this window does not fall outside of the potentials of the positive and negative electrodes, then the electrolyte will be oxidized or reduced. At the negative electrode, the potential is very low, so the energy level of the electrons is high. Therefore, if there are available energy states in the electrolytes that are below this energy level, the electrons will be injected into the electrolyte and the electrolyte will be reduced. Conversely, if there are occupied energy levels in the electrolyte at higher energy than the positive electrode, then electrons will tend to be injected into the positive electrode (oxidizing the electrolyte). This concept is also important in SSEs, as will be discussed below.

So ideally, the electrolyte should be chosen to meet the criteria for case ii in Figure 2.3. Practically, there are few materials that meet these criteria. In fact, even in today's best LIBs, the electrolyte is not stable against the electrodes.[37] At the very low potentials (high energy) of the negative electrode, the organic solvents and Li salts that make up the electrolyte can easily be reduced. Fortunately, the products of this reaction are ionic conductors

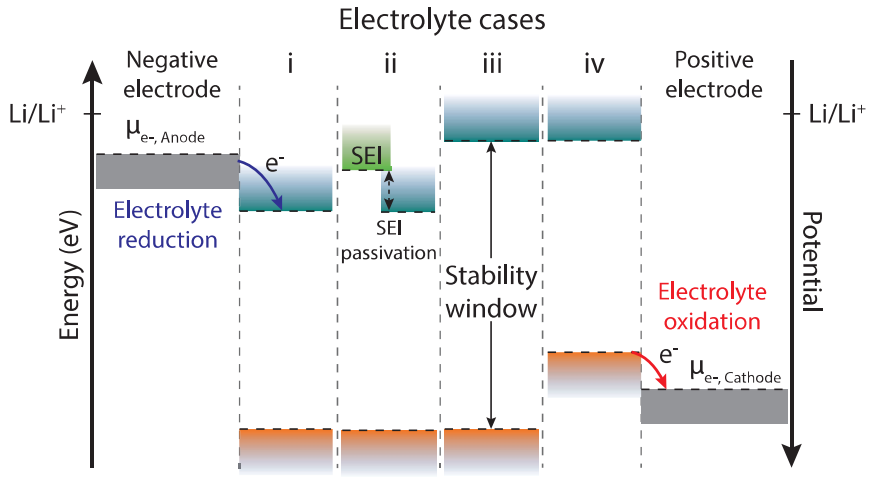

Figure 2.3: *Schematic representation of the stability window for electrolytes in 4 cases, i) reductively unstable at the negative electrode, ii) reductively unstable with SEI passivation, iii) stable at both positive and negative electrodes, and iv) oxidatively unstable at the positive electrode. The unoccupied (blue) and occupied (orange) energy levels are general representations and could be considered as the lowest unoccupied molecular orbital (LUMO) and highest occupied molecular orbital (HOMO) in an organic liquid or as the conduction band minimum (CBM) and the valence band maximum (VBM) in an SSE.*

and electronic insulators. This means that once a layer (called the solid electrolyte interphase (SEI)) forms, it prevents the electrolyte from coming into direct contact with the low potentials of the negative electrode. Over the past several decades, electrolytes have been optimized to form a very stable SEI, and this is why LIBs can be cycled many hundreds or even thousands of times.[35]

2.2 Li Metal Batteries

For mobile systems such as EVs, high energy densities, short recharging times, long cycle-life, and battery safety are essential.[39] Presently, LIBs represent the state of the art in mobile applications. However, the high cost and limited energy density of LIBs have hindered development of long-range consumer EVs.[40] This has sparked renewed interest, particularly since 2010, in using Li metal anodes, as shown in Figure 2.4. As there is no inactive host material, Li metal anodes can store much more charge/energy in the same volume/mass

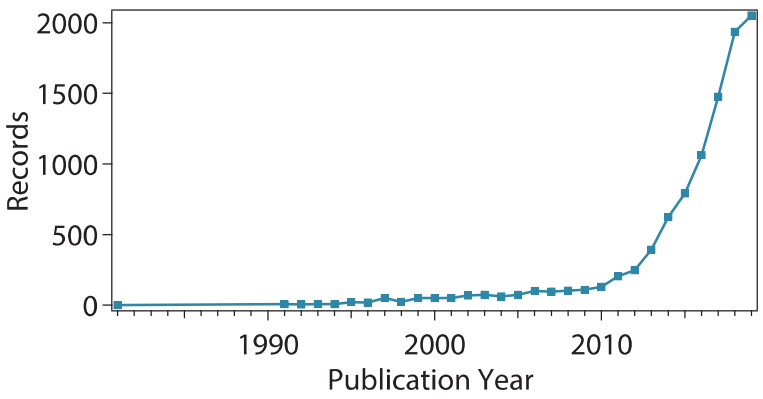

Figure 2.4: *Plot of the number of records on Web of Science for each publication year for the search "Lithium metal anode", as of 11/20/2019.*

compared with graphite (3860 vs. 372 mAh g^{-1}).[41] Additionally, enabling Li metal anodes is a key step towards beyond Li-ion technologies, such as Li-Sulfur and Li-air batteries.[42]

Unfortunately, significant technological hurdles including low Coulombic efficiency (CE), poor cycle life, and safety concerns have prevented widespread Li metal anode commercialization in rechargeable batteries.[43] These challenges can all be linked to the reactivity and volume changes of Li metal. Undesirable side reactions between the electrolyte and electrode form an SEI that does not stabilize, but continues to grow, consuming active Li[44] and leading to uncontrolled dendrite growth. For decades, researchers have tried to solve this problem, but the mechanism of nucleation and continued propagation of dendrites is still not fully understood.

It has been hypothesized that as metallic Li is plated, uneven current distributions resulting from surface inhomogeneities lead to localized hot spots where Li preferentially nucleates.[37] On pristine Li substrates this preferential nucleation results in a subsurface disturbance, causing a localized fracture in the SEI. This exposes the underlying bulk Li metal, leading to the formation of a dendrite (high surface area branching structure) at that location.[45] The dendrite surface immediately forms an SEI, consuming a significant amount of Li. When polarity is reversed and Li is stripped from the dendrite, the structure can become physically isolated via fracture or mechanical failure. Similarly, Li at the base

of the dendrite can be removed, leaving the rest of the structure electronically isolated but still attached to the surface through an insulting SEI layer. Both of these inactive structures are referred to as dead Li and will cause reduced Coulombic efficiency and result in the removal of Li from the active reservoir.[46,47]

While studies have achieved varying degrees of success in inhibiting dendrite growth,[14,41,48–50] there is no consensus on the pathway for mitigation and control of this pernicious effect. This is largely due to the lack of knowledge about the extremely complex interfaces (i.e., those between electrolyte, SEI, native surface layer, and Li metal) where charge transfer (CT) occurs in Li metal anodes.[51,52]

The morphology evolution of Li metal electrodes will be explored in detail in Chapter 4, as the morphology evolution plays a critical role in determining the performance. Due to the lack of a host material, as Li is plated and stripped from the electrode, the volume changes are very dramatic. This is constantly forming new surface area, in contrast with a graphite anode which only undergoes approximately 10% volume expansion during lithiation and as a result the SEI doesn't need to reform after the initial cycles. Many methods to suppress or control the morphology changes have been explored, but among the most promising is the use of SSE in place of the liquids. This will be the subject of Chapters 5 to 8, and will be introduced in the following section.

2.3 Basics of Solid Electrolytes

Solid-state ion conductors have been studied for many decades.[53] If an SSE material could replace the flammable liquid electrolytes that are currently used in LIBs, it could have a range of potential benefits including: dramatically improved safety, enabling Li metal anodes, reducing need for thermal management, and longer cycle life.[31]

Since the liquid electrolyte is the main cause of fires and other safety concerns with batteries, removing the liquid in favor of a non-flammable solid would have clear benefits.[36] If

the solid can suppress dendrite formation and morphology evolution, the challenges with Li metal could be overcome. As SSEs are more thermally stable than the liquids, there would be less need to control temperature in the battery pack, which could dramatically increase energy density and reduce cost at the pack level. Consumption of the liquid electrolyte is a major factor contributing to capacity fade in LIBs,[54] so switching to a solid could potentially enable extremely long cycle life.

To realize these benefits, the ideal SSE should meet the following criteria:

1. **High ionic conductivity -** In order to compete with liquid electrolytes, the material must conduct ions with low resistance.

2. **Low electronic conductivity -** In order to force the electrons through the external circuit and prevent self-discharge, the material must be electronically insulating, with the electronic conductivity at least several orders of magnitude lower than the ionic conductivity.

3. **Chemically and electrochemical stability -** The material should be resistant to oxidation or reduction by the electrode materials. In some cases this may be due to the formation of a passivating SEI like that which forms on graphite electrodes.

4. **Low resistance interfaces with electrodes** - To allow charging and discharging, the interfaces with the electrodes must allow facile charge transport.

5. **Manufacturability -** The material must be able to be easily and inexpensively fabricated as a thin film which can be incorporated into a battery architecture.

6. **Ability to suppress Li metal penetration -** In order to attain the benefit of Li metal anodes, the SSE must be able to prevent the morphology evolution of the Li/SSE interface.

Many materials have been developed that meet one or several of these criteria (Figure 2.5),[55] but meeting all simultaneously has proven challenging. For instance, one of the

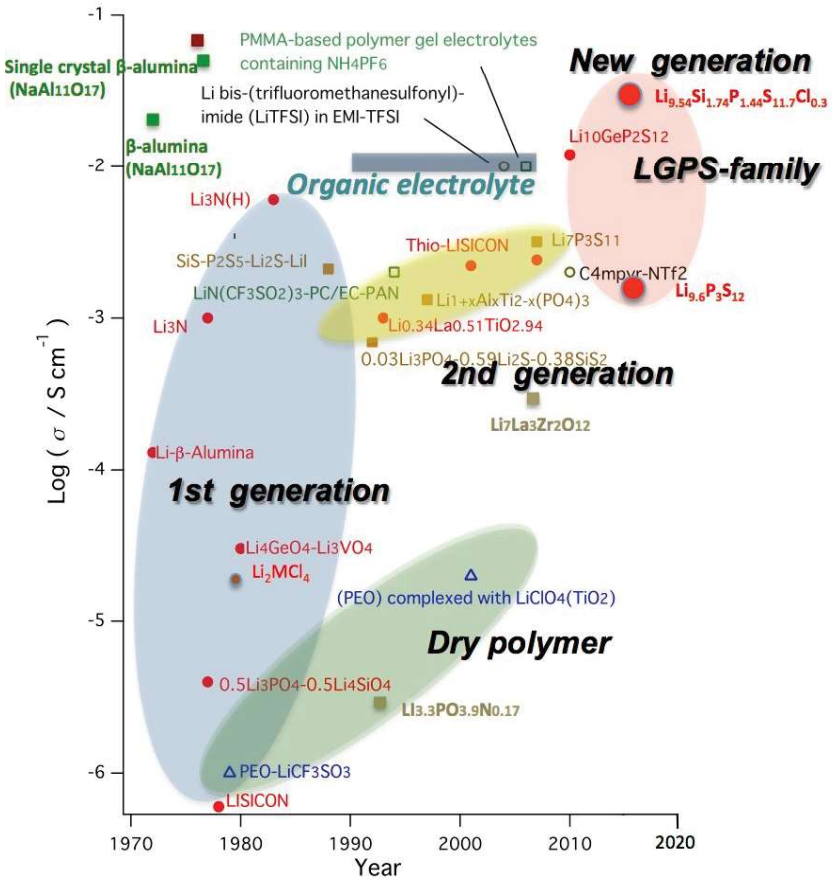

Figure 2.5: *Plot of the ionic conductivity of ALD SSE materials vs. the year of publication. A typical value for an organic liquid electrolyte is provided for reference.*[55]

most mature SSE materials is the amorphous ion conductor lithium phosphorous oxynitride (LiPON). This material is deposited as a thin film via physical vapor deposition (reactive magnetron sputtering). It has a moderate ionic conductivity ($2*10^{-6}$ S cm^{-1} at room temperature (RT)), but has been demonstrated to cycle several thousand times in contact with Li metal.[56] The scale-up has however been limited by the need for vacuum-based deposition and the limited ionic conductivity.

The 2nd and 3rd generation of SSE materials from Figure 2.5 includes a range of oxide and sulfide materials. In general the oxide materials tend to be more chemically and electrochemically stable, but have lower ionic conductivity and are more difficult to process. While the sulfides tend to have very high ionic conductivity (some even higher than

organic liquids), and can be easily processed into thin films, they suffer from limited electrochemical stability and react readily with moisture in air. Each material has its own set of advantages and challenges, but overall criteria 3-6 remain areas of significant research interest, with 4-6 being particularly difficult[13,57–59]

2.4 Basics of Atomic Layer Deposition

In electrochemical systems, there are many processes which occur at the interfaces between two materials (CT, decomposition reactions, mass transfer, formation of SEIs and electrochemical double layers, etc.).[29] The properties of these interfaces and/or interphases often dictate the overall performance of the system. As a result, the ability to precisely control interfacial chemistry and morphology is highly valuable for both understanding and improving interfaces in electrochemical systems.

ALD is a gas phase thin film deposition technique that provides unparalleled control over film thickness and composition even on non-planar substrates.[60] In this thesis, it will be used as a means of depositing ultrathin (generally $<$100 nm, often $<$10 nm) films to understand and improve interfaces in Li metal batteries. As such, the following is a brief review of the principles of ALD and how to characterize an ALD process, along with best practices and factors that should be considered when developing an ALD process. It is a combination of knowledge from a range of sources including several key review papers from George[60] and Miikkulainen et al.[61] and the atomiclimits blog,[62] combined my personal experience. My hope is that in addition to providing context for the work in this thesis, it will be useful to future researchers who are learning and developing ALD processes.

ALD is a modified form of chemical vapor deposition (CVD) in which gaseous precursors are sequentially exposed to the substrate.[60] The precursors are chosen such that they react in a self-limiting manner with the surface. This means that film thickness is not a function of line-of-sight, or position in the deposition chamber, only the number

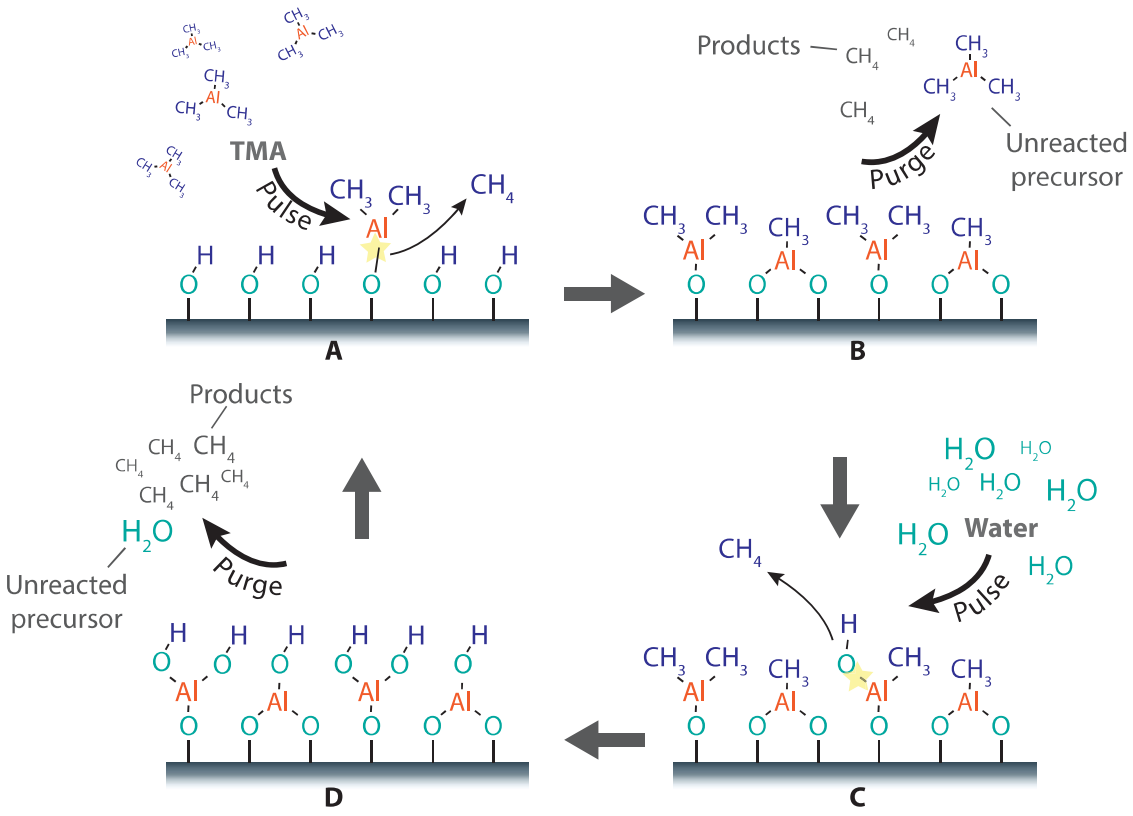

Figure 2.6: *Schematic representation of ALD process with TMA and water.*

of cycles that have been completed.[63] For example, the prototypical ALD process is using trimethylaluminum (TMA) and water to deposit Al_2O_3. The metal-organic precursor (TMA) is the source of the metal (Al), and the water serves as the oxidizer. A schematic of this process is shown in Figure 2.6.

The substrate can be modeled as initially having hydroxyl (OH-) groups on the surface. When exposed to TMA, a ligand-exchange reaction occurs at these hydroxyl sites, leading to the production of methane, and a bond between the Al atom and one or two oxygen atoms at the surface.[64] Once the surface hydroxyl sites have all reacted, no further reaction takes place, as there is no driving force for TMA to react with the methyl groups that now comprise the surface. Once the reaction is complete, the atmosphere can be purged of all unreacted TMA and the methane. Next, water is introduced, and another self-limiting reaction occurs. The water reacts with the exposed methyl groups on the surface to form

a new hydroxyl-terminated surface, forming O-Al-O bonds and again producing methane. Excess water and the methane can then be purged from the system, completing one ALD cycle. This process can be repeated until the desired thickness is achieved.

The TMA and water process is one of the most common and most "well-behaved" ALD process that has been explored.[60] There are a number of properties that are used to determine how "ideal" an ALD process is, and to optimize the deposition conditions. These properties include:

1. Thickness Control
2. Film Nucleation
3. Thickness Uniformity
4. Precursor Dose Saturation
5. Precursor Purge Saturation
6. Temperature Dependence of Growth Rate
7. Film Composition
8. Film Conformality

In a well-behaved ALD process, the self-limiting nature of the reaction makes the mass or thickness increase in each cycle very consistent, typically between 0.2 and 2.0 Å cycle^{-1} (called growth per cycle or GPC).[60,61,64] This means that when the thickness is measured and plotted as a function of the number of ALD cycles, the growth should be linear as shown in Figure 2.7a. As the number of cycles is simply programmed into the deposition recipe, the thickness can easily be controlled with sub-nanometer precision.

Figure 2.7a also shows that some deviations may occur in the first several cycles as the film growth nucleates. This can be caused by differing initial surface chemistry. For

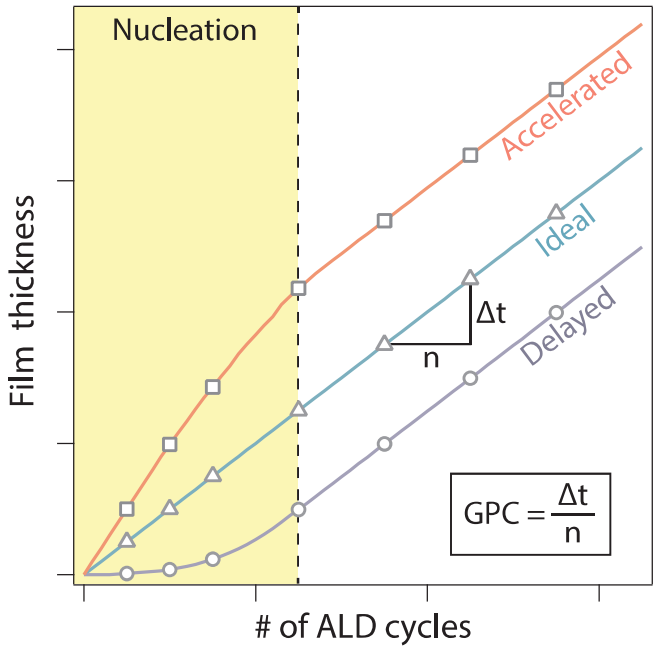

Figure 2.7: *Schematic representation of how film thickness is a function of the number of ALD cycles for ideal, delayed, and accelerated nucleation behavior.*

example, if a surface does not have many (or any) hydroxyl species on the surface, the initial reaction of the precursor with the surface cannot occur uniformly, and the growth rate will be suppressed during the initial cycles. This is called a nucleation delay.[65] In fact this behavior has been utilized to enable area-selective ALD for bottom-up patterning of thin films. Conversely, in some cases, the precursor and substrate may react in a non-ideal way that leads to increased growth initially.[66]

As mentioned above, the self-limiting nature of the reactions means that film thickness should be uniform across relatively large areas, as the growth should not be a function of position in the reaction chamber as long as enough precursor is dosed. Film uniformity can be characterized by measuring film thickness at several positions across the chamber, often with either spectroscopic ellipsometry or electron microscopy. Typical values for well-behaved ALD processes are better than ±2-5% across the reactor chamber.[67]

To verify that enough precursor is being dosed/pulsed into the chamber, a pulse saturation test is done. As shown schematically in Figure 2.8a, this involves measuring the growth

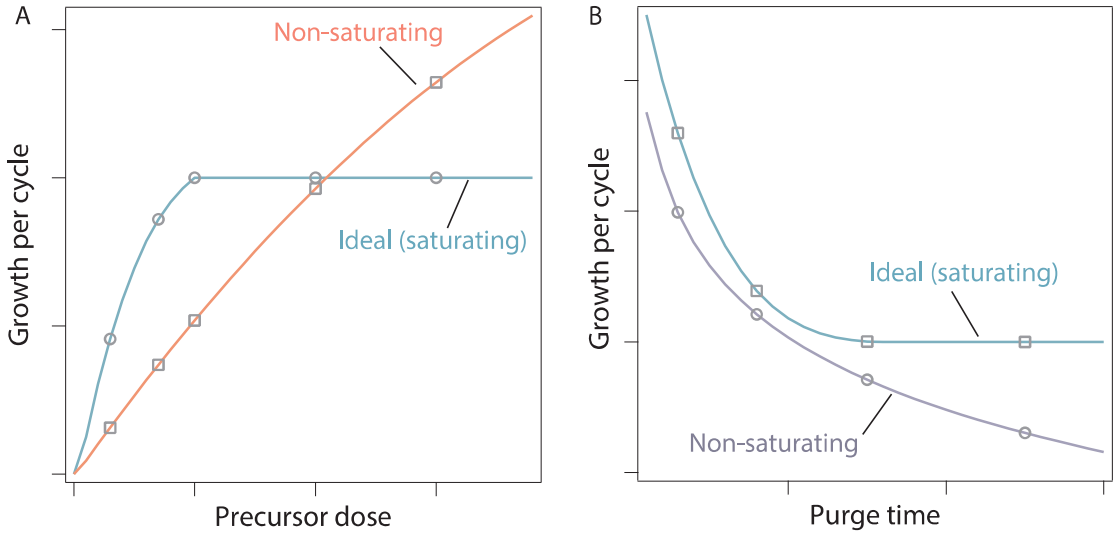

Figure 2.8: *Schematic representation of how film growth per cycle (GPC) varies as a function of precursor dose time (a), and purge time (b).*

per cycle as a function of precursor dose. At small doses, not enough precursor is being introduced to react with all of the available surface reaction sites, so the average growth rate will be low. It is important to measure the thickness at the same location in the chamber for each condition, as the film may be quite non-uniform in the sub-saturated regime. As the amount of precursor is increased the growth rate will increase until it plateaus or "saturates". At this point, increasing the precursor dose will not significantly affect growth rate. A precursor dose that is at or above the saturation point should be chosen to ensure uniform growth. This amount will increase if high surface area substrates need to be coated. If the precursor does not react with the substrate in a self-limiting manner, the growth rate will not saturate, and will continue to increase with increased precursor dose.[60]

A similar test can be done to determine the appropriate purge time after one precursor is dosed before the next precursor dose. Figure 2.8b shows the expected result for GPC as a function of purge time. If insufficient purge time is allowed, residual excess precursor molecules may still be present in the reaction chamber when the next precursor is introduced. This will often lead to non-ideal behavior and increased growth rates.

The deposition or substrate temperatures at which an ALD process exhibits ideal or

near-ideal behavior is often referred to as the *ALD window*.[60] At temperatures above or below this window, some non-ideality begins to affect the growth. Figure 2.9 shows the ALD window and several of the mechanisms that contribute to non-ideal growth when outside of this window. At low temperatures, there may not be sufficient thermal energy to enable facile reaction kinetics between the precursor molecules and the substrate, and very little growth will occur. Another possibility, particularly for precursors that have low vapor pressure, is that the precursor will condense when it contacts the substrate, like frost or dew. This will lead to elevated growth rates and highly non-uniform growth. At high temperatures, the precursor molecules may thermally decompose, enabling non-self-limiting reactions to occur. This growth mechanism is utilized in intentionally in many CVD processes, and leads to high growth rates.[68] Finally, after a precursor reacts or chemisorbs to the substrate, at high temperatures, the precursor may desorb from the surface, leading to lower growth rates. Not all ALD processes exhibit a region or window where the growth rate is constant with temperature, but saturating or self-limiting growth may still be observed. In these cases, it is especially important to maintain temperature uniformity across the substrate in order to obtain uniform film thickness.

As mentioned above, one of the unique and attractive capabilities of ALD is to deposit films with uniform thickness on complex 3-D substrates. Though it is sometimes overlooked, this is one of the most robust means of demonstrating ideal ALD behavior.[69] No other deposition process can achieve the degree of uniformity or *conformality* in 3-D structures that ALD can. As an example, ZnO deposited by ALD using diethylzinc and water onto *Morpho* butterfly wings, which are comprised of complex nanostructures is shown in Figure 2.10.[70]

Conformality can be quantified by measuring the difference in film thickness from the top to the bottom of a 3-D structure with a given aspect ratio (ratio of height to width), as shown in Figure 2.11. It is also be useful to measure the thickness in a geometry that has re-entrant texture (overhangs) like the butterfly wing, as this further tests the conformality,

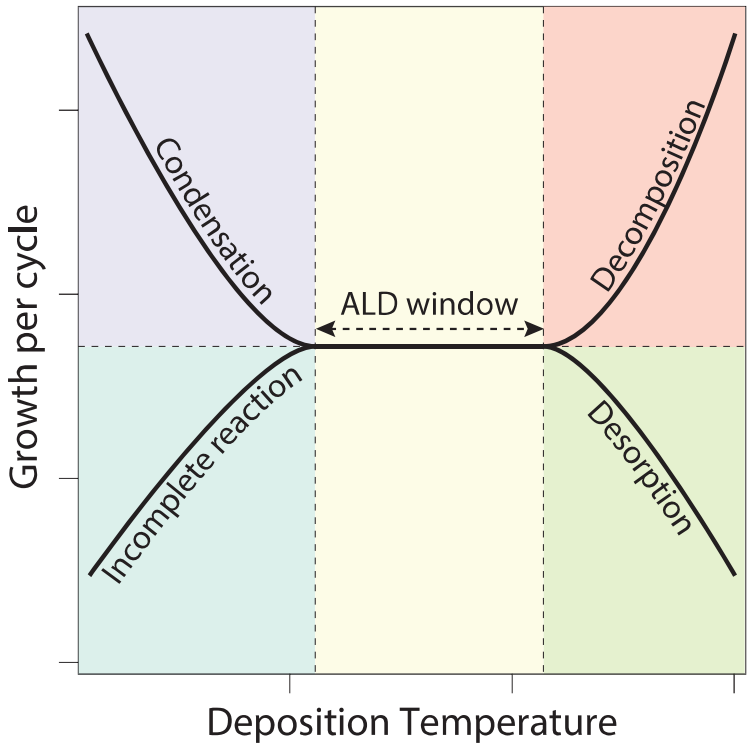

Figure 2.9: *Schematic representation of the temperature dependence of growth rate for ALD processes that may exhibit condensation, incomplete reactions, precursor decomposition, and/or desorption. It should be noted that not all ALD processes exhibit a typical ALD window.*

and better distinguishes from line-of-sight techniques such as physical vapor deposition. In Chapters 7 and 8, etched trenches in Si are used for this purpose.

Last but not least, the composition of the resulting film needs to be the desired material, and can also give insight into the ideality of the process. For example, carbon content is often used to detect non-ALD behavior, as in many processes carbon incorporation is indicative of CVD-like behavior where precursor ligands are incorporated into the film as it grows. This can be characterized in a number of ways, but XPS is perhaps the most common due to its surface sensitivity, bonding environment information, and ability to detect all elements atomic number 3 and above.

The uniformity/conformality, thickness control, relatively low deposition temperatures, and ability to deposit a wide range of materials make ALD a valuable tool for a range of applications.[63,71–74] It has enabled dramatic improvements to front-end and back-end

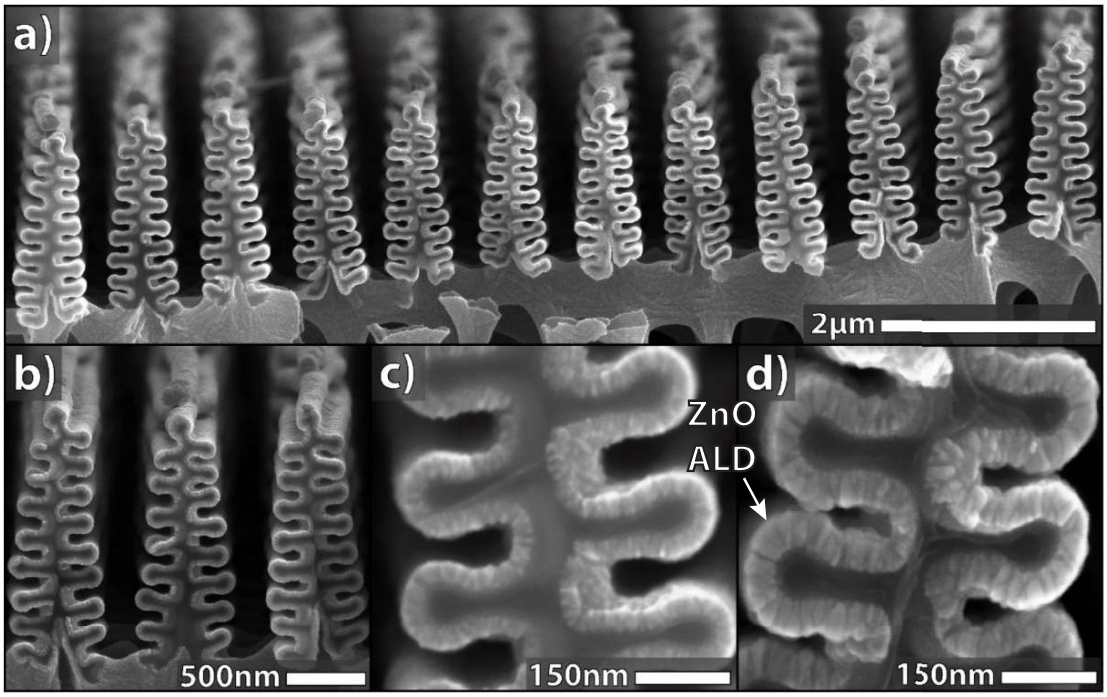

Figure 2.10: *Cross-sectional SEM images of ALD ZnO films on Morpho nanostructures.*[70]

semiconductor processing for fabricating ever-smaller transistor arrays.[75,76] More recently, it has been demonstrated to have great promise for a range of other applications including photovoltaics and batteries.[77,78] It has been shown to dramatically improve interfaces in bulk Li-ion batteries, and ALD-modified battery materials are being commercialized by several companies.[79]

2.4.1 ALD Process Development

Though there are many ALD processes that have been demonstrated previously, in chapters 7 and 8, new processes will be developed in order to deposit multinary (multi-component) oxide films that have desirable properties for use in batteries as SSEs. When developing an ALD process, there are many factors that must be taken into account in order to achieve optimal film deposition. These include:

1. Which precursors to use?

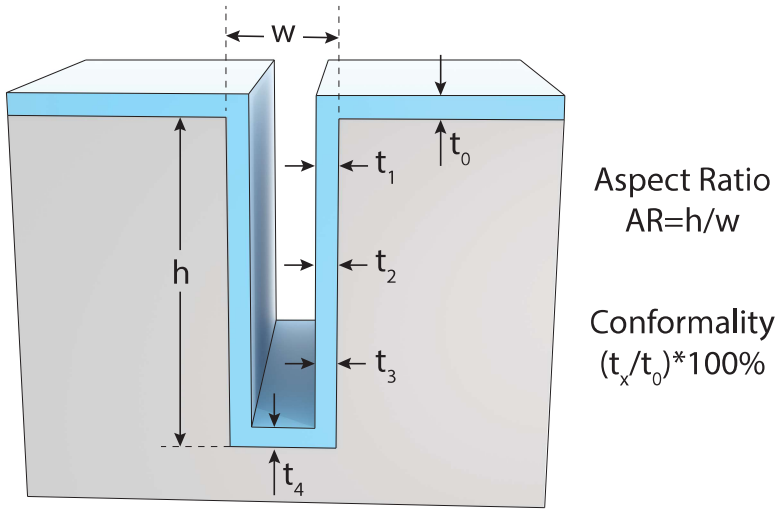

Figure 2.11: *Schematic representation of measurements needed to calculate the conformality of an ALD film in a trench of an arbitrary aspect ratio.*

2. What source temperature for the precursors?

3. What temperature should the substrate be during deposition?

4. How long to pulse and purge each precursor?

The specific conditions use may influence the growth rate, uniformity, composition, phase, etc. of the film. Therefore it is important to understand and control the effects of each parameter to achieve the desired product.

In many cases when developing ALD processes, there are existing precursors that have been used for similar chemistries. For example, when developing a process for a multinary oxide, you can often combine the processes used for each component oxide (eg. [TMA+H_2O]+[diethylzinc+H_2O] to deposit Al-doped ZnO). I will call this the *Supercycle* approach, as the full repeat-unit of the deposition process includes multiple *subcycles* each corresponding to one or more of the constituent materials. This does not always have straightforward results, however, as film nucleation may be strongly dependent on the previous subcycle, and thus the combination of the two binary processes may not obey the rule of mixtures.[80] This can make predicting the composition of a multinary process difficult.

In addition, it can be a daunting task to select which precursor to use when developing a new ALD process.

There are a wide variety of metal-organic precursors and oxidants that have been used for ALD, enabling deposition of films that can contain well over half of the elements in the periodic table. This includes oxides, sulfide, nitrides, fluorides, metals, and more. All of the ALD processes presented in this thesis will be oxides, so this discussion will focus on those processes. When identifying potential precursors to use when developing an ALD process, there are several considerations including but not limited to:

1. Deposition temperature range
2. Decomposition temperature and stability
3. Vapor pressure
4. Reactivity with different oxidizers
5. Adsorption/desorption
6. Growth rate
7. Contamination levels in film
8. Safety
9. Cost

Depending on the target application, the range of temperatures can be important, as in some cases the substrate may not be stable at high temperatures. For example, in chapter 3, ALD will be used to coat Li metal, which melts at 180.5 °C. Therefore, the precursor used must work at temperatures that avoid melting the substrate. In addition, when developing a multi-component process, the ALD windows (Figure 2.9) for each precursor used must at least overlap so they can be used together in the same process. For example, if one

precursor only reacts completely above 250 °C and another decomposes at temperatures above 200 °C, there is no temperature at which can they be used together. Deposition temperature requirements may also be a consideration when considering manufacturability, as high temperature processes are more expensive due to energy and materials costs.

Another consideration is the stability of the precursor at high temperatures. This is important not only for the deposition temperature, but for the temperature at which the precursor source is kept. Some precursors may be stable at high temperature for short periods of time and therefore deposition is not affected, but when kept at elevated temperatures for long periods of time, they may decompose. Many precursors must be heated in order to achieve sufficient vapor pressure to dose into the reactor. If sufficient doses cannot be achieved at a temperature where the precursor is stable, this can present significant challenges. Therefore, both the thermal stability and the vapor pressure as a function of temperature are important considerations during precursor selection.

While there are hundreds of different metal precursors that have been explored for depositing various metal oxides, there are fewer choices of of oxidants. The most common are water, ozone, and oxygen plasma. Certain metal precursors may react more readily (and more ideally) with certain oxidants. Additionally, depending on the application and substrate, certain oxidizers may be preferable. For example, plasma and ozone based processes are stronger oxidizers but may damage some substrates, and may not be able to penetrate as deep into high aspect ratio structures. Some substrates may be contaminated with exposure to water. Therefore, consideration of the counter-reactants needed for each metal precursor is important when developing a multinary process.

The interactions of precursors with the substrate and the reactor walls may vary between different precursors and with temperature. This will affect the required exposure times and purge times. For example, water tends to exhibit strong physisorption on surfaces, particularly at temperatures below its boiling point. This means that low temperature processes utilizing water may require longer purge times. In addition, the reaction of precursors with

substrates may not be particularly fast. This can be due to a large activation barrier that makes the reaction sluggish, even at elevated temperatures. In these cases, the exposure time may be the limiting factor rather than the amount of precursor dosed. For these precursors, a modification to the reactor may be necessary to enable prolonged exposure of the precursor to the substrate to allow for the reaction to occur. This can be accomplished either by using a bubbler to deliver the precursor vapor to the reaction chamber more steadily over time, or by using a valve to isolate the chamber from the vacuum pump temporarily before purging continues. If this requirement is not compatible with the hardware available, this may impact precursor selection as well.

In addition, the growth rate per cycle, film purity, safety, and cost of a precursor may affect precursor selection. These factors may be particularly important when considering the scalability of a process for a specific application. The speed, safety, cost, and quality of a process are important considerations for manufacturability.

CHAPTER 3

Atomic Layer Deposition for Protective Coatings on Li Metal

Adapted with permission from Kazyak, E.; Wood, K. N.; Dasgupta, N. P. Improved Cycle Life and Stability of Lithium Metal Anodes through Ultrathin Atomic Layer Deposition Surface Treatments. *Chem. Mater.* 2015, 27 (18), 64576462.

Motivated by the possibility of high energy densities if Li metal anodes could be stabilized. The first chapter of this thesis studies the role of ultrathin Al_2O_3 coatings deposited by ALD on cycling of Li metal symmetric cells.

Work in the field of Li-ion batteries has previously shown that nanoscale coatings can significantly improve the cyclability and rate capability of a variety of anode and cathode materials.[81–84] Several of these studies have shown that ultrathin Al_2O_3 layers can suppress SEI formation after electrolyte exposure, leading to reduced capacity fade and improved cyclability.[82,85,86] Recent work has also attempted to stabilize the surface of Li metal anodes either through electrolyte modification or by interfacial layers to improve the homogeneity of Li electrodeposition and stripping.[41,50,87–90] However, the majority of these papers have not explored direct coatings on the surface of bulk Li metal electrodes due to challenges associated with air instability and the low melting temperature of Li. Investigation of controlled Li electrodeposition on Cu current collectors has demonstrated the importance of improved homogeneity of Li flux to avoid dendrite formation.[50,87] Therefore, it is valuable

to extend this knowledge to facilitate homogeneous Li flux on bulk Li metal electrodes to prevent dendrite formation and enable their use in battery manufacturing.

ALD has been demonstrated as a promising approach for atomically precise modification of electrode/electrolyte interfaces. many ALD chemistries can be deposited at low temperatures in an inert environment, allowing deposition on sensitive substrates such as Li metal. ALD has been recognized as a potential means of engineering the SEI in battery systems.[71,82,86,91–93] Despite these promising results, direct ALD on the surface of Li metal had only been reported in one other study, which demonstrated that 14 nm Al_2O_3 layers (approximately 117 ALD cycles based on a reported growth rate of 1.2 Å cycle^{-1}) were able to delay corrosion in a variety of environments including air, organic solvents, and polysulfides. Significantly improved capacity retention was observed for this approach in Li-S cells after the first 100 charge/discharge cycles.[94] However, questions remained on the effects of ALD treatments upon extended cycling and eventual electrode failure. In particular, the effects of ALD on the morphological evolution of dendrites through failure, as well as the improvement of total cycle life, have not been investigated.

In this work, we present a study of ultrathin (<30 ALD cycle) Al_2O_3 coatings deposited directly on Li metal anodes without air exposure using a glovebox-integrated ALD tool. This represents a thickness regime of 2-3 nm, which is approximately 5 times thinner than was investigated previously.[94] The glovebox-integrated ALD tool allows the surface of Li metal to be precleaned, ALD treated, and assembled into coin cells under an inert (Ar) environment. Al_2O_3 was chosen as a coating material for three reasons: (1) for its ability to form passivating surface films when in contact with standard electrolytes, as demonstrated in several studies on standard Li-ion electrodes; (2) Al_2O_3 can react with Li to form a thermodynamically stable Li-ion conducting $LiAlO_x$ SSE;[95] and (3) ALD of Al_2O_3 can be completed at low temperatures, which are well below the melting point of Li.[96] All of the experiments presented herein were performed on symmetric Li/Li cells to provide a clear investigation of the behavior of ALD treated and untreated Li metal without the

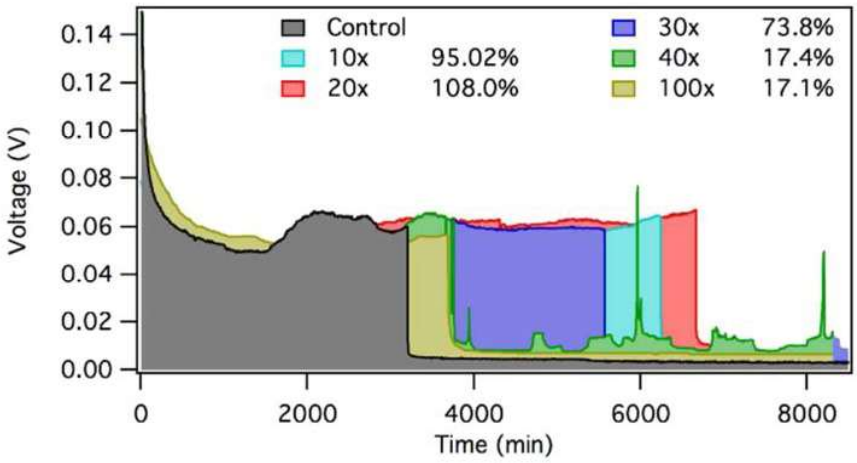

Figure 3.1: *Galvanostatic testing of Li symmetric cells at 1 mA cm^{-2}. After an initial reduction in overpotential losses, stable behavior is observed until sudden failure. Failure time is observed to vary as a function of ALD coating thickness. Percentage improvement is relative to control.*

need to decouple cathode effects.[44] The results demonstrate that after a pretreatment of only 20 ALD cycles, dendrite formation on the Li surface can be dramatically suppressed at a current density of 1 mAh cm^{-2}, leading to a doubling of the lifetime of the Li metal electrodes before shorting occurs.

3.1 Results and Discussion

To study the effect of ALD coating thicknesses on Li electrode failure, galvanostatic electroplating was performed. To avoid confusion between a single ALD deposition cycle and an electrochemical charge-discharge cycle, from this point on, we will indicate the number of ALD cycles with x (e.g., 20x indicates 20 ALD deposition cycles). Figure 3.1 shows the overpotential required to remove Li at one electrode and deposit Li at the other as a function of time. Initially, a decrease in overpotential is observed for all treatments, which has been attributed to the formation of an SEI layer.[44] After about 10 hours of operation, all cells reach a more stable voltage before an eventual increase in overpotential approaching failure. At the end of the cell lifetime, a sharp drop in voltage is observed as shorting occurs.

This is consistent with previous observations of short-circuiting due to dendrite growth in Li symmetric cells (this can be followed by erratic voltage behavior as current pathways are broken and reformed).[97] From Figure 3.1, it can be clearly seen that all treatments appear to show some improvement. The 20x sample appears to have the greatest effect, improving cell life by over 100% when compared to the uncoated control sample. The net charge passed in the 20x sample represents nearly 75% of the total anode thickness, demonstrating the ability of the ALD process to enable deep discharge in Li metal (over 100 mAh cm^{-2} or 525 μm Li assuming 100% faradaic efficiency). This is critical for the use of bulk Li metal electrodes in batteries, as deep discharge is required to fully utilize the cell capacity.

To determine the effects of ALD treatment on cycle life of Li metal electrodes, cyclic charge/discharge was conducted at a constant current density of 1 mA cm^{-2} for the control, 20x (2-3 nm), and 30x (3-4 nm) samples (Figure 3.2). In this experiment, the failure point was defined as a sudden drop in overpotential and erratic voltage behavior (e.g., change of 100 mV or greater midcycle during either the charge or discharge step). The presumed source of this erratic voltage behavior is the formation and subsequent isolation of shorting pathways, which is attributed to the formation and detachment of dendrites.

Similar to the results in Figure 3.1, an initial decrease in overpotential was observed in Figure 3.2, followed by long periods of stable, consistent overpotentials. After differing times for each sample, a steady increase in voltage is observed leading up to failure. It has been observed previously that rapid increases in overpotential can be attributed to electrolyte decomposition.[44] Therefore, we hypothesize that the steady increase in overpotential as the cell nears failure is a result of electrolyte drying-up and/or decomposition leading to formation of excessive SEI and inactive Li material. Compared with the galvanostatic results, this increase in overpotential near failure is significantly more dramatic, likely due to thicker SEI formation and high quantities of dead Li created during cycling, which leads to greater electrolyte decomposition. The results of Figure 3.2 indicate that 20x of Al_2O_3

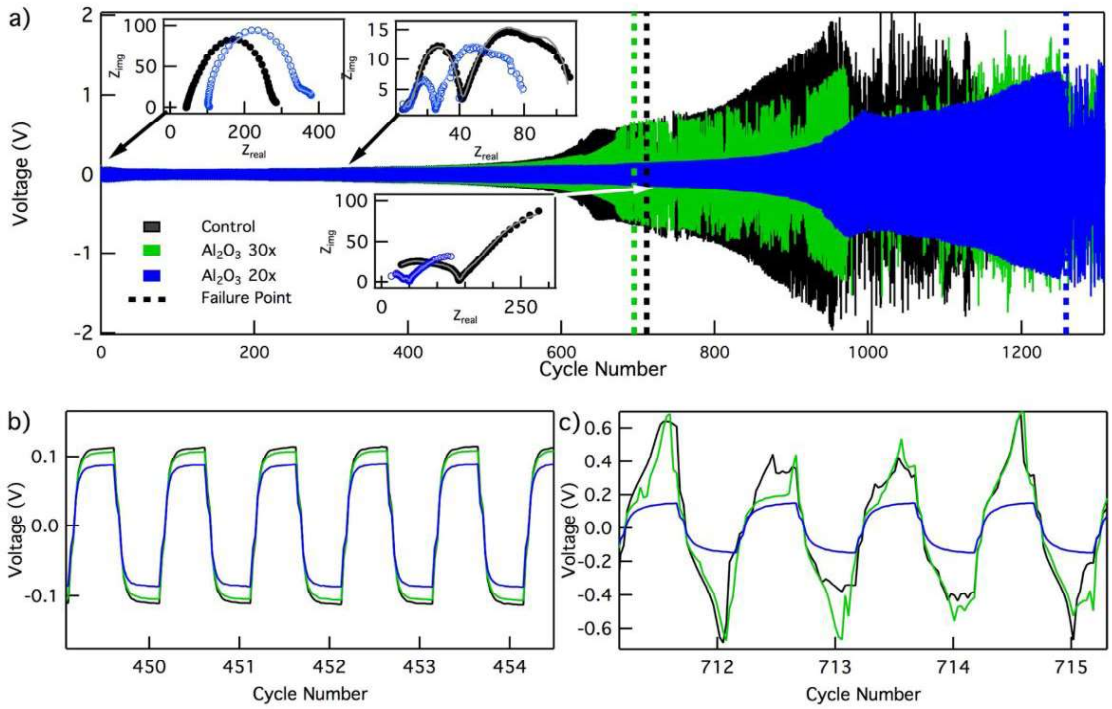

Figure 3.2: *(a) Constant current charge/discharge voltage profiles for Li symmetric cells showing the effects of ALD coatings on overpotential losses at 1 mA cm^{-2}. Each half cycle represents 0.25 mAh cm^{-2}. In this plot, the dotted lines represent the point of failure for each cell. For the control sample, this was 711 cycles for the 20x; this point was at 1259 cycles. All cells were tested to failure. EIS measurements taken after 0, 300, and 700 cycles are shown in the insets. (b) Zoom in on stable voltage overpotential regime. (c) Zoom in after failure of control and 30x samples, showing erratic voltage behavior while the 20x sample remains stable.*

limits the onset of dendrite growth and electrolyte decomposition during cycling, which improves cell life by over 80%, consistent with our galvanostatic results.

Electrolyte loss can be observed directly upon post-mortem cell disassembly and inspection. The separator material is no longer saturated with liquid electrolyte after failure, whereas separators from cells disassembled during the stable region (cycles 50 to 500; see Figure 3.2b) are still mostly saturated. Electrolyte decomposition or drying can exacerbate hot spots; because as the cell dries, there is less active area exposed to electrolyte, and therefore, the active areas of the cell experience a higher effective current density. At these current densities, unstable dendritic growth is accelerated, and shorting occurs resulting in cell failure (Figure 3.2c). The onset of erratic behavior, which could be attributed to clearing of a dendrite short, always occurs after the first short is observed.

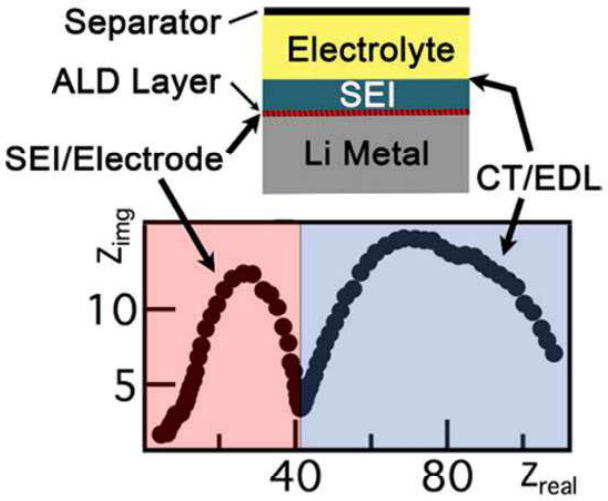

Figure 3.3: *Schematic of interface locations in cell, correlated with the relevant features in a sample EIS spectra.*

To gain insight into the evolution of the cell performance, electrochemical impedance spectroscopy (EIS) was performed at the three different regimes of cell cycling (initial: 0 cycles; stable voltage: 300 cycles; and rising voltage: 700 cycles), as shown in the insets of Figure 3.2a. It is worth noting that these two electrode EIS measurements represent the full Li-Li cell impedance, with contributions from both electrodes. The initial spectra show a slight increase in overall impedance as a result of the ALD treatment compared to the uncoated control. Once a stable voltage profile is achieved, distinct semicircles appear which have been attributed to impedances associated with both the SEI/electrode (high frequency) and the CT/electrical double layer (EDL) (lower frequencies), as illustrated in Figure 3.3. Previous studies of Li metal anodes have also suggested that these two components may consist of multiple RC circuits due to the complex nature of the multi-layer electrode/electrolyte interface.[46] Consistent with those findings, our data shows two distinct regimes that likely correspond to a superposition of RC circuits, which allow us to differentiate SEI/electrolyte interactions and CT/EDL interactions.[98]

Comparing the 20x Al_2O_3 treated sample with the control Li electrode after 300 cycles, a significantly smaller arc associated with SEI/electrode impedance is observed in the ALD

sample; however, the CT/EDL properties remain nearly the same. This is consistent with the assumption that the role of the ALD treatment is to modify the interfacial properties between the electrode and SEI, providing valuable insight into the mechanism of improved performance. Again, after 700 cycles, a similar behavior is observed for the SEI/electrode impedance; however, the CT/EDL properties are significantly altered revealing a large increase in impedance likely associated with electrolyte decomposition as the cell nears the end of its life. The trend in the EIS data therefore confirms that the coated cell experiences significantly reduced degradation upon cycling, leading to lower impedances and an increase in the number of cycles to cell failure.

To observe the morphology of the electrodes after cycling, SEM analysis was performed. These results shown in Figure 3.4 reveal a stark difference between the control and the 20x Al_2O_3. Even after the first 100 cycles (the stabilized region), dramatic differences between the electrodes can be observed. For the control electrode shown in Figure 3.4a,c, a very rough and textured surface can be observed. The ALD treated electrode shown in Figure 3.4b,d exhibits a remarkably smooth morphology. Under higher magnification, Figure 3.4d, some underlying texture can be observed, but the size, shape, and relief of these features are dramatically different than those in Figure 3.4c. After failure, the effect is even more dramatic, as the control electrode displays extreme surface roughness and porosity (Figure 3.4e,g). However, the 20x Al_2O_3 electrode demonstrates a near perfectly dense surface (Figure 3.4f) with infrequent localized dendrites (Figure 3.4h). These images show dramatic dissimilarities between the control and treated electrodes highlighting the effectiveness of the ALD treatment at both extended and localized length scales.

To further understand the role of the Al_2O_3 layer on the Li metal electrode, samples were transferred from the glovebox-integrated ALD tool into a ultra-high vacuum (UHV) XPS tool without air exposure using a custom sample-transfer holder. The XPS spectra revealed that Al was present on the Li metal surface after the initial ALD deposition. Additionally, XPS was conducted on electrodes that were galvanostatically electrodeposited

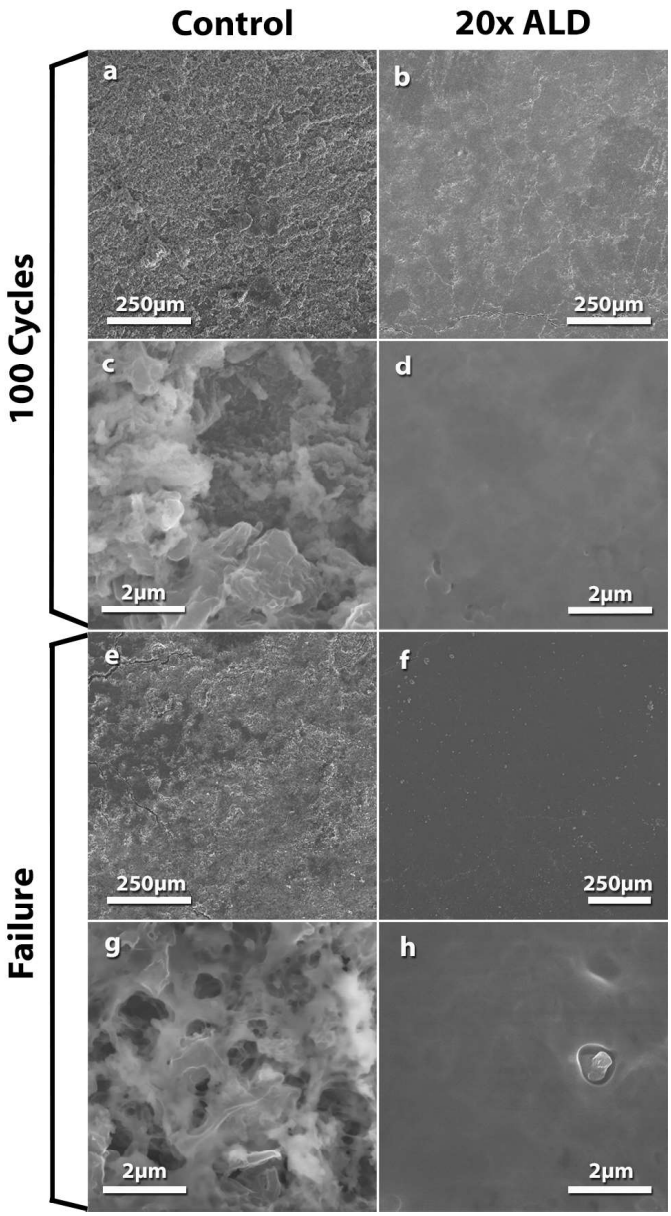

Figure 3.4: *SEM images showing the morphological changes between the control Li electrode (a, c, e, g) and the 20x Al_2O_3 sample (b, d, f, h). Images were taken after both cells exhibited failure, ca. 1,280 cycles.*

at 1 mA cm^{-2} to 8.5 mAh cm^{-2} after ALD treatment. This represents an electrodeposition of nearly 10 µm of Li. Aluminum remained on each of the electrodes (plated and stripped electrode), though in diminished quantities as shown in Table 3.1. However, after 100 charge/discharge cycles, the concentration of Al is very low (<1%), and after failure, there is no detectable Al signal in either XPS or energy dispersive x-ray spectroscopy (EDS).

Composition (atomic %)				
Treatment	Al [%]	Li [%]	O [%]	C [%]
As-received	13.5	30.1	25.7	22.8
Plated (Galv.)[a,b]	2.6	55.5	22.3	8.4
100 cycles[c]	<1	27.6	23.8	33.6
Failed[c]	0	19.2	26.9	41.2

Table 3.1: *Table of XPS survey spectra quantification showing the presence of aluminum before and after Li plating/stripping treatment.*[a] *180 s Ar Sputter to remove adventitious film.* [b] *Galvanostatically plated to 8.5 mAh cm*$^{-2}$. [c] *Plated/stripped at 1 mA cm*$^{-2}$

The presence of Al on the surface of each electrode after galvanostatic electroplating indicates that the Al_2O_3 ALD treatment influences the nature of the SEI. The SEI that is formed during initial exposure of the Li metal to the electrolyte and during the initial cycling of the Li electrodes will set the initial conditions for subsequent dendrite nucleation and growth. As discussed in the introduction, inhomogeneities in both the SEI and the underlying Li surface are widely considered to be the origin of hot spots that lead to SEI fracture and exposure of Li metal to the electrolyte. Therefore, the clear lack of dendrite formation in the ALD treated electrodes demonstrates that the treatment strongly influences the distribution of these inhomogeneities, preventing mechanical degradation of the SEI due to localized stresses during cycling.

It has been previously shown that by intentionally introducing mechanical defects onto the Li metal surface, the distribution of hot spots can be influenced through patterning, improving the cycling stability.[99] This suggests that the ability to controllably modify the flux of Li incorporation and stripping on Li metal surfaces could provide a pathway to control dendrite formation. The ALD treatment process allows for atomically precise modification of Li-electrolyte and Li-SEI interfacial chemistry, which provides a tool for engineering the homogeneity of Li flux across these interfaces. This is evidenced by the dramatically smoother morphology of the Li surface after treatment, suggesting that the initial conditions set by the ALD treatment can suppress the formation of inhomogeneous localized stresses that result in cracking of the SEI and formation of low-density dendritic structures.

Combining this with the EIS data, we conclude that the mechanism responsible for this improved homogeneity is due to an improvement of the electrode-SEI interface (Figure 3.3), which is formed upon the initial exposure of the ALD-treated Li metal to the electrolyte.

As observed in both XPS and EDS, the Al is no longer present on the surface after failure; however, the improved morphology in the SEM images can be observed through failure. This suggests that either the Al atoms are eventually incorporated into the electrode/SEI, deeper than the escape depth of excited photoelectrons (such that the concentration is undetectable), or they dissolve into the electrolyte over time. As mentioned, dendritic growth is a self-amplifying phenomenon, so the effect of the ALD treatment on initial nucleation and homogeneity of Li flux across the interface propagates all the way through to failure. Once these initial nucleation conditions have been set, both plating and stripping will preferentially occur in a more uniform manner, meaning that the improvements of the ALD continue even after Al is no longer observed.

The role of the ALD film is therefore to modify the nucleation behavior of the Li, rather than to remain fully intact and on the surface. This is supported by SEM and EDS images of the morphology of a thicker ALD film (200x) on Li metal after the coin cell was assembled and disassembled immediately (before any electrochemical testing). As shown in Figure 3.5, the ALD film is cracked and no longer a continuous dense film due to the strain of the underlying Li metal during coin cell assembly. This is unsurprising due the brittle nature of the ALD alumina and the low-yield strength, viscoplasticity of Li metal.[100]

Interestingly, the sole effect of heating in the vacuum environment during ALD treatment also appears to positively affect cell performance. While this affect appears to depend on ALD coating thickness and cycling and current density, control experiments indicate that heating under vacuum is responsible for as much as 70% of the improvement reported herein. This suggests that the observed improvement of Li metal performance in the ALD process is due to a combination of thermal and chemical effects and highlights the need for an improved understanding of the initial defect structure of the Li metal surface that

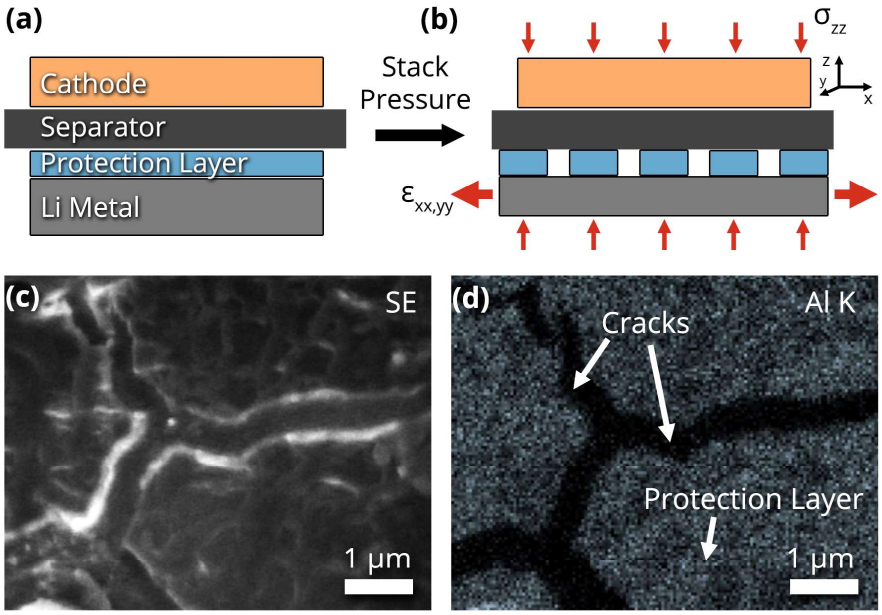

Figure 3.5: *Schematic of the morphology evolution of the ALD film upon compression during coin cell assembly (a-b). SEM image (c) and EDS map of Al K-edge showing the cracks depicted in the schematic.*[100]

leads to inhomogeneous plating/stripping. Future experiments will be performed to further investigate this treatment in more detail to better elucidate the detailed mechanism at play within this system. Nevertheless, the work presented herein underscores the ability of ALD treatment to improve the stability and cycle life of Li metal anodes by a factor of two, pushing this technology one step closer to reality.

3.2 Conclusions

This study demonstrates the importance of interfacial tuning and the unique capability to precisely control composition and behavior at electrode-electrolyte and electrode-SEI interfaces using ALD treatment. The denser film morphology seen in the SEM analysis of the 20 cycle sample is desirable as it lends itself to longer cycle life due to reduced probability of dendrite growth penetrating the separator and causing a short. It also delays cell drying caused by electrolyte decomposition by limiting the active surface area exposed to the electrolyte. The prevailing explanation for dendrite nucleation is the presence of hot

spots created by uneven current distribution on the surface of the electrode. The ALD Al_2O_3 treatment suppresses undesirable dendrite growth during the initial cycles, which then propagates throughout the lifetime of the cell, despite the apparent reduction of Al concentration at the surface. The observed effects are attributed to an improvement of the homogeneity of current distribution along the Li metal/SEI interface in the ALD treated sample such that Li plating is much more uniform and is less likely to cause the SEI layer to fracture, exposing bare Li and leading to dendrite formation.

3.3 Materials and Methods

3.3.1 Film Deposition

ALD coatings were carried out in a Savannah S200 (Veeco) ALD reactor with TMA and water as precursors. Pre-cycles of water were pulsed to provide a more reactive surface for the TMA to react with. Li metal was coated at 100 °C using TMA pulses of 0.1 s, water pulses of 0.02 s, and a carrier gas flow rate of 10 standard cubic centimeters per minute (SCCM) Ar. Li foil (Alfa Aesar) 0.75 mm thick was punched by hand into 17 mm discs and cleaned in anhydrous pentane (Aldrich) with a vortex mixer for 30 s immediately prior to treatment and/or assembly into coin cells. Determining the exact growth rate of ALD Al_2O_3 on Li metal is very difficult, as standard film thickness measurement techniques (spectroscopic ellipsometry, x-ray reflectivity, cross-sectional TEM) are not possible at the current moment due to the air instability of Li metal. Therefore, the number of ALD cycles performed (which we know exactly) is reported, rather than listing a film thickness. However the growth rate on (100) silicon was measured at 1.0 $Åcycle^{-1}$ was measured using a Woollam M-2000DI spectroscopic ellipsometer.

3.3.2 Cell Fabrication

Coin cells were assembled in an Ar glovebox (Mbraun) with coin cell shells, spacers, and wave springs purchased from MTI Inc. After coating, Li was immediately assembled into coin cells using 45 µL 1M $LiPF_6$ in 1:1 ethylene carbonate (EC)/ethylmethyl carbonate (EMC) (Soulbrain) and an MTI coin cell crimping press taken up to 1000 psi 3 times, relaxing between each time. The cells were symmetrical Li/Electrolyte-Separator/Li, allowing simplified investigation of behavior of the anode material. Cells were uncrimped using a disassembly die in the same MTI crimping press and electrodes were removed for further characterization after rinsing with DMC.

3.3.3 Electrochemical Testing

Cell cycling was done with a C-2001A (Landt Instruments) using coin cell holders at RT. Charge rates were normalized based on electrode area to current densities at 1 mA cm^{-2}. High-resolution electrochemical characterization, including 2-electrode EIS, was conducted with a Gamry interface 1000. EIS was conducted in a frequency range of 0.1 mHz-1 MHz at a direct current (DC) voltage of 0V (Li/Li^+) with an applied AC current of $\pm$10 µA. Morphology was observed using field emission SEM on an FEI Nova 200 Nanolab. Chemical composition was measured using XPS on a Kratos Axis Ultra XPS. In order to transfer the air-sensitive battery electrodes between the glovebox and the XPS, a custom sample-transfer enclosure was used that was opened inside of the XPS after pumping down to a fine vacuum ($<10^{-6}$ torr).

CHAPTER 4

Operando Visualization in Liquid Electrolytes

In Chapter 3, it was demonstrated that surface heterogeneity plays a key role in determining the performance of Li metal electrodes during cycling. However, it was difficult to build mechanistic understanding of how the initial surface heterogeneities and the electrode morphology dynamically evolve with cycling.

One of the practical challenges to gaining this understanding of Li metal behavior stems from the extremely reactive nature of liquid electrolytes and Li metal. This reactivity has restricted *in situ* experimental observation in meaningful cell geometries that are representative of battery operation. This limits fundamental knowledge of the process, including the exact location of Li electrodeposition and electrodissolution on electrode surfaces. While a few groups have utilized *in situ* optical microscopy to observe Li dendrite formation,[52,89,101–104] no previous report had ever linked the time evolving morphological changes observed in the visualization cell with the corresponding changes in electrochemical (voltage) response. This has allowed a level of detail in our mechanistic understanding of reaction pathways and the relationships between morphology and electrochemistry during cycling that has not been previously realized. Recently, *in situ* TEM has provided insight

into some aspects of Li dendrite growth at a highly localized scale;[48,50,97,105] however, many questions remain on the effects of dendrites at larger length scales and in cell geometries relevant to practical battery operation.

To this end, we explore in detail the time-dependent voltage response for an applied galvanostatic perturbation in Li vs. Li symmetric cells, and the resulting changes in electrode morphology. Specifically, the evolution of electrode morphology is observed through *operando* high-resolution video capture, and is directly correlated to time synchronized voltage traces. A continuum-scale numerical model is developed to relate electrode morphology and competing electrochemical kinetics to cell voltage. This allows for an in-depth understanding of the electrochemical processes occurring on the electrode surfaces, and how the transitions between reaction pathways for electrodeposition and electrodissolution lead to characteristic variations in cell polarization. Based on these results, we demonstrate that galvanostatic voltage traces can be used to infer morphological changes occurring during operation of coin cell battery architectures (where researchers are typically blind to morphology evolution). Finally, this interpretation is applied to provide detailed insight into the performance of Li electrodes in electrolytes that exhibit high CE. This work provides a level of detailed understanding that will help researchers take the next steps towards making todays holy grail of batteries, Li-metal anodes, a commercial reality.

4.1 Visualization Cell Approach and Observations

4.1.1 Approach

Evaluation of Li vs. Li symmetric cells is typically performed by galvanostatic cycling at a fixed current density. This subjects the Li electrode to similar operating conditions to real-world batteries without the need to deconvolute the processes occurring at dissimilar cathode materials. This allows for an evaluation of 1) the cell polarization required to drive electrodeposition and electrodissolution of Li; 2) the cycle life to failure of Li metal elec-

trodes; 3) a quantitative comparison of electrode behavior under varying current densities and electrolytes; and 4) cumulative capacity losses, leading to an evaluation of the average Coulombic efficiency (aCE).[106] Our recent study on Li vs. Li symmetric cells also demonstrated that the temporal variations in cell voltage observed during galvanostatic cycling provide an important indication of electrode degradation throughout the cell lifetime. This degradation could be significantly improved through nanoscale surface modifications using ALD.[41] Thus Li vs. Li symmetric cells represent and important platform to quantitatively evaluate new strategies for stabilization of Li metal, including surface protective layers and new electrolyte chemistries.

Data from a typical two-electrode voltage trace during galvanostatic cycling are shown in Figure 4.1. Because this is a Li vs. Li symmetric cells, time-dependent variations in the cell polarization during cycling are directly representative of overpotentials in the system. In the first half-cycle, an initial decrease in cell voltage is always observed. In subsequent half-cycles, the cell polarization 1) first decreases, 2) reaches a minimum, 3) rises to a local maximum, and 4) decreases again. As a result, a characteristic peaking behavior in the voltage trace is observed, as seen in Figure 4.1. This general form of the voltage trace is consistently observed across a wide range of current densities, electrolyte systems, and cell configurations, while the magnitude and detailed shape of the voltage trace vary based on these parameters. Therefore, an improved understanding of galvanostatic voltage traces provides an important means for evaluating electrode performance.

This general voltage trace behavior has also been observed in a previous study on Li vs. Li symmetric cells, in which galvanostatic testing and EIS were used to examine changes in impedance and cell polarization as a function of time.[44] Combining this electrochemical data with post-mortem SEM, a mechanistic explanation of the overpotential variations was hypothesized based on the observed results. However, *ex situ* microscopy does not allow for real-time observation of the evolution of dendrite formation and surface pitting, and does not allow for direct correlation of these morphological variations with time-synchronized

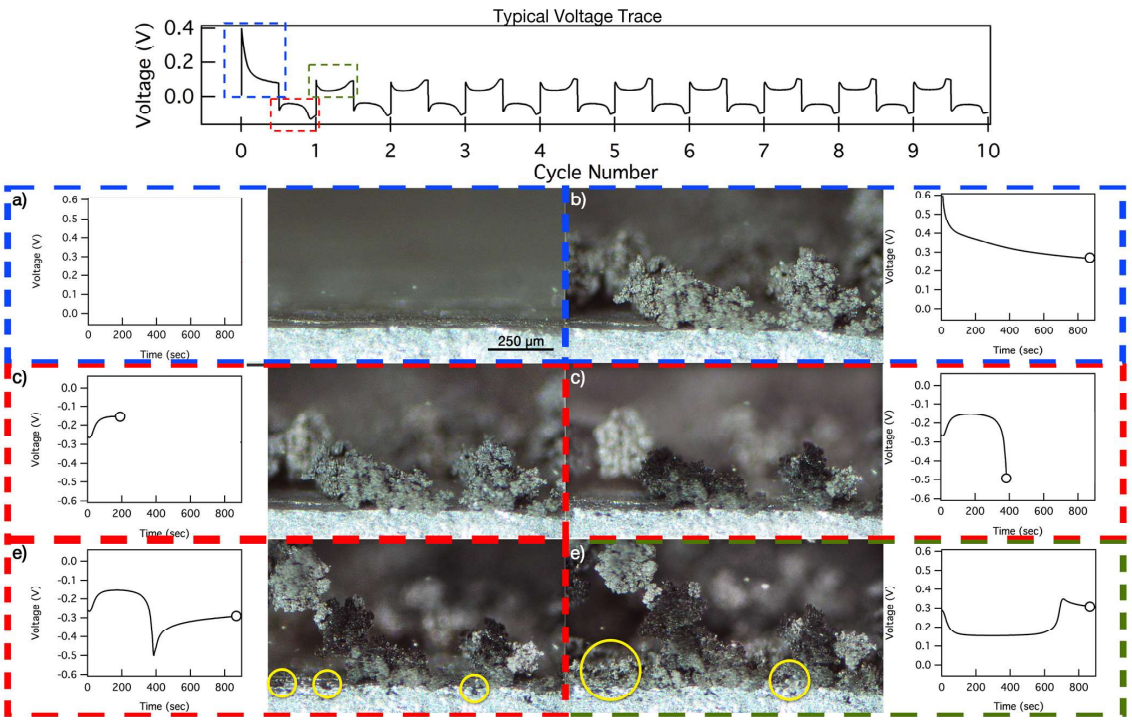

Figure 4.1: *Video 4.2 still frames for a cell cycled at 5 mA cm^{-2} (two-electrode measurement). EL-b morphology and corresponding voltage trace are shown at times (a) before cycling; (b) after first half-cycle (deposition at EL-b); (c) at cell polarization minimum (dissolution at EL-b); (d) at cell polarization maximum; pitting not yet evident; (e) morphology at end of half-cycle; pitting observed (examples highlighted in yellow circles); (f) morphology at end of third half-cycle (deposition at EL-b); new dendrites are deposited in the pits which formed at the end of the previous half-cycle (yellow circles).*

electrochemical profiles. Moreover, the process of disassembling, drying, and observing a Li metal electrode *ex situ* does not capture the morphology of the electrode during cell operation, and may lead to significant changes in the surface morphology, affecting the resulting conclusions. To address this challenge, we have developed an *operando* visualization cell, which allows for direct correlation of real-time high-resolution video capture of the cell morphology during electrochemical cycling to the measured galvanostatic voltage traces (Figure 4.3).

This cell is depicted in Figure 4.4. In this cell, two Li electrodes are held parallel beneath a quartz window to enable a cross-section view of the electrodes as Li is plated and stripped. Though the electrodes are spaced further apart than in a typical coin cell or other cell architecture, a uniform electric field distribution across the cell is maintained.

Figure 4.2: *Synchronized morphology and voltage changes for 1 M $LiPF_6$ in EC/DMC cycled at 5 mA cm^{-2}.*

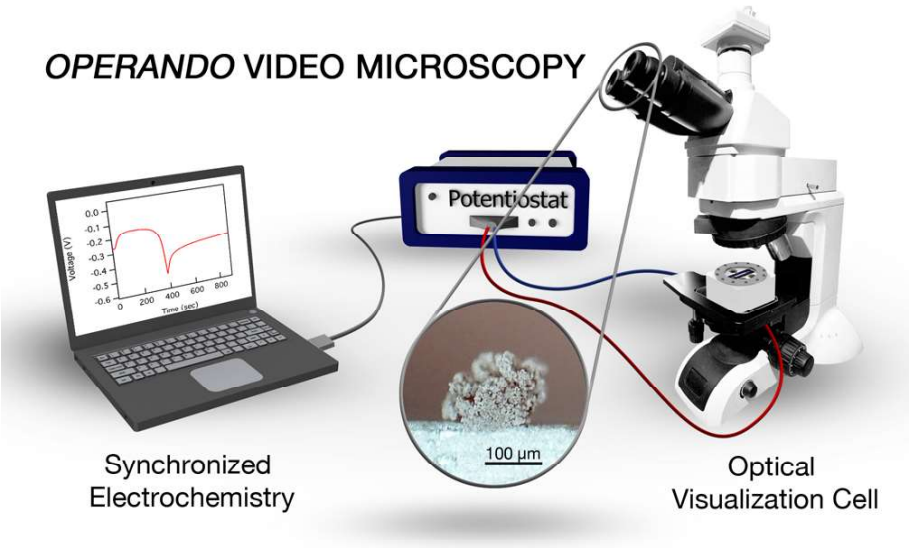

Figure 4.3: *Schematic of synchronized electrochemistry/video microscopy concept.*

4.1.2 Experimental Observations

Operando videos of the electrode surface were time-synchronized with the corresponding voltage traces of the cell, as seen in Video 4.2 and Figure 4.1. For this initial video, a standard 1M $LiPF_6$ in 1:1 EC/dimethyl carbonate (DMC) electrolyte was used. The results show the transient morphology of the Li electrode surface for three full cycles in the video, and the first three half-cycles of operation in Figure 4.1 [1^{st} cycle charge (1a-b); 1^{st} cycle discharge (1c-e); 2^{nd} cycle charge (1f)]. In Figure 4.1b (Video 4.2 0:00-0:10), dendrites nucleate in unsystematic locations across the surface of the working electrode, shown within the frame (which we will define as EL-b, this definition will not change when polarity is changed). Other dendrites, not in focus, can be observed in the background as well. The corresponding synchronized voltage trace, an inset in the same figure, indicates an initial decrease in cell voltage. As plating continues, the dendrites increase in size, while the morphology and position of the surrounding electrode surface does not change noticeably, implying that the vast majority of Li is plated in dendritic form or contained in the SEI (Figure 4.1b; Video 4.2 0:10). Almost immediately upon switching polarity, a maximum cell voltage is observed (Figure 4.1c; Video 4.2 0:11). The voltage then quickly decreases

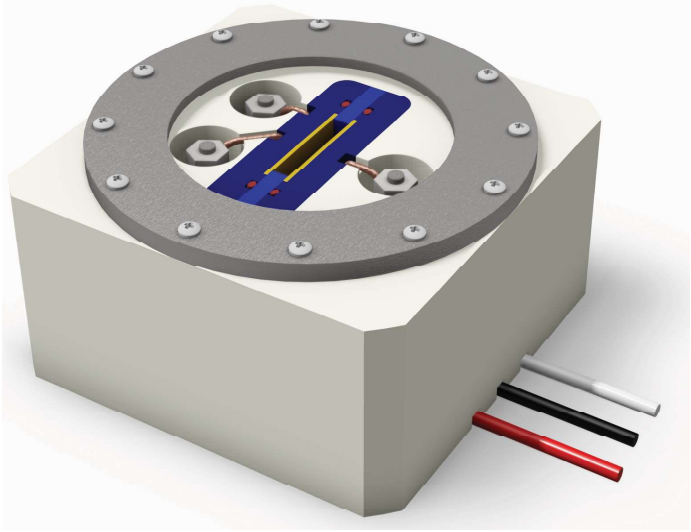

Figure 4.4: *Schematic of cell design used for operando video microscopy. The Li electrodes are shown in maize, the polyether ether ketone (PEEK) electrode holders are shown in blue, and the o-ring is shown in red/orange.*

from the initial maximum as Li continuously transfers to the counter electrode (which we will define as EL-a, this electrode is not in view in Figure 4.1; this definition will refer to the counter electrode throughout the paper and does not change when polarity is switched), until a minimum in voltage is reached (Figure 4.1c; Video 4.2 0:12).

As Li is further stripped from the dendrites, a strong color shift (darkening) is detected on the surface of the stripped dendrites, which correlates with an increase in cell voltage (Video 4.2 0:13). As this reaction proceeds, Li continues to be removed from the previously plated Li (which is exclusively in the form of dendrites on the electrode surface), until all of the electrochemically active Li is removed from the dendritic structures on EL-b (Figure 4.1d; Video 4.2 0:14). A local maximum in cell voltage is reached as the source of Li electrodissolution from EL-b is observed to be transitioning from previously plated dendritic Li, to fresh bulk Li from the surrounding electrode surface. Here, large portions of the dendrites have changed color to black and are no longer electrochemically active, which we will refer to as dead Li (Figure 4.1d; Video 4.2 0:14). From this point on in the half-cycle, the color, size, and shape of the dendrites no longer change. As electrodissolution progresses, pits begin to form on the surface of the bulk Li (Figure 4.1e, Video 4.2 0:14-

0:19), a transition that can be very clearly seen in Video 4.2. This transition coincides with a second decrease in voltage. Pits continue to increase in size, becoming more pronounced. It can also be seen that detached (dead) Li floats to the surface of the electrolyte in Video 4.2 at time 0:19.

Upon switching polarity, it can be observed from Figure 4.1f that new dendrite growth on the surface of EL-b occurs directly within the pits created during the previous half-cycle. This results in a greater number of dendrites on the surface during the second cycle, which are smaller in size than those observed during the first cycle. We note that some of the pitting during the previous half-cycle occurred directly below the locations where dead Li is observed. Nucleation of new dendrites in these locations causes the dead Li to be displaced upwards. It can also be observed that the exact same shape of the galvanostatic voltage trace is observed for this half-cycle and subsequent half-cycles: two local maxima, a local minimum, and a decrease in cell voltage after pitting begins to occur (Figure 4.1e-f). This behavior was confirmed to be consistent for more than 100 charge/discharge cycles, as well as in the presence of a polymer separator (Video 4.6, Figure 4.5).Figure 4.5 also shows how voltage profiles reach a more consistent shape for each half cycle as increasing cycles are carried out.

Additionally, control experiments in which the current was periodically interrupted without changing polarity demonstrate that the peaking behavior is not due to a capacitive effect (Figure 4.7). Comparing a) with c) reveals that the overpotential and peak position are identical for the same amount of charge passed. This can be clearly seen for the second peak, associated with electrodissolution from the bulk, where that peak appears after ~420 mC cm^{-2} (for the 1 mA cm^{-2} graph) of charge was passed and at an overpotential of ~150 mV regardless of the interrupted current.

Figure 4.7c also shows that the position of the dissolution peak shifts toward later time once sufficient Li has been deposited during the previous half cycle. This can be observed by comparing the 5^{th} and 6^{th} half cycles. Since only 900 mC cm^{-2} were passed during the

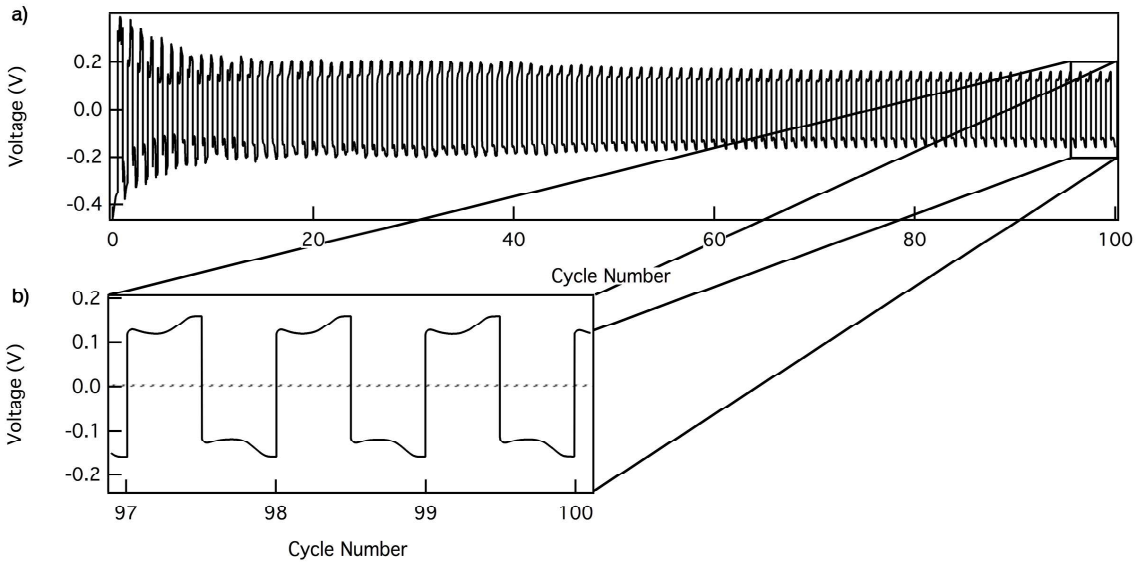

Figure 4.5: *Voltage profile for visualization cell with a separator cycled in $LiPF_6$ cycled for over 100 cycles. The characteristic peaking behavior is obvious for each half cycle. The corresponding video is shown in Video 4.6.*

4th half cycle the peak associated with dissolution from the bulk occurs close to that point (~840 mC cm^{-2}). However, after 5400 mC cm^{-2} was passed during the 5th half cycle, that same peak appears after ~5000 mC cm^{-2} in the 6th cycle.

Additionally, the part of Figure 4.7c labeled (i) shows how pitting evolves once all the active Li sites are removed from the dendrites during the 5th half cycle. The portion labeled (ii) shows the length of plating during the 6th half cycle.

This general form of initial galvanostatic voltage traces are also observed in Li-Li symmetric coin cell and Swagelok cell geometries. Figure 4.8 shows that regardless of cell geometry and other variables, the peaking behavior is very consistent. This type of behavior has also been observed in many previous reports.[14,44,50,107] As a result, mechanistic insight into Li metal electrode evolution under operating conditions in typical cell formats and operating pressures can be gained.

Figure 4.6: *Operando video of Li/Li symmetric cell with a celgard separator above the working electrode during cycling 100 times.*

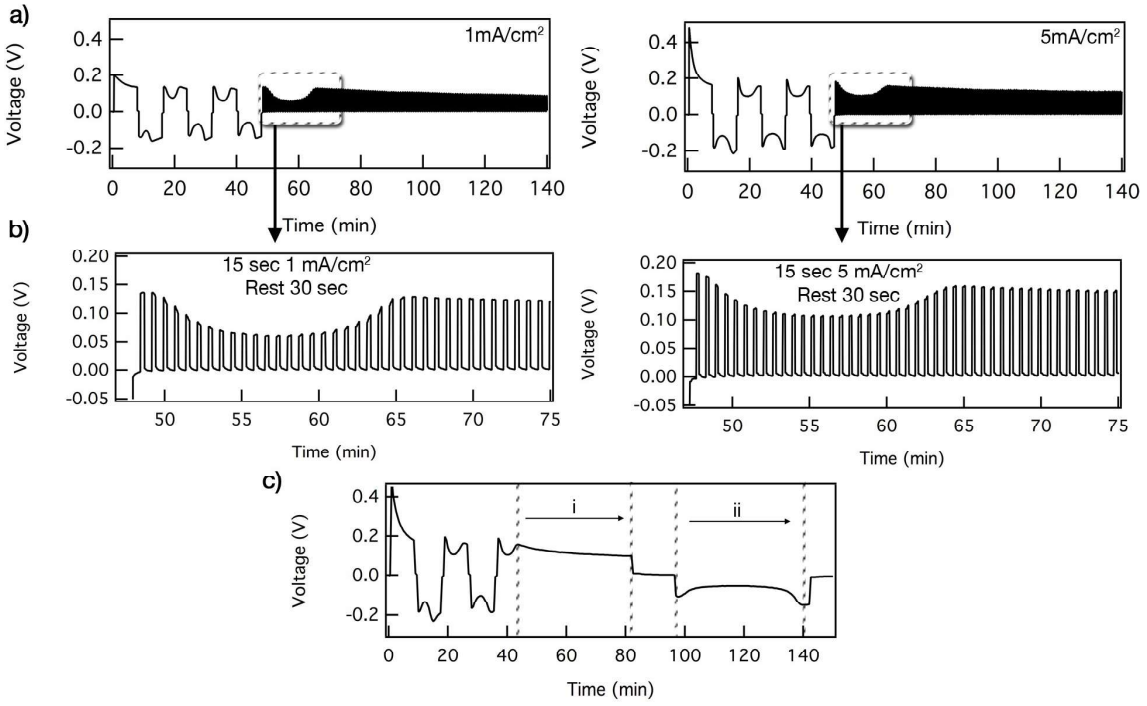

Figure 4.7: *Voltage profile of a Li-Li symmetric cell where the first six half cycles were cycled for 7.5 min. Subsequent half cycles were cycled for longer periods of time. In a) the longer cycle was a sequence of cycling at either 1 mA cm^{-2} or 5 mA cm^{-2} for 15 s followed by a rest period of 30 s. For a more detailed view see b). This sequence was carried out until the amount of time under galvanostatic conditions was 45 min. In c) the cell was cycled at 2 cm^2; the first 4 half cycle were 7.5 min and the subsequent 2 half cycles were for 45 min.*

4.2 Numerical Model

To complement the experimental data, a numerical model was developed by our collaborators to simulate the early cycling behavior of the visualization cell during galvanostatic cycling. This one-dimensional numerical continuum-scale model was based on their previous efforts to study the deposition and dissolution of magnesium metal anodes.[108] The model solves the time-based evolution of the Poisson-Nernst-Planck system of equations to describe the electrochemical mass transport and the electrostatic potential across the cell. Further details can be found in the publication.[15]

The resulting simulated galvanostatic voltage trace is shown in Figure 4.9. It can be observed that overall there is very good agreement between the experimental and simulated voltage traces, and both exhibit a characteristic peaking voltage profile. In both cases, the

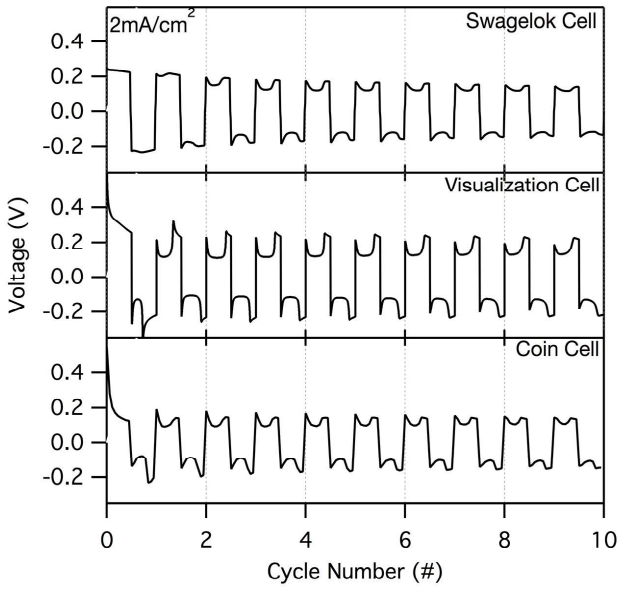

Figure 4.8: *Comparison of voltage traces for various geometries, as labeled in each panel.*

cell voltage exhibits a sharp peak at the start of each half-cycle, followed by an asymmetric trough and a subsequent sharp increase leading to a blunted peak before the end of the half-cycle. We note that the model does not fully capture the experimentally observed behavior of the first cycle. This is expected because the model is parameterized for a system that has already been cycled once, which exhibits fundamentally different physical properties than the initial system.

4.3 Results and Discussion

Using a combination of numerical modeling and experimental observations, we develop a general framework for interpretation of galvanostatic voltage traces. This framework can be used to provide mechanistic insight into phenomena occurring on Li metal anodes during cycling in a range of relevant battery systems.

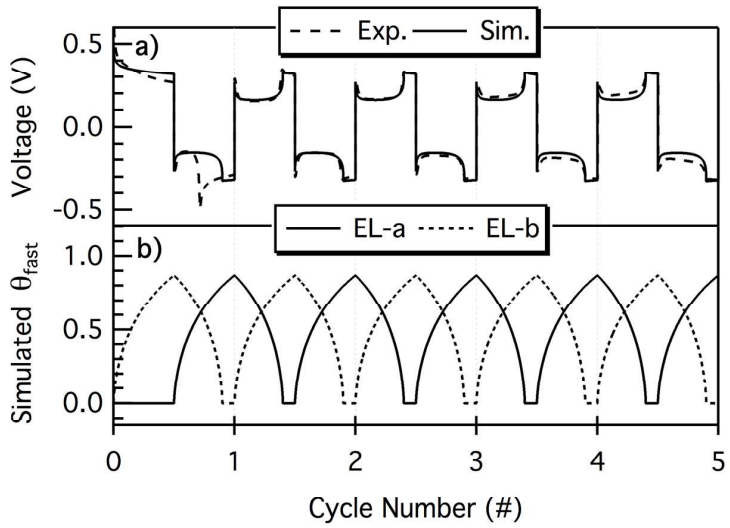

Figure 4.9: *(a) Numerical modeling results of cell polarization showing agreement with experimental data. (b) Simulated area fraction associated with the kinetically fast reaction (θ_{fast}) on each electrode during cycling. When θ_{fast} at the dissolving electrode reaches zero, a maximum in cell voltage occurs.*

4.3.1 Visualization Cell Interpretation: General Framework

As current is passed through a Li metal electrode, inhomogeneities on the surface lead to an uneven current distribution, resulting in dendrite/pit formation. The kinetically fast and slow regions can be described by the fractional surface area that those regions represent, and the kinetics of those regions. Here, we define θ_{fast} and θ_{slow} as the fractions of the electrode surface area with fast and slow kinetics, respectively, and k^0_{fast} and k^0_{slow} as the rate constants of the fast and slow processes, respectively. By definition, $\theta_{fast} + \theta_{slow} = 1$ because the area fractions must sum to unity.

Contributions to the total current, I_t, passing through surfaces represented by with different reaction kinetics, (such as dendritic and bulk Li) can be expressed in the following form:

$$
\begin{aligned}
I_t &= iA_{el} \\
&= A_{el}\gamma F\left(\theta_{fast}k^0_{fast} + \theta_{slow}k^0_{slow}\right)\left[c_{Li}\exp\left(\frac{(1-\beta)\,F\eta}{RT}\right) - c_{Li^+}\exp\left(\frac{\beta F\eta}{RT}\right)\right] \\
&= g\left(\eta\right)\left(\theta_{fast}k^0_{fast} + \theta_{slow}k^0_{slow}\right)
\end{aligned}
\tag{4.1}
$$

where A_el is the area of the electrode, γ is a parameter that accounts for the roughness of the electrode surface, c_i is the charge and concentration of the i$^{\text{th}}$ species, x is the position, F is Faradays constant, R is the ideal gas constant, T is the absolute temperature, and β is the symmetry factor, and η is the overpotential of the electrode.[29,34] The roughness parameter, γ, is the ratio between the total surface area of the electrode (including deposits) and the two-dimensional projected surface area. $g(\eta)$ consolidates all terms not involving the reaction constants. If we assume that k^0_{fast} and k^0_{slow} are time-invariant, the electrode overpotential will adjust to draw the current required as θ_{fast} and θ_{slow} change. In general, when θ_{fast} is sufficiently large, the surface with fast kinetics will determine the of that electrode. Conversely, as θ_{fast} approaches zero, the kinetically slow surface must supply the current. Therefore, ηmust increase in order to maintain a constant current. This logic can be further expanded to include contributions from more than two parallel processes on an electrode. In the general case, Equation 4.1 can be expressed as:

$$
I_t = \sum_p I_p = \sum_p g_p\left(\eta\right)\theta_p k^0_p \tag{4.2}
$$

where p is an index of the contributing processes.

The total current of a Li-Li symmetric cell will have contributions from a variety of parallel processes on both the anode and cathode. As observed in the visualization cell, the major contributing processes at the anode are electrodissolution from existing dendrites

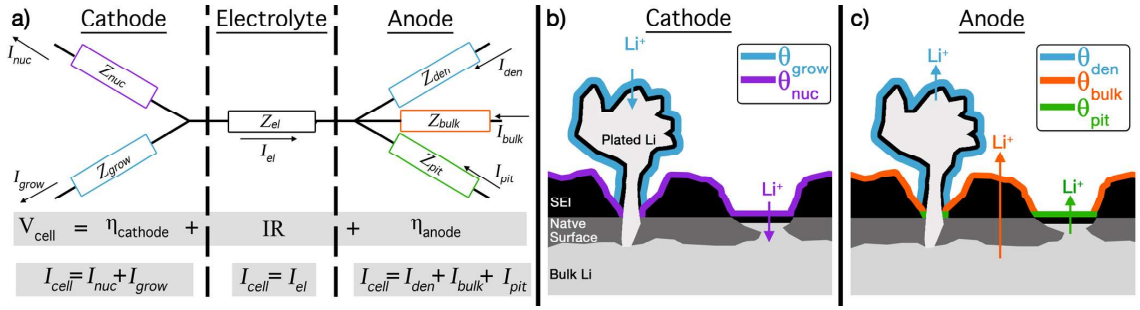

Figure 4.10: *(a) A schematic representation of reaction pathways for the cathode, anode, and electrolyte. The overpotential at each electrode is a function of the total current, which is equal to a sum of current contributions from each reaction pathway at that electrode. The magnitude of current that passes through each pathway is dependent on the impedance associated with that pathway. The dominant pathway for current at each electrode is associated with the processes with the lowest impedance (Z_p), which has the largest influence on the electrode overpotential. A schematic representation of the regions associated with the area fraction of each process, θ_p, is shown for the cathode (b) and for the anode (c). The impedance of each process is inversely proportional to θ_p and ΔG_p, as discussed in section 4.3.1.*

(I_{den}), planar bulk Li (I_{bulk}), and pitted surfaces (I_{pit}). At the cathode, the major contributing processes are electrodeposition onto dendrite surfaces (I_{grow}), and nucleation of new dendrites (I_{nuc}). The total current must be constant at both electrodes to guarantee continuity. Also, by definition, $\sum_p \theta_p = 1$ because the area fractions associated with each process must sum to unity. A schematic circuit diagram of this behavior is shown in Figure 4.10.

The differences in the kinetic constants for each of the contributing processes can be understood in terms of activation energy. Mathematically, these two quantities are related by:

$$k_p^0 = A_p \exp \frac{-\Delta G_p}{RT} \tag{4.3}$$

k_p^0 is the rate constant for the process p, A_p is the corresponding Arrhenius constant, and ΔG_p is the total energy barrier for the process, which accounts for transport through the surface layer as well as CT at the electrode surface. These different energy barriers, arise from intrinsic differences in nature of the SEI layers associated with the respective processes (e.g. the SEI layer on the dendrites may be thinner and/or more defective than that on the bulk electrode that is continuously fracturing, or it may have an entirely different

chemical composition, leading to the lower energy barrier).[109]

For a given electrode, if it is assumed that ΔG_p remains relatively constant for each process throughout cycling, then the change in the area fraction (θ_p) as morphology evolves will cause the current to shift reaction pathways (Figure 4.10). The total current will be dominated by the reaction pathway with lowest net impedance, Z_p, which is inversely proportional to both θ_p and the rate constant (k_p^0) for that specific process. The total voltage for the cell, V_{cell}, is a summation of the voltage contributions in series:

$$V_{cell} = {}_{anode} + \Delta V_{IR} + \eta_{cathode} \tag{4.4}$$

where ΔV_{IR} is the potential drop due to the internal resistance of the cell. Since constant current is applied in our experiment, we assume changes in ΔV_{IR} as a function of time to be negligible. We also assume that the initial cycling of the cell is negligibly affected by the relaxation behavior of concentration gradients (see Figure 4.7 and S9).

Under these assumptions, any changes in cell voltage for a small differential time element must be related only to changes in electrode overpotentials:

$$\delta V_{cell} = \delta\eta_{anode} + \delta\eta_{cathode} \tag{4.5}$$

where δV_{cell} is the differential change in cell voltage, $\delta\eta_{anode}$ is the differential change in anode overpotential, and $\delta\eta_{cathode}$ is the differential change in cathode overpotential. The electrode overpotentials described in Equation 4.5 are directly related to the activation barrier(s) of the dominant process(es) at each electrode (Figure 4.11), as described in Equations 4.1 through 4.3.

If we start with conditions were dendrites exist on one electrode and relatively small pits on the other, then $\theta_{den} > 0$ and $\theta_{grow} = 0$.Since we assume that $\Delta G_{bulk} > \Delta G_{den}$ (and therefore) $k^0_{den} > k^0_{bulk}$) and that $\theta_{den} > \theta_{bulk}$, I_{den} will dominate Equation 4.2. Also, since $\theta_{grow} = 0$,$I_{grow} = 0$, for which Equation 4.2 may be simplified as:

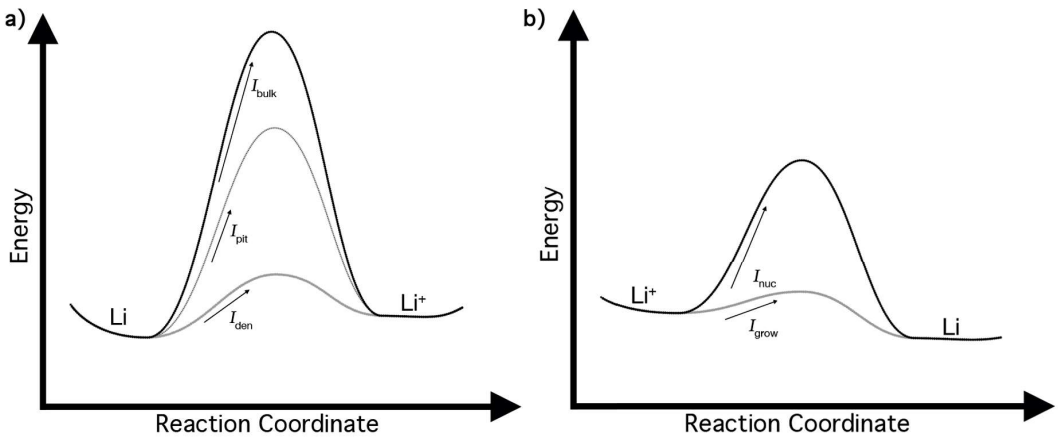

Figure 4.11: *Schematic representation of difference in activation barriers between a) the anodic (electrodissolution) processes of Li removal from either dendrites (labeled by den) or the bulk (labeled by bulk) and b) the cathodic (electrodeposition) processes involving nucleation (labeled by nuc) and growth (labeled by grow).*

$$I_{cell} \cong I_{den} \cong I_{nuc} \tag{4.6}$$

The reaction pathway at this point during the cycle can be observed schematically in Figure 4.13a. Here the exchange current densities are given by:

$$i_{0,den} = Fc_{den} f \exp\left(\frac{-\Delta G_{den}}{RT}\right) \tag{4.7}$$

$$i_{0,den} = Fc_{den} f \exp\left(\frac{-\Delta G_{den}}{RT}\right) \tag{4.8}$$

From Figure 4.11, it can be observed that i_{0nuc} will be much smaller than i_{0den} due to its large activation barrier. For the initial decay in V_{cell}, $\delta\eta_{cathode} >> \delta\eta_{anode}$, and therefore the observed decay is primarily due to the cathodic half reaction, which may be expressed as:

$$\delta V_{cell} \cong \delta\eta_{cathode} \tag{4.9}$$

As time progresses, Z_{grow} decreases, causing a transition between reaction pathways on

the cathode from nucleation to growth, until I_{nuc} becomes negligible and I_{grow} dominates the cathodic processes (Figure 4.10a). This occurs while θ_{den} on the anode is not close to zero, meaning the anodic current is dominated by dissolution from dendrites (main text Figure 4.14b). At this point, δV_{cell} has significant contributions from both the anode and the cathode.

As θ_{den} approaches zero, Z_{den} increases, and eventually becomes similar in magnitude to Z_{bulk} At this point, a transition occurs in reaction pathways at the anode from I_{den} to I_{bulk} (The unshaded region of main text Figure 4.14). Once $\theta_{den} \cong 0$, $Z_{bulk} << Z_{den}$, and I_{bulk} is the dominant current contribution at the anode (Figure 4.10a). The exchange current densities at this point can be expressed as:

$$i_{0,bulk} = nFC_{bulk} f \exp \frac{-\Delta G_{bulk}}{RT} \tag{4.10}$$

$$i_{0,grow} = nFC_{grow} f \exp \frac{-\Delta G_{grow}}{RT} \tag{4.11}$$

Here, the change in anodic overpotential will dominate the change in cell polarization, V_{cell}, such that:

$$\delta V_{cell} \cong \delta \eta_{anode} \tag{4.12}$$

which is seen graphically in Figure 4.14.

As the cycling process continues, pits form on the anode as Li is dissolved from the bulk. Consequently, fractures occur in the surface layers, resulting in a transition in reaction pathways at the anode surface to pitting, Figure 4.14d. The pitting also causes an increase in θ_{pit}, which results in a continued decrease in Z_{pit}, causing a decrease in overpotential at the anode until polarity is switched.

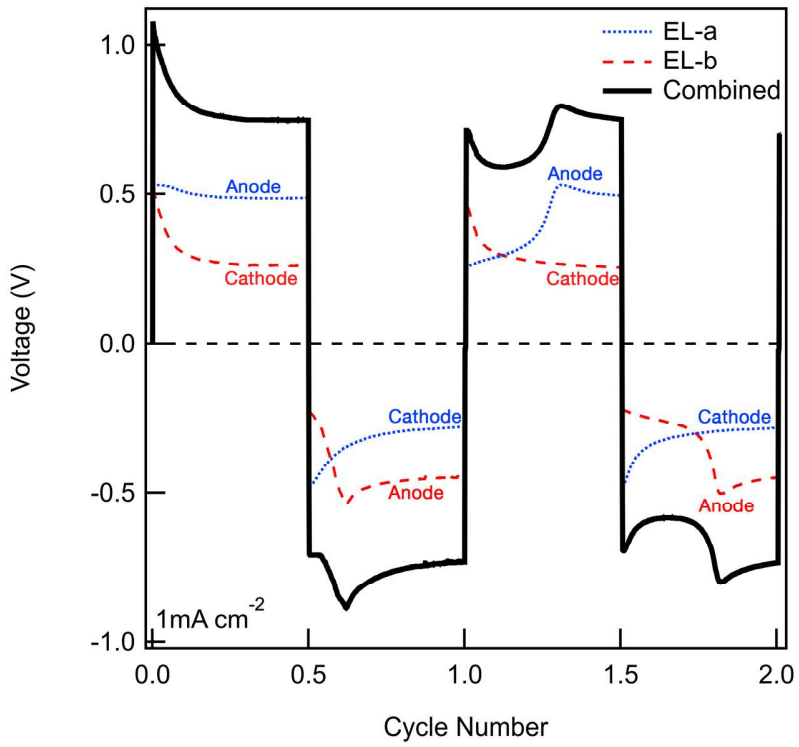

Figure 4.12: *Three-electrode measurements showing the cell polarization contributions from each electrode. Here EL-b is the working electrode (WE) and EL-a is the counter electrode (CE). For visual aid, CE has been multiplied by -1 such that the total cell polarization = CE + WE. Voltage is vs Li/Li$^+$.*

4.3.2 Visualization Cell Interpretation

Using the general framework presented in the previous section, we can directly attribute δV_{cell} to the dominant processes occurring on each electrode at specific points in a half-cycle. Through use of three-electrode measurements, shown in Figure 4.12, the contributions from individual electrodes can be directly observed. This allows for a detailed interpretation of voltage traces through analysis of the coupled morphological and electrochemical behavior of Li metal electrodes.

4.3.2.1 The First Half-Cycle

A schematic representation of the visualization cell observations described in Section 4.1.2 is shown in Figure 4.13. The initial pristine Li surfaces are composed of a bulk metallic

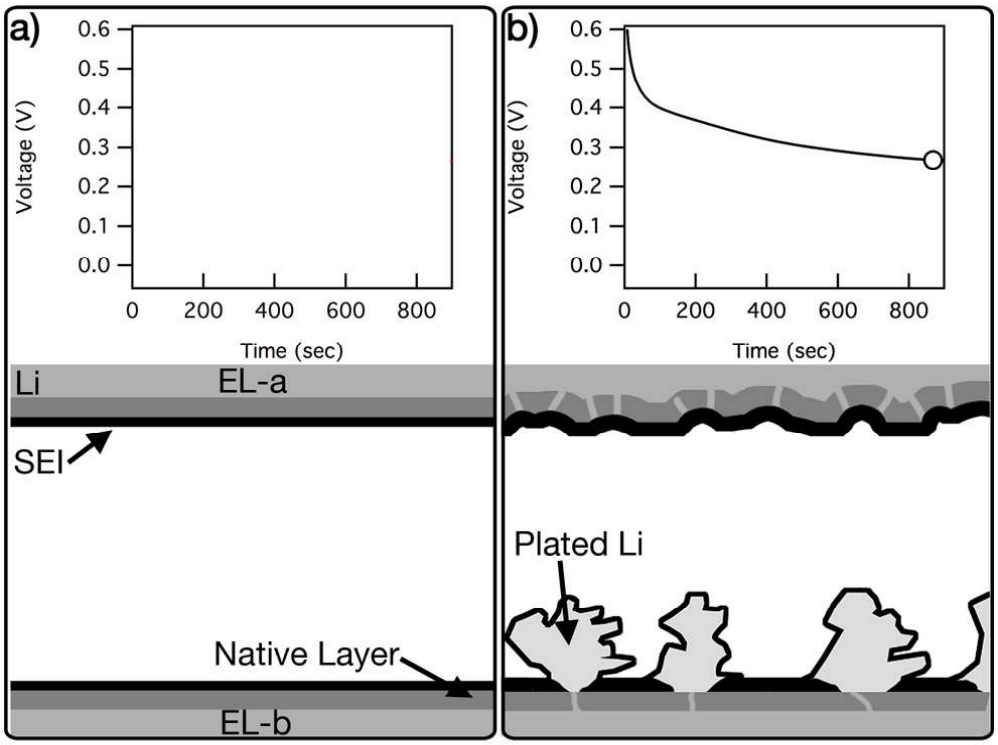

Figure 4.13: *Schematic representation of experimental observations in section 4.1.2. The upper electrode is EL-a, and the lower electrode is EL-b. (a) Before cycling. (b) End of first half-cycle: pits form at EL-a (anode), and dendrites grow on EL-b (cathode).*

Li electrode, a native surface layer,[110] and an SEI (Figure 4.13a). During the first half-cycle (Figure 4.13b), the only process occurring at the anode (EL-a, the top electrode in Figure 4.12) is pitting because no previously formed dendrites exist. On the cathode (EL-b, the bottom electrode in Figure 4.13), the observations from the visualization cell indicate that Li does not plate uniformly on the electrode surface, but rather through the nucleation (nuc) and growth (grow) of dendrites. Nucleation inherently involves an additional energy barrier, and thus the kinetics of growth is significantly faster than that of nucleation ($k^0_{nuc} < k^0_{grow}$).

As dendrites nucleate, the dominant reaction pathway at the cathode transitions from nucleation to growth (Figure 4.10). This is consistent with the visualization cell observation that additional Li+ preferentially deposits on the dendrite surfaces, rather than forming new nucleation sites (Figure 4.1b, Figure 4.13b, Video 4.2). As the area fraction of

the growing dendrites (θ_{grow}) increases, the impedance associated with dendrite growth (Z_{grow}) decreases throughout the half-cycle, such that $I_{grow} > I_{nuc}$ (Figure 4.10). Similarly, electrodissolution at the anode transitions from Li^+ removal from the bulk surface to preferential dissolution from pits (pit). This interpretation is confirmed by the three-electrode measurements. As can be seen in Figure 4.12, the initial drop in cell polarization during the first half-cycle is predominantly due to the drop in overpotential at the cathode, EL-b, which can be explained by the transition from dendrite nucleation to dendrite growth and the subsequent increase in surface area of the dendrites. The effect of pitting on the anode is noticeable, but lower in magnitude than the cathode effects.

4.3.2.2 The Second Half-Cycle

The characteristic peaking behavior previously discussed is observed in the voltage profile for subsequent half-cycles (Figure 4.1). In the second half cycle (Figure 4.12b), EL-b becomes the anode and EL-a becomes the cathode (Figure 4.14a). At this point, the area fraction of dendrites on the surface of El-b, which was equal to θ_{grow} in the previous half-cycle, is now equal to θ_{den}. As dendritic and bulk Li now exist on the anode, the proportion of current flowing though each reaction pathway will be determined by the impedance of each pathway. This impedance is a function of the energy barrier, ΔG_p, associated with each process (Equation 4.3). Schematic energy barrier diagrams are shown in the lower panels of Figure 4.14, which correlates kinetics to the morphology changes shown in the middle panel.

Immediately upon switching polarity (Figure 4.14a, Video 4.2 0:10), Li electrodissolution occurs preferentially from the dendrites on EL-b because $\Delta G_{den} < \Delta G_{bulk}$, and thus $k^0_{den} > k^0_{bulk}$. Simultaneously, a maximum in cell voltage is observed, which is due to the large activation barrier associated with nucleation (ΔG_{nuc}) on EL-a (Figure 4.11). At this point, the kinetics of each electrode are dominated by nucleation at the cathode and electrodissolution from dendrites at the anode. These results are also in agreement with the

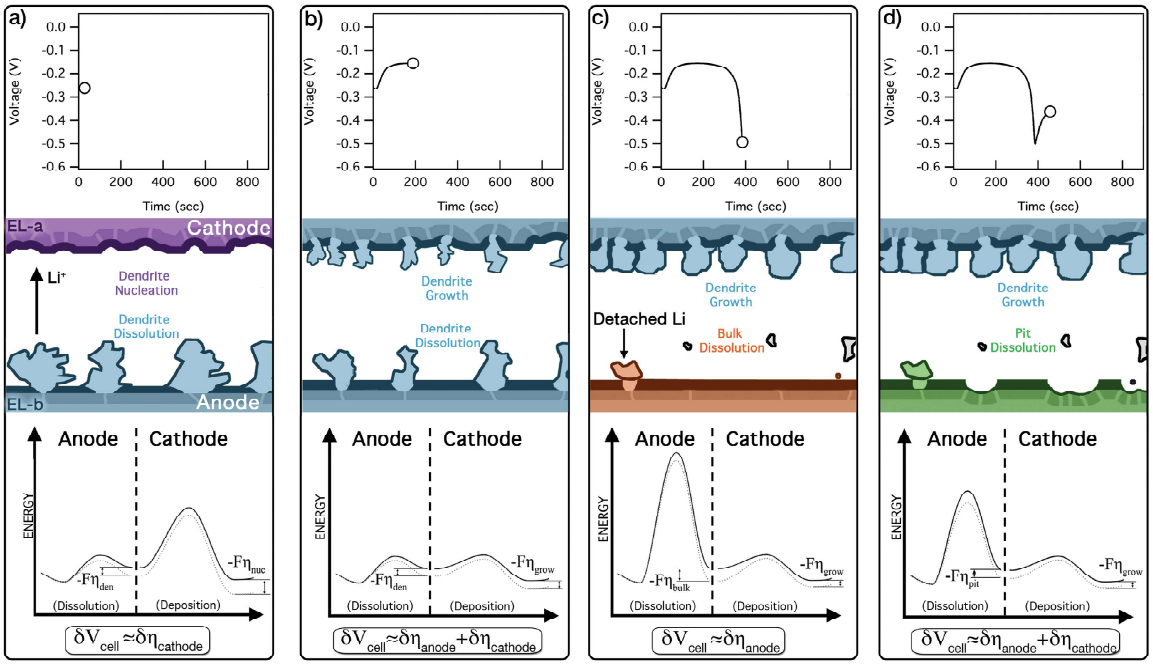

Figure 4.14: *Changes in cell polarization (top) are correlated with a schematic representation of morphology (middle; color-coded to match the appropriate reaction pathway as described in Figure 4.10) and energy barrier diagrams (bottom). In the energy barrier diagram the difference between the solid and dashed lines is for the equilibrium and bias conditions, respectively. The energy barrier diagrams display dominant reaction pathways at each electrode. This is shown at four points in the voltage trace: (a) Beginning of half-cycle: dendrite nucleation is the kinetically slow process. (b) Cell polarization minimum: dendrites present on both electrodes, kinetically fast reaction pathways. (c) Cell polarization maximum: active Li removed from dendrites; electrodissolution transitions to kinetically slow bulk dissolution. (d) Second decrease in cell polarization: pitting becomes the kinetically slow process.*

numerical model, where θ_{fast} is large on the anode and small on the cathode. As shown in Figure 4.14a, the largest contribution to δV_{cell} is associated with the activation barrier to nucleation on the cathode ($\Delta G_{nuc} > \Delta G_{den}$). This can be clearly observed in the three electrode measurements of Figure 4.12 as the initial peak is always associated with the cathode.

As deposition continues onto EL-a, cell polarization decreases. The steep initial decrease in polarization corresponds to a transition in reaction pathways from nucleation to growth of dendrites on EL-a. This occurs because θ_{grow} increases and $k^0_{grow} > k^0_{nuc}$ (as $\Delta G_{grow} < \Delta G_{nuc}$). After the transition, a local minimum in cell voltage is observed (Figure 4.14b, Video 4.2 0:11). At this point, the dominant process at the cathode is growth

of dendrites and at the anode is dissolution from dendrites. The kinetics of both of these processes are relatively fast, resulting in a minimum of V_{cell} (Figure 4.14b). This minimum is also observed in the numerical model (Section 4.2, Figure 4.9), when θ_{fast} is relatively large on both electrodes.

As active Li in the form of dendrites on EL-b is depleted, θ_{den} decreases, leading to an increase in cell voltage. Once θ_{den} is sufficiently small, it becomes necessary to dissolve Li from the surrounding bulk surface in addition to the dendrites. This causes a transition between reaction pathways on EL-b. As θ_{den} approaches zero, a maximum in cell voltage occurs (Figure 4.14c, Video 4.2 0:14). At this point in the process, Li electrodissolution from the bulk surface, a kinetically slow process (associated with k^0_{bulk} and ΔG_{bulk}), dominates on EL-b. This is also observed in the three-electrode measurements and the numerical model, as θ_{fast} on El-b becomes zero. Since the cathode is undergoing dendrite growth at this point, which is a kinetically faster process, the largest contribution to δV_{cell} is associated with the activation barrier to electrodissolution from the anode ($\Delta G_{bulk} > \Delta G_{grow}$), as shown in Figure 4.14c. Again this can be distinctly seen in Figure 4.12 as the second peak is always associated with the anode.

As electrodissolution continues from EL-b, a second decrease in cell polarization is observed. This corresponds to a transition in reaction pathways, resulting in preferential electrodissolution from pits on EL-b, rather than the bulk surface (Figure 4.14d, Video 4.2 0:19). The transition is driven by an increase in θ_{pit} and the fact that $k^0_{pit} > k^0_{bulk}$ because $\Delta G_{pit} < \Delta G_{bulk}$. At this point, the dominant process at the cathode is growth of dendrites and at the anode is dissolution from pits. As θ_{pit} and θ_{grow} continue to increase, the V_{cell} continues to decrease (Figure 4.14d). We note that this behavior is only partially captured by the numerical model because the model accounts for the increase in θ_{fast} on El-a from dendrite growth but does not explicitly account for pitting. Nevertheless, the agreement between the two and three electrode experimental data and simulated voltage traces indicate that the general behavior of the voltage originates from the transitions between kinetically

fast and slow processes.

4.3.2.3 Summary of Voltage Trace Interpretation

To provide a visual aid for the discussion above, Figure 4.15 summarizes the dominant reaction pathways at each electrode as a function of time during the half-cycle for a two-electrode measurement. Regions shaded below the voltage curve represent dominant processes at the cathode, while regions shaded above the voltage curve represent processes that dominate at the anode. The unshaded areas represent regions of transition between reaction pathways at each electrode. This clearly shows the three different reaction pathways associated with electrodissolution and the two related to electrodeposition, as described previously in Figure 4.10. This understanding allows for detailed information to be extracted about Li metal electrodes, simply by analyzing the voltage traces from galvanostatic cycling. Furthermore, Figure 4.16 shows this behavior is observed at 0.5, 0.75, 1, 2, 5, and 10 mA cm^{-2} making the interpretation of these voltage traces applicable for conditions of practical battery operation.

4.3.3 Effect of Electrolyte on Electrode Performance and Voltage Profiles

To demonstrate how the understanding of Section 4.3.2 can be more generally applied, we intentionally selected three electrolytes (1M $LiPF_6$ EC:DMC (1:1); 4M LiFSI DME; and 1M LiTFSI DOL:DME (1:1) with 0.18M Li_2S_8 and 2 wt% $LiNO_3$) with significantly different additives, concentrations, solvents, and salts (See Section 4.5 for more details). The general optimization of these electrolytes in Li-Cu cells has been well documented elsewhere.[49,103] By utilizing Li-Li symmetric cells and intentionally selecting these three significantly different electrolyte systems with known performance differences, we demonstrate that interpretation of voltage traces is a robust method for gaining mechanistic insight into Li metal electrode behavior. For simplicity we will refer to each system only by its

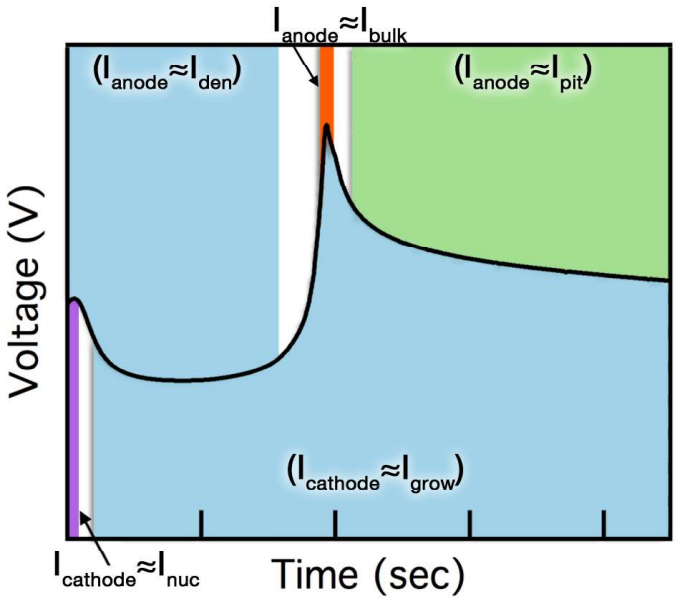

Figure 4.15: *An experimental two-electrode voltage trace showing the dominant reaction pathways at each electrode as a function of time. Shaded regions indicate dominant pathways at the anode (above profile) and cathode (below profile). Unshaded areas represent regions of transition between pathways.*

salt (i.e. $LiPF_6$, LiFSI, LiTFSI), however the compositions remain identical to those listed above. Specifically the LIFSI and LiTFSI are being investigated as potential electrolytes for Li-S batteries, making them of significant interest to the research community.

4.3.3.1 Visualization Cell Results for a variety of Electrolyte compositions

The visualization cell results for the LiFSI and LiTFSI electrolyte systems are shown in the supplementary videos of the manuscript.[15] These videos, in addition to Figure 4.17a, show that the ether-based electrolytes clearly increase nucleation density, reduce dendrite size, and lead to more complete surface coverage, especially for the LiTFSI electrolyte. As seen in the videos, the same general form of the voltage trace is observed for the LiFSI and LiTSFI systems (Figure 4.18). However, after a few cycles, the abruptness of the transitions (δV_{cell}) becomes significantly less pronounced than for the $LiPF_6$ system. This is consistent with observations in the numerical model that, as the difference between k^0_{fast} and k^0_{slow} becomes small, the transitions become less well defined.

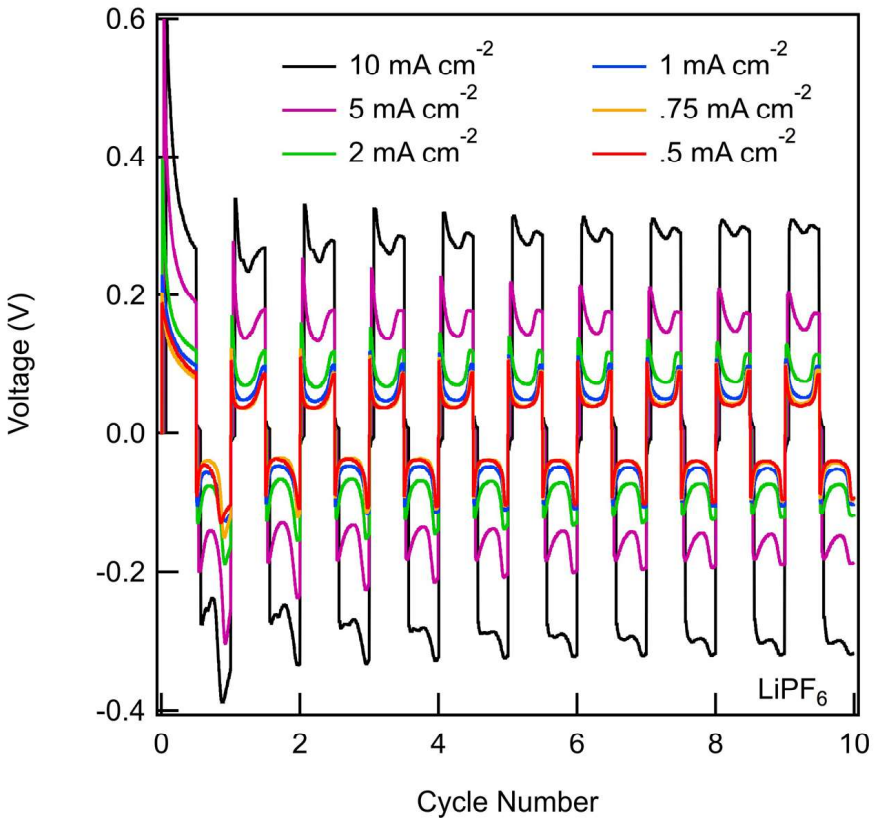

Figure 4.16: *Voltage traces for coin cells cycled in $LiPF_6$ at current densities of 0.5, 0.75, 1, 2, 5, 10 mA cm^{-2}.*

Additionally, the voltage maximum associated with transitioning between reaction pathways on the anode surface occurs later in the half-cycle (i.e., the amount of time between the voltage minimum and maximum becomes larger). We note that in the ether-based electrolytes, the time required to observe this polarization maximum may be longer than the duration of the previous half-cycle (Figure 4.17c). For this reason, the voltage traces observed during periodic galvanostatic cycling terminate before the final decrease in cell polarization occurs (Figure 4.18). This correlates to a greater duration of simultaneous Li electrodissolution from the bulk and dendrites as the reaction pathway transitions, as discussed in Section 4.3.2.2.

In order to better understand these effects, time-dependent EIS measurements were performed to study the formation, growth, and impedance of the SEI on fresh Li surfaces (Figure 4.19). The data show that the ether-based electrolytes form lower impedance and

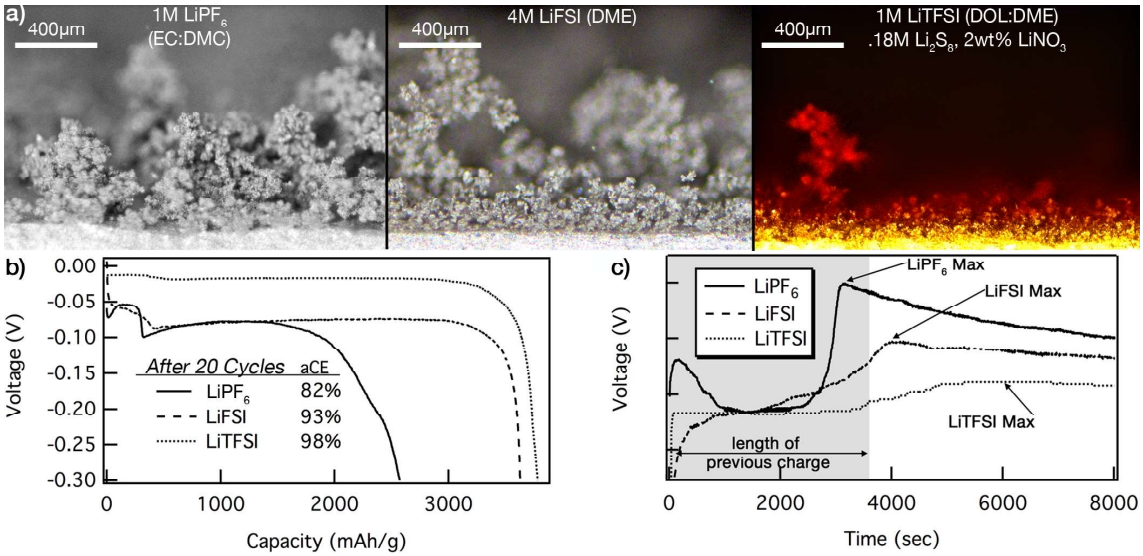

Figure 4.17: *Comparison of three very different electrolyte systems ($LiPF_6$, LiFSI, and LiTFSI). (a) Visualization cell images after 900 s of deposition at 5 mA cm^{-2}. A clear difference in dendrite size, nucleation density, and surface coverage is observed. (b) Cell discharge curves at 1 mA cm^{-2} showing remaining capacity after 20 cycles (theoretical capacity 3860 mAh g^{-1}). This performance can be linked to peak position in panel c, where voltage traces for each electrolyte system are shown.*

more stable SEI layers compared to the $LiPF_6$ system. These SEI layers thus have a lower energy barrier for electrodissolution at the anode surface, which leads to closer values of the effective rate constants. As a result, the transition in reaction pathways begins sooner in the half-cycle and lasts for a longer duration. In other words, the unshaded regions of Figure 4.15 (which for $LiPF_6$ are well defined and relatively narrow) become wider.

4.3.3.2 Comparing Voltage Traces with Performance in Coin Cells using Different Electrolyte Compositions

To show how the understanding of Section 4.3.3.1 can be observed in coin cells. Li vs. Li symmetric cells were fabricated using each electrolyte system and Li-Cu laminate electrodes (Rockwood Li, 50 µm of Li on 10 µm Cu). The cells were cycled 20 times at 1 mA cm^{-2}, such that a planar equivalent of 4.8 µm of Li was transferred during each half-cycle (1C rate). After cycling, Li on one electrode was completely dissolved from the Cu to determine the amount of Li lost during cycling. By calculating the average amount of Li

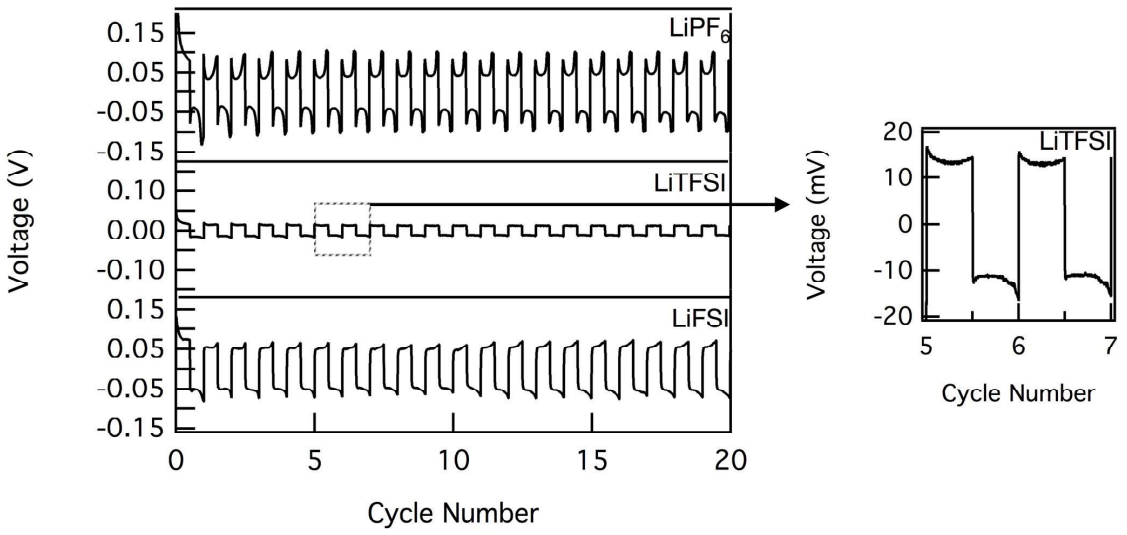

Figure 4.18: *Voltage traces for the different electrolytes studied in this work. Due to the small cell polarization for the LITFSI, a magnified portion of the voltage profile is shown to the right.*

lost during each cycle, an aCE for the Li electrode can be obtained (Figure 4.20). This is a modified version of a method developed by Aurbach et al.[111]

In Figure 4.17b,c aCE is compared to the position of the voltage maximum associated with transitioning between reaction pathways on the anode surface. Figure 4.17b shows significantly less capacity loss for the ether-based electrolytes compared to the carbonate based $LiPF_6$. This corresponds to aCE values of 82% ($LiPF_6$), 93% (LiFSI), and 98% (LiTFSI). A detailed view of the voltage profile for an extended half-cycle is shown for each system in Figure 4.17c. Consistent with Section 4.3.2, the $LiPF_6$ cell exhibited distinct transitions between reaction pathways. By comparison, the LiFSI coin cell exhibited a more blunted cell polarization maximum that occurs at a later time than the peak in $LiPF_6$, indicating less distinct transitions between reaction pathways and a lower voltage hysteresis. Finally, the LiTFSI cell displayed the lowest overpotential, the latest, most blunted cell polarization maximum and lowest voltage hysteresis.

The shifting of these cell polarization maximums is directly correlated with an increase in the aCE value. Comparing Figure 4.17a and 4.17c also shows that a smaller magnitude and delayed cell polarization maximum is directly related to denser/smaller dendrites that

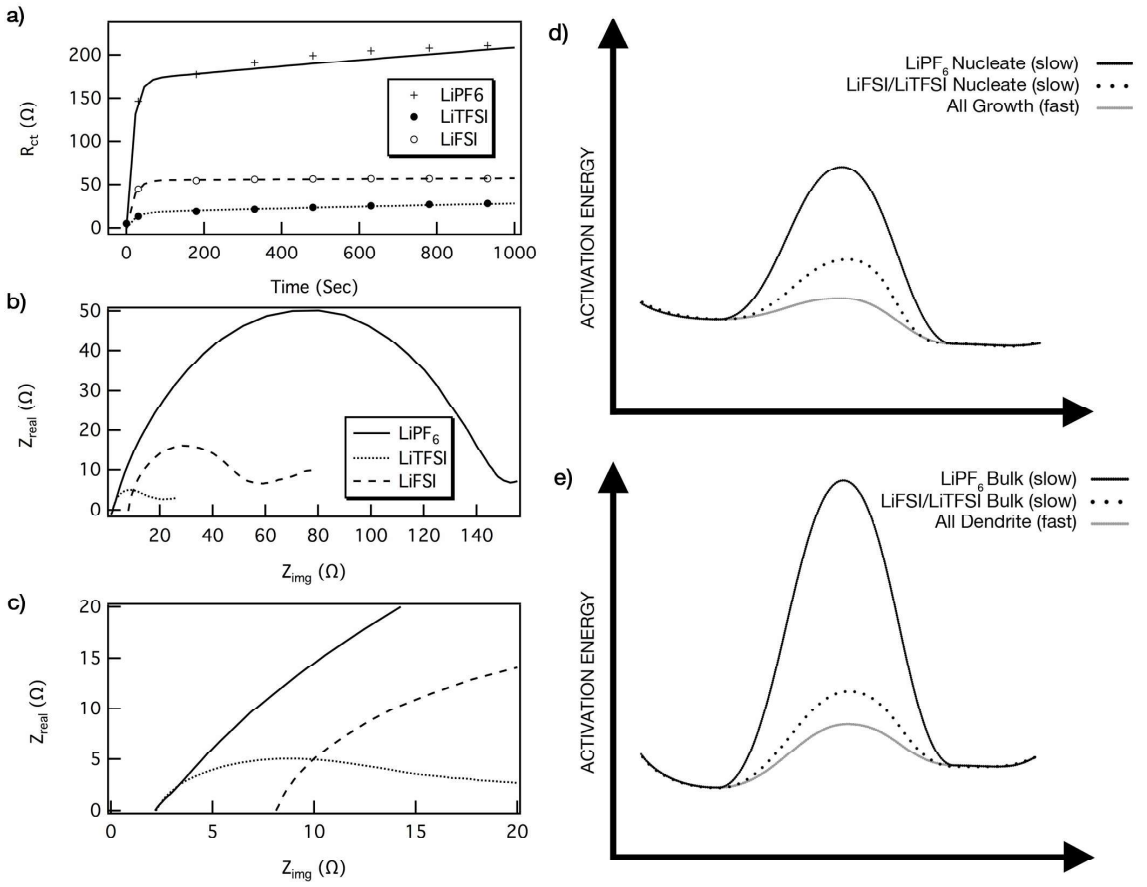

Figure 4.19: *Time-dependent EIS measurements for the LiPF6, LiFSI and LiTFSI electrolyte systems. a) Growth of impedance as a function of time for the different electrolyte systems b) EIS spectra after 30 s of contact with fresh Li c) a magnified view of the EIS spectra shown in b). The other graphics show a schematic representation of how ether-based electrolytes decrease the energy barriers of d) nucleation and e) dissolution from the bulk.*

completely cover the surface. Since this voltage behavior is observed in a wide range of battery architectures, this interpretation allows for a cycle-by-cycle comparison of Li metal electrode performance. Understanding the dominant reaction pathways at specific points in time provides a window into the time-dependent morphological and electrochemical changes occurring within the coin cell, where we are typically blind to morphology.

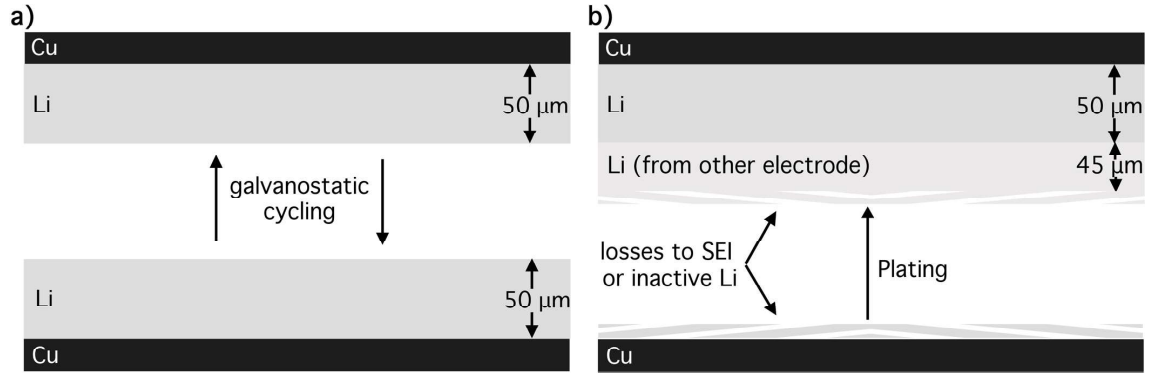

Figure 4.20: *Schematic depicting the modified version of the aCE method proposed by Aurbach et al.*[111] *a) Initial setup of the cell. Starting from this point, the cells were cycled at 1 mA cm*$^{-2}$ *such that 3.6 C cm*$^{-2}$ *of charged were passed during each of the galvanostatic half cycles. b) During the final cycle all of the Li was dissolved from one electrode and plated onto the other. The amount of Li lost to SEI formation or through dead/detachment of Li can then be calculated and divided by the number of cycles to determine an aCE value.*

4.4 Conclusions

In this work, we have shown through *operando* video evidence and numerical modeling that galvanostatic voltage traces can be directly correlated to changes in morphology of Li metal electrodes in Li vs. Li symmetric cells. This correlation has led to several key points of understanding:

1. The evolution of dendrite morphology is driven by transitions between reaction pathways

    - During the initial half-cycle, inhomogeneous dendrite nucleation occurs at the cathode. Since the SEI on freshly plated Li will have faster reaction kinetics than the bulk surface, subsequent Li deposition will preferentially occur on existing dendrites rather than nucleating new dendrites. The degree to which dendrite growth is more favorable than nucleation is dictated by the SEI, which depends on the electrolyte system. Upon switching polarity, the dominant reaction pathway at the anode is kinetically fast dissolution of dendritic Li. As the amount of active Li within the dendrites approaches zero, a characteristic increase in cell polarization appears, due to a transition to kinetically slower

dissolution from the bulk surface.

2. Pitting occurs once dissolution from the bulk surface begins

    - Electrodissolution from the bulk leads to to the formation of pits. Subsequently, as the surface layers are fractured during pitting, kinetically faster reaction pathways are formed. As dissolution continues, the surface area associated with pits continues to increase, resulting in decreasing cell polarization.

3. Transitions between reaction pathways dictate changes in voltage

    - After the first half-cycle, the initial portion of the voltage trace is dominated by the cathode, as a transition occurs from dendrite nucleation to growth. After the minimum cell polarization is reached, the kinetics at the anode begin to dominate the voltage trace, as the surface area of the kinetically fast dendrites decreases. This leads to a transition in reaction pathway from dissolution of dendrites to dissolution from the bulk surface, causing a cell polarization maximum. As pitting occurs, the decrease in cell polarization is driven by increasing surface area of both pits at the anode and dendrites at the cathode.

4. Voltage traces can be correlated to electrode performance

    - Variations in the voltage trace shape in different electrolyte systems can be linked to cell performance. For systems with poorer performance, the peak associated with the transition between dominant reaction pathways at the anode has a steeper slope, occurs at an earlier time in the half cycle and demonstrates less voltage hysteresis. Conversely, for systems with superior performance, that maximum is less distinct, occurs at a later time, and has a smaller magnitude. In general, a shifting of the cell polarization maximum can be directly correlated to improved CE.

These results provide significant new insight into the behavior of Li metal electrodes, which can assist researchers in the quest to achieve commercially viable Li-metal-anode secondary batteries. Furthermore, the experiments designed in this work can be applied to a range of battery chemistry including, Li-ion, Li-Sulfur, Li-air, Zn-air and more.

4.5 Materials and Methods

4.5.1 Material Handling

All air sensitive materials were handled in an argon filled glovebox (MBraun), with water and moisture levels below 1 ppm. The $LiPF_6$ electrolyte (Soulbrain) contains <7ppm water, while the battery-grade solvents used in the sulfur-based electrolytes were purchased from BASF Inc, and contain <20 ppm water.

4.5.2 Visualization Cells

Operando tests were conducted in a custom-built visualization cell (Figure 4.4), allowing simultaneous collection of electrochemical and morphological information. The entire assembly is air-tight with a quartz viewing window and O-ring seal so that it can be removed from the glovebox after assembly and placed under an optical microscope for viewing. Air-tight electrical feedthroughs connect the electrodes with the potentiostat. All visualization cell experiments were carried out using a Gamry 1000 or Biologic VSP potentiostat using 1M $LiPF_6$ in 1:1 EC:EMC, 1M LiTFSI in 1,3-dioxolane/1,2-dimethoxyethane (DOL:DME) with 0.18M Li_2S_8 and 2 wt% $LiNO_3$, and 4M LiFSI in DME. The LiFSI and LiTFSI electrolytes were synthesized following a formulation similar to the those described previously.[50,92] For each half-cycle, 4.5 C cm^{-2} of charge was passed for 10 complete charge and discharge cycles. After each half-cycle, the system was allowed to relax for 30 s. The optical microscopy images were taken with a Nikon LV150N microscope at 5x with a plan

objective, n.a. 0.10, w.d. 31 mm.

4.5.3 Three-electrode Measurements

Three-electrode measurements were experimentally conducted using a hermetically sealed glass-wear setup. The reference electrode (RE) was a scraped, cleaned and stabilized piece of Li foil. The data was collected using the bi-potentiostat capabilities of the Biologic VSP system, which can measure the potential of the counter electrode and working electrode vs. RE simultaneously.

4.5.4 Coin Cells

Symmetric Li coin cells were assembled with CR2032 coin cell shells, spacers, and wave springs (MTI Corp.). The Li-Cu laminate electrodes (99.9%, Rockwood Li) were pentane cleaned[14] and immediately assembled into coin cells using 45 µL of the electrolytes described above. A hydraulic crimping press was used to compress these coin cells to 1000 psi. Low resolution cycling was completed on a Landt 2001a battery testing system.

CHAPTER 5

Surface Chemistry of LLZO

Adapted with permission from Sharafi, A.; Kazyak, E.; Davis, A. L.; Yu, S.; Thompson, T.; Siegel, D. J.; Dasgupta, N. P.; Sakamoto, J. Surface Chemistry Mechanism of Ultra-Low Interfacial Resistance in the Solid-State Electrolyte $Li_7La_3Zr_2O_{12}$. *Chem. Mater.* 2017, 29 (18), 79617968. Copyright (2017) American Chemical Society.

Despite the fact that Li metal anodes have been studied for more than 40 years, it has remained very challenging to achieve stable, high Coulombic efficiency cycling when used with liquid electrolytes. Chapter 4 developed a detailed model to understand the coupling between interfacial inhomogeneity, morphology evolution, and electrochemical performance of Li metal anodes. The SEI that formed upon contact between the Li metal and the liquid, and the unconstrained volume expansion of the Li metal in dendritic structures were shown to ultimately cause the low Coulombic efficiency and safety concerns. To overcome these challenges, there has been a surge in interest regarding the use of SSEs to replace the flammable liquid electrolytes that are currently used in LIBs.[57] Many SSEs have been developed and studied for their potential to enable Li metal electrodes while maintaining safety and long cycle-life.[31]

The garnet-type SSE, LLZO, is unique in that it is a fast Li-ion conductor (1 mS cm^{-1} at 298 K), exhibits sufficient mechanical properties,[112] and is also chemically and electrochemically stable against metallic Li.[113] Despite these promising attributes, additional challenges must be overcome before SSBs based on LLZO are viable. Demonstrating low

Li-LLZO interfacial resistance ($R_{Li\text{-}LLZO}$) is a critical milestone along the path to commercialization. While several studies have characterized $R_{Li\text{-}LLZO}$, nearly all report values significantly higher than conventional LIBs employing liquid electrolytes (approximately 10 Ω cm^2).[114–116] Thus, strategies to reduce $R_{Li\text{-}LLZO}$ to values comparable to, or lower than, LIBs are needed.

Recently, coating of the LLZO surface was investigated to reduce $R_{Li\text{-}LLZO}$. For example, Tsai et al. sputter coated Au on LLZO and demonstrated a $R_{Li\text{-}LLZO}$ of 58 Ω cm^2 at 25 °C.[117] It was hypothesized that the Au coating provided uniform conductivity at the Li-LLZO interface, lowering $R_{Li\text{-}LLZO}$. In related work, Han et al. suggested that an Al_2O_3 coating could reduce $R_{Li\text{-}LLZO}$, but the interface resistance was not directly measured using EIS; instead, $R_{Li\text{-}LLZO}$ was extrapolated from DC cycling data, making it difficult to quantitatively interpret efficacy. The authors attributed the reduction in $R_{Li\text{-}LLZO}$ to enhanced Li wettability of the LLZO surface.[118] However, the mechanism of how surface modifications led to improved performance has not been explicitly determined.

Thus, while the use of coatings can in some instances improve performance, the underlying physical and chemical mechanisms that control interfacial resistance are not well understood, which has limited interfacial chemical modification studies to largely empirical observations. A mechanistic understanding of the coupling between interfacial chemistry, Li wettability, and interfacial resistance would accelerate the rational design of engineered interfaces having low $R_{Li\text{-}LLZO}$. Such an understanding would also address the question of whether low interfacial resistance could be achieved without the need for coatings, as these add additional processing steps, create additional interfaces, and could compromise cycle life if the coating does not maintain integrity upon cycling.

In this study, we provide a mechanistic understanding of the interplay between interfacial chemistry and electrochemical performance at solid-solid interfaces in SSBs. This understanding provides design rules for engineering low-resistance interfaces. Accordingly, we demonstrate that the Li-LLZO interfacial resistance can be nearly eliminated (2

Ω cm^2) through a simple, coating-free process to modify the surface chemistry of LLZO.

The importance of Li wettability in achieving low-resistance Li-SSE interfaces in SSBs has been discussed in a few recent studies.[117–120] However, a quantitative evaluation of Li wettability as a function of SSE surface chemistry is currently lacking. To address this, molten Li contact angle measurements using a sessile drop test were conducted on several relevant surfaces including LLZO with varying surface chemistry. Trends in the measured contact angles are consistent with those calculated with DFT and demonstrate the connection between surface chemistry and Li wettability.

Our study quantitatively demonstrates the relationships between interfacial chemistry, Li wettability, and facile charge transport. Equipped with this understanding, we demonstrate that controlling interfacial chemistry enables a straightforward pathway toward viable SSBs.

5.1 Results and Discussion

5.1.1 Surface Chemical Analysis

As has previously been shown, the surface chemistry of LLZO is sensitive to air exposure.[116,121] A contamination layer readily forms and is predominantly composed of lithium carbonate (Li_2CO_3), lithium hydroxide (LiOH), and other adventitious carbon species,[116,121] which collectively result in high interfacial resistance between LLZO and metallic Li.[116,122] It has been reported that dry polishing (DP) in an inert atmosphere can lower the interfacial resistance by partially cleaning the surface; however, the efficacy of this approach is limited to reducing the interface resistance from approximately 1000 Ω cm^2 to ~100 Ω cm$_2$.[116,122] Here, several surface conditioning protocols, including DP, Wet polishing (WP), and heat treatment (HT), were employed in an attempt to reduce the interfacial resistance, and their impact on LLZO surface chemistry was evaluated (details regarding the DP and WP conditions are explained in section 5.3). HT between 200 and

500 °C in an inert atmosphere was conducted after DP and WP.

The surface chemistry of LLZO was analyzed using XPS after each conditioning protocol (Figure 5.1). Measurements were performed on samples transferred without air exposure between an argon-filled glovebox and the UHV XPS chamber. Figure 5.1a shows that in samples conditioned with DP or WP (no HT) a surface layer blocks nearly all the signal attributed to La and Zr. In these cases, the surface layer is composed almost entirely of H, Li, C, and O (H content cannot be directly detected by XPS but can be observed as hydroxyl bonds). The nature of the bonds in which these species participate can be examined through high-resolution core-scans. The O 1s peak reveals a significant difference between the surface layer after WP vs. DP (Figure 5.1b). The WP surface consists of predominantly hydroxide species, while a greater concentration of carbonate species exists on the DP sample. This suggests that the use of polishing fluid protects the LLZO surface from reformation of carbonate species.

Samples that underwent HT were first polished (DP or WP in ambient air) and then immediately transferred into an argon filled glovebox where the samples were heated to different temperatures. Subsequent XPS analysis demonstrated significant variations in the surface chemistry of these samples. In Figure 5.1a, a plot of the ratio of the C content to the summed La and Zr contents is used as a metric to quantify the amount of surface contamination. The lower the ratio, the more closely the surface resembles bulk LLZO. Some adventitious carbon is always observed on the LLZO surface, even for samples kept continuously in an argon atmosphere after HT, Figure 5.1c. The amount of contamination is observed to dramatically decrease after heating to 400 and 500 °C. This is consistent with the O 1s core scans shown for these samples, which demonstrate that the predominantly hydroxide and carbonate surfaces before heating are converted to primarily oxide species (as expected in bulk LLZO) after heating (Figure 5.1b).

In contrast, heating a DP sample to 400 °C did not change the surface as dramatically, with carbonate species still dominating (Figure 5.2). A plot of the fractional surface com-

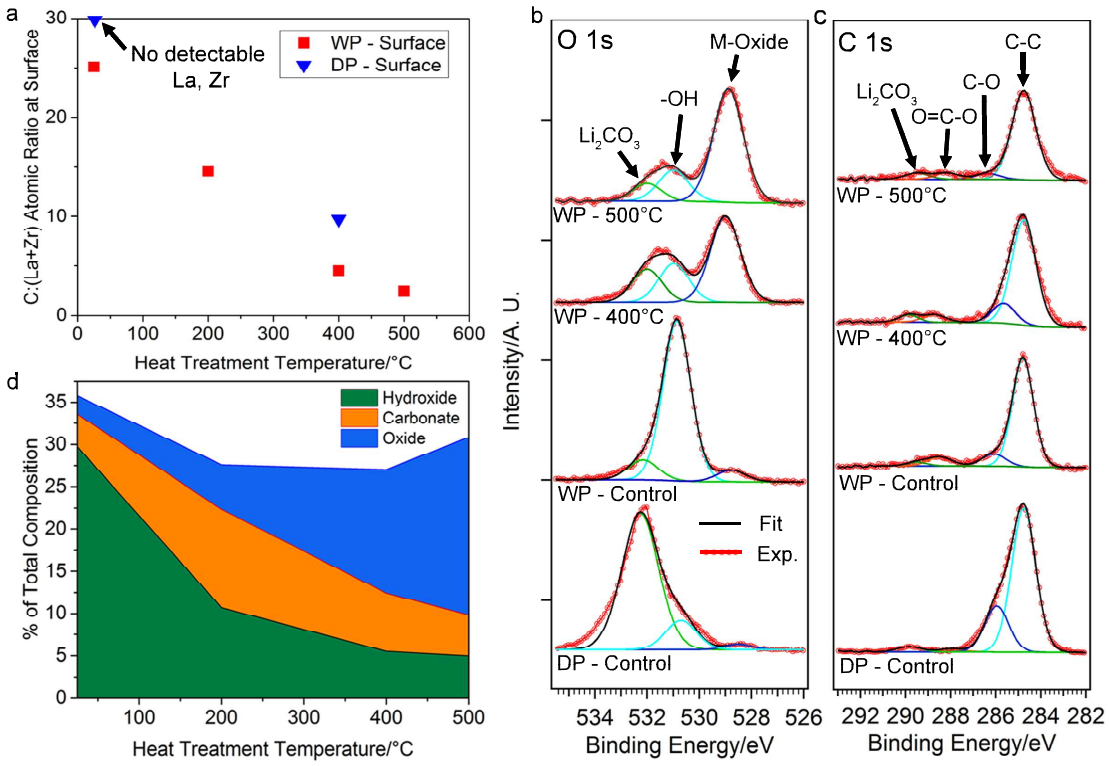

Figure 5.1: *XPS analysis of LLZO before and after HT at 400 and 500 °C. (a) C:(La+Zr) atomic ratio as a function of HT temperature; (b) O 1s and (c) C 1s core levels; (d) percentage of total composition of different oxygen species on the LLZO surface as a function of HT temperature after WP.*

position of the oxygen containing species is shown in Figure 5.1d for WP samples heated to different temperatures. As the HT temperature increases to 500 °C, the oxide fraction steadily increases, the hydroxide fraction decreases, and the amount of carbonate remains roughly constant. In total, these observations suggest that (1) compared to DP, WP is more effective at achieving a surface with low carbonate content, (2) HT up to 500 °C can remove LiOH but is less effective at removing Li_2CO_3, and (3) of the strategies examined, the successive combination of WP and HT is the most effective at removing both carbonate and hydroxide surface contamination layers.

The removal of LiOH species at temperatures between 400 and 500 °C is consistent with prior thermogravimetric analysis, mass spectroscopy, and first-principles calculations.[122,123] This suggests that the surface layer that reforms as a result of WP is more easily removed by HT, thereby making the combination of WP and HT in an inert atmosphere an

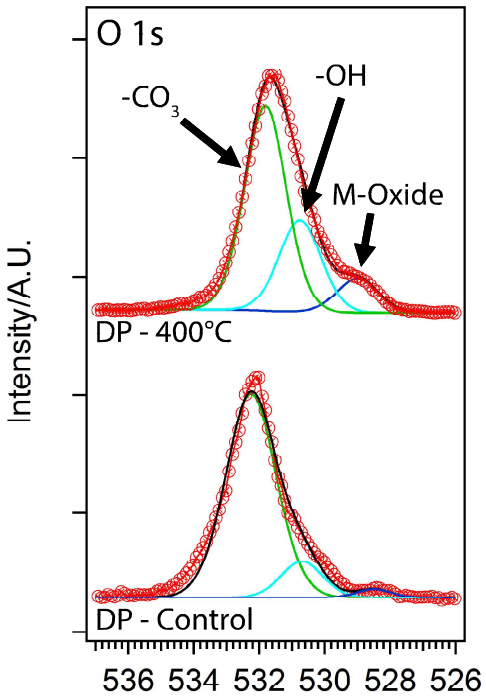

Figure 5.2: *XPS analysis of LLZO showing the O 1s core level of sample after DP (DP-Control) and after DP and HT at 400 °C (DP-400 °C).*

attractive option to achieve a well-controlled LLZO surface prior to forming the Li-LLZO interface.

5.1.2 Contact Angle Measurements and Calculations

The wettability of a SSE by metallic Li has been proposed to influence interfacial resistance in SSBs.[117,118,120,124,125] However, quantitative analysis of the Li contact angle and direct correlation with surface chemistry have not been reported. To characterize wettability, sessile drop tests were performed to measure the contact angle of molten Li on Li_2CO_3 and on LLZO samples after various surface conditioning processes (Figure 5.3). Molten Li was deposited onto heated Li_2CO_3 or LLZO from a heated stainless-steel syringe. Both the surfaces and the syringe were kept above the Li melting temperature. Importantly, the native layers (composed of oxide, nitride, and carbonate species)[126] present on the surface of the Li foil did not melt and thus were easily removed from the molten Li source.

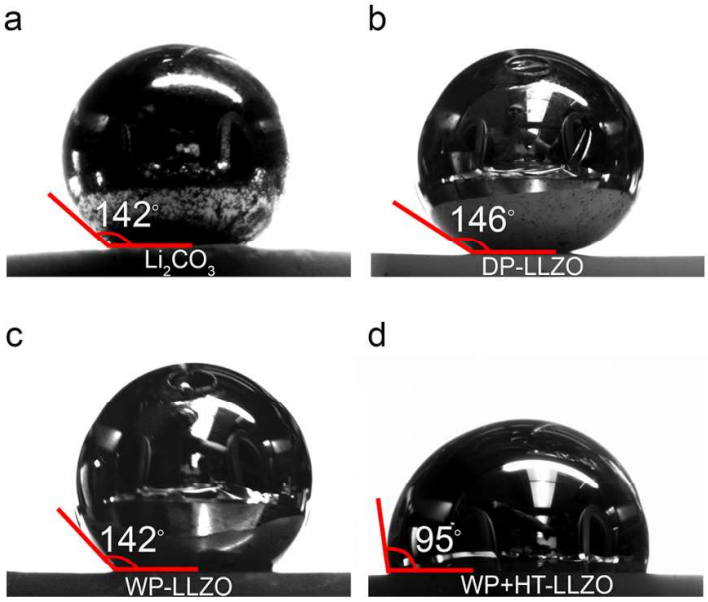

Figure 5.3: *Contact angle measurements of molten metallic Li on (a) Li_2CO_3, (b) DP-LLZO, (c) WP-LLZO, (d) WP-LLZO after HT at 500 °C.*

This allowed for deposition of purified molten Li onto the LLZO surface. The present approach differs from a scenario involving the melting of solid Li foil directly on LLZO, as wettability in the latter approach will be influenced by the presence of native layers on the Li surface and at the Li-LLZO interface. All experiments were performed inside an argon-filled glovebox, and high-resolution cross-sectional images were captured and digitally analyzed to determine contact angles.

As shown in Figure 5.3, the DP-LLZO sample exhibited the highest contact angle among all LLZO samples, $\theta = 146°$, which was nearly identical to the value measured for a pure Li_2CO_3 surface ($\theta = 142°$). Such a large contact angle is consistent with a non-wetting interaction typical of an interface exhibiting weak adhesion. The similar wetting behavior observed for both the DP-LLZO sample and Li_2CO_3 is expected, given that the DP-LLZO surface is composed predominantly of Li_2CO_3. Similarly, the WP-LLZO contact angle was $141°$, which is consistent with the presence of the hydroxide and carbonate contamination layer, which was observed with XPS. Figure 5.4 demonstrates the similarly lithiophobic nature of Li_2CO_3 and DP-LLZO as molten Li easily rolls off these surfaces.

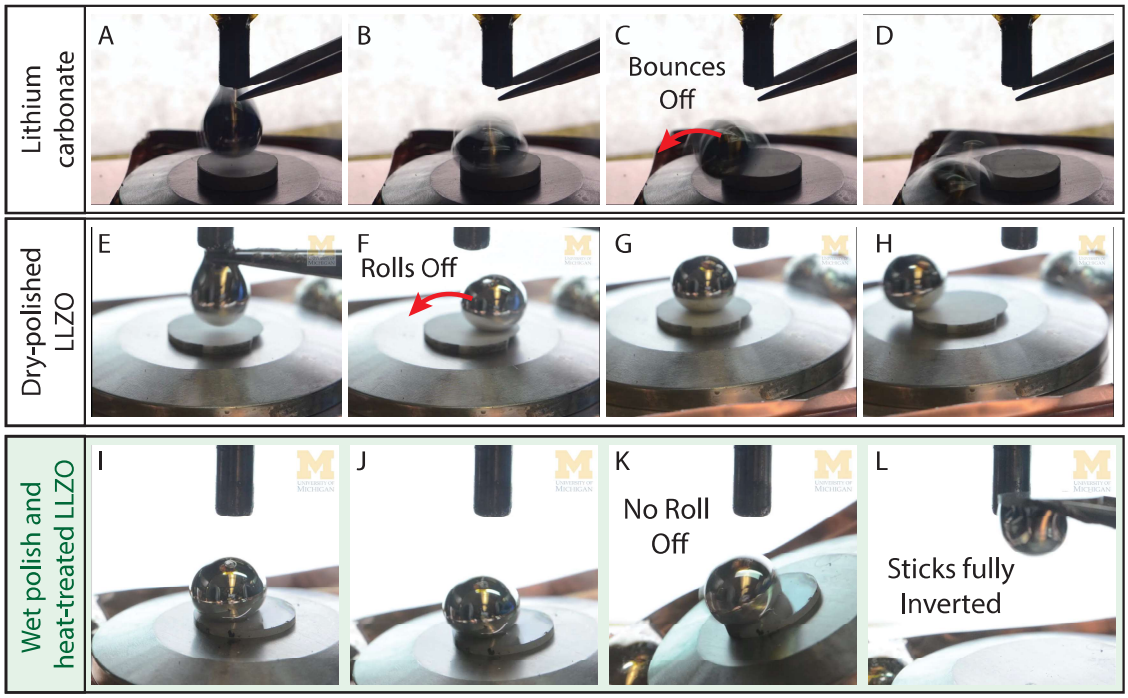

Figure 5.4: *Time-series images showing molten Li droplet bouncing off of a lithium carbonate pellet (A-D), rolling off of a DP LLZO pellet (E-H), and adhering to the WP+HT LLZO surface even when fully inverted (I-L).*

In contrast, the WP-LLZO, heated to 500 °C, exhibited a significantly lower contact angle ($\theta = 95°$). We hypothesize that this reduction in contact angle is caused by the removal of hydroxide and carbonate species, resulting in a surface more closely resembling bulk LLZO, which interacts more strongly with Li metal. Figure 5.4 demonstrates the more lithiophilic nature of this interface, as molten Li maintains adherence to the LLZO surface even when fully inverted vertically.

To validate the correlation between surface chemistry and wettability, the wetting angle of Li on LLZO, Li_2CO_3, and LiOH was evaluated by our collaborators using DFT calculations.[104] The contact angle, θ, for these interfaces was calculated by combining the Young-Dupré equation, $W_{ad} = \sigma_{Li}[1 + \cos(\theta)]$, with DFT calculations of the interfacial work of adhesion, W_{ad}, and the surface energy of Li, σ_{Li} = 0.45 J m^{-2}. More details of these calculations can be found in the paper.[16]

The trend predicted by these calculations - that Li strongly wets LLZO, but not Li_2CO_3,

is consistent with the measurements shown in Figure 5.3. More specifically, the wetting angle predicted for the Li-Li_2CO_3 interface, $\theta = 142°$, is in excellent agreement with the measured value ($142°$, Figure 5.3a) indicating a weak interfacial interaction between Li and Li_2CO_3 ($W_{ad} = 0.10$ J m^{-2}). In contrast, the calculated W_{ad} for the Li-LLZO interface is nearly seven times larger, $W_{ad} = 0.67$ J m^{-2}, resulting in a relatively small wetting angle, $\theta = 62°$. This value is qualitatively consistent with the measured value of $95°$ reported in Figure 5.3d. The smaller value predicted by the calculations is expected, given that approximately 15% of carbonate or hydroxide remains on the LLZO surface after heating to 500 °C (Figure 5.3d).

5.1.3 Electrochemical Characterization

EIS was performed on Li-LLZO-Li symmetric cells (Figure 5.5a) to measure the LLZO bulk (R_{bulk}), grain boundary (R_{gb}), and Li-LLZO interfacial ($R_{Li\text{-}LLZO}$) resistances for WP and HT samples between 200 and 500 °C. EIS data were modeled using an equivalent circuit shown in Figure 5.5b. This approach allowed for the direct measurement of the individual contributions to cell resistance and involves the correlation between characteristic frequencies and transport phenomena.[127] Representative EIS spectra for a cell consisting of a WP and HT at 500 °C LLZO sample before and after preconditioning at 175°C are shown in Figure 5.5c (preconditioning was used to ensure good contact between metallic Li and LLZO by heating the Li-LLZO-Li cell to 175 °C for 12 h).[115] From Figure 5.5c, it is apparent the LLZO total resistance (R_{bulk} + R_{gb}) has remained constant (500 Ω cm^2), while $R_{Li\text{-}LLZO}$ dramatically decreased upon preconditioning at 175°C and cooling. Initially, $R_{Li\text{-}LLZO}$ was approximately 400 Ω cm^2, which is significantly lower than previous values reported for LLZO after DP in literature.[115] After preconditioning at 175 °C, a further dramatic reduction in $R_{Li\text{-}LLZO}$ was observed. The combination of WP, HT, and preconditioning results in an extremely small interfacial resistance of 2 Ω cm^2.

Figure 5.5d shows $R_{Li\text{-}LLZO}$ after preconditioning for WP LLZO samples with no HT

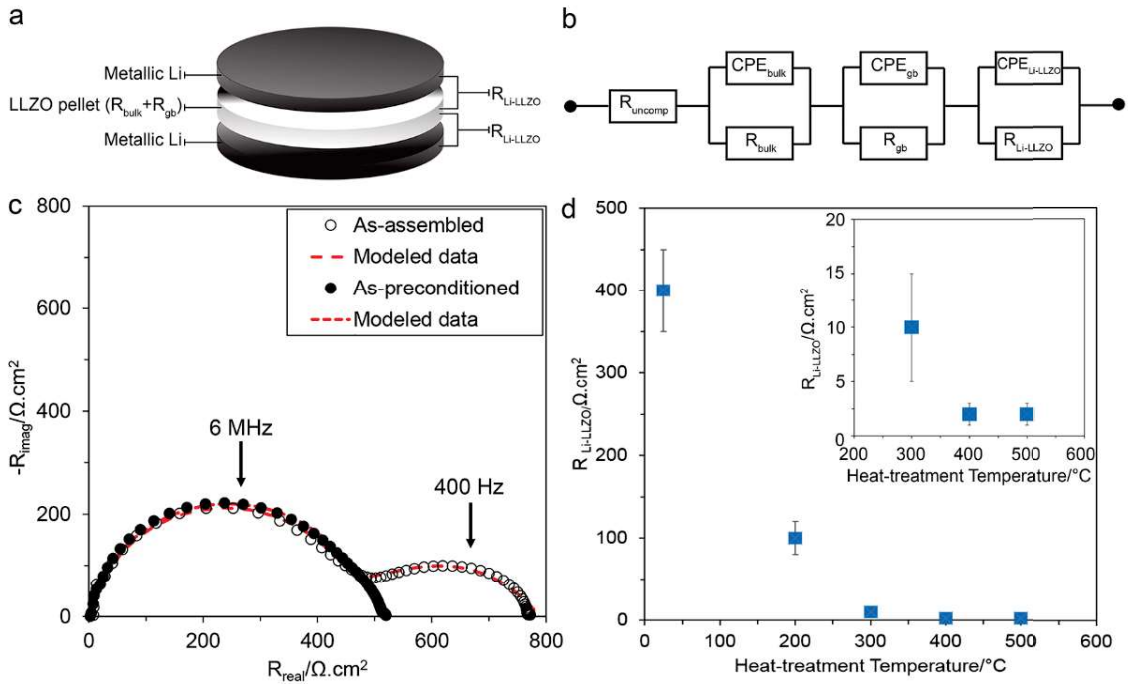

Figure 5.5: *(a) Schematic of the all-solid-state Li-LLZO-Li cell, (b) equivalent circuit used for modeling the EIS data, (c) representative Nyquist plot of the Li-LLZO-Li cell (for LLZO heated to 500 °C), as-assembled and after preconditioning at 175 °C. Markers indicate experimental data and dotted lines represent from the equivalent circuit model simulation using the circuit shown in panel b, (d) the Li-LLZO interfacial resistance after preconditioning at 175 °C versus the HT temperature. N = 3 for each HT condition. Error bars represent standard deviations.*

and HT at several temperatures between 200 and 500 °C. With increasing HT temperature, $R_{Li\text{-}LLZO}$ decreases from 400 to 2 Ω cm^2. Importantly, the low interfacial resistance coincides with the removal of the surface contamination layer. Furthermore, the decrease in interfacial resistance closely follows the trend in surface chemistry with HT temperature observed in XPS measurements, and with the improved wettability of the LLZO surface after HT. Taken together, these observations provide quantitative evidence of the strong coupling between surface chemistry, wettability, and interfacial resistance.

The cycling behavior and critical current density (CCD) of a WP-LLZO sample HT to 500°C (WP+HT) were characterized using a combination of DC cycling and EIS analysis (Figure 5.6). The CCD is defined as the lowest current density at which cell shorting occurs due to Li metal penetration.[115,128] After removal of the surface contamination, the CCD was determined to be 0.3 mA cm^{-2} (Figure 5.6a). The CCD from the WP+HT sample

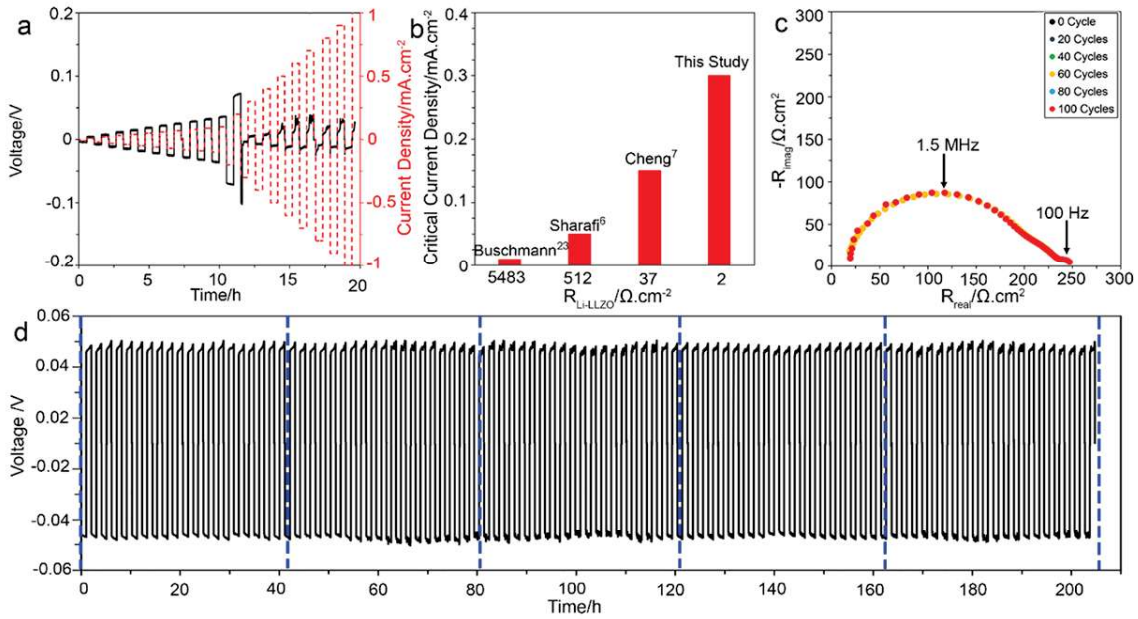

Figure 5.6: *(a) DC cycling of Li-LLZO-Li cells (LLZO HT to 500 °C after WP) at RT, stepping the current density from 0.01 to 1 mA cm^{-2}, (b) the CCD versus Li-LLZO interfacial resistance comparing the results of this study with other studies available in the literature, (c) Nyquist plots of a Li-LLZO-Li cell after each 20 cycles for cell cycled 100 times, (d) galvanostatic cycling of Li-LLZO-Li cell at 0.2 mA cm^{-2} for 100 cycles at 0.4 mAh cm^{-2}. The blue dotted line shows the times at which EIS was collected and is shown in panel c.*

prepared here is compared in Figure 5.6b to other Li-LLZO-Li symmetric cells reported in the literature.[115,116,129] The CCD measured in this study is one the highest values reported in literature for an LLZO SSE. Our data indicate that the CCD and $R_{Li\text{-}LLZO}$ are inversely correlated, suggesting that higher power density can be achieved by controlling interfacial chemistry, and thus $R_{Li\text{-}LLZO}$.

To evaluate the stability of the interface after WP+HT upon cycling, a Li-LLZO-Li cell was cycled for one hundred cycles at ±0.2 mA cm^{-2} at RT (Figure 5.6d). After every 20 cycles, EIS analysis was conducted to assess changes in R_{bulk}, R_{gb}, and $R_{Li\text{-}LLZO}$. Figure 5.6c shows that negligible changes in the EIS spectra were observed, implying excellent stability of the interface and the absence of short-circuiting. Furthermore, the total cell resistance (R_{bulk} + R_{gb}+ $R_{Li\text{-}LLZO}$) estimated using the DC cell polarization voltage (230 Ω cm^2) (Figure 5.6a) agrees well with the total cell resistance measured using EIS (240 Ω cm^2). This agreement further validates the interpretation of the EIS data.

The DC and EIS characterization illustrate the importance of controlling interfacial chemistry. First, a low $R_{Li\text{-}LLZO}$ enables a path toward low resistance solid-state cell designs employing metallic Li anodes. Second, reducing $R_{Li\text{-}LLZO}$ increases the CCD. Although 0.3 mA cm^{-2} is one of the highest reported CCD values, it must be further increased to demonstrate relevance to vehicle electrification; the data in Figure 5.6b suggest further tuning surface chemistry and reducing $R_{Li\text{-}LLZO}$ may be an approach to achieve higher CCD. Lastly, a clean and discrete Li-LLZO interface is preferred to minimize side reactions and mechanical degradation. In preliminary cycling tests, the interface kinetics appear to be stable when cycling at ±0.2 mA cm^{-2} at RT. Altogether, the electrochemical characterization suggests WP+HT could enable the use of metallic Li anodes and LLZO in SSBs.

5.2 Conclusions

In closing, this study reveals the mechanism by which surface chemistry controls the resistance of the Li-LLZO interface. By exploiting this mechanism, very low interfacial resistances, 2 Ω cm^{-2}, comparable to solid-liquid interfaces in Li-ion cells, can be achieved without the need for coatings. The removal of LLZO surface contamination was demonstrated to enhance Li wetting of LLZO, which was quantitatively evaluated using molten Li contact angle measurements through sessile drop tests. The interfacial chemistry and wettability measurements agree with atomic-scale DFT calculations of interfacial adhesion and wetting angle. The effects of surface chemistry and wettability were quantitatively correlated with the Li-LLZO interfacial resistance. The lower interfacial resistance made possible by controlling surface chemistry resulted in a doubling of the CCD. Moreover, this low interfacial resistance was preserved for one hundred cycles with no sign of short circuiting. This study clarifies the relationships between interfacial chemistry, Li wettability, interfacial resistance, and stable cycling. The knowledge gained enables the rational design of electrode/electrolyte interfaces and has general implications for solid-state trans-

port phenomena.

5.3 Materials and Methods

5.3.1 LLZO Specimen Preparation

Cubic Al-doped LLZO with nominal composition of $Li_{6.25}Al_{0.25}La_3Zr_2O_{12}$ was prepared using solid-state synthetic technique.[122] The methodology has been explained elsewhere in more detail. The calcined powder was densified using a custom rapid induction hot-press (RIHP) at 1100°C and 62 MPa for 1 h in graphite dies under argon shielding gas to achieve >97% relative density. Each sample was cut into 1.0±0.2 mm discs using a slow speed diamond saw. The discs were polished using 400 grit SiC sandpaper in air to ensure the parallel faces.

5.3.2 Surface Conditioning

Various surface conditioning processes including DP, WP, and HT were used. For DP, LLZO samples were polished manually using 400, 600, and 1200 grit sandpaper (Norton Corporation) in air without polishing fluid. For WP, an automated polisher (EcoMet 300 Pro, Buehler) was used. First, LLZO samples were ground using 1200 sand paper (Norton Corporation). After grinding, the samples were polished on Technotron polishing cloth (Leco Corporation) loaded with glycol-based diamond paste extender as the polishing fluid (Leco Corporation) and diamond polishing abrasives. The diamond polishing abrasive sequence ranged from 15, 6, 1 and down to 0.5 µm. After each diamond abrasive, samples were rinsed with ethanol to remove the residual polishing fluid from surface. Immediately after polishing, samples were transferred to an argon-filed glovebox. HT was conducted by placing the samples in a MgO boat and heating to temperatures between 200 to 500 °C in 100°C intervals in a muffle furnace (MTI Corporation) for 180 min using 4°C min^{-1} as

heating and cooling rate.

5.3.3 Surface Chemistry Characterization

A Kratos Axis Ultra was used for all XPS experiments. A custom O-ring sealed airtight transfer device was used to transfer samples into the XPS tool without air exposure. Survey scans used a pass energy of 160 eV and were quantified using Shirley backgrounds and Kratos sensitivity factors for the La 3d, Zr 3p, C 1s, O 1s, and Li 1s peaks in CasaXPS. Core scans used a pass energy of 20 eV and were energy calibrated using the C-C bond energy at 284.8 eV. The O 1s peak was fitted with three species, LiOH at 531.1 eV,[130] Li_2CO_3 at 532.0 eV,[131] and oxide species at 528.6-529.0 eV.[131] The C 1s peak was fitted with four species, adventitious carbon at 284.8 eV, which was used to calibrate the spectra, C-O at 286.0 eV,[132] O-C=O at 289 eV,[133] and Li_2CO_3 at 290.0 eV.[131]

5.3.4 Contact Angle Measurements

Li foil was melted in a crucible by heating on a hot plate in the glovebox. While melting, a thin film of impurities, likely composed of oxide, nitride, and carbonate species that originate from the native surface layers of the bulk foil, was observed to form on the top of the molten Li. The film was removed from the molten Li source using tweezers and a razor blade. This process was repeated until no surface layer was apparent, and the molten Li was purely liquid phase. Cold-pressed Li_2CO_3 and LLZO with various surface treatments were placed on a hot plate at 300°C inside an argon-filled glovebox to ensure the sample temperature was higher than melting temperature of Li (>180°C). Subsequently, molten Li was injected on the surface with a stainless-steel syringe. The stainless-steel syringe was also heated to T >180°C to avoid solidification of molten Li. The contact angle measurement was performed by determining the tangent angle of the Li liquid drop with the sample surface. In this method, the shape of a droplet resting on a solid surface is dependent on the mechanical equilibrium of the drop under the three interfacial tensions in-

cluding; solid-vapor (γ_{SV}), solid-liquid (γ_{SL}), and liquid-vapor (γ_{LV}). This is described by the Young-Duprees equation.[134] A high-resolution camera (Grasshopper GRAS-50S5M-C) with a Fujinon HF75SA-1 lens was used to capture the image and measure contact angles. The contact angle plugin tool in ImageJ software was used to measure the contact angle.

5.3.5 Electrochemical Measurements

Electrochemical measurements were performed to determine the effect of HT on $R_{Li\text{-}LLZO}$ and the CCD. Metallic Li electrodes were prepared by scraping with a stainless-steel spatula to expose a clean surface. Li-LLZO-Li cells were compressed under a constant 350 kPa uniaxial pressure during cycling. EIS measurements were conducted on symmetric cells after assembly using a 100 mV amplitude in the frequency range of 7 MHz to 1 Hz using a VMP-300 biologic and EC-Lab V11.02 software. To ensure good contact between metallic Li and LLZO, cells were heated to 175 °C for 12 h as has been reported by Sharafi et al. (preconditioning step).[115] After cooling to RT, the change in cell resistance with a focus on $R_{Li\text{-}LLZO}$ was measured by EIS again. First, the entire spectrum was normalized for the contact area between Li and LLZO (area = 1.26 cm^2). Then an equivalent circuit model was used to interpret the data. The EIS data were modeled using the equivalent circuit model shown in Figure 5.5b. In this model, a combination of a resistor and a capacitor in parallel was used to represent each transport phenomenon in the cell. Thus, three parallel combinations were used in the model representing the bulk (Rbulk), the grain boundary (R_{gb}), and the Li-LLZO interface ($R_{Li\text{-}LLZO}$). Ideal capacitors were replaced with contant-phase element (CPE)s to account for any nonideal behavior and dispersion in the time constant. The ideality of the CPE is represented by the coefficient α (α= 1 shows the component is behaving as an ideal capacitor).[135] The Q values for the CPE should be on the order of 10^{-12}, 10^{-8}, 10^{-6} F for bulk, grain boundary, and Li-LLZO interface, respectively.[26,135] Cycling behavior of Li-LLZO-Li symmetric cells was measured at RT between 0.01 and 1 mA cm^{-2} to determine the CCD (the current density at which the cell voltage dropped to

0 V). Cycling was continued until evidence of short-circuiting was observed and marked by a sudden drop in polarization voltage. To examine the cycling behavior of LLZO, Li-LLZO-Li cells were galvanostatically cycled at ±0.2 mA cm^{-2}. During cell cycling, the cell impedance was measured every 20 cycles to evaluate the impact of electrochemical cycling on cell impedance and its stability. In this study, all tests have been repeated three times to ensure reproducibility.

CHAPTER 6

Operando Visualization in Solid Electrolytes

In Chapter 5, a method to achieve a relatively pristine LLZO surface was demonstrated in order to achieve ultra-low interfacial impedance. It was shown that by reducing the interfcial impedance, the rate-capability of the material can be dramatically increased. This was attributed to the improved wettability of the Li/LLZO interface. However, even with this advance, and the many advances made by researchers to improve the performance of a wide variety of SSE materials, rate capability remains a major challenge in many of them.[57,58]

In many material systems, Li filaments tend to nucleate and grow towards the positive electrode at high current densities, eventually causing short-circuit.[58] The current density at which this occurs varies among different material systems. For example, in state-of-the-art ceramic electrolytes such as garnet $Li_7La_3Zr_2O_{12}$ (LLZO), the CCD at which Li penetration occurs has been increased to above 1 mA cm^{-2} through careful control of material processing.[16,128,136–138] However, increasing the CCD to higher current densities has been hindered by the lack of mechanistic insight into the origins of Li penetration/propagation. Understanding and overcoming this challenge is vital to the implementation of LMSSBs in applications where fast charging times are required, including EVs.

Several recent studies have attempted to elucidate the underlying mechanisms for the nucleation and growth of Li filaments/dendrites within SSEs, but a range of questions remain.[58,128,136,139–142] There is significant variation in the terminology used to describe these

structures in literature, but we will use the general terms Li filament and Li penetration. Among the key remaining questions are when, why, and where Li penetration occurs, and what determines the path of propagation? Towards answering these questions, it has become increasingly evident that understanding how coupled electro-chemo-mechanical phenomena dynamically evolve during cycling is of critical importance.[143]

Early work studied Li filament propagation in polycrystalline LLZO.[128] It was found that Li propagated along grain boundaries. However, whether or not filaments entered at grain boundaries could not be determined. Regardless, it is possible that grain boundaries could serve as preferential sites for nucleation and pathways for propagation.[128] More recent computational work suggested that the localized mechanical properties at grain boundaries could be a rationale for this.[144]

Porz et al. proposed a mechanical model that links the overpotential to stress within a Li-filled crack, and predicted a critical flaw size that would grow at a given applied overpotential.[58] Several SSE systems were studied, including single-crystal LLZO and glassy Li_2S-P_2S_5 (LPS). The observation of Li penetration in SSEs without grain boundaries demonstrates that Li filaments can also propagate along other paths. A follow-on study attempted to induce Li penetration at intentionally introduced surface flaws, but found that nucleation preferentially occurred near the electrode edge instead due to current-focusing.[139] *Operando* electron microscopy has also been used to study the nucleation of Li penetration at a current collector/LLZO interface.[145] Changes in the morphology of plated Li at the surface of the SSE were linked with electrochemical measurements. This provided insights into the role of heterogeneity at the Li/SSE interface on short-circuit behavior.

A different underlying mechanism for nucleation of Li filaments has also been proposed, which stems from the inherent electronic conductivity of the SSE.[140,146] This mechanism was used to rationalize uniform, isolated accumulation of Li within the bulk of the SSE, which was indicated by *operando* neutron depth-profiling and ex-situ electron microscopy.[140]

In addition, little is known about the dynamic evolution of Li metal electrodes in LMSSBs during cycling and deep discharge conditions. Several recent studies examined the role of diffusion within the Li metal electrode on nucleation of Li filaments and on void formation at the Li/LLZO interface.[136,141] These studies probed the diffusion of Li away from the cathodic interface and Li vacancies away from the anodic interface. Wang et al. hypothesized that if the diffusion of Li away from the interface cannot keep up with the rate of plating, there could be a build-up of Li at hot-spots that then act as a nucleation site for a Li filament.[136] Krauskopf et al. studied the formation of voids in the absence of stack pressure and proposed that vacancies form at the interface during dissolution of Li from the electrode and cannot diffuse away from the interface as fast as they are being created.[141] Wang et al. demonstrated that CCD in Li/LLZO/Li cells is dependent on stack pressure, which is attributed to the rate of mechanical deformation to replenish Li at the stripping electrode.[147] Interfacial voids lead to a decrease in interfacial contact area, which corresponds with an increase in interfacial impedance and lower CCD.

It has also been shown that the interface/interphase between Li and the SSE plays an important role in determining the current density at which Li penetration is observed.[148] In LLZO, reduction of interfacial impedance through rigorous surface cleaning and/or interfacial layers, has enabled current densities up to 1-2 mA cm^{-2} for planar cells at RT.[136,137,149,150] Li^7 nuclear magnetic resonance chemical shift imaging was used to show that morphology evolution at both the plating and stripping interfaces is linked with the Li penetration.[151] Interphase formation between Li metal and $Li_{1.4}Al_{0.4}Ge_{1.6}(PO_4)_3$ has also been shown to play a role in mechanical fracture of the bulk SSE during cycling.[148]

Given the breadth of proposed mechanisms that drive Li nucleation and propagation in SSEs, there is a need for additional *operando* investigations to elucidate the nature and dynamic evolution of Li penetration during cycling under realistic conditions.[58,140,152,153] Specifically, techniques that simultaneously enable high spatial and temporal resolution would help to enable further characterization of the location and morphological evolution

of individual filaments in 3-D. Filling the knowledge gaps mentioned above would provide researchers and engineers with the tools and knowledge needed to design high performance LMSSBs. Towards this goal, this study implements an *operando* visualization technique that enables optical observations within the bulk of LLZO during cycling at relevant current densities (>1 mA cm^{-2}) with low interfacial resistances (<5 Ω cm^2). The time-synchronization of voltage response (voltage trace) with video microscopy enables significant new insights into the mechanisms that lead to the coupled electro-chemo-mechanical response of the system.[15,154]

Al-doped LLZO was used as a model system for this work, as the inherent chemical stability against Li metal simplifies the analysis, and translucent/transparent electrolyte films can be fabricated based on recent advances in material processing.[155] In addition, the mechanical and transport properties have been well-documented,[112,113,156,157] allowing for a detailed analysis.

Using both TP and in-plane cell geometries, Li penetration is imaged during propagation and time-synchronized with the corresponding electrochemical signatures. In addition, reversible plating and stripping of the Li within these structures and the formation of dead Li during cycling, are directly observed. Four distinct morphologies of Li filaments are identified and described using a combination of *operando* optical and post-mortem electron microscopy, illustrating the fact that a singular mechanism/mode of failure is insufficient to capture the full complexity of Li penetration in SSEs. The velocity of Li filament propagation is quantified as a function of applied current density, providing insight into the coupling between mechanical and electrochemical behavior. Additionally, deep discharge behavior is observed, and the dynamic evolution of the Li/SSE interfacial area is quantified and correlated with changes in interface resistance. Finally, the in-plane platform is applied to a glassy Li_3PS_4 SSE, demonstrating the power of the in-plane architecture and the implications of the results for SSEs more broadly.

6.1 Results and Discussion

6.1.1 Through-plane *Operando* Visualization

First, the TP cell shown in Video 6.1, Figure 6.4 was fabricated by cutting an LLZO pellet and polishing the cut surface to view the cross-section during cycling (further details in Section 6.3). Initially, when currents <0.1 mA cm^{-2} were applied, no changes to the electrode or electrolyte morphology were observed. The stable voltage response to successively increasing current densities below the CCD is shown in Figure 6.3. As shown in Video 6.1 and Figure 6.4, when a current density of 0.5 mA cm^{-2} is applied, Li filaments immediately nucleate and a gradual drop in polarization occurs as the filaments propagate across the cell. The Li penetration appears as branching 3-D structures, and are dark silhouettes due to the back lighting. This continues until one filament reaches the counter electrode, corresponding with a simultaneous rapid drop in polarization to near zero when short-circuit occurs (2.5 s in Video 6.1). This is expected when an electronically conductive pathway of metallic Li is formed between the two electrodes.

The gradual decrease in polarization while the filaments propagate towards the counter electrode can be explained as a result of three factors: [1] an increase in active interfacial area of the cathodic electrode as the structures grow, which decreases interfacial impedance; [2] a decrease in distance between the Li filament and the anode, decreasing the impedance associated with ionic conduction in the SSE;[151] and [3] formation of a kinetically faster interface for CT, similar to dendrites in liquid electrolytes.[15] This demonstrates the power of the *operando* video microscopy platform to provide mechanistic insight into the origins of electrochemical signatures, which can be used in real battery applications where optical access to the cell is not available. For example, this characteristic drop in cell voltage could be used to identify the propagation of a Li filament in one cell of a battery pack with on-board diagnostics during charging to avoid a catastrophic short-circuit failure.

Figure 6.1: *Operando video of TP cell cycling. Time-synchronized voltage trace with cross-sectional optical microscopy of Li/LLZO/Li cell during galvanostatic plating of 0.5 mA cm^{-2} under stack pressure. Flash player must be enabled for playback.*

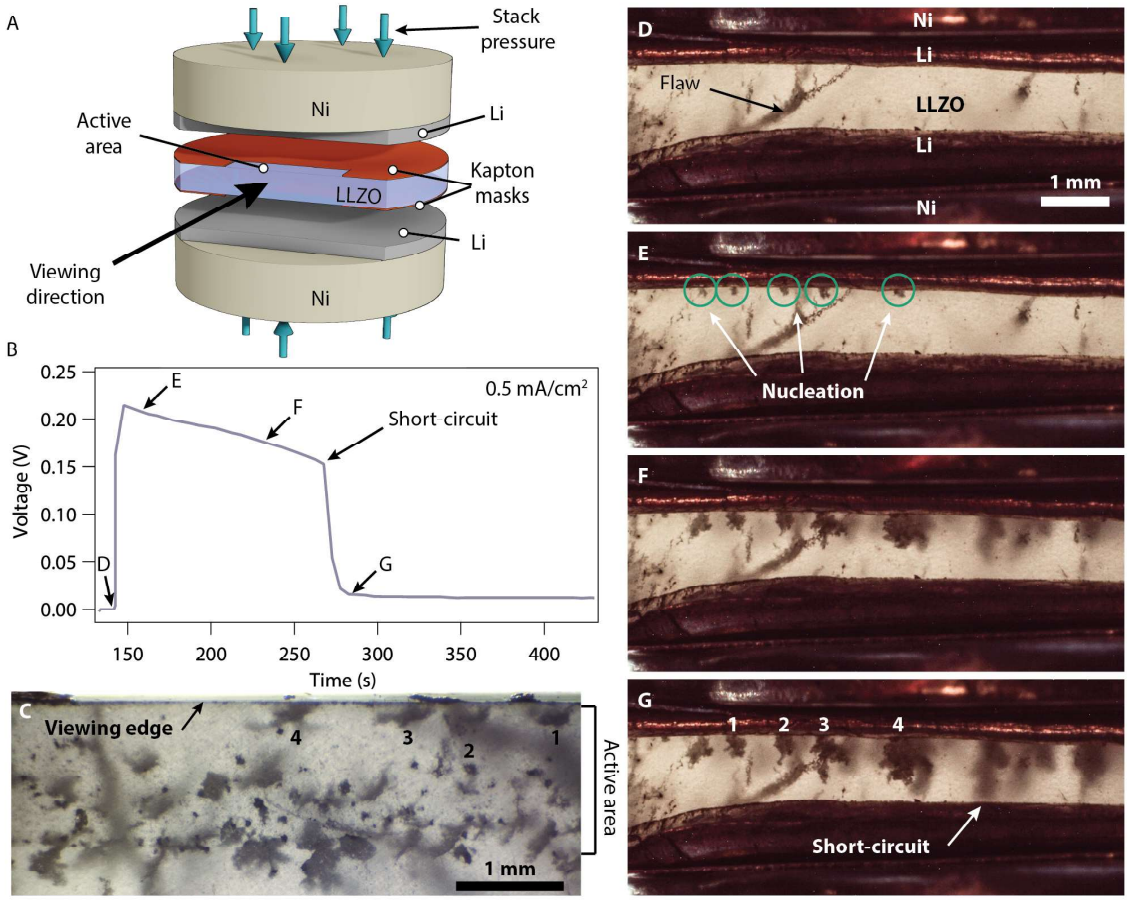

Figure 6.2: *Through-plane cycling in LLZO with operando cross-sectional visualization. Images, schematic, and electrochemical data from operando TP Li/LLZO/Li cell (a) schematic showing cell geometry, (b) Voltage response of cell during galvanostatic plating at 0.5 mA cm^{-2}, (c) post-mortem image of active area of electrode interface that was plated to, (d-g) Image series from TP visualization cell.*

Although the results from this experiment provide valuable insights and clearly show the propagation of Li filaments and the synchronized voltage trace, this platform is not ideal to enable high-resolution imaging and post-mortem analysis. First, this setup requires a very transparent SSE material, and while this is possible to achieve in LLZO, it requires high sintering temperatures (>1300 °C) and long sintering times to achieve large-grained, high density pellets.[155] This makes throughput very low, and it is difficult to make comparisons to SSEs with conventional processing. In addition, the geometry of the cell means that the electrode edges are preferred nucleation sites, as can be seen in the post-mortem images in Figure 6.2c and Figure 6.3. A majority of the filaments nucleated either at the

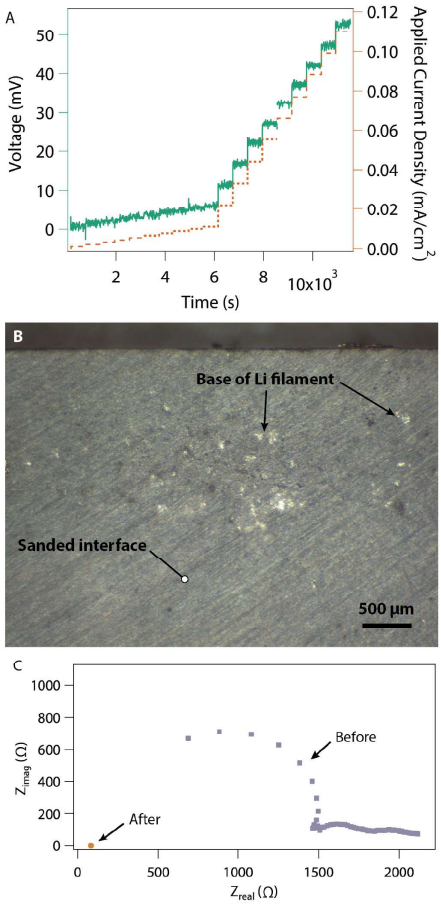

Figure 6.3: *(a) Applied current density and measured cell polarization as current is increased in the TP cell. (b) Optical image of active area of cell after the Li electrode was removed and the interface was gently sanded to reveal the base of the Li filaments. (c) EIS before cycling and after short-circuit.*

viewing edge (labels 1-4) or at the opposite edge of the active area.

6.1.2 The In-Plane Visualization Platform

To overcome challenges with the TP platform, an in-plane electrode architecture was developed that enables: [1] high-quality interfaces with low interfacial impedance; [2] improved optical imaging; [3] higher throughput; [4] use of representative SSE materials; and [5] quantitative *operando* and post-mortem analysis without the need to remove electrodes. A schematic of this cell geometry is shown in Figure 6.4a. By depositing both electrodes on the same surface of a polished LLZO pellet, Li filaments that grow can be clearly observed

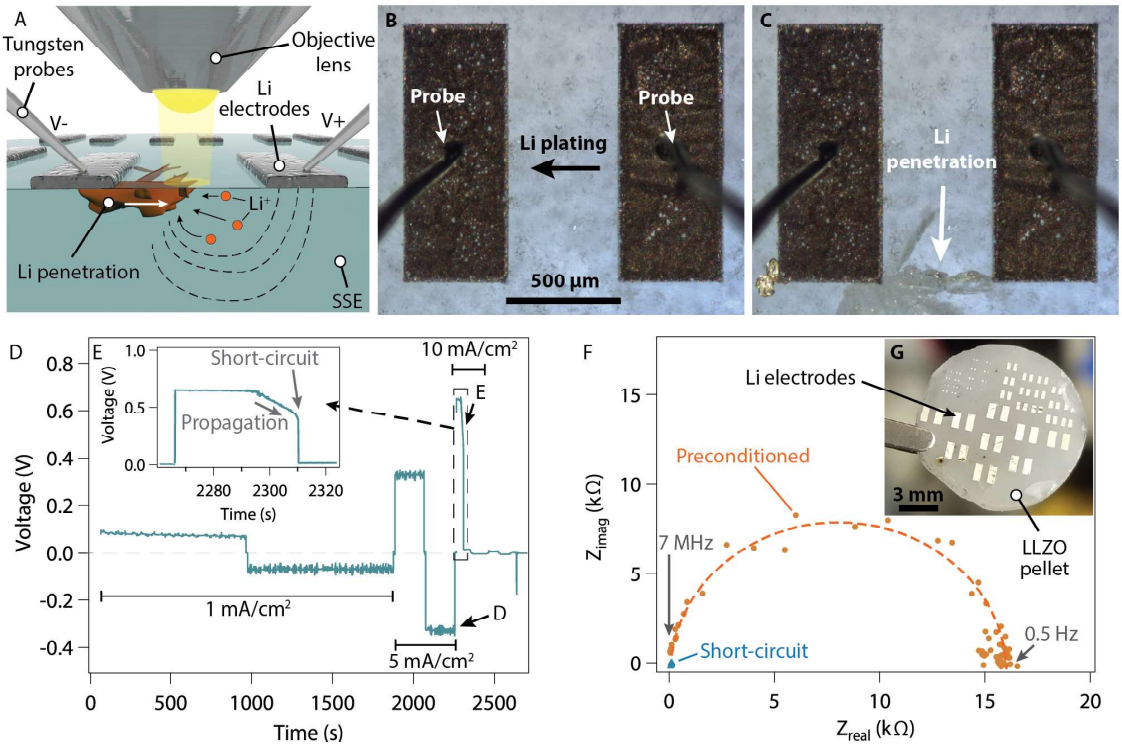

Figure 6.4: *Demonstration of in-plane visualization platform. (a) Schematic representation of in-plane cell geometry and experimental setup, (b,c) Images of in-plane Li/LLZO/Li cell before and after Li penetration and short-circuit, (d) voltage response of cell during stepped current, with zoom-in shown in (e), (f) Nyquist plots of in-plane cell before and after cycling until short-circuit, and (g) image showing pellet with multiple in-plane cells deposited on the surface.*

as they propagate between the two electrodes.

This architecture allows for many cells to be fabricated on the same SSE pellet. For example, Figure 6.4g shows 39 pairs of electrodes of 3 different sizes all fabricated in parallel by thermal evaporation of Li through a shadow mask (further details in Section 6.3). This enables direct comparison of cells under different operating conditions (current density, depth of discharge, etc.) with an identical SSE. Furthermore, after any individual cell has short-circuited via Li penetration, the SSE can continue to be tested in adjacent cells.

Figure 6.5: *Measurement of CCD with in-plane cell architecture. Operando video microscopy of CCD test on in-plane Li/LLZO/Li cell with time-synchronized voltage response during the current steps. For each current step, 0.25 mAh cm^{-2} of Li was plated in each direction.*

6.1.3 Experimental Validation of the In-Plane Visualization Platform

To validate the in-plane geometry experimentally, CCD tests were performed that mirror those typically used to demonstrate rate capability of SSEs.[16,149,150,158] Any representative platform for *operando* characterization should be capable of cycling Li at sufficiently high current densities (>0.5 mA cm^{-2}) and cell polarization (<1 V) without Li penetration. To achieve this, a clean Li/LLZO surface was formed by a combination of WP and HT, which has been previously shown to eliminate interfacial impedance and improve wettability of molten Li.[16] Li metal electrodes were deposited by thermal evaporation and heated to 250 °C without stack pressure for 5 min, then cooled to room-temperature. This process melted the Li and improved Li-LLZO contact. The Nyquist plot from EIS analysis after this HT in Figure 6.4f shows a single semi-circular feature associated with ionic conduction in the bulk, indicative of interfacial impedance below what could be detected by EIS in this case (<5 Ω cm^2). An example of EIS on a pair of as-deposited electrodes is shown in Figure 6.6 for comparison, and exhibits a second semicircle from the interfacial impedance at low frequencies.[115]

To compare the behavior of the in-plane cell to typical bulk SSE cells, a constant charge of 0.25 mAh cm^{-2} was plated in each direction, and then current was successively increased until short-circuit was observed. Under these or similar conditions, the highest reported CCDs at RT for planar LLZO samples without an interlayer coating is ~1 mA cm^{-2} with an applied stack pressure.[136,150] A Li/Mg alloy electrode[137] and an MoS_2 interlayer[149] have been demonstrated to approximately 2 mA cm^{-2}. In this in-plane cell, even without any stack pressure, flat voltage plateaus and no Li filaments were observed at 1 and 5 mA cm^{-2} (Figure 6.4b,d, Video 6.5). At 10 mA cm^{-2}, a small feature grows from the bottom left corner of the left-hand electrode, but no significant change is observed in the voltage profile, and the structure stops growing fairly quickly. This will be called a spalling type morphology, and will be described in more detail below. After 30 s of plating, a branching structure grows out from the bottom right corner of the electrode towards the other side.

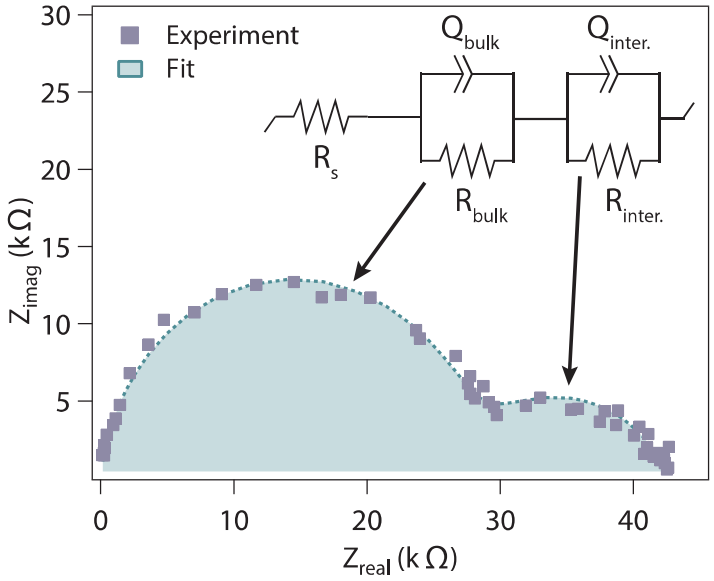

Figure 6.6: *Nyquist plot of in-plane cell with as-deposited Li metal electrodes (prior to annealing) with inset of the equivalent circuit model used to fit the EIS data collected throughout the manuscript.*

As this Li filament grows, the cell polarization drops steadily (Figure 6.4e), similar to the drop observed as the filaments propagated in the TP cell above. Approximately 15 s later (Video 6.5, 32 s), a sudden drop in cell impedance is observed when the filament reaches the opposite electrode and provides an electronic pathway.

Overall, the in-plane cell closely mirrors what is seen in typical TP LLZO cells,[128,159] but occurs at significantly higher current density (~5-10x higher). The rate capability was consistently high in cells with annealed Li, as shown in Figure 6.7, where the highest safe current density (where Li penetration was not observed) is plotted with the corresponding cell polarization for each of the equivalent cells tested. This high rate capability is likely a result of two factors: 1) smaller electrode area, meaning there is a smaller chance of a large/critical flaw within the electrode;[160] and 2) the Li metal was melted, whereas in many studies the Li is heated to just below the melting temperature.[16,115,128,136,147,159] This demonstrates that under some conditions, a Li-LLZO interface can be stabilized at high current densities without the need for stack pressure.

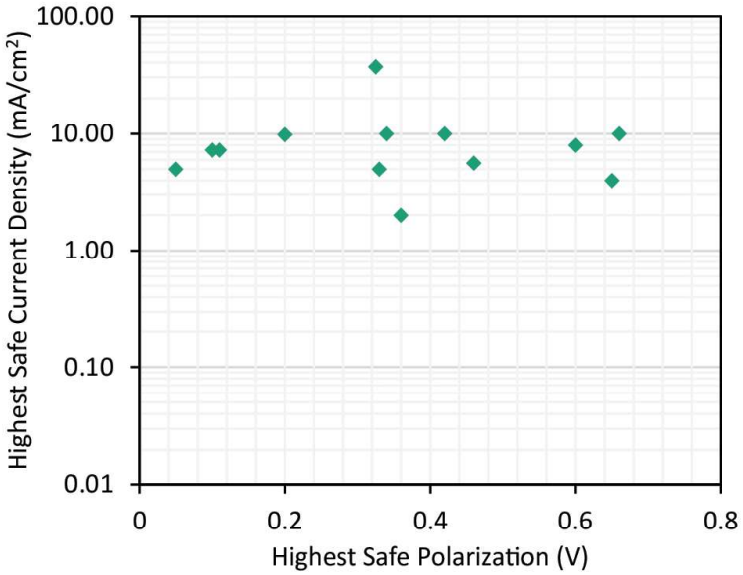

Figure 6.7: *Highest safe current density and cell polarization for each of the in-plane cells with annealed Li electrodes.*

6.1.4 Li Penetration Morphologies

Several different types/morphologies of Li filaments were observed when cycling above the CCD. Here, we classify them into four groups, each of which is shown in Figure 6.8. The first three, which we will refer to as straight, spalling, and branching, were commonly observed during these experiments, and appear similar in nature. The fourth, which we call diffuse, was less common, and was not observed in any of the optimized cells which had Li electrodes with low interfacial impedance (and high CCD). This type appears fundamentally different from the other three, as described below.

The straight type is shown in Figure 6.8a-c and is typified by a single approximately linear path of propagation. The overall geometry is a subsurface plane intersecting the electrolyte surface as a linear crack. In the optical image shown in Figure 6.8a, the projection of the subsurface plane onto the top surface of the electrolyte appears as a dark region, with the linear surface crack visible as the left boundary. This type of feature is often observed in post-mortem observations of typical LLZO cells after removing the Li electrodes.[128,149] A FIB section of this feature shown in Figure 6.8b reveals a cross-sectional view of the planar

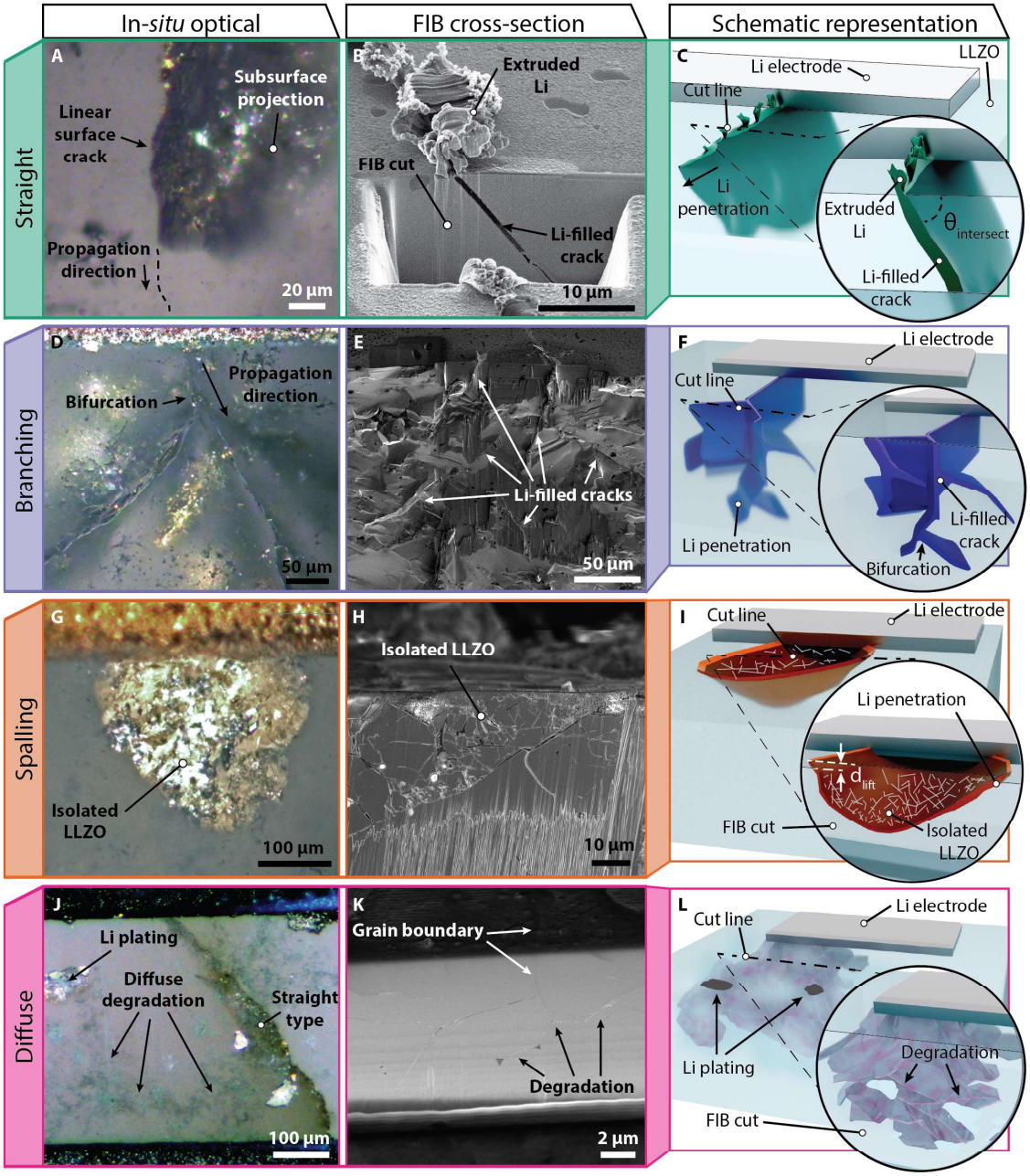

Figure 6.8: *Different types or morphologies of Li penetration. Optical images, SEM images, and schematics of straight Li penetration type (a-c), branching type (d-f), spalling type (g-i), diffuse type (j-l). Contrast and brightness adjustments were made to the entire image in (a,j) to make features more evident in in-situ optical images.*

crack extending from the surface down into the electrolyte. The angle at which these cracks intersect the surface ($\theta_{intersect}$) varies between individual cracks. These planar features are filled with metallic Li. This is evident from: [1] the metallic luster of the buried surfaces; [2] the extrusion of Li out of the crack at the surface (Figure 6.8b,c), which is a result of the viscoplasticity of metallic Li;[100,161] and [3] the ability to strip Li from within the crack during subsequent cycling, as shown below. Straight Li filaments are often responsible for short-circuit due to rapid propagation directly towards the opposite electrode.

The second type of structure is branching (Figure 6.8d-f). It is typified by the dendritic, branching appearance that it is named for. In this type, there is a tendency for the crack to bifurcate as it grows. This leads to a 3-D branching structure. Post-mortem characterization of a branching structure is shown in Figure 6.9. The SSE was manually fractured through the structure (Figure 6.9b) and partially polished by FIB to reveal the subsurface features. Figure 6.9a,c clearly show the branched planar structure in SEM and optical images, respectively. Each of the branches of these structures are Li-filled planes, as evidenced by the metallic luster in Figure 6.9c and dramatically lower brightness in back-scattered electron (BSE) imaging (Figure 6.9e). Isolated impurity grains are also visible in these images. XRD analysis indicated that the LLZO pellet was very high purity (98.8% cubic garnet, 1.1% lithium zirconium oxide, and 0.1% lanthanum zirconium oxide). However, the small amount of impurities can be differentiated from the metallic Li in the BSE images, as the Li appears much darker due to z-contrast. These impurities were not a result of cycling, as they were observed in cells that had not been tested.

The exact cause of the branching/bifurcation is unknown, however in several cases during post-mortem FIB analysis, impurity grains were observed at the same locations where the crack bifurcated or deviated. A series of SEM images as the FIB removed thin slices of material was used to create a 3-D reconstruction of one such location (Figure 6.10). This appears similar to crack deflection in ceramic matrix composites.[162–164] The ~1% of impurities may play a significant role in determining the path of Li filament propagation.

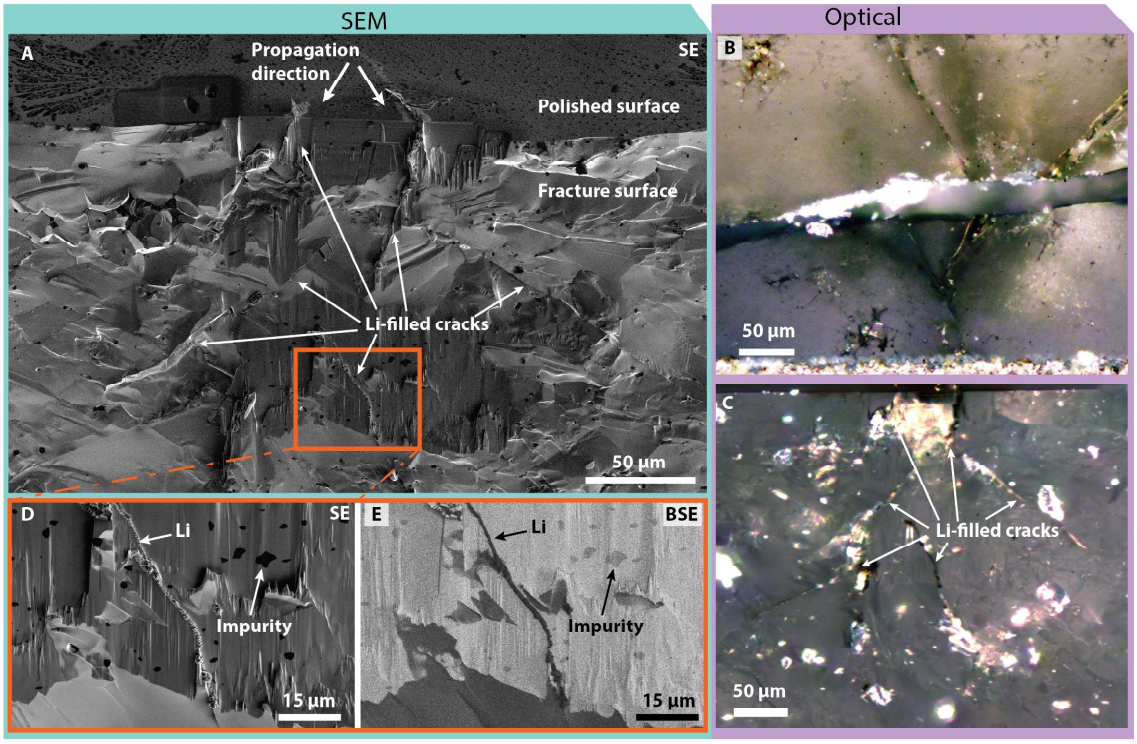

Figure 6.9: *Cross-sectional analysis of branching-type Li filament. Post-mortem characterization of Li penetration morphology with scanning electron and optical microscopy. Secondary (a,d) and backscattered (e) electron images of LLZO cross-section through branching-type Li filament at location shown in the optical images shown in (b). Optical image of same area of cross-section shown in (c).*

In the 18 in-plane cells examined, the branching type always occurred at high current densities, and never occurred at low current densities. As shown in Figure 6.11, cells in which nucleation occurred below 0.2 mA cm^{-2} never had the branching type, while in cells where nucleation occurred at above 0.3 mA cm^{-2}, the branching type was always one of the observed morphologies. This suggests that the bifurcation of cracks is linked to the higher driving force provided by the higher current density.

The third type, spalling, is named for the similarity in appearance to a piece of glass spalling off from a larger sheet (Figure 6.8g-i). In this case, a Li-filled crack similar to the straight type follows a curved path instead of a straight one. If a complete circle or closed loop is made by the crack at the surface, the LLZO in the center becomes isolated from the bulk of the pellet and can be lifted up (d_{lift}, Figure 6.8i, Figure 6.12e). As the addition of

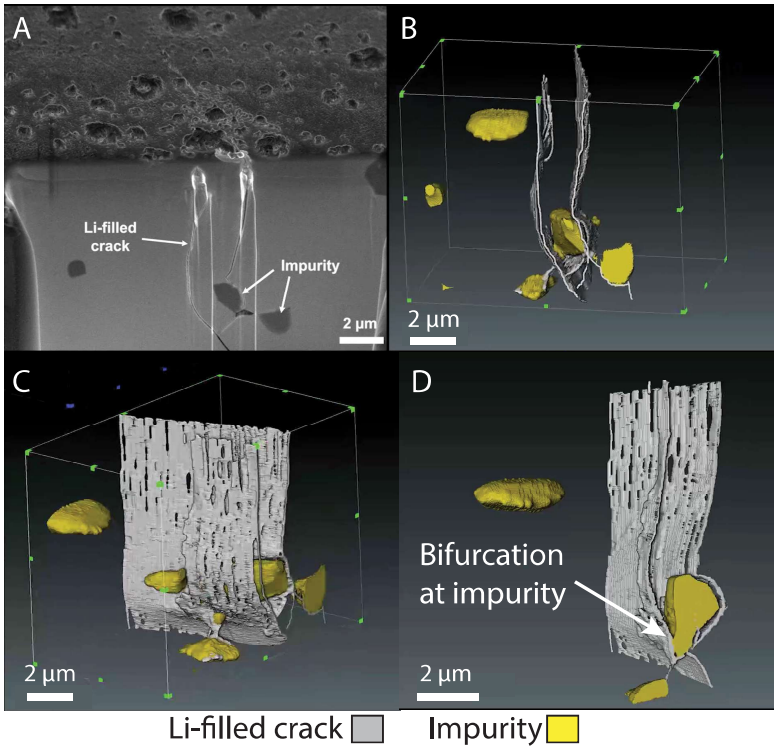

Figure 6.10: *3-D reconstruction of crack bifurcation in LLZO at an impurity. FIB-SEM images of cross-section slices through branching type Li penetration (left) with resulting 3-D reconstruction (right) showing Li penetration in gray and impurities in yellow.*

Li through electroplating inside the crack can be accommodated by the isolated region of the LLZO lifting up, there is no longer sufficient stress to propagate a crack further into the LLZO. At this point, the feature typically stops growing macroscopically, although Li is still being plated into the crack, so it is still active.

Unlike the straight and branching types, the spalling type does not correlate with a decrease in polarization, and never led to short-circuit in the experiments run during the preparation of this manuscript. For these reasons, it was classified separately. The spalling-type feature shown in Figure 6.12a-d,f has many cracks within the isolated section of LLZO that have pulverized that portion of the LLZO. These cracks grew during the plating rather than during the cross-sectioning of the sample, as they are filled with Li (Figure 6.12a,b). Not all spalling-type filaments exhibit this pulverization, however, some are a single crack like that in Figure 6.12e. The red coloration of the spalling feature after FIB sectioning in

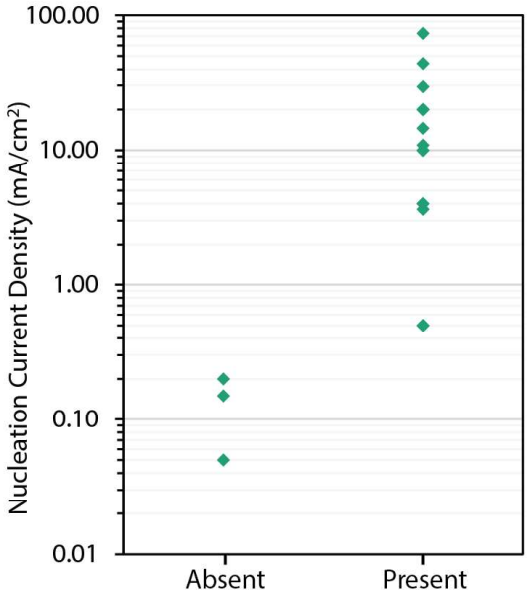

Figure 6.11: *Presence/absence plot for branching-type Li filaments, and the current density at which nucleation occurred for each of the in-plane cells tested.*

Figure 6.12f is attributed to the reaction of metallic Li within the network of cracks with nitrogen to form lithium nitride, which has a characteristic reddish color.

The final type of morphology, diffuse, was observed only twice during the preparation of this manuscript, and was never observed in the optimized cells which had low interfacial impedance and high CCD. The *operando* video of a cell that exhibited diffuse degradation is shown in Video 6.13 along with the synchronized voltage trace. During the first three current densities shown (0.7, 0.8, 0.9 mA cm^{-2}), there is no visible formation of Li filaments. During the 1 mA cm^{-2} cycle, a subtle diffuse darkening within the SSE is observed. The strong backlighting helps to make the features more visible. As it propagates, a dark spot forms in between the two electrodes. Upon post-mortem optical inspection at higher magnification and with lighting from the top (Video 6.13, Figure 6.8j), it is apparent that the diffuse darkening is due to the formation of a network of very thin structures, and the dark spot is Li metal that has plated out. The variety of lighting options enabled by the in-plane architecture make it possible to see the subtle changes (Figure 6.14)

As the diffuse darkening propagates and reaches the other side, there is almost no

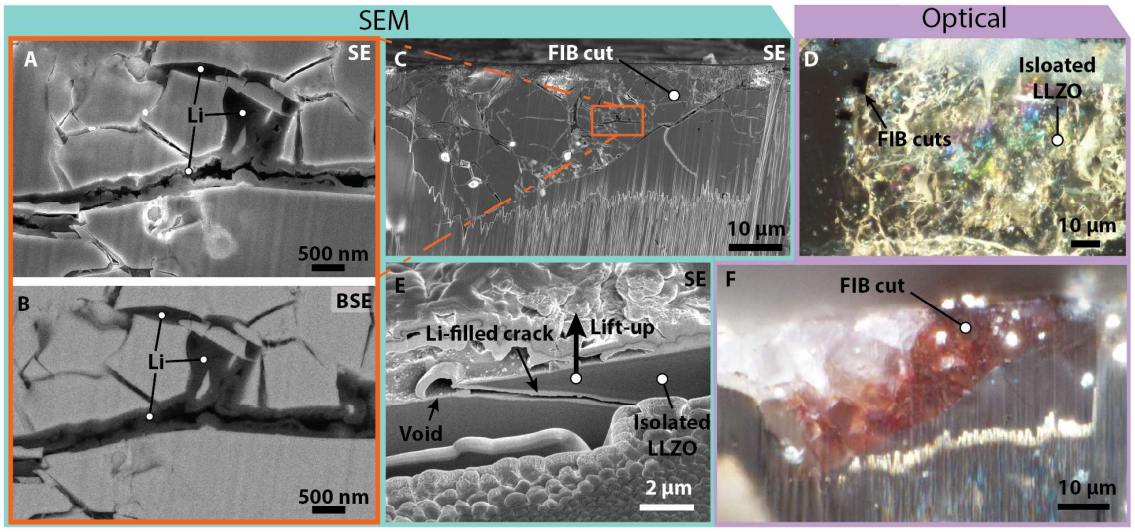

Figure 6.12: *Cross-sectional analysis of spalling-type Li filament. Secondary (a,c,e) and backscattered (b) electron images of FIB cross-sections through spalling-type Li filaments. Top-down (d) and cross-sectional (f) optical images of the same feature shown in (c).*

change in the cell polarization. A brief and very small drop is observed when the structure stops growing. This suggests that either the electronic conductivity of this feature is low, or that the fuse effect occurred almost instantaneously. This phenomena occurs when the electronically conductive pathway between electrodes is melted (like a fuse), and the pathway is broken.[97] When the polarity is reversed at 1.5 mA cm^{-2}, the structure does not noticeably shrink, but several more spots of Li plating in the middle are observed. Finally, during the last current pulse, a straight type Li filament grows across the cell and causes short-circuit.

Figure 6.8k shows an FIB cross-section of a similar diffuse darkening structure. The presence of degradation along grain boundaries (visible both on the pellet surface and in the subsurface degradation) is dramatically different from the structures in the previous three types, and suggests that the propagation mechanism may be different. As this type was rare in cells with optimized interfaces, the remainder of the analysis will focus on the first three types. This demonstrates that multiple types of Li penetration can be observed in a given cell, further emphasizing that a single mechanism or explanation is insufficient to capture the full complexity of the observed phenomena. The multiple failure types are reminiscent

Figure 6.13: *Video of diffuse type Li penetration. Operando video microscopy of CCD test on in-plane Li/LLZO/Li cell with time-synchronized voltage response during the current steps. The Li electrodes in this cell were not annealed prior to testing. Back-lighting was used, making Li penetration features appear as silhouettes. Contrast and brightness adjustments were made to the entire images to make features more evident in the video.*

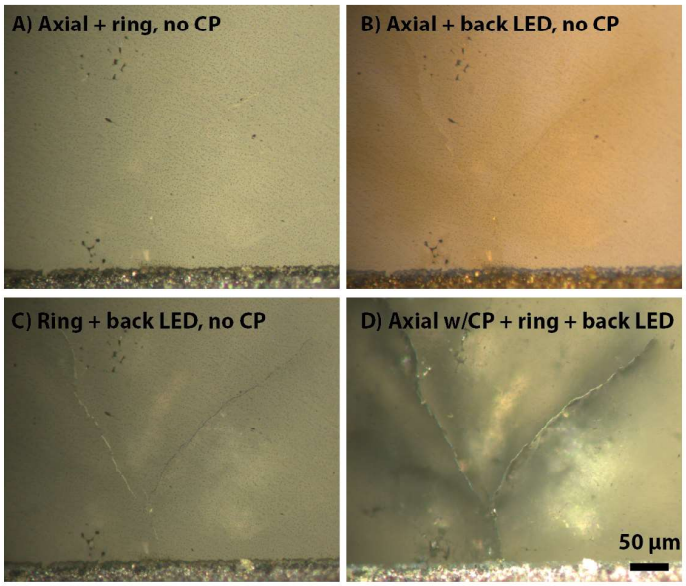

Figure 6.14: *Optical images of the same branching type Li filament with different lighting, as labelled in the panels. CP stand for cross-polarization.*

of the multiple failure modes observed in Na β-Al_2O_3 SSEs.[165] Moving forward, it is important for the research community to note that the details of the SSE, interface, and test performed may impact the observed Li penetration dramatically.

6.1.5 Reversibility and Cycling

In addition to studying the conditions that lead to initial Li penetration and the morphology evolution of the interface under those conditions, the in-plane *operando* experimental platform is ideal for studying the dynamic evolution of filament morphology during cycling. To study this behavior, a cell with smaller electrodes ~250 µm wide and ~500 µm tall and a larger spacing between electrodes was used. The increased distance allows more time to observe Li filament propagation before short circuit occurs. To initially nucleate Li penetration, a two second pulse of high current at a nominal current density of 75 mA cm^{-2} was applied. As shown in Figure 6.15a and the corresponding video in the publication,[17] several branching-type structures almost immediately nucleate at the left-hand electrode. As described above, the polarization gradually decreases as the branching structures grow.

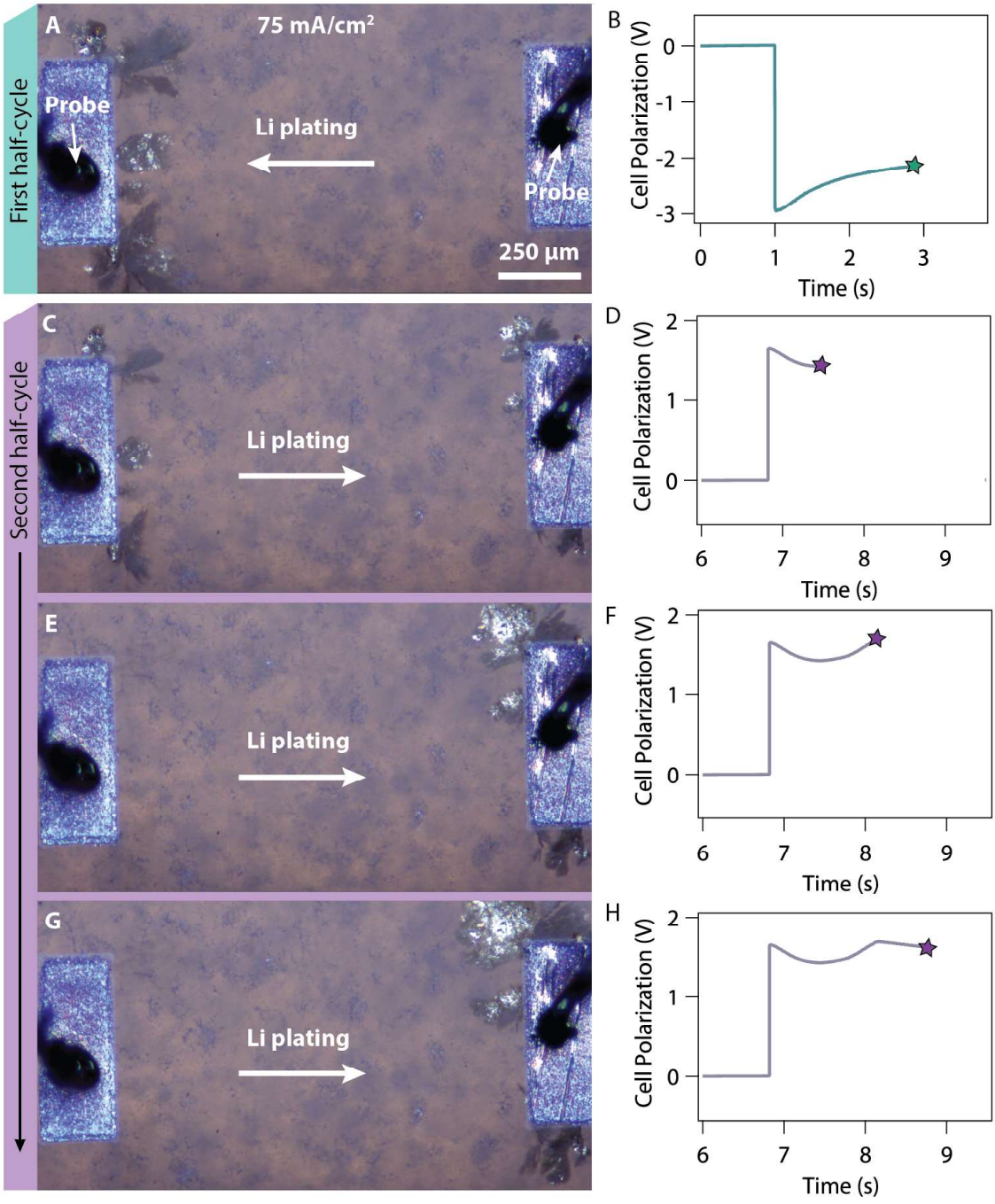

Figure 6.15: *Reversibility and cyclability of Li filaments First cycle. (a) Optical image of in-plane Li/LLZO/Li cell at end of first half-cycle at 75 mA cm^{-2}, (b) corresponding voltage trace, (c) image during second half-cycle before Li is exhausted from filament structures on the left, (d) corresponding voltage trace, (e) image at point in second half-cycle when filament structures are exhausted of Li (disappear from view), (f) corresponding voltage trace, (g) image from end of second half cycle, (h) corresponding voltage trace.*

When polarity is reversed at the same current for 2 s, the branching structures recede as Li is preferentially stripped from the surface of the Li filaments that grew during the first pulse. While this is happening, similar branching structures nucleate and grow on the opposite side (Figure 6.15c). Interestingly, nearly all of the Li can be removed from the structures leaving almost no visual evidence that the filaments had ever existed (Figure 6.15e,g). To the authors knowledge, this is the first time reversibility of Li penetration prior to short-circuit has been directly observed within an inorganic SSE. This behavior is very different from what was observed in a PEO-based polymer electrolyte, which exhibited little to no reversibility.[166]

Examination of the voltage trace in Figure 6.15h during this pulse reveals several distinct features. The cell polarization initially drops, then reaches a minimum, then increases to a maximum value before again decreasing. Time-synchronized *operando* microscopy has been previously used to study Li metal electrodes in liquid electrolytes to understand the coupled electrochemical signatures and morphology.[15] In that work, a strikingly similar peaking profile in the voltage trace was observed. This voltage profile in liquid electrolytes is attributed to spatially varying kinetics along the electrode/electrolyte interface, and 3-electrode measurements allowed for the contributions from each electrode to be decoupled.

The preferential plating into and stripping from the dendritic structures suggests that there is a difference between the two interfaces. This behavior was also observed in liquid electrolytes, where it was attributed to a thinner SEI on the freshly plated Li inside the dendritic structures. A similar mechanism is likely occurring in the LLZO. Despite all efforts to create a clean and pristine LLZO interface prior to Li evaporation, it is known that some contamination remains.[16] In contrast, when a dendritic structure forms, the newly formed Li/LLZO interface is truly pristine. For this reason, Li plating into the dendritic structures is the preferred reaction pathway.

As mentioned above, the initial decrease in polarization during the first pulse (Figure 6.15b) is a result of increasing surface area and the decreasing distance between the elec-

trodes. When polarity is reversed, new Li filaments nucleate and grow on the right-hand electrode. This leads to the initial drop in voltage during the second pulse. The minimum/valley corresponds to the time during which Li is being stripped primarily from the branching structures on the left, and plated into the branching structures on the right (Figure 6.15C,D). During this period, both plating and stripping are occurring on kinetically fast surfaces, and thus the overpotentials are low.

As the Li inside the branching structures on the left starts to be exhausted, the polarization begins to rise. The peak occurs at the same moment when the Li is exhausted from the Li filaments on the left (Figure 6.15e,f; also shown in video included in manuscript). Stripping is forced to proceed from the less-preferred (kinetically slower) interface that was formed by evaporation. After the peak, the polarization slowly decreases again due to the continued propagation of the Li filaments on the right (Figure 6.15g,h).

Following this initial cycle at high current density, the same amount of charge was repeatedly cycled at nominal current densities of 5 mA cm^{-2} (5 cycles) and then 10 mA cm^{-2} (5 cycles), as shown in Figure 6.16. During the first half-cycle at 5 mA cm^{-2}, Li is plated back into one of the dendritic structures on the left that formed during the initial high current pulse (Figure 6.16b). This indicates that despite the structure disappearing optically, the crack that remains after stripping acts as a preferential site for Li plating during subsequent cycling. Interestingly, no Li is plated back into the other Li penetration sites. It is unclear why this is the case, however it could be the result of void formation in the Li electrode at the base of the crack during the previous stripping, similar to the void shown in Figure 6.12e. As cycling continues, the structures on both sides propagate slightly further each time they are plated into.

Although the structures appeared fully reversible during the first cycle, one of the branching structures had visible Li remaining after the second cycle (Figure 6.16d). This Li became electrically isolated from the rest of the electrode, and thus it is now inactive or dead. The formation of dead Li is well documented in liquid electrolyte systems, but has

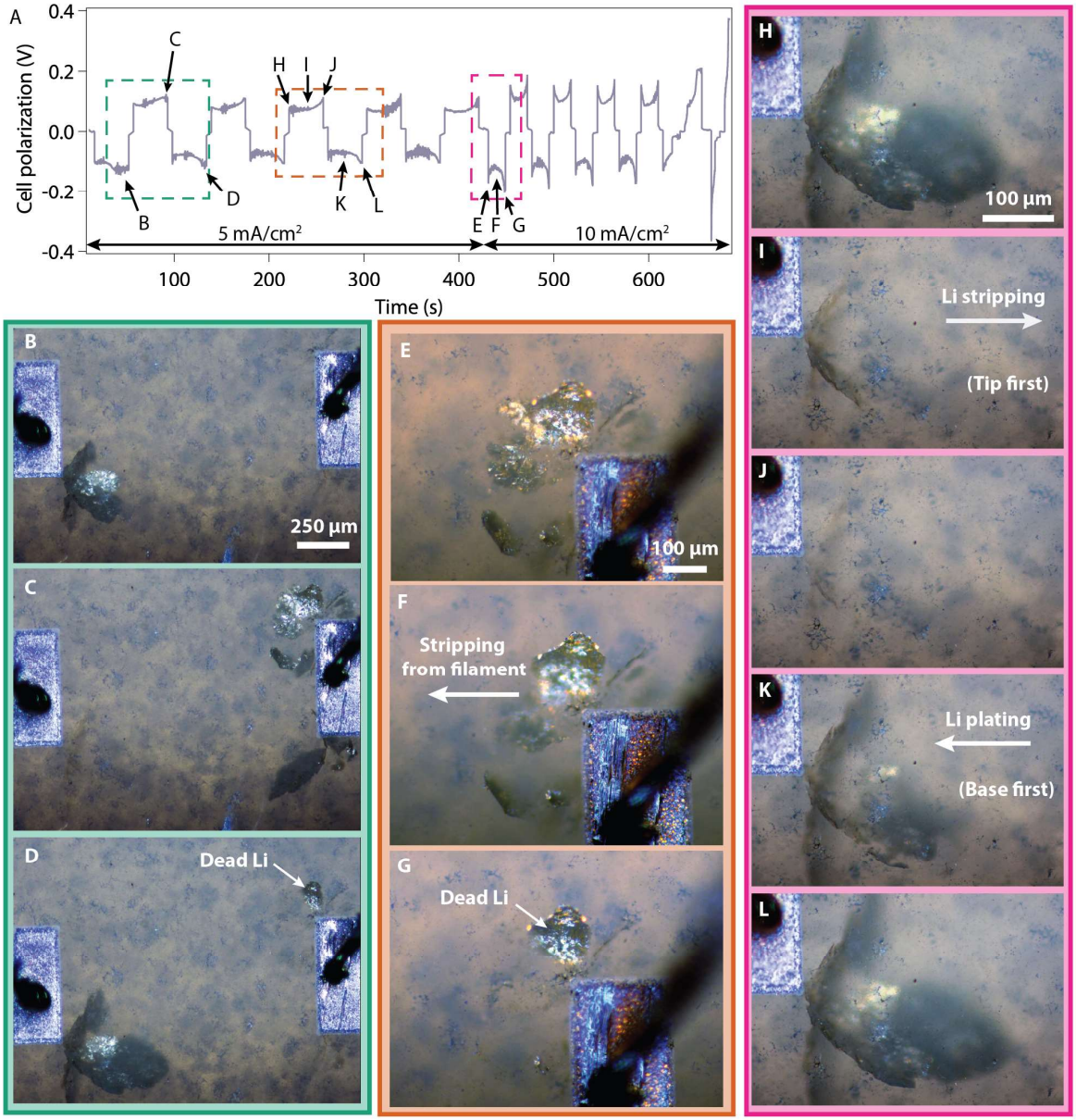

Figure 6.16: *Reversibility and cyclability of Li filaments: Subsequent cycles. (a) Voltage profile of in-plane Li/LLZO/Li cell during galvanostatic cycling at 5 mA cm^{-2} and 10 mA cm^{-2} with points in time labelled corresponding to the operando optical images in (b-l).*

not been reported previously in SSEs. Based on the video of this cell, the formation of dead Li occurs by a similar mechanism to that in liquid cells, with Li stripped out of the base of the Li filament removing the electrical pathway to the rest of the electrode. However, unlike liquid electrolytes, an insulating SEI does not form around the isolated Li region. Therefore, when Li is plated back into the base, the dead Li can be reconnected to the bulk electrode and grow larger. Despite this, the base remains a hot spot for Li stripping and therefore, in each subsequent stripping half-cycle, the dead Li reforms. A higher magnification sequence of images is shown of the same dead Li during a later cycle in Figure 6.16e-g.

Figure 6.16h-l shows higher magnification set of images that captures the stripping from and plating into the branching structure on the left electrode. Li is first removed from the tips of the filament (closest to the counter electrode), and the structure appears to contract back towards the base. When polarity is reversed, Li begins plating back into the structure first from the base and then out towards the tips. This indicates that the features of the structure that remain behind do not serve as an electronically conductive pathway, as in that case plating would begin at the tips. This effect could be significantly different in an SSE that reacted with Li metal and in which the resulting interphase could be electronically conductive ($Li_{10}GeP_2S_{12}$ for example).[167]

Since the structures propagated slightly further each cycle, the structures from the two sides eventually met and short-circuit occurred. In an actual battery, there would only be the potential to form Li filaments from the negative electrode, so failure in this way would not occur, but rather the filament from the Li electrode would reach all the way across to the positive electrode.

6.1.6 Li-Filled Crack Growth Analysis

One of the primary benefits of the in-plane cell architecture is that the high-quality images can be used for quantitative analysis in ways that have not been possible previously. For

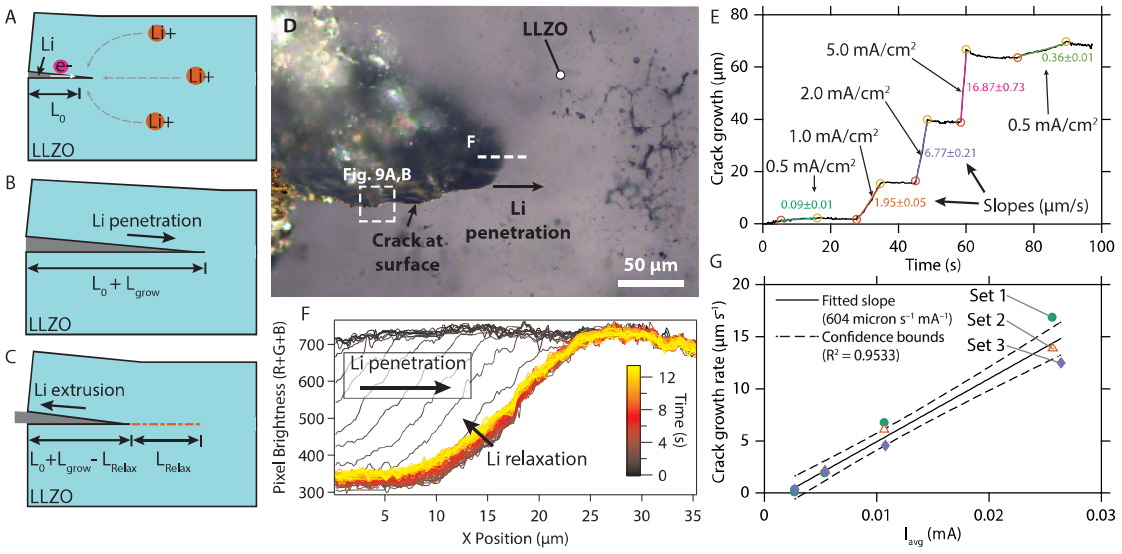

Figure 6.17: *Analysis of Li propagation rate. (a-c) Schematic representation of Li propagation and relaxation inside of a crack, (d) representative operando optical image of a Li-filled crack with areas analyzed in (f) and Figure 6.20 labelled, (e) Plot of crack growth over time during a representative set of current pulses, with a hyperbolic tangent fit of the curve that was used to track crack position, (f) plot of pixel brightness vs. position along a line across the crack tip for frames during and after a current pulse, (g) plot of crack growth rate vs. applied current.*

example, the rate of Li filament propagation was measured as a function of applied current and a linear relationship was observed (Figure 6.17). The extension (L_{grow}) of a single straight-type Li filament was monitored during a sequence of galvanostatic pulses (Figure 6.17a,b). After each galvanostatic pulse, the electrodes were held at open-circuit potential, and the Li filament length was monitored to measure any change in crack length (L_{relax}; Figure 6.17c).

For each frame in the *operando* video, the extension of the leading edge of the Li filament was measured by fitting the abrupt increase in brightness between the darker Li filament and the brighter SSE ahead of the Li filament (Figure 6.18). Further details of this method for tracking Li filament position are provided in the Section 6.3.

The Li filament position was measured during three sets of galvanostatic pulses. Each set consisted of pulses at nominal current densities of 0.5, 1, 2, and 5 mA cm^{-2}. The duration of the pulses was scaled to maintain the same charge for each current in each set.

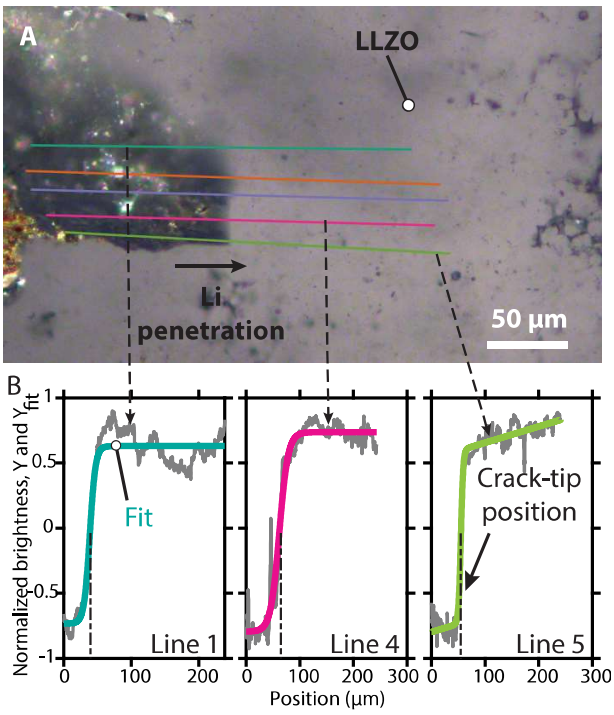

Figure 6.18: *(a) Representative frame from operando imaging during pulsed crack growth experiment with lines overlaid where pixel brightness values were extracted. (b) Extracted pixel brightness values after normalization, along with the hyperbolic tangent fit that was used to track crack-tip position over time.*

The rate of change in filament length was higher for pulses with higher current, as shown by the labelled slopes in Figure 6.17e. For the three sets of pulses, the crack growth rate was proportional to pulse current (Figure 6.17g).

At the lowest pulse current, the crack growth rate approached zero, and the intersection of the fit with the x-axis is non-zero. This points to the existence of a critical threshold current for Li-filament propagation. Further measurements at low current densities would be necessary to better evaluate this threshold of Li penetration and will be the subject of future study.

During open-circuit holds after the pulses above 1 mA cm^{-2}, the Li filament receded. For example, over a period of 6 s after a pulse of 5 mA cm^{-2}, the filament length shortened by L_{relax}, approximately 3 µm (Figure 6.17f). A possible explanation for this Li filament relaxation stems from the viscoplastic mechanical response of Li. Within a range of con-

Figure 6.19: *Pulsed current with filament growth measurements. Operando video microscopy with time-synchronized voltage response and corresponding measurements of filament growth during short stepped current pulses.*

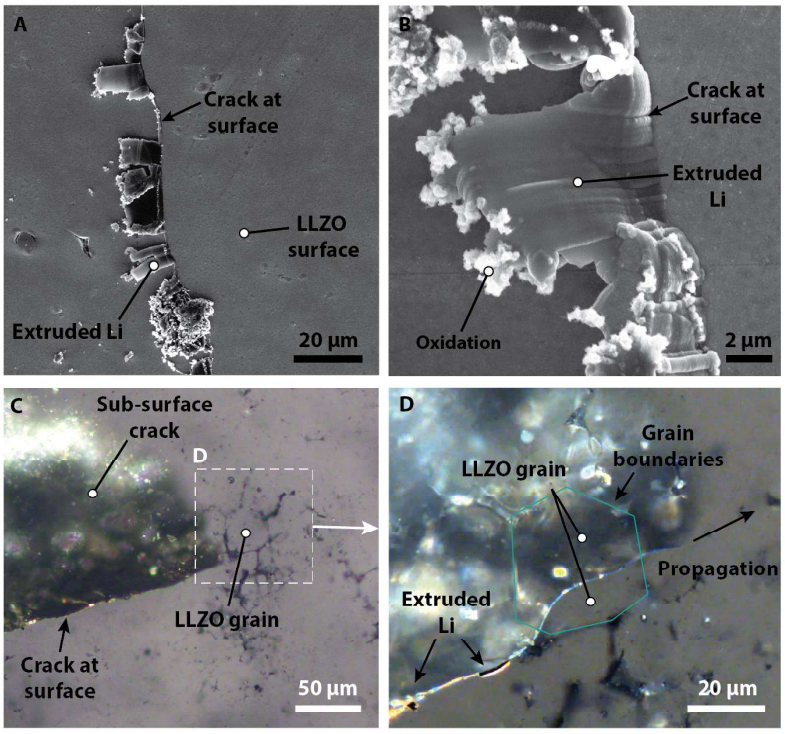

Figure 6.20: *Electron and optical microscopy images of straight type crack propagation. (a,b) SEM images of Li that has been extruded out of the crack where it intersects the surface of the LLZO pellet. (c,d) Operando optical images of straight type Li penetration.*

ditions that are typical of Li metal batteries, the mechanical deformation of Li is strongly dependent on temperature and strain rate.[100,161] Owing to this, Li is susceptible to creep at RT, which would allow the Li within a crack to extrude backwards when current is stopped. As further evidence of this behavior, Li that was extruded out of the crack is visible in post-mortem SEM (Figure 6.20a,b). The relaxation is more dramatic at higher current densities. This is consistent with the fact that the strain rate in Li increases with current density, which leads to a higher stress accumulation at the crack tip. When current is stopped, stress relaxation occurs and the Li filament recedes. This is further evidence that the Li within the crack is under compressive stress, and thus the propagation of the crack is mechanically driven.

On polished LLZO surfaces, grain boundaries are typically not easily visible in optical or electron microscopy. In some cases, however, the different properties of the grain

Figure 6.21: *High-magnification video of straight-type Li filament propagation. Operando video microscopy of an in-plane Li/LLZO/Li cell showing propagation of the Li filament through an LLZO grain, and Li being extruded out of the crack at the surface.*

boundaries make them visible. In Figure 6.20c,d, optical images show a Li filament propagate through the middle of a grain visible at the surface of the pellet. A video of this process is shown in Video 6.21. This suggests that grain boundaries are not the only path of propagation for the straight-type Li filaments in LLZO. The video also shows Li being extruded from the crack at the surface.

6.1.7 Deep Discharge and Void Formation

For Li metal batteries to outperform Li-ion, the amount of excess Li must be limited, as it is extra inactive weight and space in the cell. Thus, understanding the dynamic evolution of electrode morphology during deep discharge is of critical importance. To this end,

current pulses of 4 mA cm^{-2} (just below the measured CCD above) were applied, with a rest period and EIS measurement between each pulse. The resulting *operando* images and electrochemical response are shown in Figure 6.22, and a video will be included in the resulting manuscript. In total, the six 1-min. pulses and eight 2-min. pulses total nearly 1.5 mAh cm^{-2} (based on the original electrode area). This is equivalent to ~7 μm of Li plating. Based on QCM measurements during the deposition of the electrodes, approximately 8 μm of Li was originally deposited, so this represents ~85-90% of the total electrode mass being stripped.

As this Li was stripped (right to left in Figure 6.22a-c), areas of the LLZO beneath the electrode became visible as all of the Li was stripped from those regions. These locally depleted regions are visible throughout the electrode, confirming that the entire electrode area is active. The spatial variation in initiation and spread of these depleted regions may be attributed to several factors. First, as a result of the electrode fabrication process, slight thickness variations are present in the Li surface, which can be seen as ripples in Figure 6.22a. The thinner areas will be depleted first as stripping progresses. Additionally, spatially varying kinetics along the Li/SSE interface could lead to hot spots for stripping. The Li/Electrolyte interface is heterogeneous in nature, with grain boundaries, variations in surface chemistry, and grain orientation (in both the electrolyte and the Li metal) all potential sources of inhomogeneity.[15,16,58,144,146]

During the first pulse, a slight decrease in interfacial resistance is observed (Figure 6.22f), which may be attributed to improved interfacial contact when current flowed the first time. The cell polarization is fairly constant during pulses 1-9 (Figure 6.22d), and the EIS fitted with the equivalent circuit in Figure 6.6 shows only small changes to the interfacial and bulk resistance (Figure 6.22e). In subsequent pulses, as the cell polarization starts to increase, the interface resistance also increases sharply. Nearly all of the increase in total impedance in the EIS is due to the interfaces.

To gain insight into the coupled electrochemical-morphological evolution of the system,

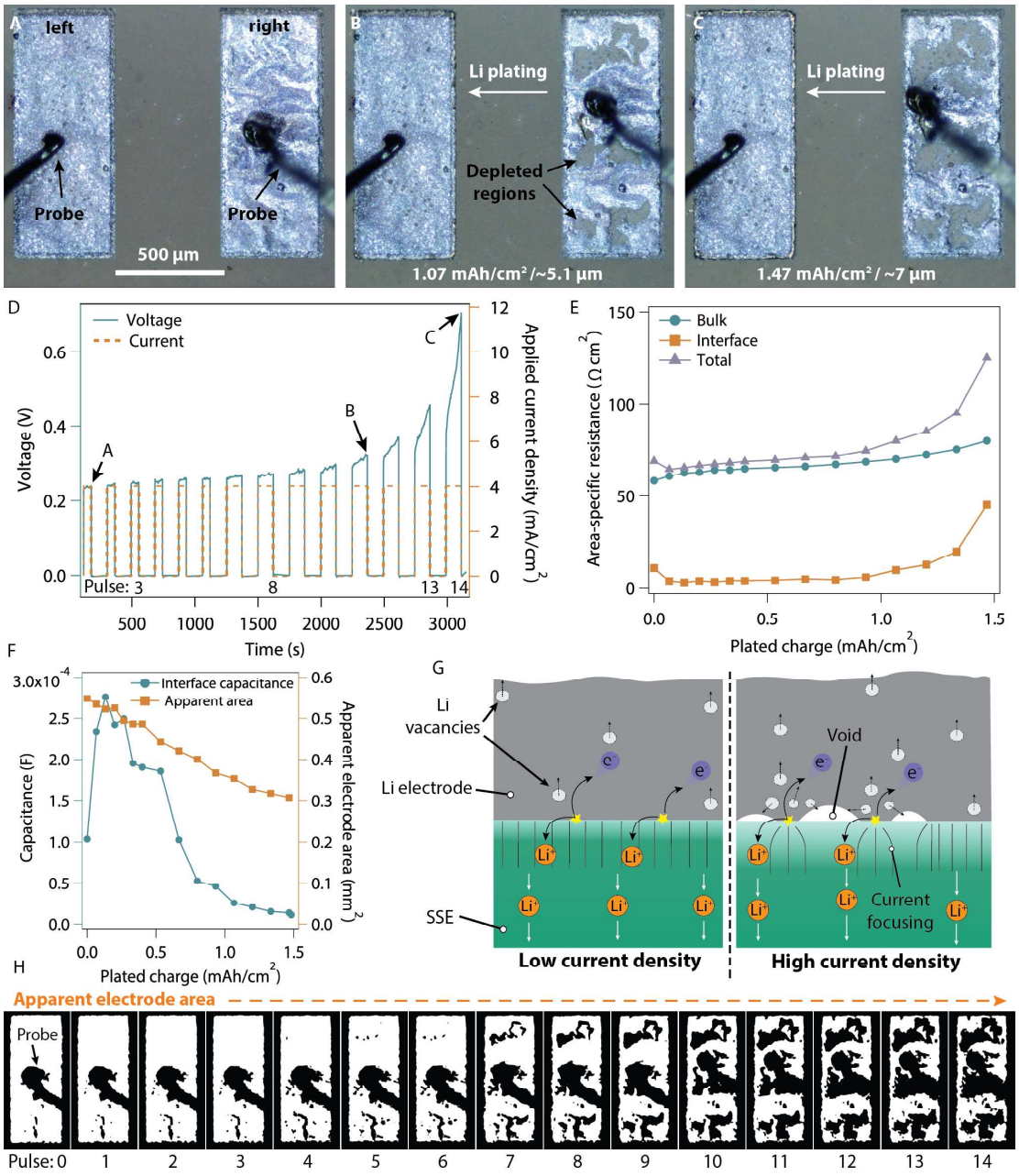

Figure 6.22: *Analysis of in-plane Li/LLZO/Li cell behavior during extended galvanostatic plating. (a-c) Operando optical images at different points in time during Li plating, (d) voltage response to the 4 mA cm^{-2} current pulses with inset showing voltage decay after the current pulses for selected pulses, (e) Area-specific resistance (based on the initial electrode areas) of interface, bulk, and total from EIS after each current pulse. (f) Interface capacitance and apparent electrode area after each current pulse. (g) Schematics of void formation at high current densities. (h) Optical images of anode after each current pulse, processed using thresholding and outlier removal in imageJ so that white area represents metallic Li.*

the *operando* optical images were analyzed. Images corresponding to the end of each current pulse were converted to the binary images shown in Figure 6.22h, where the white regions represent metallic Li (further details in the Section 6.3). The results of this analysis are shown in Figure 6.22f, where the apparent electrode area is plotted along with the interface capacitance extracted using EIS.

After the initial increase during the first current pulse, the capacitance exhibits a decreasing trend, as does the apparent electrode area. A decreasing capacitance with depth of charge was also observed in a recent study of Li/LLZO interfaces.[141] The apparent electrode area decreases approximately linearly with charge, while the capacitance exhibits a highly non-linear decrease. In particular, an abrupt drop in capacitance can be observed between 0.5 and 0.8 mAh cm^{-2}.

This deviation between capacitance and apparent electrode area is unexpected, as capacitance should scale linearly with area for an SSE/electrode interface.[168] This discrepancy could be a result of multiple factors, including: [1] the apparent electrode area not accurately representing the actual area of Li contact with the LLZO due to interfacial void formation; [2] chemical and/or structural heterogeneities along the Li/LLZO interface, which would affect the local capacitance along the interface. Both of these effects could also contribute to the increase in interfacial resistance with time, and will be discussed in further detail below.

As depicted in Figure 6.22g, at low current densities, diffusion of Li vacancies inside the Li metal electrode establishes a steady-state condition with the injection of Li+ into the SSE. As the apparent electrode area decreases (and current remains constant), the local current density increases. Eventually, vacancy diffusion cannot keep up and vacancies accumulate near the interface, coalescing into larger voids.[141] This further decreases the active area and results in current focusing at the contact points between the Li and the SSE, leading to faster void formation in a positive feedback loop.

Representative SEM analysis on FIB cut cross-sections of the Li/LLZO interface con-

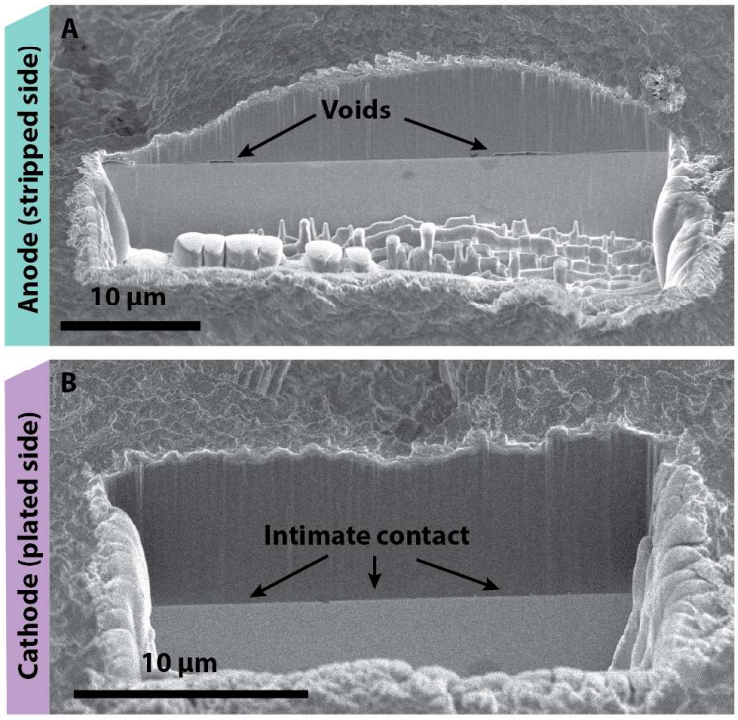

Figure 6.23: *Cross-sectional SEM images of FIB-cut Li/LLZO interfaces. (a) after stripping, and (b) after plating.*

firms the presence of voids at the anodic interface (Figure 6.23). The electrode that was stripped from has several voids, while the side that was plated onto has intimate contact between the Li and the LLZO along the interface. Multiple areas in both electrodes were examined to confirm this was a general trend. This is evidence that void formation contributes to the discrepancy between apparent electrode area and the measured capacitance, and to the increase in interfacial resistance.

Chemical and/or structural heterogeneities along the Li/LLZO interface could also contribute to the evolution of both interfacial resistance and capacitance over time. As Li will be preferentially removed from areas of the interface with faster kinetics (lower activation barrier), these areas will be exhausted of Li more quickly than areas which have slower kinetics. For example, we have previously shown that even after the LLZO surface preparation techniques used in the present work, a non-zero fraction of the surface has Li_2CO_3 present.[16] Furthermore, the presence of the peaking voltage behavior described in the re-

versibility and cycling section above indicates that the kinetics of the bulk Li-SSE interface are slower than at the new interface formed as Li propagation occurs.

As stripping proceeds at the anode, kinetically faster regions along the Li/SSE interface will experience higher local current densities. This will lead to faster vacancy accumulation in the Li in these regions, increasing the likelihood of void formation (Figure 6.22g). As a result, subsequent injection of Li+ ions into the SSE is forced to occur at locations with slower kinetics. The result is an increase in the area-specific resistance. This demonstrates how interfacial heterogeneities may be ultimately responsible for the non-linear increase in interface resistance and decrease in interface capacitance observed at 0.5-0.8 mAh cm^{-2} through the formation of voids.

The fact that stripping of Li at high rates leads to electrode morphology evolution in the form of depleted regions and voids indicates that the design of experimental conditions for evaluating rate capability should take into consideration the intended application. In any LMSSB, stripping of Li from the Li/SSE interface would occur during discharge of the battery, and plating would occur during charging. Thus, the formation of voids would occur during a fast discharge. For example, in EVs or personal electronics applications, fast charge is more important than fast discharge, as the goal is to make the battery last at least several hours of use time. This suggests that an asymmetric cycling protocol may be a better indicator of performance than the symmetric tests above.

6.1.8 Demonstration in a Sulfide Solid-State Electrolyte

All of the experiments above were conducted in the model system of LLZO, but the in-plane architecture can be used in a range of SSE materials. For example, similar behavior to nearly all of the results in LLZO above was also observed in a glassy LPS material, where multiple morphologies (straight and spalling) nucleated in the cycle immediately following the first rapid increase in cell polarization during a current pulse. As shown in Figure 6.24, the in-plane platform can be used even in electrolytes that have very limited

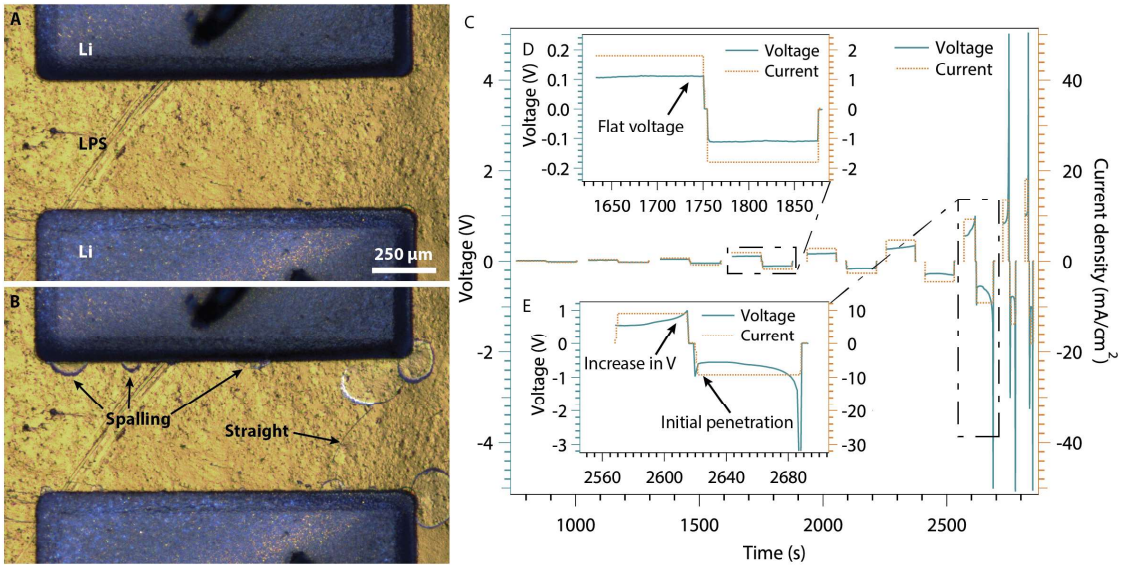

Figure 6.24: *Demonstration of in-plane visualization architecture in glassy LPS. (a,b) Operando optical images of in-plane Li/LPS/Li cell before and after Li penetration. (c) Electrochemical data from cycling of the same cell, with insets (d,e) showing zoom-in on a cycles before and during Li filament nucleation.*

transparency, as the features of interest are near to the electrolyte surface. The voltage profile corresponding to cycling shows that below the CCD, the voltage exhibits relatively flat plateaus for each current density (Figure 6.24d). At the CCD, a sharp rise is observed (due to void formation), and in the subsequent half cycle, Li penetration occurs (Figure 6.24e). This is similar to the results in the LLZO electrolytes.

A detailed analysis of this electrolyte system is beyond the scope of this work, but this result shows the parallels between these two substantially different electrolyte systems. They have different anions (S vs. O), structure (glassy vs. garnet), electrochemical stability (narrow vs. wide), interphase formation (significant vs. little/none),[57] but exhibit very similar Li propagation and electrode evolution in this case. This demonstrates the wider implications of this study for Li metal LMSSBs in general. At any Li/SSE interface, the morphology evolution of the Li metal electrode plays a key role in determining the rate capability. Whether that is Li penetration (of various types), void formation, or wetting/dewetting, it is critical to understand the coupled chemo-electrochemical-mechanical

phenomena that drive interfacial performance and stability in LMSSBs.

6.2 Conclusions

In this work, an in-plane cell geometry was demonstrated that enables high quality optical *operando* imaging of SSEs at battery-relevant current densities. With this platform, several key observations were made:

1. Multiple different morphologies of Li penetration (straight, branching, spalling, and diffuse) are possible in LLZO SSEs, indicating that a single mechanism is insufficient to explain the complexity of this system.

2. The Li within these structures can be reversibly cycled, and the signatures of this are evident in the corresponding voltage trace.

3. At relatively high current densities, the most common types of Li filaments propagate by a mechanical crack-opening mechanism, and the rate of propagation is proportional to the current density.

4. The morphology evolution of the Li electrode (void formation, dewetting, and reduction of contact area) during electrodissolution of Li at high rates demonstrates the importance of considering the impact of both plating and stripping on the Li/SSE interface.

5. Similar Li penetration behavior was observed in a glassy LPS SSE, demonstrating the application of the in-plane architecture for other SSE materials.

These results provide significant new insight into the underlying mechanisms that drive failure in SSE materials, including how/why Li penetration and void formation occurs, what the nature of the structures is, and how they evolve during cycling. This understanding informs future work to suppress the formation of these structures and enable fast-charging of LMSSBs.

6.3 Materials and Methods

6.3.1 Electrolyte Synthesis

Cubic Al-doped LLZO (Al-LLZO) with a nominal composition of $Li_{6.25}Al_{0.25}La_3Zr_2O_{12}$ was prepared for the TP cell using the solid-state synthetic technique. The methodology has been explained elsewhere in more detail.[16,155] A combination of hot-pressing and annealing was used to grow grains and prepare transparent LLZO specimen in this study. First, the calcined powder was densified using a RIHP at 1100 °C under a uniaxial 62 MPa pressure for 1 h in a graphite die under flowing argon atmosphere to achieve >97% relative density. Then, the hot-pressed pellets were embedded in LLZO mother powder with the same nominal composition and annealed in a tube furnace under flowing argon for 50 h at 1300 °C. Details about the method to prepare transparent LLZO can be found elsewhere.[155]

Al-LLZO samples for in-plane cells were synthesized from starting powders of Li_2CO_3, Al_2O_3, La_2O_3, and ZrO_2 from a solid-state reaction method, calcined at 1000 °C for 4 h in dry air. Densification of Al-LLZO was achieved by RIHP green bodies of calcined Al-LLZO at 1225 °C, 48 MPa for 40 min in an argon atmosphere.

For all pellets, polishing and surface preparation to attain low interfacial resistance was done following a previously reported procedure,[16,155] adding a final polishing step of 0.1 µm of diamond polishing abrasive for the in-plane cells before HT at 400 °C for 3 h in an Ar atmosphere.

The amorphous $25Li_2S$-$75P_2S_5$ (mol %) SSE was synthesized from crystalline Li_2S (99.98%, Aldrich) and P_2S_5 (99%, Sigma Aldrich) by mechanochemical synthesis after being mixed in an agate mortar and pestle. The mixed precursors were placed in a 45 cc zirconia pot with 10 zirconia balls of 10 mm in diameter and 10 zirconia balls of 5 mm in diameter, sealed in a dry Ar-filled glovebox (water concentration below 0.5 ppm), placed inside stainless steel vessels and transported in an inert atmosphere. The pots were spun at 510 RPM for 10 h in a Planetary Micro Mill (Pulverisette 7, Fritsch GmbH), with 2

hour intervals of milling followed by 10 min rest intervals at RT. Milled LPS powder was hot-pressed at 200°C for 4 h at 270 MPa with a heating rate of 0.7 °C min^{-1}.

6.3.2 Electrode Fabrication

Immediately following the HT procedure, the LLZO pellets for the TP cells were pressed against Li foil (99.9%, Alfa Aesar) that had been scraped with a stainless steel spatula, with areas apart from the active surfaces masked with kapton tape. In-plane cells were loaded into a glovebox-integrated thermal evaporator (ngstrom Engineering Inc.). Laser-cut Ni foil was gently clamped on the pellet surface to define the geometry of the electrodes. Molten Li (99.9%, Alfa Aesar) in a Mo crucible was heated to 550 °C while the sample was spinning and thickness was monitored by QCM until the desired thickness was reached.

6.3.3 Optical Imaging

Optical imaging of the TP cell was performed with a 12 megapixel color camera (Amscope) and a 75 mm c-mount lens (Fujinon) in an Ar glovebox. A 3-watt white LED (Cree) with focusing optics was used for back-lighting while an LED ring light (Amscope) was used for top lighting.

In-plane cells were imaged using a Nikon LV-150 microscope in an Ar glovebox. A 5 megapixel color camera (IDS) was used to capture still images and video. 5x, 10x, 20x, and 50x objectives (Nikon) were used for various experiments. A halogen lamp was used for axial illumination with circular polarizers on the incoming light and in the imaging column for cross-polarization. A 3-watt white LED (Cree) with focusing optics was used for back-lighting while an LED ring light (Amscope) was used for top lighting. Varying the relative intensity of each light source allowed tunability to maximize image quality and contrast.

Extended depth of focus images shown in figures 6.8 and 6.9 were made by recording images a range of focal positions and blending the images with auto-blend layers in Photo-

shop (Adobe). White balance, brightness, and contrast of the entire images was done using Photoshop or Lightroom (Adobe) to match realistic appearances and make features as clear as possible.

6.3.4 Electrochemical Measurements

Electrochemical measurements were conducted with an SP-200 potentiostat (Bio-Logic) connected to the sample through BNC feedthroughs into the glovebox. Through-plane cells were contacted through the Ni pins that applied stack pressure. In-plane cells were contacted with tungsten needles and xyz manipulators (Signatone).

6.3.5 Image Processing

For the crack growth measurements, optical images were synchronized with corresponding electrochemical measurements using MATLAB®. The Li filament was initiated by first imparting a small scratch on the LLZO surface at the edge of the cathodic electrode with a diamond scribe and then plating Li at a nominal current density of 1 mA cm^{-2} until the filament propagated beyond the end of the scratch by a distance (L_0) of ~60 μm. For each video frame, the Li-filament position was measured from the abrupt change in brightness along the leading edge of the Li filament. Each video frame was aligned with a reference image to remove vibration. Then the image brightness values were extracted for each pixel along 5 lines (5 pixels wide) that spanned across the Li filament and into the SSE ahead of the filament, in the direction of crack extension (Figure 6.18). For each line, the image brightness was normalized between -1 and 1 for all of the frames during the galvanostatic pulses. For position along each line (x), the normalized image brightness (Y) was fitted with a brightness function (Y_{fit}). The objective function for minimization was $(Y-Y_{fit})^2$, with

$$Y_{fit} = A \tanh\left[B\left(x - C\right)\right] + Dx + E \tag{6.1}$$

The fitted function Y_{fit} utilized a hyperbolic tangent function with five fitting terms: brightness magnitude (A) of the hyperbolic tangent, crack position scale (B) and shift (C), linear brightness scaling (D), and brightness shift (E). The key fitting term of interest is the crack position shift (C), with the growth of the Li filament between frames given by the change in C.

For the analysis of electrode area during deep discharge, a color threshold on the R channel was applied in ImageJ. Then the image was converted to greyscale and another threshold was applied to convert the image to binary white and black. Outlier removal of both light and dark regions smaller than 20 pixels was used to reduce noise. Electrode area was then calculated by counting white pixels in each frame with Matlab.

6.3.6 Electron Microscopy

Post-mortem electron microscopy and FIB cutting was performed on an FEI Helios 650 Nanolab dual beam SEM/FIB. Air exposure during transfer into the instrument was minimized, usually less than 60 s between first air exposure and reaching 10^{-3} Torr vacuum levels, with UHV levels reached within 2 min after that. SEM imaging was performed at 1-2 kV accelerating voltage and 100 pA to minimize charging and other artifacts. FIB cross-sectioning and tomography was performed using Ga+ ions with an accelerating voltage of 30 kV and a beam current of 21 nA.

6.3.7 3-D Reconstruction

Reconstruction of a series of SEM images during successive FIB polishing cuts was performed using the Avizo software package (Thermo Fisher Scientific Inc.). Images were aligned and shear-corrected, and a non-local means filter was applied for noise reduction. Subsequently, segmentation based on brightness was performed to assign regions of interest.

CHAPTER 7

Atomic Layer Deposition of $Li_7La_3Zr_2O_{12}$ Solid Electrolyte Materials

Adapted with permission from Kazyak, E.; Chen, K.-H.; Wood, K. N.; Davis, A. L.; Thompson, T.; Bielinski, A. R.; Sanchez, A. J.; Wang, X.; Wang, C.; Sakamoto, J.; et al. Atomic Layer Deposition of the Solid Electrolyte Garnet $Li_7La_3Zr_2O_{12}$. *Chem. Mater.* 2017, 29 (8), 37853792.

In parallel to the work described in Chapters 4 to 6, I developed processes to deposit SSE materials by ALD. It is well known that the properties of the interfaces in electrochemical systems, like batteries, play a large part in determining the overall performance. It is therefore desirable to be able to precisely control those properties, for instance with coatings that can improve electrochemical stability.[169] ALD has proven to be a valuable tool for modifying electrode/electrolyte interfaces in both liquid and SSBs.[71,92,118,170] Much of this work, however, has been limited to just a few materials that are most readily deposited by ALD. In many cases, it would be desirable to deposit a film that conducts ions but not electrons. This could be used to passivate an electrode surface against an electrolyte, or to reduce interface resistance. Unfortunately, there are very Li-ion conductors that have been deposited by ALD. The goal of the next two chapters is to develop such materials, and demonstrate that they have the properties necessary to be used as either stand-alone SSEs, or as interlayers and coatings at electrode/electrolyte interfaces.

Many potential target materials were considered. One of the most promising SSE ma-

terial systems is the Li-rich garnet LLZO, due primarily to its high ionic conductivity at RT (10^{-3} S cm^{-1}) and improved stability against Li metal.[38,113] Through aliovalent doping, the superionic conducting cubic phase can be stabilized at RT, and this material has shown promise for integration in practical battery systems. Two of the primary challenges remaining for commercialization are formation of stable low impedance interfaces with both anode and cathode materials and the manufacturing of thin dense films required for high overall energy density.

Previous studies have developed processes for deposition of LLZO thin films with techniques including physical vapor deposition,[171] pulsed laser deposition,[172] and CVD.[173] These techniques are limited in their ability to conformally coat high-aspect-ratio 3-D structures, require high-temperatures, and are limited in scalability while maintaining precision and quality control during manufacturing of nanoscale architectures.

Li-ion batteries rely on the ability of liquid electrolytes to penetrate into porous electrodes to facilitate ionic transfer and conduction. With SSEs, this is a major challenge, as a planar electrolyte in contact with a porous electrode will suffer from increased impedance due to a lack of ion conduction pathways and low interfacial area. Moving to 3-D and porous electrode architectures could enhance rate capability and enable high areal capacity loading, increasing the energy density.[174,175] This presents a significant challenge for SSE manufacturing, as it requires intimate contact between a complex 3-D geometry and an SSE film.

Following the pioneering work on ALD interlayers in Li-ion batteries,[77,82] several studies have investigated ALD films as SSEs. Specifically, ALD SSEs are promising for 3-D battery architectures, porous electrode coatings, encapsulation, etc.[176] These studies have fabricated a range of oxide, phosphate, and sulfide materials with a wide range of ionic conductivities (10^{-10} to 10^{-7} S cm^{-1}).[95,177–191] The highest reported ionic conductivity in an ALD film was in LiPON: $3.7*10^{-7}$ S cm^{-1} in solid-state or $6.6*10^{-7}$ S cm^{-1} in a liquid cell.[177,192] LiPON has been used to make thin-film batteries, and have shown promising

electrochemical stability for application in high voltage systems. The recent work by Pearse et al. highlights the potential of ALD electrolytes for 3-D architectures and demonstrates a proof-of-concept device.[175] One potential limitation of the ALD LiPON films, however, is that the ionic conductivity still lags behind that of sputtered LiPON (1.8-3.3*10^{-6} S cm^{-1}[193]) and is well behind that of bulk SSEs (10^{-4} to 10^{-2} S cm^{-1}).[57] For this reason, materials with higher conductivities that maintain wide electrochemical stability windows are of great interest.

Herein we present a thermal ALD process for Al-doped LLZO SSEs. The pentenary ALD process was developed by careful combination of constituent binary oxide ALD processes. In ALD of multi-element compounds, the precursors must be chosen carefully to avoid unwanted reactions, incompatible temperature requirements, and impurities.[63] Moreover, there are many critical aspects of ALD chemistry that can affect film composition, crystallinity, and morphology, including gas-phase ion-exchange reactions,[194] chemical etching,[195] thermal decomposition,[196] and precursor-specific reaction pathways. Thus, a detailed understanding of ALD chemistry at the atomic scale is critical to enable rational design of materials, which was quantitatively analyzed in this study using *in situ* QCM measurements of the ALD growth.

Additionally, challenges associated with Li loss during annealing ultrathin Li-containing films arise due to the high ionic mobility and reactivity of Li.[197] To address these challenges, in this study we perform *in situ* synchrotron XRD experiments to obtain the cubic garnet crystal structure. A highly phase pure cubic garnet film is obtained through precise control of the annealing environment, showing the potential of this process to be used for interfacial engineering and electrolyte deposition in 3-D battery architectures.

7.1 Results and Discussion

ALD of Li-containing films has proven to be a challenge due to the lack of a sufficiently volatile precursors with reasonable growth rate and low impurities. In this study, lithium tert-butoxide (LiOtBu) was selected due to previous reports of its reasonable success in ternary films.[185,198–200] Tris(N,N'-di-i-propylformamidinato)lanthanum (LaFAMD) was chosen for its improved volatility and growth rate compared to other La precursors.[201,202] Tetrakis(dimethylamido)zirconium (TDMAZ), and TMA were chosen as they are well-understood precursors capable of yielding high quality films under a wide range of conditions.[61] Ozone (O3) was used as the oxidizer in all cases to avoid potential complications resulting from the hygroscopic nature of the Li_2O, La_2O_3, and resulting LLZO films.[203] The constituent binary processes for Li_2O, La_2O_3, ZrO_2, and Al_2O_3 were first optimized on their own. The pulse saturation curves measured by *in situ* QCM are shown in Figure 7.2. Each of the processes was characterized to verify saturated pulse and purge times, growth rate, and low (<1%) impurities. The constituent processes were then combined as shown in Figure 7.1 to yield dense LLZO films. The rule of mixtures was used to provide an initial estimate of the required ratio between subcycles A, B, C, and D in Figure 7.1 to deposit stoichiometric Al-doped LLZO (Al-LLZO). This method, detailed previously, uses the individual process growth rates and atomic densities to estimate multinary growth rates and resulting composition.[195] Minor empirical adjustments were needed to correct for the non-ideal behavior of the multi-element processes due to different nucleation and growth behavior of the ALD on different surface terminating species than in the binary processes.

With a ratio of 8:28:12:1 (Li:La:Zr:Al) ratio of pulses, the resulting film was close to the targeted stoichiometry of $Li_{6.28}La_3Zr_2O_{12}Al_{0.24}$, and had low carbon content (<1%) as shown by XPS in Figure 7.3. This ratio of constituent subcycles is defined as one super-cycle, and can be repeated as needed to deposit films of a desired thickness. The oxygen content is lower than expected, likely due to preferential oxygen removal during Ar sputtering to remove surface contamination.[204] For this reason, the cation ratio for the ALD film

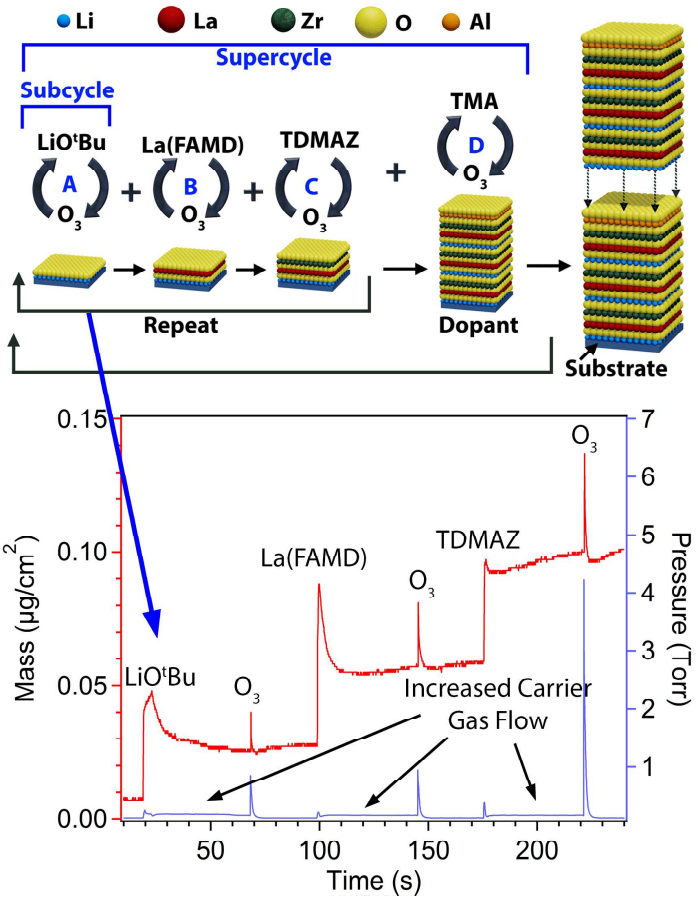

Figure 7.1: *Schematic representation of an ALD supercycle composed of constituent binary ALD processes (top) and plot of film mass uptake (left, measured by QCM) and chamber pressure (right) vs time (bottom). Each binary process shown (A, B, C) has a mass increase associated with the metal-organic precursor pulse.*

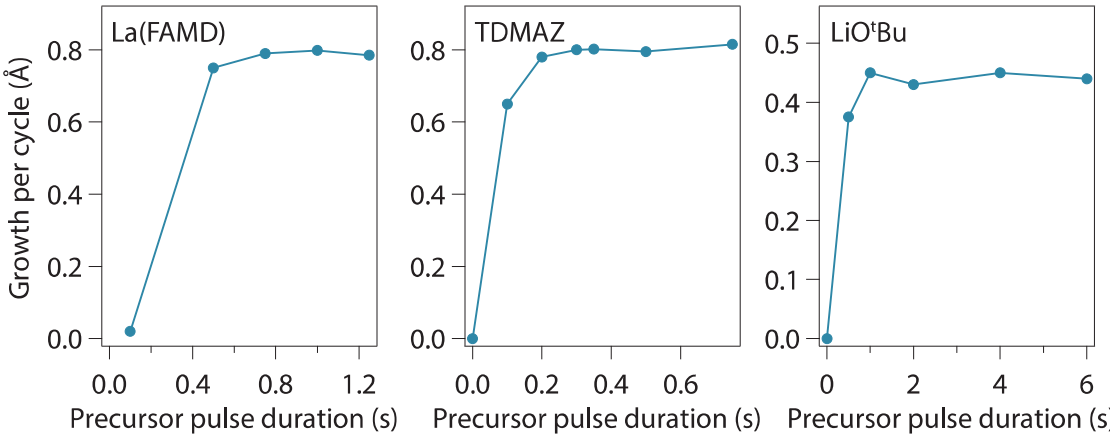

Figure 7.2: *Pulse length saturation curves for (a) LaFAMD, (b) TDMAZ, and (c) LiO^{t}Bu with ozone measured by in situ QCM, assuming bulk density.*

and for stoichiometric LLZO is shown in Figure 7.3. The QCM data shown in Figure 7.4 indicates linear growth over many supercycles.

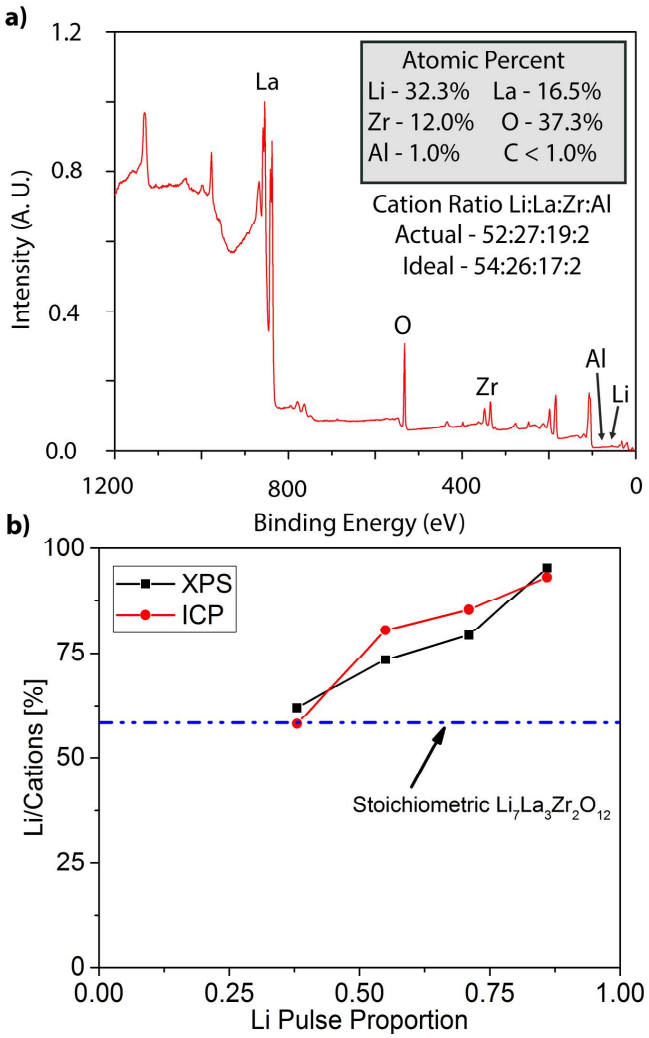

Figure 7.3: *(a) XPS survey scan of an as-deposited ALD LLZO film (inset compares ideal and actual compositions) and (b) plot of Li content (no. of Li atoms/total no. of cations) vs the proportion of total subcycles that is Li.*

By simply altering the ratio of subcycles, the composition of the film can be easily tuned. To demonstrate this further, a set of films with varying Li content was deposited. As shown by both XPS and ICP-OES in Figure 7.3, the ratio of Li to the total cations increases as the proportion of Li subcycles is increased. This can therefore be used as a means of controlling Li content to alter conductivity and compensate for Li loss during subsequent annealing.

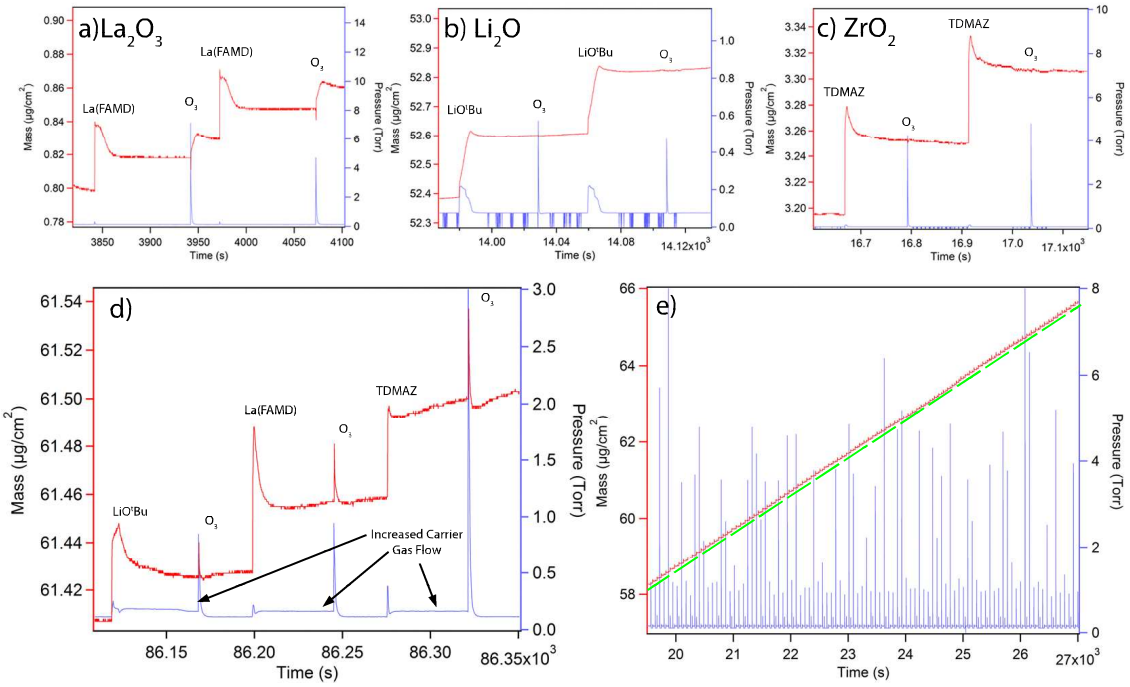

Figure 7.4: *In situ QCM data showing the uptake in mass during the binary processes for LaFAMD/O_3 (a), LiO^{t}Bu/O_3 (b), and TDMAZ/O_3 (c). The mass uptakes during one repeat unit of the supercycle for the LLZO ALD process showing that each process results in growth when combined (d). Wide view of LLZO ALD process showing linear growth over many supercycles.*

Despite the fact that the ratio of B(La):C(Zr) subcycles was held constant for this experiment, a clear trend was observed in the La:Zr ratio in the deposited films. As the proportion of Li subcycles increased, the La:Zr ratio in the film decreased. To investigate this behavior, *in situ* QCM was used to conduct a nucleation experiment to measure the growth of the first subcycle of La after a series of 5 previous subcycles of LaFAMD+O_3, TDMAZ+O_3, or LiO^{t}Bu+O_3. This study revealed that the growth rate of La dramatically decreased when the previous subcycle was Li, and slightly increased when the previous subcycle was Zr (Figure 7.5). This is consistent with the trend that with increased Li content in the LLZO film, the La content decreased relative to Zr. This change in nucleation can be corrected for by increasing the B:C ratio when increasing the Li content of films.

The thickness of 18 supercycles of the stoichiometric ratio deposited on (100) Si was measured by ellipsometry as 86.5 nm, which is in agreement with the thickness measurement by cross-sectional SEM shown in Figure 7.6a. The as-deposited film is amorphous,

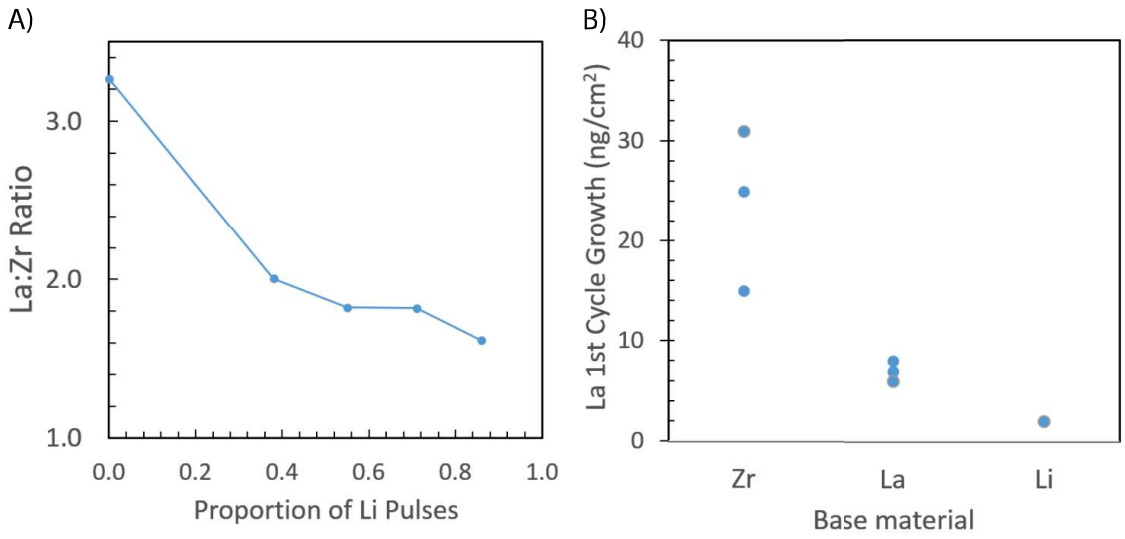

Figure 7.5: *Plot showing decrease in La:Zr ration as a function of Li pulse proportion in ALD Supercycle as measured by ICP-OES (a). Plot of average La_2O_3 mass uptake during subcycles immediately following various base materials (b). La nucleation is dramatically suppressed when the previous subcycle was LiO^tBu-O_3 and significantly increased when the previous subcycle was TDMAZ-O_3.*

as shown by synchrotron grazing incidence XRD (Figure 7.7) and TEM selected area electron diffraction (SAED), Figure 7.6f. The SAED pattern shows clear spots corresponding to the underlying ZnO nanowire that was used as a template, with only an amorphous halo present from the film, which is consistent with an amorphous ALD coating. This ability to deposit conformal ultrathin (<100 nm) amorphous LLZO films at low temperature with a scalable process is unique.

To demonstrate the ability of this ALD process to deposit conformal films on 3-D structured substrates, 9 supercycles were deposited on a Si wafer with trenches of various sizes (Figure 7.6b-d). As can be seen in the cross-sectional SEM images, even within the trench with an aspect ratio of ~30, the ALD film conformally coats undercuts and vertical faces with a homogeneous thickness throughout the full depth of the trench (step coverage >95%). To further illustrate the conformal nature of deposition, one supercycle of ALD LLZO was deposited on single crystal ZnO nanowires, grown by the same hydrothermal process reported previously.[205] As seen in the lattice-resolved high-resolution

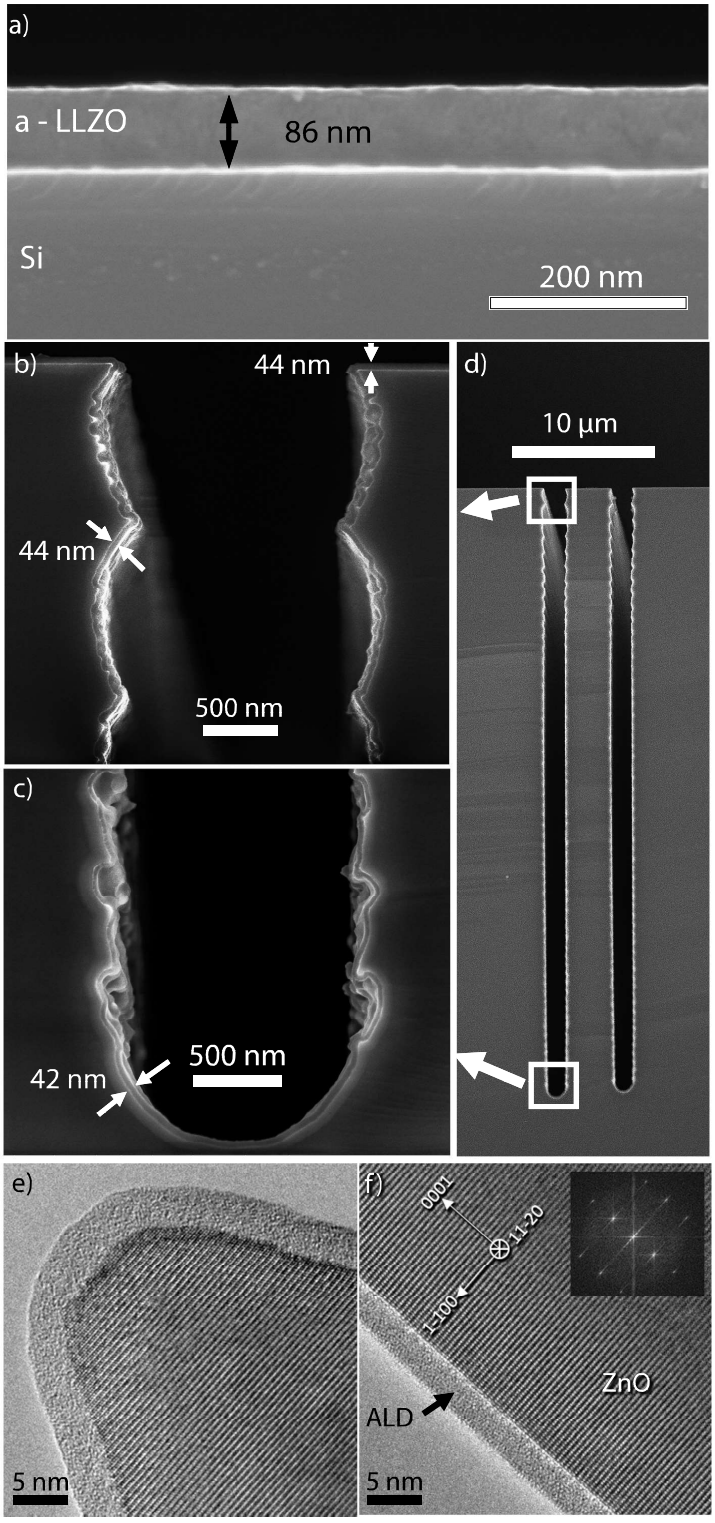

Figure 7.6: *(a) SEM image showing as-deposited ALD LLZO film on a Si substrate, (b) SEM image showing the ALD film from the top of a Si trench shown in (c), (d) SEM image showing the ALD coating at the bottom of a Si trench, (e) TEM image showing the ultrathin conformal coating at the tip of a ZnO nanowire, and (f) TEM image showing a sharp film/wire interface, with electron diffraction (inset) showing the amorphous nature of film.*

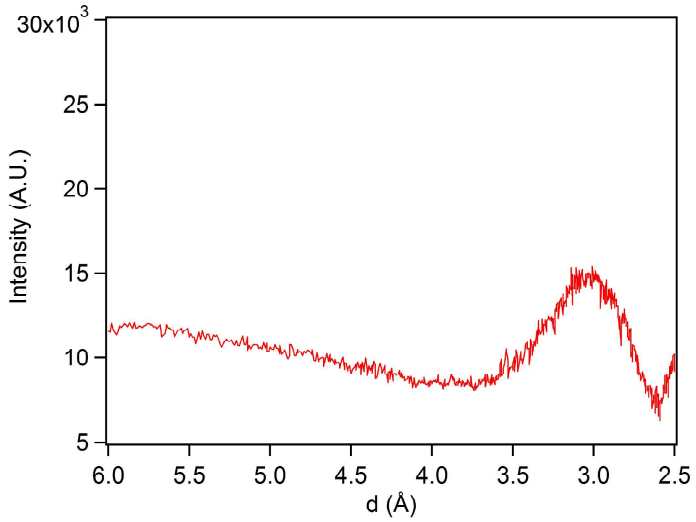

Figure 7.7: *Synchrotron grazing incidence XRD pattern of as-deposited 100 nm LLZO showing amorphous nature of the film.*

transmission electron microscopy (HRTEM) image of Figure 7.6, the dense amorphous ALD film uniformly coats the surface of the ZnO nanowire, leaving an atomically sharp interface between the two phases.

Due to the potential attractiveness of amorphous electrolytes that require no annealing and can coat complex 3-D geometries, the ionic conductivity of the as-deposited films was measured and fit to an equivalent circuit for LLZO with blocking electrodes.[135] Both in-plane and TP measurements were conducted, and provided similar values. Using Pt interdigitated electrode (IDE)s for an in-plane measurement, the Al-doped stoichiometric film had an ionic conductivity of 7.8 $*10^{-5}$ S cm^{-1} at 200 °C and 1.2$*10^{-6}$ S cm^{-1} at 100 °C, giving an activation energy of 0.63 eV $atom^{-1}$ and a calculated conductivity of approximately 1$*10^{-8}$ S cm^{-1} at 25 °C (Figure 7.8). The Li content of the film was varied by changing the number of Li subcycles between half and double the stoichiometric proportion, but there was not a significant effect observed in the conductivity or activation energy.

LLZO has primarily been of interest to the community due to the high ionic conductivity (approaching 1 mS cm^{-1}) of the cubic garnet phase LLZO (c-LLZO) phase. This phase is typically stable only at temperatures above 645 °C, but can be stabilized at RT by aliovalent doping that creates Li vacancies and prevents the Li from ordering and transforming

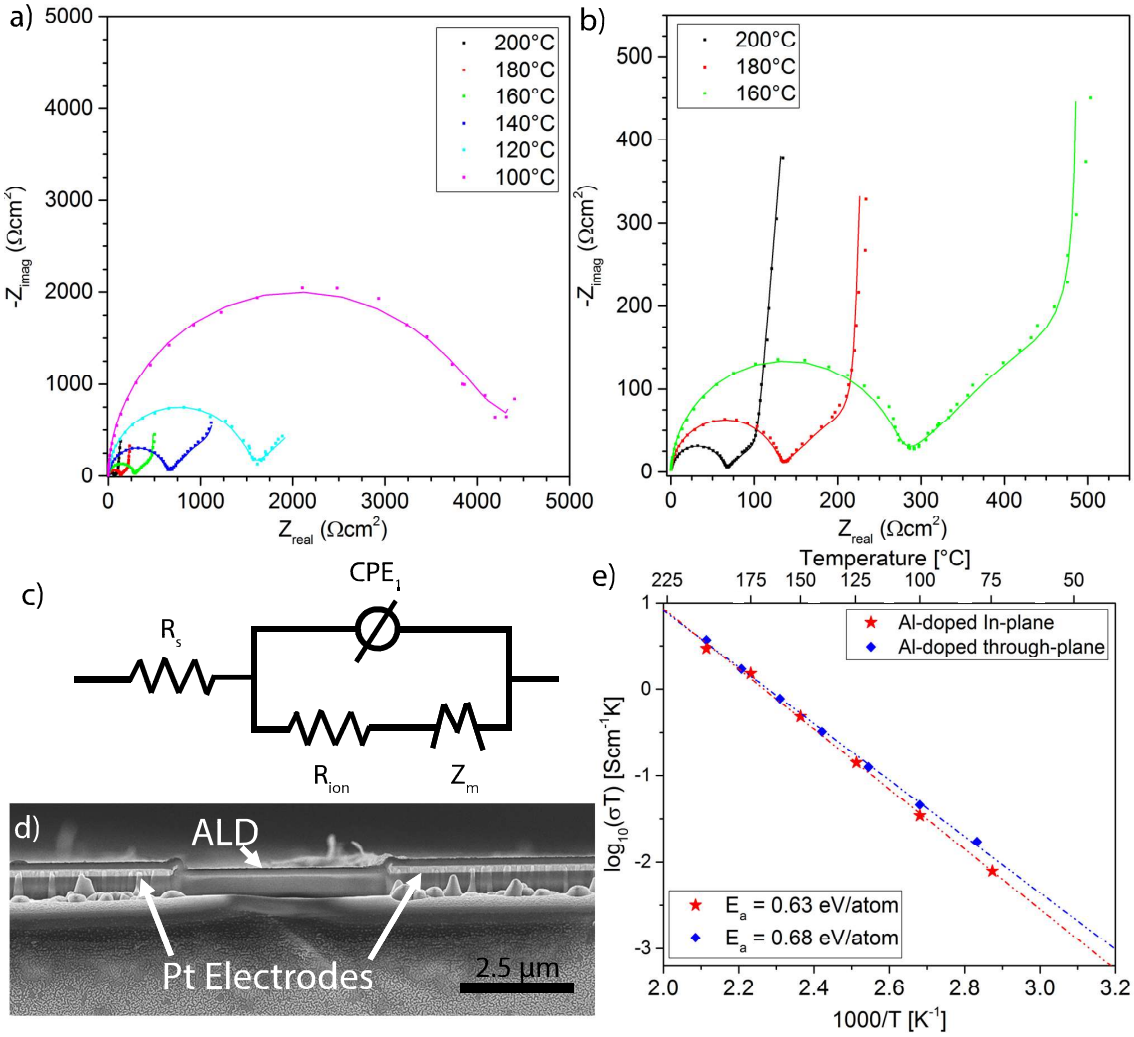

Figure 7.8: *EIS spectra showing Nyquist plots for a range of temperatures on the IDEs (a) with zoom in on low-impedance region shown in (b). Markers are experimental data and solid lines are fitted curves using equivalent circuit model shown in (c). (d) Ion-beam milled cross-sectional SEM image of ALD film on IDE structure. (e) Arrhenius plot for both TP and in-plane measurements along with the calculated activation energies for each. Conductivities of the films could only be directly measured down to 100 °C due to high impedance.*

back to the lower temperature tetragonal phase.[206] In order to form the cubic phase in the ALD films shown here, annealing at high temperature is necessary.

Initial attempts to anneal ALD LLZO films on Si and Si_3N_4 substrates resulted in severe reactivity with the substrate, loss of Li content, and film delamination. To address these concerns, many potential substrates were screened, including Cu foil, stainless steel foil, Ni foil, Mo Foil, sputtered Pt on Si, evaporated Ni on Si, soda-lime glass, fused quartz,

Al_2O_3, ZrO_2, and MgO. Single crystal MgO (100) substrates were used for subsequent annealing experiments, as they did not show signs of reaction with the ALD films during annealing, as observed by XPS.

Several annealing strategies were explored in order to achieve the desired c-LLZO phase. Synchrotron XRD, which we previously demonstrated as a powerful technique for analysis of ultrathin crystalline ALD films,[205] was used to quantify the complex phases (unit cell = 192 atoms) in these thin films. Standard spectra were obtained from the inorganic crystal structure database (ICSD) for comparison. Figure 7.9 shows synchrotron XRD patterns for three of these conditions: I) Rapid thermal annealing to 600 °C for 10 min. in O_2 atmosphere II) Furnace anneal to 600 °C for 1 h in Ar atmosphere III) Sealed furnace anneal to 555 °C for 30 min in He atmosphere with Li source. Condition I resulted in the Li-free pyrochlore phase $La_2Zr_2O_7$.

Incidentally, there are several interesting potential applications for the formation of this phase by ALD. Lanthanum zirconates have excellent thermal and phase stability, low thermal conductivity, and have been used in many applications including thermal barrier coatings in turbines,[207,208] high temperature catalysis,[209] and immobilization of species in radioactive waste.[210] Bulk synthesis methods typically require heating in excess of 1200 °C, meaning ALD represents a promising means of low-temperature fabrication.[211] The second condition resulted in a small amount of c-LLZO, but again was predominantly pyrochlore. These results indicate that the films did not retain Li during the high-temperature annealing process.

It is well known in the bulk synthesis community that a small amount of excess Li is needed to compensate for the Li loss during high temperature annealing, typically 5-15 weight percent.[120,212] In thin films, more excess Li is necessary due to the large surface area to volume ratio, and the small ratio of sample volume to annealing atmosphere volume.[173,213,214] These factors increase Li loss to the annealing atmosphere, which leads to the formation of Li-deficient pyrochlore impurity phase. To address these challenges, a

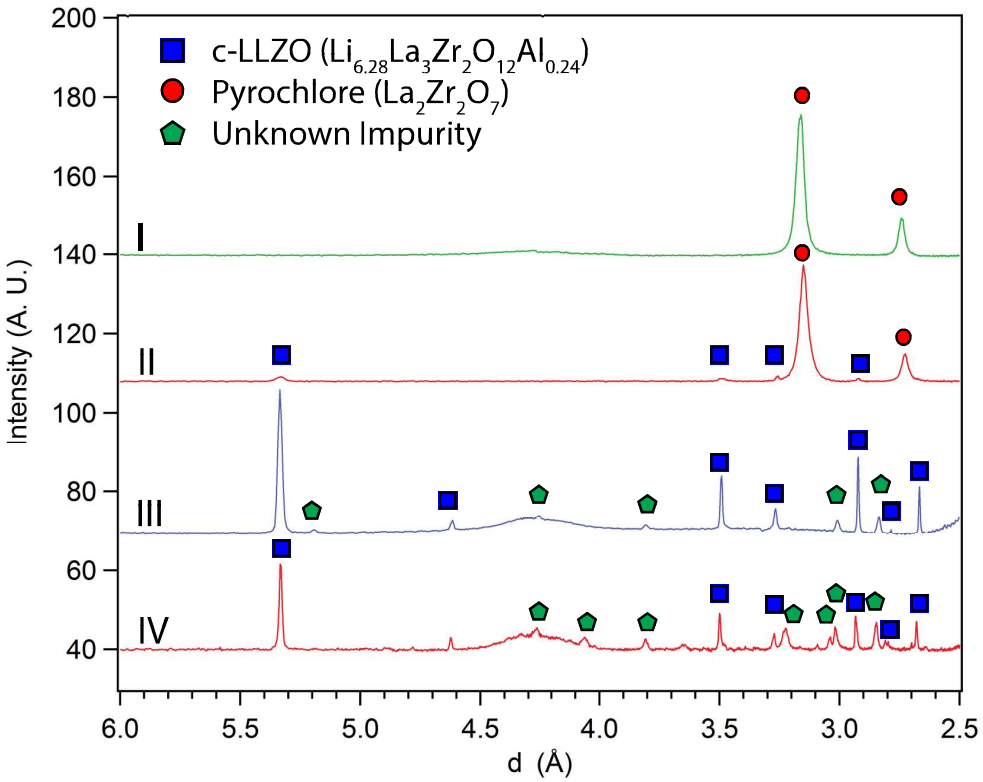

Figure 7.9: *XRD patterns with peaks assigned to appropriate phases for four annealing conditions: (I) 600 °C rapid thermal annealing with a 10 min hold in a O_2 atmosphere, (II) 600 °C muffle furnace annealing for 1 h in a Ar atmosphere, (III) 900% excess Li film, with 555 °C sealed furnace annealing for 30 min in a He atmosphere with $LiMnO_2$ present as the Li source while the sample was at 555 °C, and (IV) 400% excess Li film, with 540 °C sealed furnace annealing for 30 min in a He atmosphere with $LiMnO_2$ present as the Li source.*

sealed or semi-sealed vessel was used to restrict the flow of Li vapor and reduce losses to outgassing. Additionally, by placing a Li-containing powder ($LiMn_2O_4$) inside of the annealing environment, the partial pressure of Li was increased, further reducing the driving force for Li loss to outgassing. In addition, the proportion of Li subcycles in each supercycle was multiplied by a factor of 10 to increase the starting concentration of Li in the film. According to ICP-OES measurements, this was approximately 900% excess Li.

The third condition in Figure 7.9 shows the effectiveness of these methods, demonstrating a nearly pure phase c-LLZO film at a temperature of 555 °C, with no pyrochlore and only trace amounts of other impurities remaining. This is significant, as bulk methods typically require significantly higher temperatures to remove pyrochlore impurities.[215,216]

Definitive identification of the trace impurity peaks present has proven challenging.

The synchrotron XRD pattern for the third condition shown in Figure 7.9 was collected at 555 °C, during *in situ* annealing at the Advanced Photon Source at Argonne National Laboratory. The temperature profile and corresponding XRD patterns are shown in Figure 7.10. As the film was cooled, the c-LLZO transformed to the tetragonal garnet LLZO (t-LLZO) phase, observed as clear peak splitting in the XRD pattern.

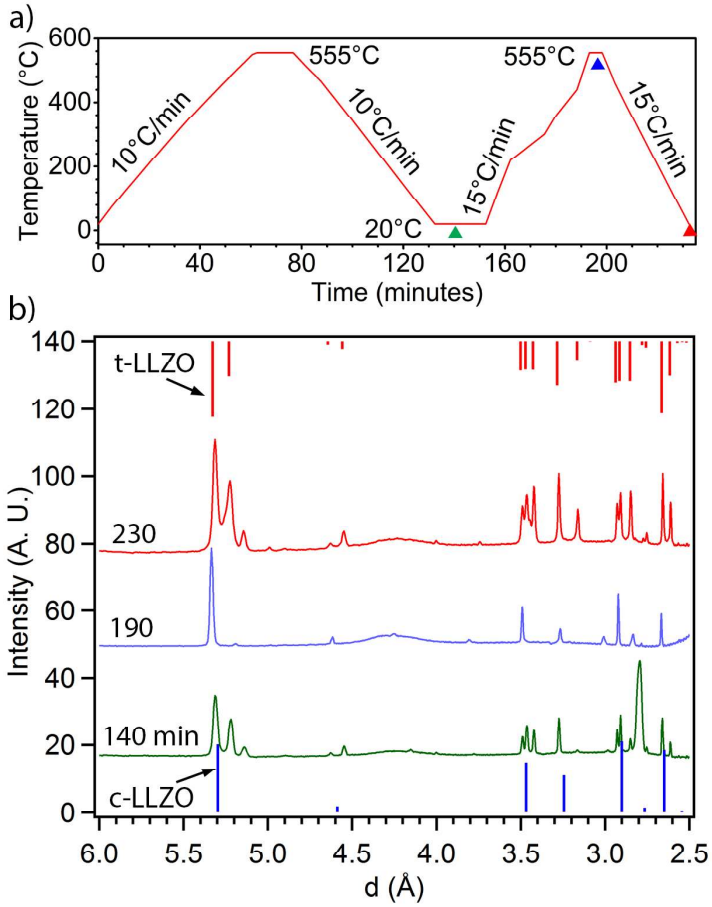

Figure 7.10: *(a) Temperature profile measured during in situ annealing experiment. Colored triangles correspond to the points in time when the XRD patterns shown in (b) were collected. Lines shown on the top and bottom axes are powder standards for t-LLZO and c-LLZO, respectively (ICSD 246816 and 261302).*

After an initial heating step to 555 °C, a spectrum was taken at RT 140 min. into the experiment (Figure 7.10a). The data reveal the presence of t-LLZO with a significant impurity peak at 2.8 Å. When reheated to 555 °C, the film transformed back to c-LLZO

(data collected during heating) and the large impurity peak almost completely disappeared. This is one of the lowest reported annealing temperatures demonstrated to yield high-purity c-LLZO. It should be noted that a slight shift of all of the peaks to larger d spacing values was observed due to thermal expansion during the *in situ* XRD analysis. As the film cooled, it transformed back to t-LLZO with lower impurities. This phase transformation is likely due to excess Li remaining in the film, causing the Li lattice to order upon cooling, as has been hypothesized by a recent report on the stability of LLZO interfaces.[217] This suggests that the measures taken to compensate for Li loss left excess Li in the film, which is consistent with the presence of Li_2CO_3 impurities. Further optimization should alleviate this effect by balancing excess Li with Li loss.

We also note that while the phase can be fully indexed as c-LLZO, a preferential crystallographic texture is observed in the diffraction pattern compared to powder standards in literature. The ratio of the intensities of the (211) (~5.3 Å) and (024) (~3.1 Å) reflections is much larger than in the powder standard (ICSD 261302). This suggests a textured film with preferred (211) orientation on the single crystal substrate. We cannot fully quantify this relationship based on ratios of integrated peak areas, as the number of grains sampled in the thin film may not be sufficient to provide statistically meaningful results, however this trend was observed on multiple samples. The limited number of grains can be observed in the area detector data shown in Figure 7.11 as spottiness rather than bands or partial bands.

Stabilization of the cubic phase down to RT is key to achieving a high ionic conductivity film, and for this reason, we reduced the amount of excess Li from ~900% to ~400% by tuning the supercycle. The XRD pattern after cooling to RT is shown in Figure 7.9, condition IV. The film is predominantly c-LLZO. With additional tuning of the ALD film and annealing conditions, it should be possible to get even higher phase purity films at RT.

While adding excess Li and utilizing a Li-rich annealing atmosphere was demonstrated as a method to achieve the desired phase, the morphological evolution of the film during annealing proved to be a major challenge during annealing. The loss of excess Li and long-

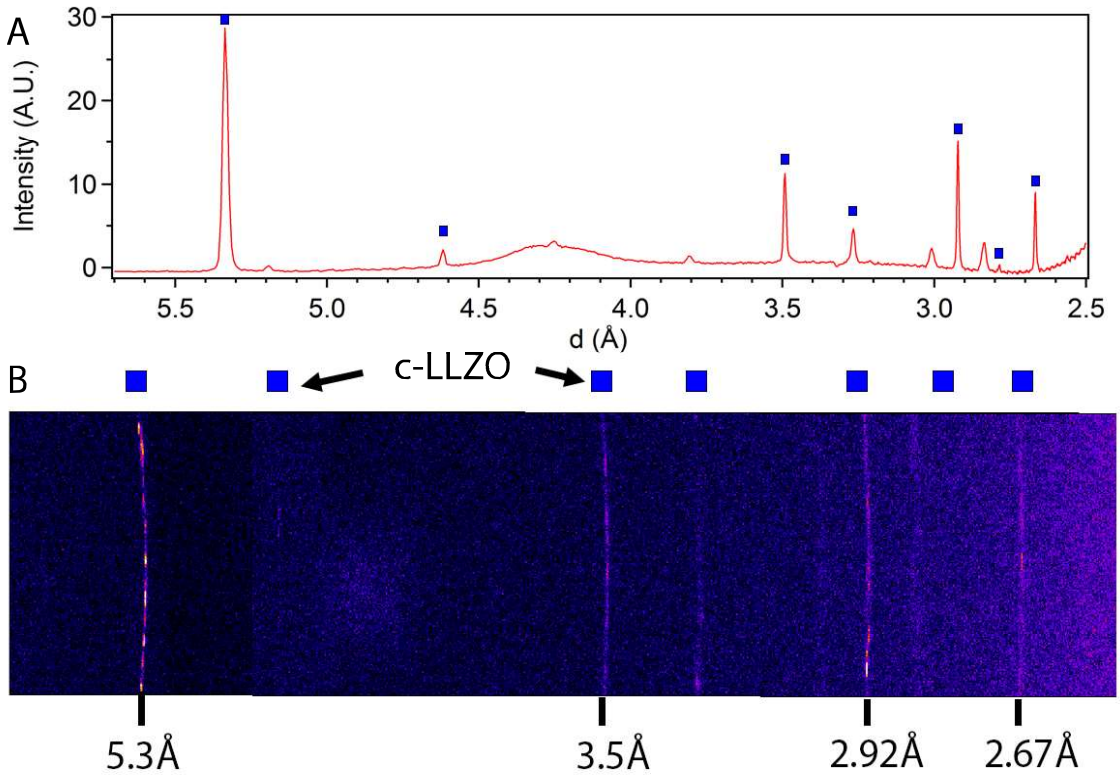

Figure 7.11: *Area Detector data from ALD film annealedin situ in He environment at 555 °C with $LiMnO_2$ as a Li source to prevent Li loss. The spottiness of many of the peaks indicates a relatively small number of grains sampled, and means that peak ratios may not be statistically meaningful to determine preferential texture within the ALD film. The horizontal axis of the area detector is linear in 2θ, but not in d, so the plot above does not match perfectly, but the intensity and order of the peaks does match.*

range diffusion led to segregation of the dense amorphous film into isolated crystalline islands, which disrupted the film continuity and made it impossible to measure meaningful conductivity values in the crystalline films.[214]

The morphology resulting from the fourth annealing condition is shown in Figure 7.12. In both electron microscopy images, an island morphology is clearly observed after annealing. Interestingly, the islands exhibit clear faceting, and there is a strong relationship between the faceted edges of the film (observed as squares and rectangles) and the underlying MgO substrate (orientation shown in Figure 7.12a). Consistent with the above discussion of preferential crystallographic texture, this suggests that coherency be-tween the film and substrate occurs during the annealing process, and that there is a preferred

direction for grains in the ALD film to nucleate and grow on the MgO (100) substrate. This relationship with the substrate could be partially responsible for the significantly decreased temperature required to form the cubic garnet phase compared to most previous studies, and could contribute to the driving force for the phase transformation. Therefore, the MgO (100) substrate appears to play a critical role in both minimizing chemical reactivity and Li loss to the substrate, as well as promoting the desired cubic phase transformation during annealing.

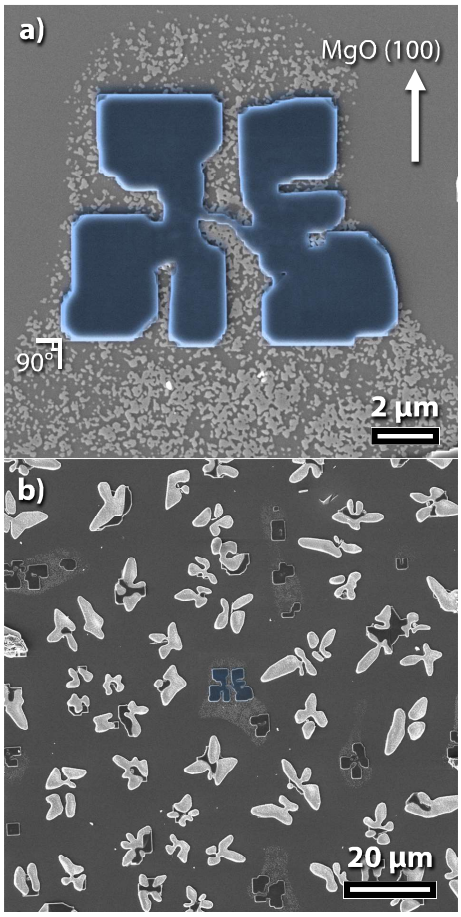

Figure 7.12: *SEM micrographs showing high-magnification (a) and wide-view (b) ALD film morphology under annealing condition IV in Figure 7.9. Falso color is used to highlight the faceted feature in both (a) and (b).*

Island formation was also observed in a recent study that used similar annealing conditions.[214] The islands in that study were more similar to the morphology we observed when annealing films with lower Li content at 900 °C, as shown in Figure 7.13. Under those con-

ditions, we also observed long-range diffusion of the Al dopant and formation of perovskite $LaAlO_3$ impurities. The phase segregation is easily observed by EDS mapping.

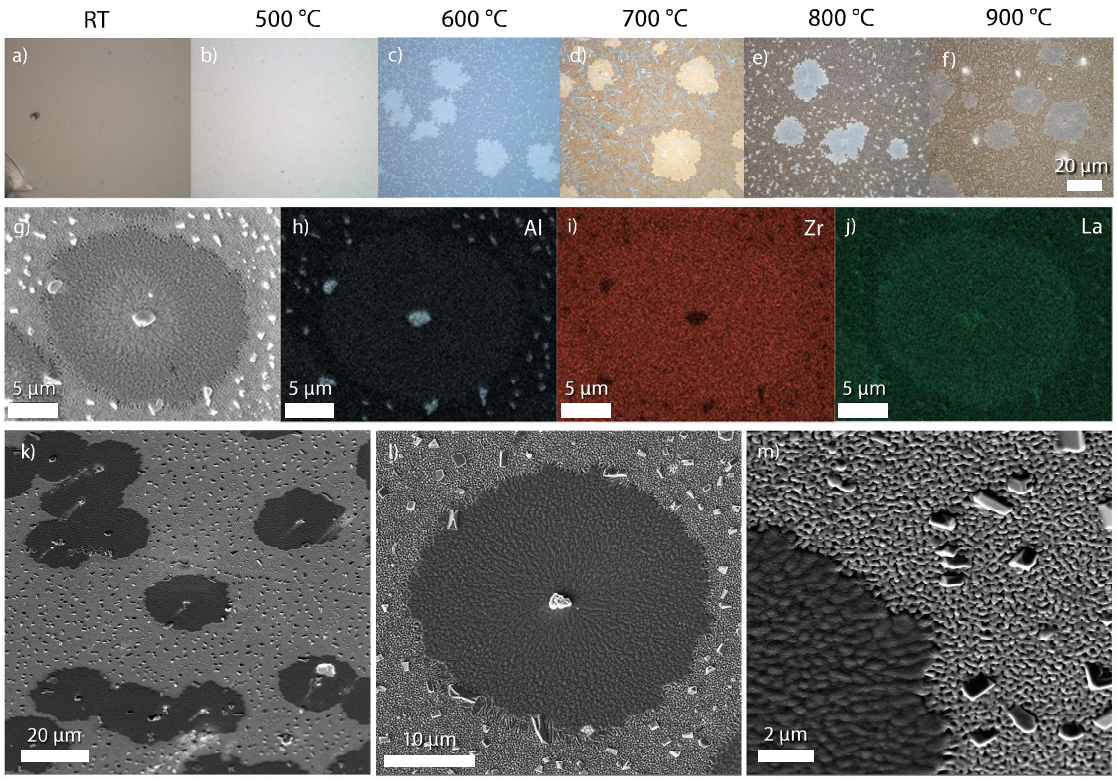

Figure 7.13: *(a-f) Low magnification optical images showing evolution of film microstructure after annealing at different temperatures. Phase segregation and clear crystalline grains appear starting at 600 °C, with islands forming. These islands remain up to 900 °C, with smaller grains appearing in both 800 °C and 900 °C. These smaller grains can be seen in the SEM images shown in (g, k-m), and in the EDS maps shown in (h-j), which show that the smaller grains are aluminum and lanthanum rich, and zirconium deficient. This matches with the perovskite $LaAlO_3$ impurity observed in XRD patterns observed under those conditions. In addition the film is no longer dense and pinhole free, but rather a porous matrix of interconnected particles as seen in (m).*

In order to improve the resulting morphology and stabilize the c-LLZO phase at RT, a layered structure was deposited. A base layer of 200 cycles and a capping layer of 600 cycles of LiO^tBu+O_3 were used to sandwich an ALD LLZO film with approximately 200% excess Li. After annealing to 650 °C, the resulting film was c-LLZO at RT, but significant impurity peaks were still observed. The morphology of this film after annealing was improved to some degree, but voids and delamination are still present. This approach, which is very simple to implement via ALD, is a promising means of compensating for Li loss

and improving the morphology of annealed LLZO thin films, however further tuning of Li_2O layers, excess Li, and annealing parameters is necessary to obtain a completely dense and continuous c-LLZO film, to enable meaningful ionic conductivity measurements and incorporation into battery architectures.

7.2 Conclusions

In summary, we have demonstrated a viable ALD process for depositing pentenary Al-LLZO films with low impurities, tunable composition, and self-limiting behavior. This is a route for depositing ultrathin, ionically conductive, electrochemically stable, conformal coatings for interfacial engineering in next-generation SSBs. In addition, measures were developed in order to compensate for extreme Li loss during annealing of the ultrathin electrolyte films. These approaches enabled the formation of high purity, pyrochlore-free, cubic garnet films, as shown by synchrotron XRD. It is the first report of ALD of LLZO, one of the most promising SSE candidates for implementation in SSBs. This could provide pathway towards 3-D all-solid-state microbatteries based on the superionic garnet phase. Future experiments on highly controlled annealing, including encapsulation of the film will be required to further optimize the morphology to enable meaningful ionic conductivity measurements, especially when placed in contact with active electrode materials.

7.3 Materials and Methods

7.3.1 Film Deposition

ALD was carried out in a glovebox-integrated Savannah S200 reactor (Veeco/Cambridge Nanotech). The ability to prevent air exposure before and after deposition reduces the possibility of reactions leading to undesirable surface reactions that alter the composition and purity of the films prior to characterization. 225 °C was used as the substrate tem-

ALD Process Conditions					
Element [subcycles per supercycle]	**Precursor [Abbreviation]**	**Source Temp. [K]**	**Pulse time [s]**	**Purge time [s]**	**Binary Growth Rate [µg cm^{-2} cycle^{-1}]**
Al [1]	trimethylaluminum [TMA]	RT	0.075	30	0.036
La [28]	lanthanum tris(diisopropylformamidinate) [LaFAMD]	423	1	45*	0.0531
Li [8]	lithium tert-butoxide [LiO^{t}Bu]	443	4	45*	0.0166
Zr [12]	tetrakis(dimethylamido)zirconium [TDMAZ]	353	0.35	45*	0.0306
O	ozone [O_3]	RT	0.1	30	-

Table 7.1: *For each precursor used, the source temperature, pulse and purge times, growth rate, and number of subcycles in each supercycle. *Carrier gas flow rate increased to 20 SCCM during purge step.*

perature for the process, as it falls within the ALD window for all of the constituent processes. A carrier gas flow of 10 SCCM ultra-high purity (UHP) Ar during pulses and 20 SCCM during purging was used. Pulse and purge times necessary for saturated growth were determined using ellipsometry and *in situ* QCM. The deposition parameters chosen for each constituent process are shown in Table 7.1. Lithium tert-butoxide (99.9%, Alfa Aesar), lanthanum tris(N,N-di-iso-propylformamidinate) (Dow Electronic Materials), tetrakis(dimethylamido)zirconium (99.99%, Sigma Aldrich), trimethylaluminum (97%, Sigma Aldrich) were used as precursors with ozone from an ozone generator (Ultratech, Inc.) as the oxidant.

7.3.2 Film Characterization

Elliipsometry was conducted with a Woollam M-2000 with a Si (100) substrate and data was fit with a Cauchy model. All annealing and XRD was done using MgO (100) substrates. Synchrotron XRD was carried out at Argonne National Laboratory at beamline 33-BM-C with 9.4 or 17.6 keV x-rays. Grazing Incidence XRD was used to reduce the signal from the single crystal substrate and amplify signal from the thin film. For the*in situ* experiments, a custom air-tight annealing chamber with an x-ray transparent beryllium dome was used. Helium was flowed at 10 SCCM during the experiment to maintain an inert atmosphere and reduce absorption of the x-ray beam. An FEI Nova Nanolab 200 was used for SEM analysis. A Nikon LV microscope was used for optical microscopy. The HRTEM images were captured using Titan 80-300 (FEI, Hillsborough, OR USA) microscope, which is operated at 300 kV and fitted with a spherical aberration corrector for the objective lens. The TEM sample was prepared by touching the lacey carbon TEM grid against the grown sample to pick up the nanowire.

A Kratos Axis Ultra was used for XPS analysis. A monochromated Al source was used with 160 eV pass energy and 700x300 μm sample area, and CasaXPS was used for peak fitting with Shirley backgrounds. ICP-OES analysis was done using a Perkin-Elmer Optima 2000 DV, using 1 mg L^{-1} yttria internal standard and a set of 7 standards. Calibration curves achieved correlation coefficients above 0.997. ICP-OES samples were prepared by fully dissolving the ALD film (>100 nm) on samples approximately 4 cm^2 in 1 mL aqua regia and then diluting to 10 mL for analysis. Three replications of each measurement were performed, and standard deviations were less than 5% of the measured concentration in all cases, and below 1% in most cases.

In-plane impedance measurements were conducted using a microprobe station inside of an Ar filled glovebox. ALD films were deposited onto Pt IDEs with a 5 μm gap (Dropsens). Each electrode had 250 fingers each 6760 μm in length. Through-plane conductivity measurements were conducted by sputtering 80 nm of Pt on Si_3N_4 coated Si, followed by the

ALD LLZO coating, and then an array of 310 μm x 310 μm Pt electrodes was sputtered on top using a shadowmask after ~5 min. air exposure. The bottom electrode was exposed by scratching through the ALD film using a diamond scribe, and contacted using a tungsten needle on a microprobe station inside an Ar glovebox. EIS was carried out using a Gamry interface 1000 potentiostat between 1 MHz and 1 Hz with a 30 mV amplitude. An equivalent circuit based on a model developed by Huggins was used. The circuit elements normally associated with grain boundaries were omitted due to the amorphous nature of the films. As expected, the capacitance of the semi-circular feature is on the order of 10^{-10} F, confirming the resistance values correspond to conduction in the bulk amorphous film. A diffusion element associated with restricted diffusion was used to model transport in the sputtered thin-film electrodes.

CHAPTER 8

Atomic Layer Deposition of Lithium Borate Solid Electrolytes

Adapted with permission from Kazyak, E.; Chen, K. H.; Davis, A. L.; Yu, S.; Sanchez, A. J.; Lasso, J.; Bielinski, A. R.; Thompson, T.; Sakamoto, J.; Siegel, D. J.; et al. Atomic Layer Deposition and First Principles Modeling of Glassy Li_3BO_3-Li_2CO_3 Electrolytes for Solid-State Li Metal Batteries. *J. Mater. Chem. A* 2018, 6 (40), 1942519437. Copyright (2018) Royal Society of Chemistry.

In Chapter 7, an ALD process was demonstrated for Al-doped LLZO, one of the most promising bulk SSEs.[18] Unfortunately, the ionic conductivity of the amorphous as-deposited films was low (~10^{-8} S cm^{-1}), and uncontrolled morphology evolution during crystallization at elevated temperatures posed additional challenges. As such, ALD films that exhibit high ionic conductivity without requiring high temperature annealing are preferable. In this regard, amorphous/glassy electrolytes are particularly attractive due to the potentially detrimental effects of grain boundaries[218,219] and intergranular Li metal propagation[128] in many crystalline materials.[58]

One promising candidate for an amorphous/glassy ALD SSE, Li_3BO_3 - Li_2CO_3 (LBCO), has been considered for bulk SSEs. First proposed more than four decades ago,[220] the glassy and crystalline phases have been studied as stand-alone SSEs,[221–224] and more recently there have been several reports that use the material as an interfacial layer or in composite electrodes.[225,226] A range of compositions have been reported, varying both Li

content and carbon content to achieve ionic conductivities as high as 10^{-5} S cm^{-1}.[227] Despite these promising properties, there have been no studies to date that use ALD to deposit LBCO.

In this work, an ALD process is demonstrated for glassy LBCO. The film growth is shown to be self-limiting and linear over a range of deposition temperatures. The structure and properties of the film is tuned by varying the deposition and post-treatment conditions, and the electrochemical performance of the films is characterized. The films exhibit higher ionic conductivity than any previously reported ALD film ($>10^{-6}$ S cm^{-1} at 25°C) with a high ionic transference number of above 0.9999, and are shown to be stable over a wide range of potentials relevant for SSBs, and the electrochemical stability is also correlated with DFT calculations of the phase stability and band gap. Finally, optimized ALD LBCO films are demonstrated as stand-alone SSEs in thin-film batteries with Li metal electrodes. These cells display stable cycling and exemplify the promise of this process for application both as an electrolyte and as an interfacial layer in LMSSBs.

8.1 Results and Discussion

8.1.1 Process Development

The first step in development of an ALD process for LBCO films was identification of precursors. LiOtBu was selected as the Li source due to its demonstrated use in other ALD processes.[18,181,187,203] Moreover, by varying the ALD conditions, carbon incorporation into the films can be controlled, which is leveraged in this study to synthesize LBCO films with tunable compositions. Ozone was used as the oxidant[18] to avoid any exposure to moisture, as many battery materials are moisture sensitive.

An obvious choice of boron precursor does not exist. There have been few reports of ALD of binary boron oxide, and its extreme air-reactivity complicates characterization.[228–231] There are two reports of using triisopropylborate (TIB), $[(CH_3)_2CHO]_3B$ as a

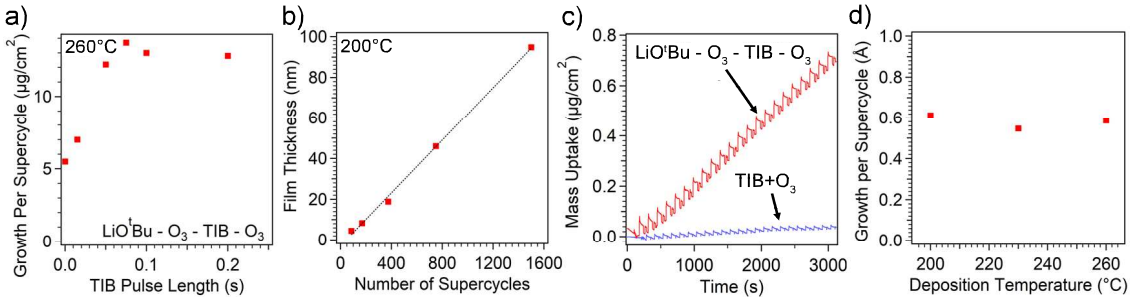

Figure 8.1: *Characterization of ALD film growth with in situ QCM (a and c) and spectroscopic ellipsometry (b and d) showing (a) saturation of growth rate with increasing TIB pulse time, (b) linearly increasing film thickness with number of supercycles, (c) dramatically enhanced growth of the LBCO ALD process compared to the binary boron oxide process, and (d) consistent growth rate across a range of deposition temperatures.*

boron source in a ternary B-doped ZnO film, despite the binary process resulting in little to no film growth.[232,233] Therefore, in this study, TIB was selected, as it also has favorable physical properties including being a non-pyrophoric liquid with a vapor pressure of 13 Torr at 25°C.

The LBCO ALD process was first tested with a 1:1 ratio of LiO^{t}Bu-O$_3$ subcycles to TIB-O$_3$ subcycles. As shown in Figure 8.1a, by adding TIB subcyles to an optimized LiO^{t}Bu-O$_3$ process,[18] pulse saturation was observed using an *in situ* QCM. Linear growth with a growth rate of 0.65 Åcycle^{-1} was measured by spectroscopic ellipsometry (Figure 8.1b), indicating a well-behaved ALD process. The binary TIB-O$_3$ process was also tested, but very little growth was observed by QCM (<0.1 Åcycle^{-1}, Figure 8.1c), consistent with the previous report that used water and O$_2$ plasma as oxidants. Substrate temperatures between 200 °C and 260 °C yielded a relatively consistent growth rate (Figure 8.1d).

8.1.2 Film Characterization

Further characterization of the growth characteristics of the LBCO ALD process was carried out on etched Si trenches. 50 nm of ZnO was deposited via ALD to provide a conductive surface to minimize charging and increase contrast between the LBCO film and the substrate. As shown in Figure 8.2, the deposited film has uniform thickness along the full

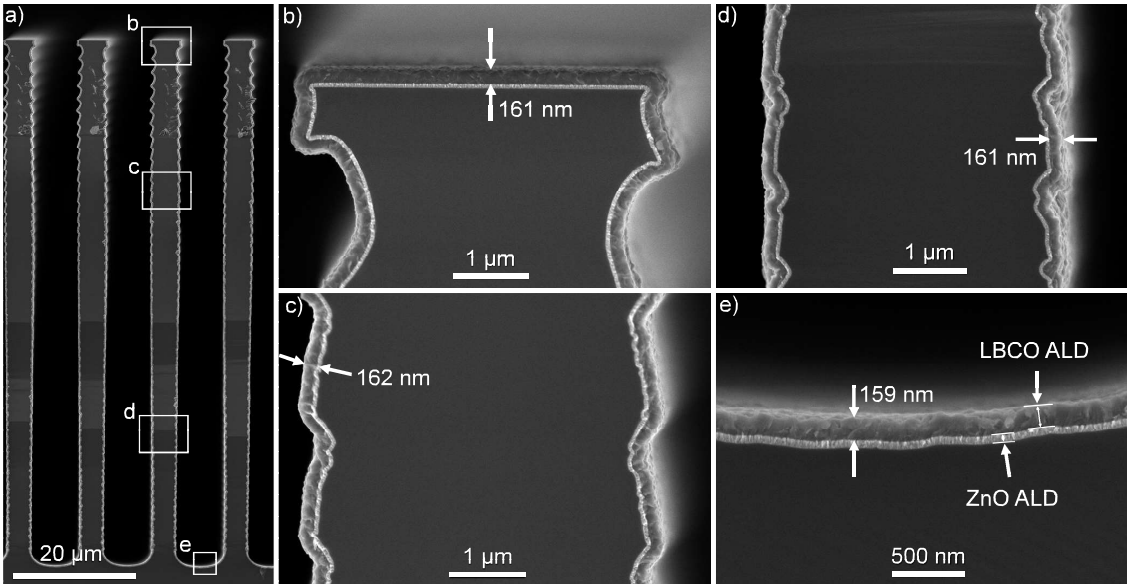

Figure 8.2: *SEM images of etched Si trenches with ALD ZnO (to reduce charging and increase contrast) and LBCO showing conformality. Full trench shown in (a) with locations along height of trench highlighted and shown in (be) with measured thicknesses.*

height of the trenches. The thickness variation was measured as 1.2% along the trench with an aspect ratio of 13. This capability to uniformly coat high aspect ratios is unique to ALD, highlighting the potential of this process for 3-D battery architectures. The ALD film also conformally coats the contours and texture on the sidewalls of the trenches, as it is not a line-of-sight process. This capability could enable the use of less ordered 3-D architectures while maintaining a uniform pinhole-free electrolyte film throughout the structure.

Once the growth conditions had been optimized, the resulting film composition was characterized by XPS. The films were transferred from an Ar filled glovebox to the UHV XPS chamber without air-exposure. As shown in Figure 8.3a, the films obtained have a nearly constant Li:B ratio of 3 across the temperature range. The carbon content, however, increases at lower deposition temperatures (Figure 8.3c). This is consistent with a previous study of binary processes with LiO^tBu where increasing Li_2CO_3 character was observed at lower deposition temperatures with O_2 plasma.[203] The ability to tune the carbon content relative to boron is of particular interest for achieving high ionic conductivity, as mixtures of Li_2CO_3 and Li_3BO_3 have been shown to have significantly higher ionic conductivity

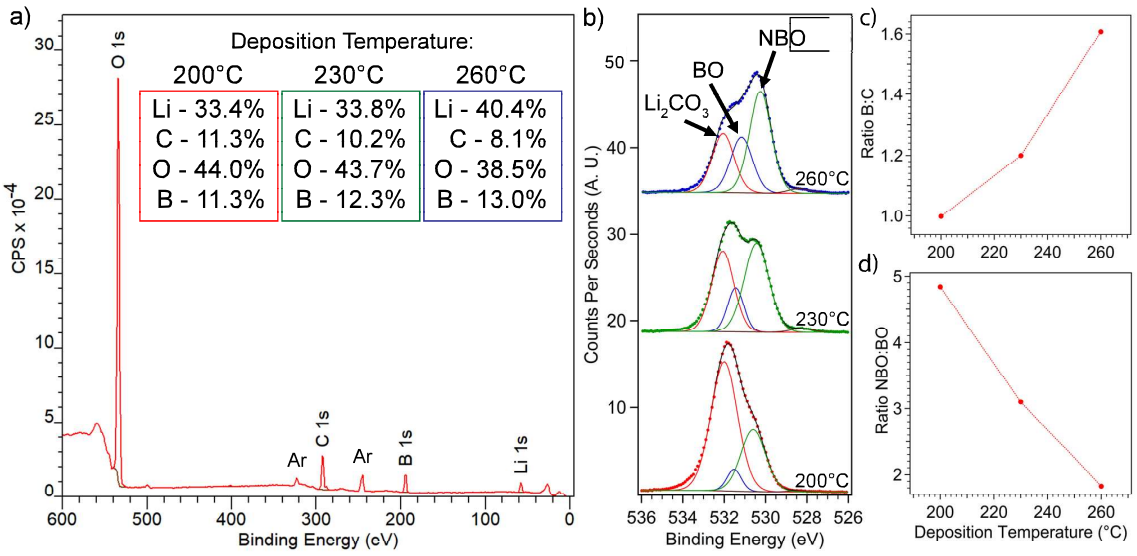

Figure 8.3: *(a) XPS survey scan for 200 °C deposition temperature with insets showing calculated compositions for each as-deposited film at the three deposition temperatures. (b) XPS O 1s core scan showing changes in oxygen bonding environment with deposition temperature. (c) Plot of the ratio of boron to carbon and (d) the ratio of NBO to BO with deposition temperature. All data shown are after 15 min. of sputtering with Ar ions to remove surface layers.*

than either of the individual ternary compounds.[220]

The structure of heavily-lithiated borate glasses has been studied previously by both experiment and computation.[221,234] Briefly, as Li_2O is added to the system, the coordination environment of the boron atoms is altered, resulting in a depolymerization in which structures with bridging oxygen (BO) groups are converted to structures with non-bridging oxygen (NBO). This has been correlated with an increase in Li conductivity, owing to the more open structure and the possible percolation of NBO-rich regions that facilitate faster ion diffusion through the glassy network.[234] In the current study, these phenomena are convoluted with the structural differences that arise due to the presence of Li_2CO_3 in the film. As a result, further analysis of the ALD LBCO films is required to extract the differences in oxygen bonding, particularly the oxygen associated with boron in the glassy structure.

To quantify the presence of NBO in the ALD LBCO films, high-resolution XPS core scans were performed on the O 1s peak. Consistent with prior reports,[16,235] 4 different species can be assigned in Figure 8.3b. First, Li_2CO_3 is assigned to the highest binding

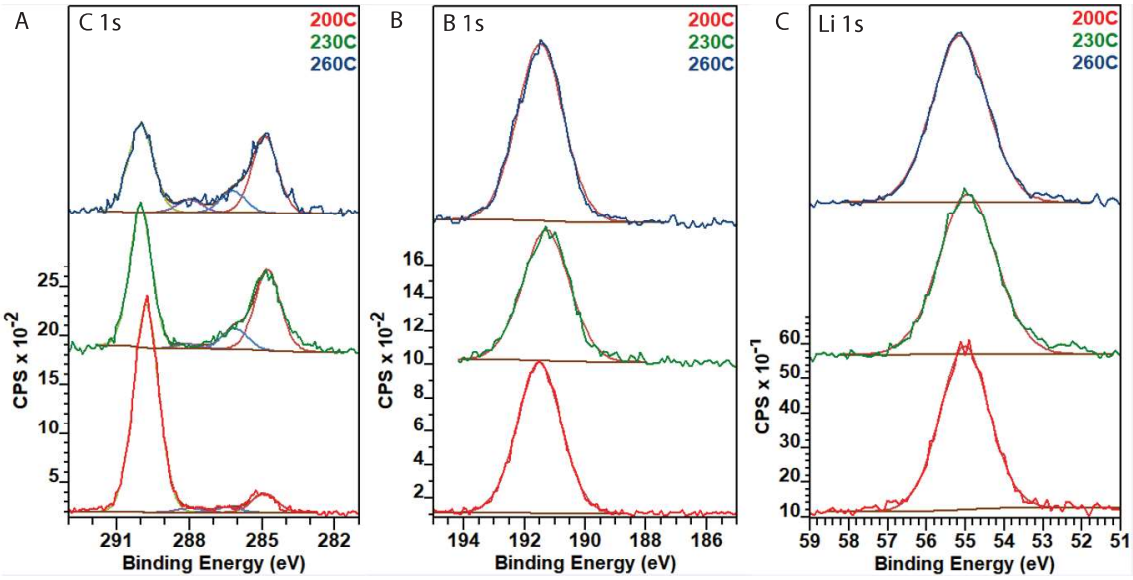

Figure 8.4: *XPS C 1s (A), B 1s (B), and Li 1s (C) core scans for the three deposition temperatures. The C 1s cores were used to determine the relative amount of Li_2CO_3 in the film for deconvolution of the Li_2CO_3 and BO in the O 1s core scans shown in Figure 8.3.*

energy species at 532 eV. The smallest component at the lowest binding energy (528.5 eV) is assigned to Li_2O, and is present only in trace amounts (<2%) in these films. This leaves the intermediate binding energy peaks that are associated with Li_3BO_3 species. From a previous study of the structure of lithium borate via XPS, the higher binding energy species at 531.4 eV is BO (solid blue line), and the lower binding energy peak at 530.4 eV is NBO (solid green line).[235] As shown in Figure 8.4, no significant differences were observed in the Li 1s or B 1s core scans.

Due to the proximity of the BO peak to the Li_2CO_3, the C 1s core scans and survey scans were used to validate the deconvolution of the two components (Figure 8.4, Section 8.3). Analysis of the fitted O 1s components reveals that the ratio of NBO:BO decreases as deposition temperature increases (Figure 8.3d). The tendency to form more NBO at higher temperatures was reported previously based on molecular dynamics calculations.[234] In this case however, it appears that the differences in Li_2CO_3 content have a stronger influence on the oxygen bonding environment than the deposition temperature alone. As NBO species result in higher ionic conductivity, the ability to tune NBO content by varying

the ALD processing conditions is of great interest. This observed trend in oxygen bonding environment will be correlated with ionic conductivity in the following section.

8.1.3 Ionic Conductivity

To measure the ionic conductivity of the films and evaluate their electrochemical stability, several measurement geometries were used. First, IDEs with 5 μm spacing were used for EIS. This in-plane configuration, with two blocking electrodes in the same plane eliminates the need for subsequent deposition of a top electrode, and eliminates the possibility of a short-circuit or an artificially high conductivity due to a pinhole or thinner region in the film. The geometry of these IDEs and other sample configurations discussed below, including TP measurements on gold substrates, are detailed in Figure 8.5. Both blocking and non-blocking electrode configurations were used to gain a more complete understanding of the film properties.

When studying the temperature-dependent conductivity of the LBCO ALD films, an irreversible increase in conductivity was observed upon heating of the sample. This effect appears as a non-linearity in the heating curve in the Arrhenius plot (Figure 8.6a). Upon cooling, the conductivity at 30 °C returns to a higher value than the initial point. Similar behavior was reported previously in sputtered lithium borate films.[227] In the sample shown, this occurs below 100 °C, and very little further increase is observed up to 300 °C. In some samples, a more dramatic increase was observed between 200°C and 300°C. A complete mechanistic understanding of this phenomenon is beyond the scope of this work; however, we attribute this behavior to structural changes in the film during annealing. As discussed above, elevated temperatures have previously been shown to result in an increase in NBO, which leads to higher ionic conductivities. We have not observed any crystalline diffraction peaks in the film after this procedure in XRD (Figure 8.7), suggesting the film remains amorphous/glassy, however due to the low x-ray scattering cross section of the thin film, we cannot eliminate the possibility of some local ordering.

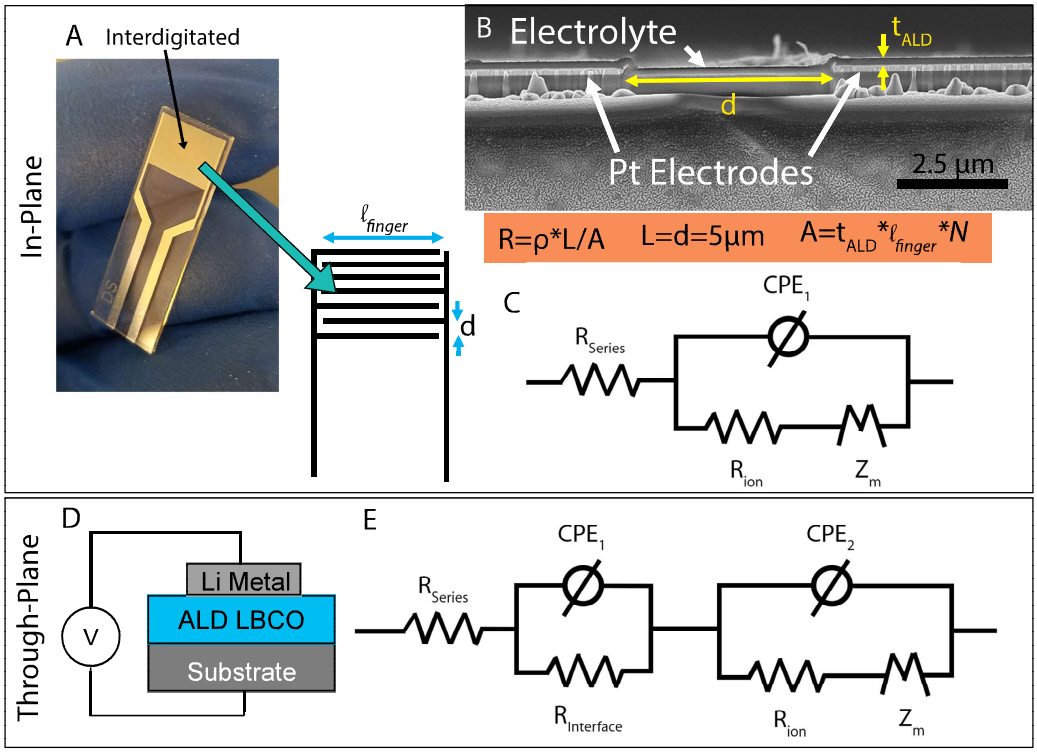

Figure 8.5: *Image and schematic (A) and SEM image and equations (B) detailing how the Pt IDEs were used to measure ionic conductivity in an in-plane cell architecture, along with the equivalent circuit models used to fit the EIS spectra (C,D)*

Because of the improved performance of the film after annealing, all of the subsequent electrochemical data reported, including conductivity, stability, and cycling performance is after the films were annealed to 300 °C with a hold time of 5 min. The ionic conductivity as a function of deposition temperature is shown in Figure 8.6b. The 200 °C deposition temperature yielded the highest conductivity films. This is the film with the highest amount of carbon (approximately a 1:1 B:C ratio), and is the film in which the carbon has the highest proportion of Li_2CO_3 character (Figure 8.4). The incorporation of carbon is desirable owing to its role in increasing ionic conductivity in lithium borate (LBO) glasses. This is consistent with previous measurements of bulk $Li_{2+x}C_{1-x}B_xO_3$, wherein a maximum ionic conductivity was also observed at a 1:1 B:C ratio (x=0.5).[220] Lower deposition temperatures were not tested to avoid potential condensation in the LiO^tBu delivery lines, as the precursor must be heated to 170 °C for sufficient vapor pressure.

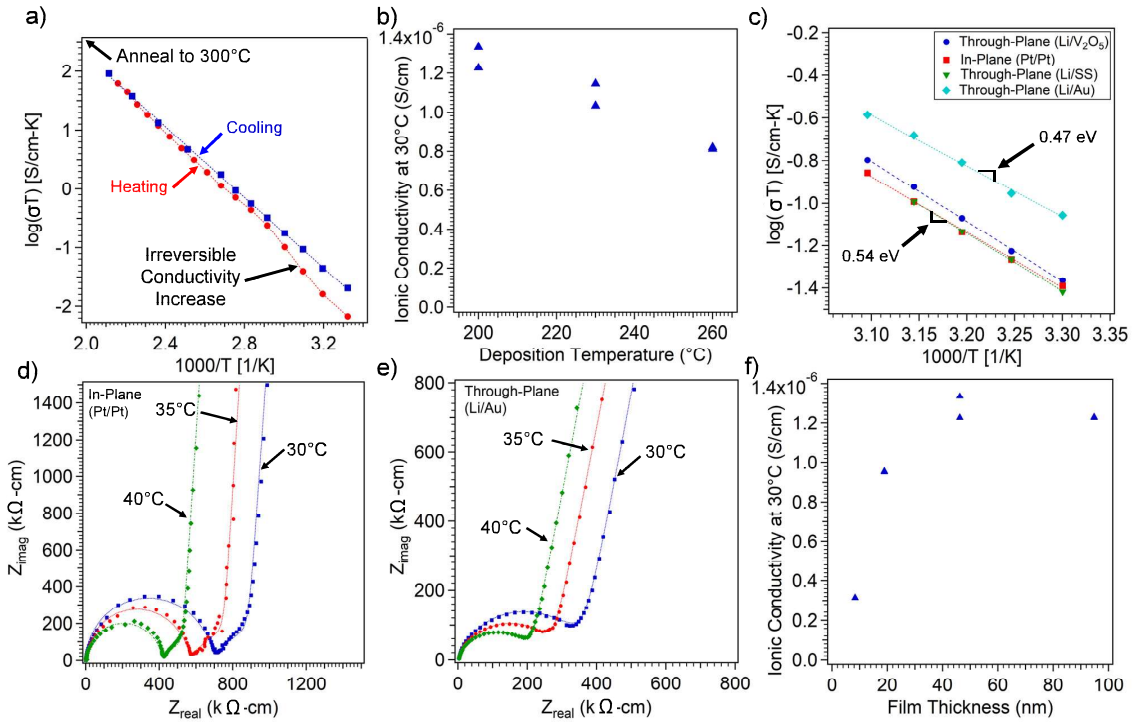

Figure 8.6: *(a) Arrhenius plot for IDE sample with 44 nm film deposited at 260 °C, showing irreversible increase in conductivity upon annealing in Ar glovebox. (b) Plot showing ionic conductivity as a function of deposition temperature. (c) Arrhenius plot for each of the measurement configurations for the 95 nm film deposited at 200 °C. Nyquist plots for 95 nm film deposited at 200 °C for 30, 35, and 40 °C for (d) Pt IDE and (e) TP Li vs. Au. Experimental data are shown by the point markers and the equivalent circuit fits are shown by the dotted lines. (f) Plot showing the thickness dependence of the ionic conductivity for films deposited at 200 °C, two data points are shown for each thickness, but most fall on top of each other and are not visible.*

The Nyquist plots for films deposited at 200 °C (after annealing to 300 °C) are shown in Figure 8.6d-e for both in-plane IDEs (using Pt-Pt blocking electrodes) and TP configurations (using Au-Li blocking-nonblocking electrodes). The equivalent circuits used to fit each of the configurations are shown in Figure 8.5. The general shape is quite similar between all of the conditions, with a semi-circular feature at high frequency and a diffusion tail at low frequencies. The abrupt slope change is due to the thin nature of the electrolyte, and is captured by a modified restricted diffusion element.[18]

The fitted values for the ionic conductivity for each measurement configuration (TP and IDE) are shown in Figure 8.6c. The TP-Li/Au cells have an activation energy of 0.47 eV atom^{-1} and an ionic conductivity of 2.9*10^{-6} S cm^{-1} at 30 °C 2.23*10^{-6} S cm^{-1} at 25 °C).

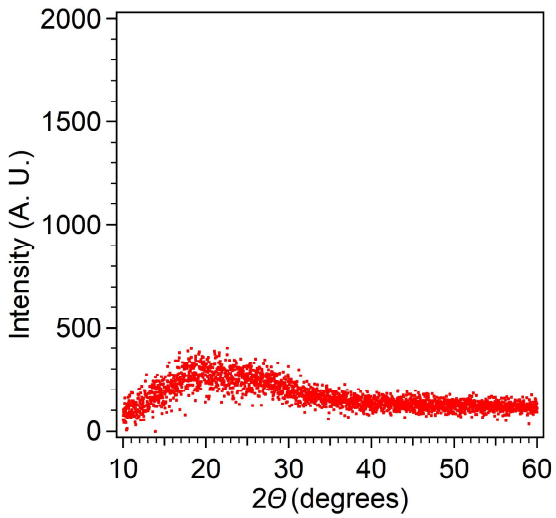

Figure 8.7: *XRD of as-deposited LBCO film at 200 °C on glass substrate with no visible diffraction peaks, indicating an amorphous or glassy structure.*

The TP-Li/SS, TP-Li/V_2O_5, and Pt IDE all give very similar results, with a conductivity of 1.2-1.4*10^{-6} S cm^{-1} at 30 °C and an activation energy of 0.54-0.56 eV $atom^{-1}$ (1*10^{-6} S cm^{-1} at 25 °C). The TP-Li/Au cells gave consistently higher ionic conductivities than the other 3 configurations. We hypothesize that this is a result of improved interfacial contact between the SSE and the current collector. In other SSE systems, Au is used as an interfacial wetting layer to reduce interfacial impedance.[117] In this case, because the films are so thin and the interfacial impedance cannot be deconvoluted from the bulk by EIS (only one semicircle is visible), the effect is a drop in total impedance of the cell. This is likely a more accurate estimate of the bulk conductivity of the cells, as the interfaces play a smaller role.

The thickness dependence of the conductivity was studied by depositing films of 4 different thicknesses on the Pt-IDEs. As shown in Figure 8.6f, while the thinner films exhibited lower conductivity, the 46 nm and 95 nm thick films had very similar conductivities, suggesting that any thickness dependence of conductivity has plateaued by 46 nm. To put the ionic conductivity of this LBCO ALD film in the context of previous work, the progression of ALD SSE development over the past 5 years is shown in Figure 8.8. The ionic conductivities of the ALD LBCO films presented here are significantly higher than

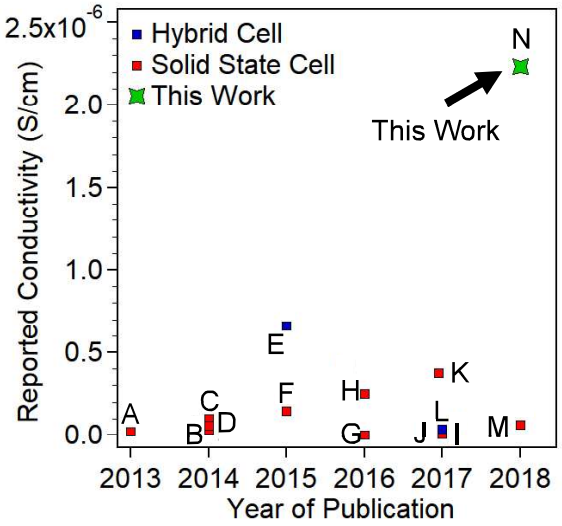

Figure 8.8: *Plot showing reported ionic conductivity values for ALD films since the first report in 2013. Labels correspond with Table 8.1.*

any previously reported ALD film.

The conductivity is comparable to the state-of-the-art sputtered LiPON, which is often reported at approximately $2*10^{-6}$ S cm^{-1}.[236] With this level of conductivity and the ability to fabricate cells with electrolytes less than 100 nm thick, the ASR is $<5\ \Omega\ cm^2$. This is lower than the interfacial impedance of conventional Li-ion batteries (typically $10\ \Omega\ cm^2$), and thus will not be the limiting factor in most applications. Comparing this film to bulk SSB materials, this electrolyte would have the same ASR as a 50 µm thick SSE with an ionic conductivity of 10^{-3} S cm^{-1}, which is difficult to achieve with traditional processing due to challenges in manufacturing and handling of thin ceramic materials. Figure 8.9 puts the ALD LBCO film ASR in the context of other state-of-the-art SSE materials.

8.1.4 Electrochemical Stability

In addition to high ionic conductivity, an ideal SSE would be stable under operating conditions against both the anode and the cathode. In order to test the electrochemical stability of the ALD electrolyte, several experiments were performed. First, the impedance of the electrolyte film was measured over time after evaporation of a Li metal electrode on the sur-

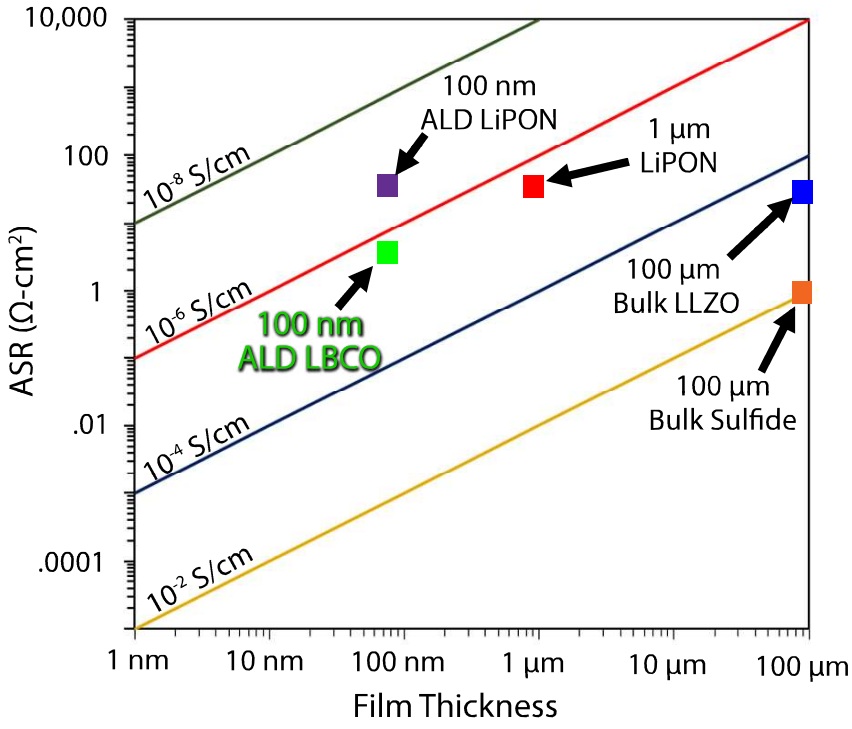

Figure 8.9: *Plot of the ASR vs. film thickness showing ionic conductivity iso-lines, with several common and state-of-the-art SSE materials plotted for context.*

face. Next, cyclic voltammetry (CV) was performed on a blocking/non-blocking electrode cell with a Li metal top electrode to examine the current response to an applied voltage. Finally, staircase potentiostatic electrochemical impedance spectroscopy (SPEIS) was used to measure both ionic and electronic conductivity as a function of applied potential.

As shown in Figure 8.10a, the cell impedance did not change measurably over 25 days in contact with Li metal. Due to the period of several hours needed to cool and vent the Li evaporator and then begin the test, it is difficult to determine whether there is an initial reaction or not; however, if a reaction does take place, it appears to passivate or become kinetically limited in the initial period of exposure to the Li metal. Regardless of mechanism, the electrolyte remains an ionic conductor with an ionic transference number of ~1 after several weeks in contact with Li metal.

The CV scan at 0.1 mV s^{-1} shown in Figure 8.10d for a Li vs. SS (non-blocking vs. blocking) cell shows no peaks in the range between 0 and 3.8 volts vs. an evaporated

Reported ALD Solid Electrolytes					
Label	Material System	Ionic Conductivity [S cm^{-1}]	Measurement Temperature [K]	Activation Energy [eV/atom]	Reference
A	LiTaO	$2x10^{-8}$	299	0.55	[237]
B	LPO	$3.3x10^{-8}$	299	0.51	[181]
C	LiAlSiO	$1.0x10^{-7}$	298	0.84	[180]
D	LiAlO	$5.6x10^{-8}$	298	0.56	[95]
E	LiPON*	$6.6x10^{-7}$	298	?*	[177]
F	LiPON	$1.5x10^{-7}$	298	0.55	[179]
G	LiAlO	$1.0x10^{-10}$	298	0.8	[182]
H	LiAlS	$2.5x10^{-7}$	298	0.48	[183]
I	LiSiO	$5.7x10^{-9}$	303	0.8	[190]
J	LiAlLaZrO	$1.0x10^{-8}$	298	0.63	[18]
K	LiPON	$3.7x10^{-7}$	298	0.55	[192]
L	LiAlF*	$3.5x10^{-8}$	298	?*	[186]
M	LiNbO	$6.4x10^{-8}$	303	0.62	[184]
N	LBCO	$2.2x10^{-6}$	298	0.47	[19]

Table 8.1: *Table of reported SSEs deposited by ALD and their properties, corresponding with the ionic conductivity values plotted in Figure 8.8.*

Li counter electrode. This indicates that the ALD electrolyte is stable within this voltage window. This window was chosen as it is similar to the voltage window used for the full cell cycling below. There is a slight deviation as the voltage goes below ~0.2 volts, but the current is still extremely small. The CV to -0.05 volts shown in Figure 8.10e demonstrates the ability to plate and subsequently strip Li metal in an all-solid-state cell using this electrolyte. The ratio of anodic to cathodic peak areas is a measure of coulombic efficiency, and in this case the ratio was ~99%, indicating a reversible process.

To further characterize the electrochemical stability window of the LBCO, SPEIS was used. A schematic and description of this measurement protocol are included in 8.3. This technique allows measurement of both ionic and electronic conductivity as a function of applied potential. Using these values, the ionic transference number is calculated. The results for the ALD LBCO deposited at 200 °C, shown in Figure 8.10c, show very little change in the electronic conductivity as a function of applied potential. The currents measured were very close to the noise floor of the instrument, so the electronic conductivity may be

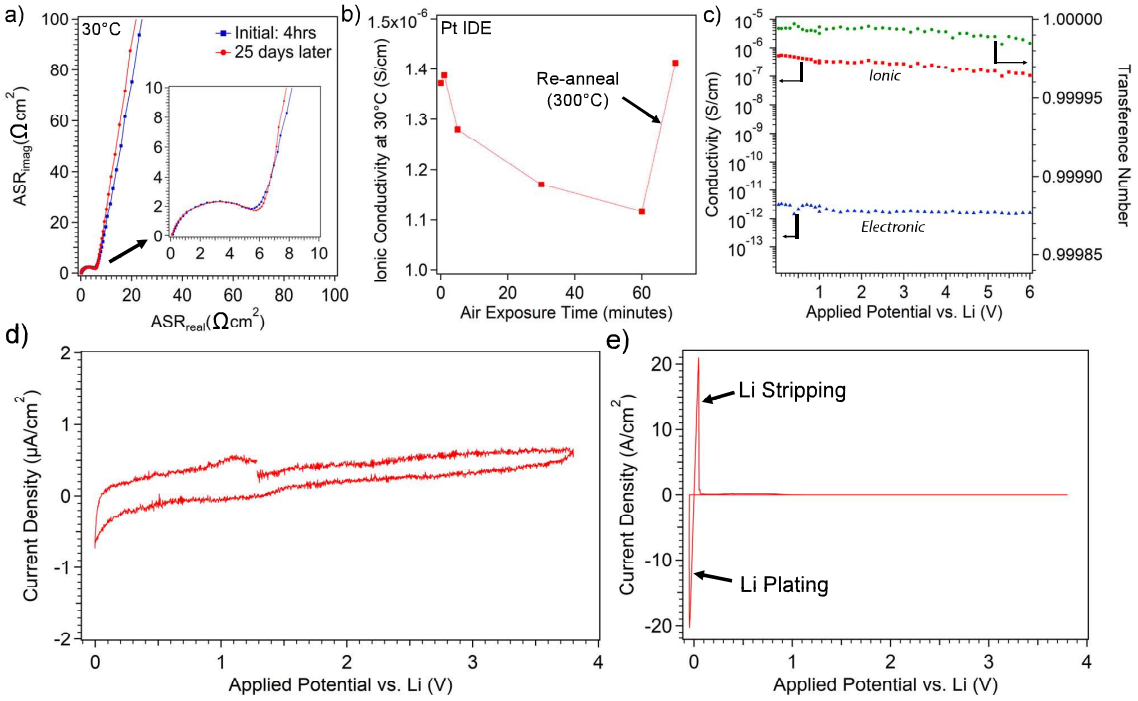

Figure 8.10: *(a) EIS over time after deposition of a Li metal electrode. (b) Ionic conductivity of an IDE exposed to air and then re-annealed. (c) SPEIS results showing plot of ionic and electronic conductivity as a function of applied potential along with the ionic transference number. (d) CV scan at 0.1 mV s^{-1} showing stability of LBCO in voltage window between 0 and 3.8 volts. (e) Same cell as (b) swept to -0.05 volts showing Li plating and stripping at the blocking stainless steel electrode.*

even lower. The ionic conductivity increased slightly as the potential was decreased, and decreased as the potential increased, particularly above 4 volts. Despite this decrease, the value of the ionic conductivity remained above 10^{-7} S cm^{-1} out to 6 volts, and the transference number remained above 0.99998. This suggests that the electrolyte could potentially be used with high voltage electrode materials in addition to Li metal anodes.

To gain further insight into the stability of crystalline LBO, amorphous LBCO, and crystalline Li_2CO_3, phase diagram calculations were performed by combining energetics from the present first-principles calculations with data from the Materials Project.[238,239] The results of these calculations are not shown here, but are included in the resulting publication.[19] The results predict that LBO and LBCO are not thermodynamically stable to 0V vs. Li metal, and thus the measured stability may be due to a kinetic stability or the formation of a passivation layer. The bandgaps of LBO and LBCO were also calculated, and predict

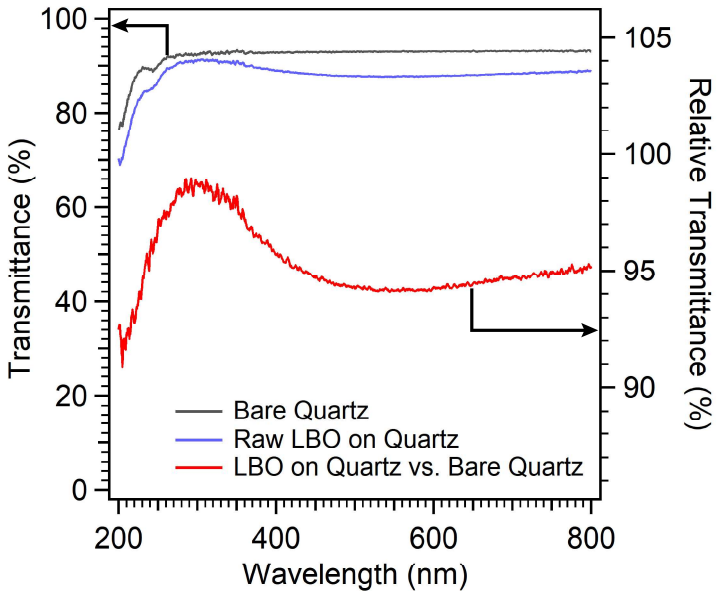

Figure 8.11: *UV-vis spectroscopy of 100 nm 200 °C as-deposited LBCO ALD film on a quartz substrate. Relative transmittance above 90% throughout the measured range is an indication of a large optical bandgap, consistent with the values predicted by DFT calculations.*

wide bandgaps of above 6 volts. The predicted wide band gap is consistent with experimentally measured ultraviolet (UV)-visible spectroscopy in Figure 8.11, which shows low absorbance over the entire visible range.

8.1.5 Full Cell Fabrication and Cycling

To demonstrate the feasibility of using ALD LBCO as a SSE in a SSB, an ALD-deposited V_2O_5 cathode was deposited prior to the LBCO deposition. Cells with the architecture shown in Figure 8.12 were fabricated with a 14.5 nm thick amorphous V_2O_5 and a 95 nm LBCO electrolyte. Amorphous ALD V_2O_5 has previously been demonstrated as a cathode material.[240] Evaporated Li metal was used as an anode. These thin-film batteries were tested at varying rates with constant current charging between 1.6 and 3.7 volts.

The cell architecture is shown in the SEM image of a FIB cross-section in Figure 8.12a, and schematically in the inset of Figure 8.12d. The charge and discharge curves at different rates are shown in Figure 8.12b, and the corresponding plot of discharge capacity vs.

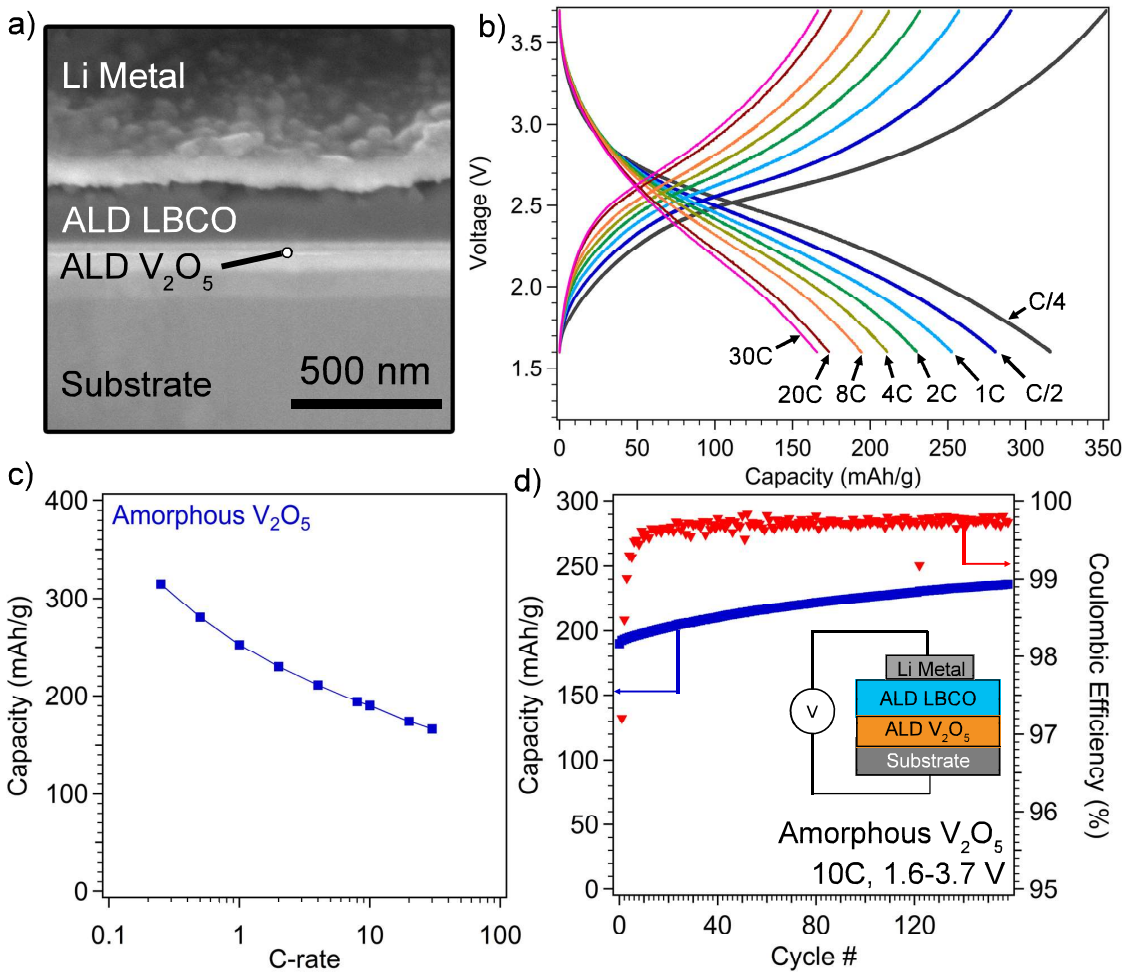

Figure 8.12: *(a) SEM image of FIB cross-section of full cell stack used in electrochemical measurements. (b) Charge and discharge curves at different rates for full cells, with schematic inset of cell architecture. (c) Discharge capacity at varying rates corresponding for crystalline and amorphous ALD V_2O_5 cathode films (d) plot of discharge capacity and coulombic efficiency for cell cycled at 10C.*

charging rate is shown in Figure 8.12c. The cells demonstrate high rate capability, suggesting their use in fast-charging thin-film architectures. Another cell was cycled at 10C for over 150 cycles, and the capacity was still increasing at the end of the experiment as shown in Figure 8.12d. This behavior could be due to improved contact at interfaces within the cell or improved transport within the cathode upon cycling. The demonstration of stable cycling in a Li metal thin-film battery is a critical milestone, illustrating that the electrochemical stability of the LBCO electrolyte extends to dynamic cycling conditions. Overall,

these results demonstrates the potential of ALD LBCO SSEs, both in 3-D thin-film SSB architectures and as interfacial layers in bulk SSEs against Li metal.

8.2 Conclusions

This work presents significant advances in several key areas of work relevant to SSBs. First, a new ALD process was developed for fabrication of conformal thin films of the amorphous SSE lithium borate-carbonate, or LBCO. The degree of Li_2CO_3 incorporation can be tuned by adjusting deposition temperature, which enables control over ionic transport properties. The role of carbon in increasing the conductivity has been elucidated both by first principles calculations and experiments. Increased Li_2CO_3 content increases the ionic mobility of the Li and O in the structure, increasing diffusivity (and ionic conductivity). The films can be grown on high-aspect-ratio 3-D structures with excellent uniformity, opening the door to 3-D architectures for thin-film batteries.

Second, these films exhibited significantly higher ionic conductivity than any previously reported ALD film, while remaining electrical insulators even in very thin films ($<$100 nm). Ionic conductivities up to $2.23*10^{-6}$ S cm^{-1} at 298K were attained, making this material comparable or even superior to sputtered LiPON in terms of ionic transport. This high conductivity coupled with the ability to fabricate cells with $<$100 nm thick electrolytes means that ASR values of <5 Ω cm^2 can be achieved.

Third, the LBCO films were shown to be stable against anode and cathode materials, and proof of concept devices were fabricated that demonstrate the potential of this material for thin-film battery manufacturing. The ionic transport number of the film remained approximately 1 from 0-6 volts, and the impedance behavior was stable against a Li metal electrode. In full cells containing Li metal anodes, the ionic conductivity remained high, and excellent cycling stability was observed. The use of computational modelling in this work shows that the wide band gap and stability window in addition to a high diffusivity

were indicators of a promising material for application as an electrolyte or interfacial layer. This approach could be used more generally to rapidly screen other material systems to identify promising materials to explore experimentally.

These advances have implications not only for thin-film batteries, as demonstrated here, but could be relevant in next-generation bulk SSBs as interfacial layers and/or protective coatings. The ability to conformally coat a material with high ionic conductivity and good electrochemical stability could enable new approaches, architectures, and manufacturing strategies for high performance SSBs.

8.3 Materials and Methods

8.3.1 Film Deposition

LBCO films were deposited in a Savannah S200 (Ultratech/Cambridge Nanotech, Inc.) integrated with an Ar-filled glovebox. The ability to prevent air-exposure before and after deposition reduces the possibility of reactions leading to undesirable surface reactions that alter the composition and purity of the films prior to characterization. Lithium tert-butoxide (97%, Sigma Aldrich) was heated to 170 °C in a stainless steel cylinder and pulse time of 4.0 s, exposure time of 2.0 s, and purge time of 60 s was used. triisopropyl borate (98%, Sigma Aldrich) was kept at ambient temperature in a stainless steel cylinder and a pulse time of 0.15 s, exposure time of 2.0 s, and purge time of 20 s was used. A carrier gas flow rate of 20 SCCM UHP Ar was used during purging of the LiO^tBu, 10 SCCM during purging of the TIB and ozone, and 5 SCCM during precursor exposure. Ozone was produced by a UV ozone generator (Ultratech, Inc.) from UHP O_2. Substrate temperatures between 200 °C and 260 °C were used. A lid-integrated *in situ* QCM was used to monitor film growth.

8.3.2 Film Characterization

Ellipsometry was conducted with a Woollam M-2000 with a Si (100) substrate and data were fit with a Cauchy model. An FEI Helios Nanolab 650 SEM/FIB was used for SEM analysis. The etched Si trenches were first Piranha cleaned to remove contaminants. A 50 nm ZnO film was deposited via ALD to provide a conductive surface to minimize charging and increase contrast between the LBCO film and the substrate. Following the LBCO deposition, the structure was cleaved perpendicular to the trenches to reveal the cross-section.

A Kratos Axis Ultra was used for XPS analysis. A monochromated Al source was used. For survey scans, a 160 eV pass energy and 700x300 μm sample area. An Ar ion source with 4 kV accelerating voltage and 200 μA extractor current was used for sputtering off any surface film. For high resolution core scans, a pass energy of 20 eV was used, and the C-C peak at 284.8 eV was used for energy calibration. CasaXPS was used for peak fitting with Shirley backgrounds.

Due to the proximity of the BO peak to the Li_2CO_3, the C 1s core scans and survey scans were used to further deconvolute the two components. First, the C 1s core scans were fitted with the same 4 components used in our previous work[cite] (Figure 8.4), and the relative amount of carbon in Li_2CO_3 to total carbon was extracted. Next, assuming a 3:1 ratio of oxygen to carbon as in Li_2CO_3 for charge neutrality and the overall compositions shown in Figure 8.3a, the percentage of oxygen associated with Li_2CO_3 can be calculated. This value was then checked against the components fit to the O1s core scans. For all three deposition temperatures, the Li_2CO_3 peak area in the O 1s was within 2% of the value calculated from the C 1s and survey scans. This agreement acts as a check of the peak deconvolution in the O 1s core scans, enabling higher confidence in the following analyses.

8.3.3 Computational Modeling

A detailed description of the computational methods used by our collaborators is available in the publication.[19]

8.3.4 Electrochemical Characterization

8.3.4.1 Ionic Conductivity

In-plane impedance measurements were conducted using a microprobe station inside of an Ar filled glovebox. ALD films were deposited onto Pt IDEs with a 5 μm gap (Dropsens). Each electrode had 250 fingers each 6750 μm in length. Through-plane conductivity measurements were conducted by depositing the electrolyte on a conductive substrate (Au, SS) and then evaporating Li metal through a shadowmask to define the top electrode. A Nexdep evaporator (Angstrom Engineering, Inc.) with a Molybdenum crucible was used to deposit a 2 μm Li film. The bottom electrode was exposed by removing the ALD film using 2000 grit sandpaper, and each electrode was contacted using a tungsten needle on a microprobe station (Signatone) inside an Ar glovebox. Potentiostatic EIS was carried out using an SP-200 potentiostat (Bio-logic) between 7 MHz and 0.1 Hz with a 10 mV amplitude. Temperature was controlled and monitored with a Watlow EZ-zone controller connected to a Watlow ultramic heater, and temperatures were allowed to stabilize for 5 min. prior to measurement. Not all samples were directly measured at 25 °C due to the need for active cooling of the glovebox atmosphere and long cooling times necessary to reach that temperature after heating. For samples for which this was not done, the activation energy was used to extrapolate down to 25 °C. Ionic conductivity values were calculated from resistance values fitted to the equivalent circuits shown in Figure 8.5.

8.3.4.2 Electrochemical Stability

Electrochemical stability was tested in the TP-Li/SS cells by several methods. First EIS was conducted periodically to monitor changes in the impedance of the film. Second, CV was performed with a scan rate of 0.1 mV s^{-1} to observe the flow of current at a range of applied potentials. Finally, SPEIS was performed in both the positive and negative scan directions from V_{oc}. Since these cells have an open circuit voltage of more than 1 volt, one cell is used for the positive step direction, and another is used for the negative step direction. In this method, 20 a DC bias is applied to the cell for a period of time that allows the current to stabilize, in this case 600 s was used. A measure of the DC conductivity was calculated from the average current in the final 100 s. Subsequently, potentiostatic EIS is performed about that DC bias potential, and fitting to an equivalent circuit is used to extract an ionic conductivity. A schematic of the applied voltage and current response for this technique is shown in Figure 8.13. This technique provides both ionic and electronic conductivity as a function of applied potential. This provides a more complete picture of the stability of a SSE material than CV.

8.3.4.3 Full Cell Fabrication

Full cells were fabricated by depositing V_2O_5 via ALD. vanadium oxytriisopropoxide (VTIP) and water were used as precursors. The deposition was performed in a custom lab-built ALD tool with an Ar carrier gas flow rate of 70 SCCM, a pressure of 3.5 Torr, and a temperature of 150 °C. Additional Ar gas was used in a "vapor boost" setup to assist in mass transport of the VTIP to the deposition chamber due to the low vapor pressure of the VTIP. The as-deposited V_2O_5 films are amorphous by XRD. The films are then moved into the Ar glovebox and the LBCO SSE is deposited on top of the V_2O_5. Immediately following this deposition, 2.2 mm diameter Li metal top electrodes were deposited through a shadowmask. The bottom current collector is contacted by sanding away the ALD films, and the top electrode/current collector (Li metal) is contacted with a microprobe, as de-

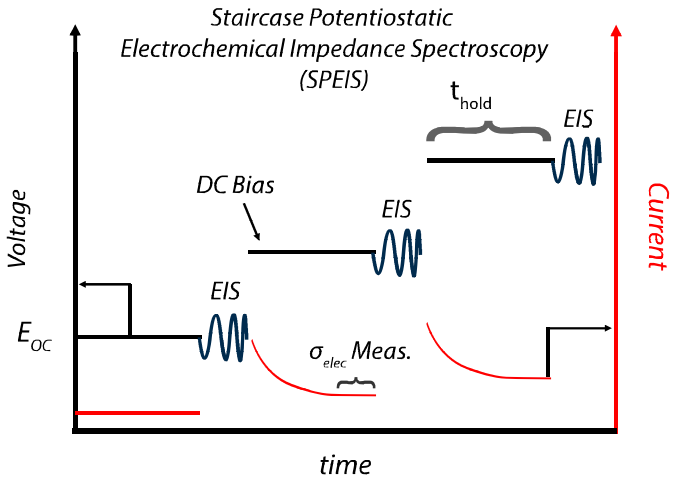

Figure 8.13: *Schematic description of SPEIS method that was used to measure ionic and electronic conductivities as a function of applied potential in a SS vs. Li blocking/non-blocking cell. A DC bias is applied, after sufficient time for the resulting current to stabilize, an average value is taken in the stable region to determine electronic conductivity. Subsequent EIS is performed about the bias potential to extract ionic conductivity from a fitted Nyquist plot. This procedure continues for a range of applied potentials.*

scribed above.

CHAPTER 9

Conclusions and Future Work

9.1 Conclusions

This work has made significant contributions to the field of Li metal anodes by: 1) building understanding of the coupled electro-chemo-mechanical phenomena that drive performance of Li/SSE interfaces and by 2) demonstrating novel characterization techniques and methods of interfacial modification.

More specifically, chapters 3 and 4 explored the role of heterogeneities on the surface of Li metal that drive non-uniform plating in liquid electrolytes. The resulting morphology evolution ultimately leads to cell failure by either cell-drying or short-circuit. By developing and utilizing *operando* video microscopy, a mechanistic model was developed to describe how spatially varying kinetics and morphology evolution at the Li/electrolyte interface drive transitions between different reaction pathways. These transitions have distinct signatures in the electrochemical response that then can be used to gain insight into cell performance. This understanding has enabled us and others to utilize analysis of voltage trace shapes to diagnose phenomena occurring within cells in which *in situ* characterization is difficult.

Chapter 5 demonstrated the coupling between surface chemistry, Li wetting, interfacial impedance, and rate capability of LLZO. Knowledge of these connections allowed the development of a surface treatment to remove the surface contamination layer and enable

ultra-low interfacial impedance (<2 Ω cm^2). XPS analysis showed that WP prevented the formation of a Li_2CO_3 layer by avoiding exposure to air, and that a subsequent anneal in inert atmosphere could remove the LiOH layer that did form during the polishing. Removal of this contamination layer was shown to decrease the contact angle of molten Li from 142°to 95°, as measured by the molten Li sessile drop testing setup that was developed for this work. The improved interfacial adhesion was demonstrated to reduce the interface impedance dramatically, and thereby increase the CCD from ~50 μA cm^{-2} to 300 μA cm^{-2}.

Chapter 6 adapted operando video microscopy to SSEs. Using a novel in-plane cell architecture, it was shown that there are at least 4 distinct morphologies of Li metal penetration in SSEs, straight, branching, spalling, and diffuse. It was determined that branching-type filaments are most common in LLZO when the interfacial impedance is low and CCD is high, while diffuse-type penetration was only observed in cells where the Li metal was not annealed and the CCD was relatively low. This points towards multiple mechanisms of failure in SSEs, and could explain why there are widely differing hypothesis about the mechanism of Li penetration in ceramic SSEs. Several of the morphologies were shown to be reversible, as the Li metal from inside the cracks can be stripped out and then re-plated. The growth rate of a Li-filled crack was shown to be proportional to the applied current, and stress-relaxation of the Li within the crack via extrusion was directly observed. This supports that the propagation of Li filaments within ceramic SSEs is due to the build up of compressive stress in the Li within the crack, leading to opening of the crack tip. The formation of voids after extended stripping was shown to cause an increase interfacial resistance and decrease in interface capacitance. Finally, a glassy sulfide SSE was shown to exhibit largely the same behavior, demonstrating that the results in LLZO have wider implications for the SSE field as a whole.

Chapters 7 and 8 demonstrated processes for ALD of two SSE materials. The LBCO films in particular show great promise for a wide range of applications in both bulk-type and thin-film batteries based on the properties measured in this work. The film exhibits the

highest ionic conductivity of any reported ALD film by a factor of 6, and can conformally coat complex high-aspect-ratio structures. The film is stable in contact with Li metal, relatively stable in air, and retains a high ionic transference number across a wide range of potentials from 0-6 volts vs. Li/Li^+. Proof of concept full cells were fabricated using vanadium oxide as the cathode and Li metal as the anode. These cells exhibited good rate capability, high Coulombic efficiency, and excellent capacity retention.

This thesis demonstrated several new characterization techniques and methods of controlling interfacial properties. It utilized these techniques to build mechanistic understanding of the coupled phenomena that govern interfacial bahavior. Finally, the knowledge gained is leveraged to enable rational design of high performance interfaces. The intersection of mechanistic understanding, precise control of interfacial properties, and rational design is a promising route to enabling Li metal anodes for a wide range of applications that will have tremendous impact on society.

9.2 Future Work

This work has already impacted or directly led to other work in the field, and there are numerous opportunities to expand upon the understanding and techniques developed in this thesis. This section will briefly explore some of those opportunities.

Chapter 5 clearly demonstrates that by first building mechanistic understanding of the properties that determine interfacial performance, improved performance can be achieved through rational design, rather than empirical trial and error. *Operando* video microscopy will continue to be a valuable technique for building this type of mechnistic understanding that can be used to improve performance. Following my work, other members of my group have applied *operando* video microscopy to later stages of cycling,[241] different viewing angles, and other materials systems. It has proven to be a powerful technique for understanding the dynamic evolution of coupled phenomena in a wide range of systems, and

there are many which have yet to be explored.

Many studies go to great lengths to enable *in situ* or *operando* characterization techniques (TEM, x-ray computed tomography, neutron depth profiling, atomic force microscopy (AFM), etc.) by making highly specialized cells and setups. In contrast, optical microscopy offers a combination of spatial resolution, time resolution, and the ability to use representative cell geometries that is often difficult to achieve with other techniques. It is also relatively low cost, and does not require specialized facilities or equipment. Therefore, *operando* video microscopy can be used to study a wide range of materials and systems by a wide range of researchers. The optical platform is also readily integrated with other characterization techniques that can provide enriched datasets. By combining with XPS, XRD, SEM, Raman spectroscopy, AFM, and other techniques, the time-synchronized optical data could be complemented by detailed information about the composition, microstructure, phase, surface chemistry, local conductivity, and more. Each of these approaches could provide further insight into the mechanisms of failure, which in turn could lead to improved performance.

The morphology of the observed failure in Chapter 6 is highly dependent on the properties of the interface. Therefore, comparisons between different research groups and techniques must take into account the properties of the specific system studied. Future studies of the impact of interfacial properties (roughness, ASR, SEI species, current focusing, wetting) and the bulk properties (grain size, porosity, void morphology, ionic conductivity, electronic conductivity) on cell performance will help to identify the key characteristics that can enable high rate performance in SSEs.

Modification of Li metal surfaces to improve cycleability of Li metal anodes in liquid electrolytes remains an area of great research interest. Based upon Chapters 3,4, and8, coatings which exhibit high ionic conductivity, electrochemical stability, and can remain intact during cycling could enable long cycle-life Li metal batteries with liquid electrolytes. Though the LBCO ALD film meets the first two criteria, a more ductile/flexible film may

better withstand the mechanical stresses that are imparted during cell assembly and cycling. Hybrid inorganic/organic films may offer the ideal combination of properties for these applications. Similarly, coatings may offer improved performance of Li/SSE interfaces. As the morphology evolution at these interfaces is driven by inhomogeneities at the interface, coatings could be used to homogenize the surface and suppress the unwanted morphology evolution (Li penetration, void formation).

The unique combination of properties make LBCO ALD films an attractive option for interfacial coatings and passivation layers. ALD films have already been shown to dramatically improve performance by coating electrodes in LIBs. LBCO films are more stable and more ionically conductive than the films that have been studied previously, and therefore could be substantially better suited for this application. Thicker coatings could be used without increasing impedance dramatically, and the films could inhibit or modify SEI formation. Further, LBCO films could change the nucleation behavior of Li plating on graphite electrodes.

There are a wide range of potential application spaces that should be explored, from coatings on liquid and SSB materials, use as a sintering aid, thin-film batteries with 3-D architectures, multifunctional batteries, and more. It can also be used as a model system to better understand the phenomena that drive performance of solid-solid interfaces in batteries. The ability to precisely control thickness with sub-nm precision and coat complex structures provides a unique ability to fabricate cells for a variety of characterization techniques including scanning probe techniques, electron microscopy, XPS, and more.

In summary, there are many opportunities moving forward from the work included this thesis to improve both our understanding and the performance of Li metal anodes. This work could have a significant impact on the trajectory of next-generation batteries, and the way that our society uses energy.

BIBLIOGRAPHY

(1) United Nations *World Population Prospects 2019*; 141; 2019, p 1.

(2) De Long, J. P.; Burger, O. Socio-economic instability and the scaling of energy use with population size. *PLoS ONE* **2015**, *10*, 1–12.

(3) Rayner, N. A. Global analyses of sea surface temperature, sea ice, and night marine air temperature since the late nineteenth century. *Journal of Geophysical Research* **2003**, *108*, 4407.

(4) Parmesan, C.; Yohe, G. A globally coherent fingerprint of climate change impacts across natural systems. *Nature* **2003**, *421*, 37–42.

(5) Stocker, T.; D. Qin, G.-K.; Plattner, M.; Tignor, S.; Allen, J.; Boschung, A.; Nauels, Y.; Xia, V.; Midgley, B.; P.M., *Climate Change 2013 - The Physical Science Basis*; Intergovernmental Panel on Climate Change, Ed.; Cambridge University Press: Cambridge, 2014.

(6) Energy Information Administration U . S . Primary Energy Consumption by Source and Sector., 2018.

(7) Energy Information Administration Carbon intensity of energy use is lowest in U.S. industrial and electric power sectors., https://www.eia.gov/todayinenergy/detail.php?id=31012 (accessed 11/20/2019).

(8) Hoekstra, A. The Underestimated Potential of Battery Electric Vehicles to Reduce Emissions. *Joule* **2019**, *3*, 1412–1414.

(9) Schmuch, R.; Wagner, R.; Hörpel, G.; Placke, T.; Winter, M. Performance and cost of materials for lithium-based rechargeable automotive batteries. *Nature Energy* **2018**, *3*, 267–278.

(10) MacKenzie, J. D.; Ho, C. Perspectives on energy storage for flexible electronic systems. *Proceedings of the IEEE* **2015**, *103*, 535–553.

(11) Coppez, G. The importance of energy storage in Renewable Power Generation: A review - IEEE Conference Publication. *45th International Universities Power Engineering Conference UPEC2010* **2010**, 1–5.

(12) Boulanger, A. G.; Chu, A. C.; Maxx, S.; Waltz, D. L. Vehicle electrification: Status and issues. *Proceedings of the IEEE* **2011**, *99*, 1116–1138.

(13) Albertus, P.; Babinec, S.; Litzelman, S.; Newman, A. Status and challenges in enabling the lithium metal electrode for high-energy and low-cost rechargeable batteries. *Nature Energy* **2018**, *3*, 16–21.

(14) Kazyak, E.; Wood, K. N.; Dasgupta, N. P. Improved Cycle Life and Stability of Lithium Metal Anodes through Ultrathin Atomic Layer Deposition Surface Treatments. *Chemistry of Materials* **2015**, *27*, 6457–6462.

(15) Wood, K. N.; Kazyak, E.; Chadwick, A. F.; Chen, K.-H.; Zhang, J.-G.; Thornton, K.; Dasgupta, N. P. Dendrites and Pits: Untangling the Complex Behavior of Lithium Metal Anodes through Operando Video Microscopy. *ACS Central Science* **2016**, *2*, 790–801.

(16) Sharafi, A.; Kazyak, E.; Davis, A. L.; Yu, S.; Thompson, T.; Siegel, D. J.; Dasgupta, N. P.; Sakamoto, J. Surface Chemistry Mechanism of Ultra-Low Interfacial Resistance in the Solid-State Electrolyte Li 7 La 3 Zr 2 O 12. *Chemistry of Materials* **2017**, *29*, 7961–7968.

(17) Kazyak, E.; Garcia-Mendez, R.; LePage, W. S.; Sharafi, A.; Davis, A. L.; Sanchez, A. J.; Chen, K.-H.; Haslam, C. G.; Sakamoto, J.; Dasgupta, N. P. Li Penetration in Ceramic Solid Electrolytes: Direct Observation of Morphology, Propagation, and Reversibility via Operando Video Microscopy. *(In Review)* **2019**.

(18) Kazyak, E.; Chen, K. H.; Wood, K. N.; Davis, A. L.; Thompson, T.; Bielinski, A. R.; Sanchez, A. J.; Wang, X.; Wang, C.; Sakamoto, J.; Dasgupta, N. P. Atomic Layer Deposition of the Solid Electrolyte Garnet Li7La3Zr2O12. *Chemistry of Materials* **2017**, *29*, 3785–3792.

(19) Kazyak, E.; Chen, K. H.; Davis, A. L.; Yu, S.; Sanchez, A. J.; Lasso, J.; Bielinski, A. R.; Thompson, T.; Sakamoto, J.; Siegel, D. J.; Dasgupta, N. P. Atomic layer deposition and first principles modeling of glassy Li3BO3-Li2CO3 electrolytes for solid-state Li metal batteries. *Journal of Materials Chemistry A* **2018**, *6*, 19425–19437.

(20) Crabtree, G. The energy-storage revolution. *Nature* **2015**, *526*, S92.

(21) Nevelius, E. The Nobel Prize in Chemistry 2019., 2019.

(22) Whittingham, M. S. Electrical Energy Storage and Intercalation Chemistry. *Science* **1976**, *192*, 1126–1127.

(23) Mizushima, K.; Jones, P.; Wiseman, P.; Goodenough, J. LixCoO2 (0¡x¡=1): A new cathode material for batteries of high energy density. *Materials Research Bulletin* **1980**, *15*, 783–789.

(24) Akira Yoshino Kenichi Sanechika, T. N. Secondary battery, US patent 4668595A., 1986.

(25) Yoshino, A. In *Lithium-Ion Batteries*; Elsevier: 2014, pp 1–20.

(26) Huggins, R. A., *Advanced batteries: Materials science aspects*; Springer US: 2009, pp 1–474.

(27) O'Hayre, R.; Cha, S.-W.; Colella, W.; Prinz, F. B., *Fuel Cell Fundamentals*, 3rd; John Wiley & Sons, Inc: Hoboken, NJ, USA, 2016.

(28) Kittel, C., *Introduction to Solid State Physics*, 8th; John Wiley & Sons, INC.: 2004.

(29) Newman, J.; Thomas-Alyea, K. E., *Electrochemical Systems*, 3rd; John Wiley & Sons, INC.: Hoboken. NJ, 2004.

(30) Ge, H.; Qian, H. Physical origins of entropy production, free energy dissipation, and their mathematical representations. *Physical Review E - Statistical, Nonlinear, and Soft Matter Physics* **2010**, *81*, 1–5.

(31) Tarascon, J.-M.; Armand, M. Issues and challenges facing rechargeable lithium batteries. *Nature* **2001**, *414*, 359–367.

(32) Ohzuku, T.; Iwakoshi, Y.; Sawai, K. Formation of Lithium-Graphite Intercalation Compounds in Nonaqueous Electrolytes and Their Application as a Negative Electrode for a Lithium Ion (Shuttlecock) Cell. *Journal of the Electrochemical Society* **1993**, *140*, 2490–2498.

(33) Dahn, J. R.; Zheng, T.; Liu, Y.; Xue, J. S. Mechanisms for lithium insertion in carbonaceous materials. *Science* **1995**, *270*, 590–593.

(34) Bard, A. J.; Faulkner, L. R., *Electrochemical Methods: Fundamentals and Applications*; John Wiley & Sons, INC.: New York, 2001.

(35) *Lithium-Ion Batteries*; Pistoia, G., Ed.; Elsevier: 2014.

(36) Wang, Q.; Ping, P.; Zhao, X.; Chu, G.; Sun, J.; Chen, C. Thermal runaway caused fire and explosion of lithium ion battery. *Journal of Power Sources* **2012**, *208*, 210–224.

(37) Aurbach, D. Review of selected electrode-solution interactions which determine the performance of Li and Li ion batteries. *Journal of Power Sources* **2000**, *89*, 206–218.

(38) Thompson, T.; Yu, S.; Williams, L.; Schmidt, R. D.; Garcia-Mendez, R.; Wolfenstine, J.; Allen, J. L.; Kioupakis, E.; Siegel, D. J.; Sakamoto, J. Electrochemical Window of the Li-Ion Solid Electrolyte Li 7 La 3 Zr 2 O 12. *ACS Energy Letters* **2017**, *2*, 462–468.

(39) Goodenough, J. B.; Kim, Y. Challenges for rechargeable Li batteries. *Chemistry of Materials* **2010**, *22*, 587–603.

(40) IEA *Global EV Outlook 2019*; Paris: International Energy Agency, 2019.

(41) Xu, W.; Wang, J.; Ding, F.; Chen, X.; Nasybulin, E.; Zhang, Y.; Zhang, J.-G. Lithium metal anodes for rechargeable batteries. *Energy & Environmental Science* **2014**, *7*, 513–537.

(42) Bruce, P. G.; Hardwick, L. J.; Abraham, K. Lithium-air and lithium-sulfur batteries. *MRS Bulletin* **2011**, *36*, 506–512.

(43) Gallagher, K. G.; Goebel, S.; Greszler, T.; Mathias, M.; Oelerich, W.; Eroglu, D.; Srinivasan, V. Quantifying the promise of lithium-air batteries for electric vehicles. *Energy & Environmental Science* **2014**, *7*, 1555.

(44) Bieker, G.; Winter, M.; Bieker, P. Electrochemical in situ investigations of SEI and dendrite formation on the lithium metal anode. *Physical Chemistry Chemical Physics* **2015**, *17*, 8670–8679.

(45) Harry, K. J.; Hallinan, D. T.; Parkinson, D. Y.; MacDowell, A. A.; Balsara, N. P. Detection of subsurface structures underneath dendrites formed on cycled lithium metal electrodes. *Nature Materials* **2014**, *13*, 69–73.

(46) Yoshimatsu, I.; Hirai, T.; Yamaki, J. i. Lithium Electrode Morphology during Cycling in Lithium Cells. *Journal of the Electrochemical Society* **1988**, *135*, 2422–2427.

(47) Selim, R.; Bro, P.; Mallory, P. R. Some Observations on Rechargeable Lithium Electrodes in a Propylene Carbonate Electrolyte. *Journal of the Electrochemical Society* **1974**, *121*, 1457–1459.

(48) Ding, F.; Xu, W.; Graff, G. L.; Zhang, J.; Sushko, M. L.; Chen, X.; Shao, Y.; Engelhard, M. H.; Nie, Z.; Xiao, J.; Liu, X.; Sushko, P. V.; Liu, J.; Zhang, J.-G. Dendrite-Free Lithium Deposition via Self-Healing Electrostatic Shield Mechanism. *Journal of the American Chemical Society* **2013**, *135*, 4450–4456.

(49) Schweikert, N.; Hofmann, A.; Schulz, M.; Scheuermann, M.; Boles, S. T.; Hanemann, T.; Hahn, H.; Indris, S. Suppressed lithium dendrite growth in lithium batteries using ionic liquid electrolytes: Investigation by electrochemical impedance spectroscopy, scanning electron microscopy, and in situ 7Li nuclear magnetic resonance spectroscopy. *Journal of Power Sources* **2013**, *228*, 237–243.

(50) Qian, J.; Henderson, W. A.; Xu, W.; Bhattacharya, P.; Engelhard, M.; Borodin, O.; Zhang, J.-G. High rate and stable cycling of lithium metal anode. *Nature Communications* **2015**, *6*, 6362.

(51) Mehdi, B. L.; Qian, J.; Nasybulin, E.; Park, C.; Welch, D. A.; Faller, R.; Mehta, H.; Henderson, W. A.; Xu, W.; Wang, C. M.; Evans, J. E.; Liu, J.; Zhang, J. G.; Mueller, K. T.; Browning, N. D. Observation and quantification of nanoscale processes in lithium batteries by operando electrochemical (S)TEM. *Nano Letters* **2015**, *15*, 2168–2173.

(52) López, C. M.; Vaughey, J. T.; Dees, D. W. Morphological transitions on lithium metal anodes. *Journal of the Electrochemical Society* **2009**, *156*, 726–729.

(53) Owens, B. B. Solid state electrolytes: Overview of materials and applications during the last third of the Twentieth Century. *Journal of Power Sources* **2000**, *90*, 2–8.

(54) Aurbach, D.; Zinigrad, E.; Teller, H.; Dan, P. Factors which limit the cycle life of rechargeable lithium (metal) batteries. *Journal of the Electrochemical Society* **2000**, *147*, 1274–1279.

(55) Solid electrolytes open doors to solid-state batteries., https://www.titech.ac.jp/english/news/2016/033769.html (accessed 11/20/2019).

(56) Dudney, N. J. Solid-state thin-film rechargeable batteries. *Materials Science and Engineering B: Solid-State Materials for Advanced Technology* **2005**, *116*, 245–249.

(57) Zhang, Z.; Shao, Y.; Lotsch, B.; Hu, Y.-S. S.; Li, H.; Janek, J.; Nazar, L. F.; Nan, C. W.; Maier, J.; Armand, M.; Chen, L. New horizons for inorganic solid state ion conductors. *Energy & Environmental Science* **2018**, *11*, 1945–1976.

(58) Porz, L.; Swamy, T.; Sheldon, B. W.; Rettenwander, D.; Frömling, T.; Thaman, H. L.; Berendts, S.; Uecker, R.; Carter, W. C.; Chiang, Y.-M. M. Mechanism of Lithium Metal Penetration through Inorganic Solid Electrolytes. *Advanced Energy Materials* **2017**, *7*, 1–12.

(59) Oh, G.; Hirayama, M.; Kwon, O.; Suzuki, K.; Kanno, R. Bulk-Type All Solid-State Batteries with 5 V Class LiNi 0.5 Mn 1.5 O 4 Cathode and Li 10 GeP 2 S 12 Solid Electrolyte. *Chemistry of Materials* **2016**, *28*, 2634–2640.

(60) George, S. M. Atomic Layer Deposition: An Overview. *Chemical Reviews* **2010**, *110*, 111–131.

(61) Miikkulainen, V.; Leskelä, M.; Ritala, M.; Puurunen, R. L. Crystallinity of inorganic films grown by atomic layer deposition: Overview and general trends. *Journal of Applied Physics* **2013**, *113*, 021301.

(62) Atomic Limits., https://www.atomiclimits.com/ (accessed 11/20/2019).

(63) Johnson, R. W.; Hultqvist, A.; Bent, S. F. A brief review of atomic layer deposition: From fundamentals to applications. *Materials Today* **2014**, *17*, 236–246.

(64) Parsons, G. N.; George, S. M.; Knez, M. Progress and future directions for atomic layer deposition and ALD-based chemistry. *MRS Bulletin* **2011**, *36*, 865–871.

(65) MacKus, A. J.; Verheijen, M. A.; Leick, N.; Bol, A. A.; Kessels, W. M. Influence of oxygen exposure on the nucleation of platinum atomic layer deposition: Consequences for film growth, nanopatterning, and nanoparticle synthesis. *Chemistry of Materials* **2013**, *25*, 1905–1911.

(66) Chen, L.; Connell, J. G.; Nie, A.; Huang, Z.; Zavadil, K. R.; Klavetter, K. C.; Yuan, Y.; Sharifi-Asl, S.; Shahbazian-Yassar, R.; Libera, J. A.; Mane, A. U.; Elam, J. W. Lithium metal protected by atomic layer deposition metal oxide for high performance anodes. *Journal of Materials Chemistry A* **2017**, *5*, 12297–12309.

(67) Elers, K. E.; Blomberg, T.; Peussa, M.; Aitchison, B.; Haukka, S.; Marcus, S. Film uniformity in atomic layer deposition. *Chemical Vapor Deposition* **2006**, *12*, 13–24.

(68) Jasinski, J. Mechanistic Studies Of Chemical Vapor Deposition. *Annual Review of Physical Chemistry* **1987**, *38*, 109–140.

(69) Cremers, V.; Puurunen, R. L.; Dendooven, J. Conformality in atomic layer deposition: Current status overview of analysis and modelling. *Applied Physics Reviews* **2019**, *6*, 021302.

(70) Rodríguez, R. E.; Agarwal, S. P.; An, S.; Kazyak, E.; Das, D.; Shang, W.; Skye, R.; Deng, T.; Dasgupta, N. P. Biotemplated Morpho Butterfly Wings for Tunable Structurally Colored Photocatalysts. *ACS Applied Materials & Interfaces* **2018**, *10*, 4614–4621.

(71) Elam, J. W.; Dasgupta, N. P.; Prinz, F. B. ALD for clean energy conversion, utilization, and storage. *MRS Bulletin* **2011**, *36*, 899–906.

(72) Marichy, C.; Bechelany, M.; Pinna, N. Atomic layer deposition of nanostructured materials for energy and environmental applications. *Advanced Materials* **2012**, *24*, 1017–1032.

(73) Kim, H.; Lee, H. B. R.; Maeng, W. J. Applications of atomic layer deposition to nanofabrication and emerging nanodevices. *Thin Solid Films* **2009**, *517*, 2563–2580.

(74) Knez, M.; Nielsch, K.; Niinistö, L. Synthesis and Surface Engineering of Complex Nanostructures by Atomic Layer Deposition. *Advanced Materials* **2007**, *19*, 3425–3438.

(75) Mistry, K. et al. Pb-free Packaging. **2007**, 247–250.

(76) Faraz, T.; Roozeboom, F.; Knoops, H. C.; Kessels, W. M. Atomic layer etching: What can we learn from atomic layer deposition? *ECS Journal of Solid State Science and Technology* **2015**, *4*, N5023–N5032.

(77) Jung, Y. S.; Lu, P.; Cavanagh, A. S.; Ban, C.; Kim, G. H.; Lee, S. H.; George, S. M.; Harris, S. J.; Dillon, A. C. Unexpected improved performance of ALD coated LiCoO2/graphite li-ion batteries. *Advanced Energy Materials* **2013**, *3*, 213–219.

(78) Dingemans, G.; Kessels, W. M. M. Status and prospects of Al 2 O 3 -based surface passivation schemes for silicon solar cells. *Journal of Vacuum Science & Technology A: Vacuum, Surfaces, and Films* **2012**, *30*, 040802.

(79) Scully, L. National Lab Forms Exclusive License for Its Atomic Layer Deposition Tech. *Machine Design* **2017**.

(80) Elam, J. W.; George, S. M. Growth of Zno/Al2O3 alloy films using atomic layer deposition techniques. *Chemistry of Materials* **2003**, *15*, 1020–1028.

(81) Zhang, W.-M.; Wu, X.-L.; Hu, J.-S.; Guo, Y.-G.; Wan, L.-J. Carbon Coated Fe 3 O 4 Nanospindles as a Superior Anode Material for Lithium-Ion Batteries. *Advanced Functional Materials* **2008**, *18*, 3941–3946.

(82) Scott, I. D.; Yoon, J. S.; Cavanagh, A. S.; Yan, Y.; Dillon, A. C.; George, S. M.; Lee, S.-H. Ultrathin Coatings on Nano-LiCoO 2 for Li-Ion Vehicular Applications. *Nano Lett* **2011**, *11*, 414–418.

(83) Aricò, A. S.; Bruce, P.; Scrosati, B.; Tarascon, J.-M.; Van Schalkwijk, W. In *Materials for Sustainable Energy*; Co-Published with Macmillan Publishers Ltd, UK: 2010, pp 148–159.

(84) Myung, S.-T.; Izumi, K.; Komaba, S.; Sun, Y.-K.; Yashiro, H.; Kumagai, N. Role of Alumina Coating on Li-Ni-Co-Mn-O Particles as Positive Electrode Material for Lithium-Ion Batteries. *Chemistry of Materials* **2005**, *17*, 3695–3704.

(85) Guan, D.; Jeevarajan, J. A.; Wang, Y. Enhanced cycleability of LiMn2O4 cathodes by atomic layer deposition of nanosized-thin Al2O3 coatings. *Nanoscale* **2011**, *3*, 1465.

(86) Jung, Y. S.; Cavanagh, A. S.; Riley, L. A.; Kang, S.-H.; Dillon, A. C.; Groner, M. D.; George, S. M.; Lee, S.-H. Ultrathin Direct Atomic Layer Deposition on Composite Electrodes for Highly Durable and Safe Li-Ion Batteries. *Advanced Materials* **2010**, *22*, 2172–2176.

(87) Zheng, G.; Lee, S. W.; Liang, Z.; Lee, H.-W.; Yan, K.; Yao, H.; Wang, H.; Li, W.; Chu, S.; Cui, Y. Interconnected hollow carbon nanospheres for stable lithium metal anodes. *Nature Nanotechnology* **2014**, *9*, 618–623.

(88) Yan, K.; Lee, H.-W.; Gao, T.; Zheng, G.; Yao, H.; Wang, H.; Lu, Z.; Zhou, Y.; Liang, Z.; Liu, Z.; Chu, S.; Cui, Y. Ultrathin Two-Dimensional Atomic Crystals as Stable Interfacial Layer for Improvement of Lithium Metal Anode. *Nano Letters* **2014**, *14*, 6016–6022.

(89) Park, M. S.; Ma, S. B.; Lee, D. J.; Im, D.; Doo, S. G.; Yamamoto, O. A highly reversible lithium metal anode. *Scientific Reports* **2014**, *4*, 1–8.

(90) Lu, Y.; Tu, Z.; Archer, L. A. Stable lithium electrodeposition in liquid and nanoporous solid electrolytes. *Nature Materials* **2014**, *13*, 961–969.

(91) Meng, X.; Yang, X.-Q.; Sun, X. Emerging Applications of Atomic Layer Deposition for Lithium-Ion Battery Studies. *Advanced Materials* **2012**, *24*, 3589–3615.

(92) Liu, J.; Sun, X. Elegant design of electrode and electrode/electrolyte interface in lithium-ion batteries by atomic layer deposition. *Nanotechnology* **2015**, *26*, 024001.

(93) Jung, Y. S.; Cavanagh, A. S.; Dillon, A. C.; Groner, M. D.; George, S. M.; Lee, S. H. Enhanced stability of LiCoO2 cathodes in lithium-ion batteries using surface modification by atomic layer deposition. *Journal of the Electrochemical Society* **2010**, *157*, 75–81.

(94) Kozen, A. C.; Lin, C. F.; Pearse, A. J.; Schroeder, M. A.; Han, X.; Hu, L.; Lee, S. B.; Rubloff, G. W.; Noked, M. Next-Generation Lithium Metal Anode Engineering via Atomic Layer Deposition. *ACS Nano* **2015**, *9*, 5884–5892.

(95) Park, J. S.; Meng, X.; Elam, J. W.; Hao, S.; Wolverton, C.; Kim, C.; Cabana, J. Ultrathin lithium-ion conducting coatings for increased interfacial stability in high voltage lithium-ion batteries. *Chemistry of Materials* **2014**, *26*, 3128–3134.

(96) Groner, M. D.; Fabreguette, F. H.; Elam, J. W.; George, S. M. Low-Temperature Al2O3 Atomic Layer Deposition. *Chemistry of Materials* **2004**, *16*, 639–645.

(97) Rosso, M.; Brissot, C.; Teyssot, A.; Dollé, M.; Sannier, L.; Tarascon, J. M.; Bouchet, R.; Lascaud, S. Dendrite short-circuit and fuse effect on Li/polymer/Li cells. *Electrochimica Acta* **2006**, *51*, 5334–5340.

(98) Zhang, S. S.; Xu, K.; Jow, T. R. EIS study on the formation of solid electrolyte interface in Li-ion battery. *Electrochimica Acta* **2006**, *51*, 1636–1640.

(99) Ryou, M.-H.; Lee, Y. M.; Lee, Y.; Winter, M.; Bieker, P. Mechanical surface modification of lithium metal: Towards improved Li metal anode performance by directed Li plating. *Advanced Functional Materials* **2015**, *25*, 834–841.

(100) LePage, W. S.; Chen, Y.; Kazyak, E.; Chen, K.-H.; Sanchez, A. J.; Poli, A.; Arruda, E. M.; Thouless, M. D.; Dasgupta, N. P. Lithium Mechanics: Roles of Strain Rate and Temperature and Implications for Lithium Metal Batteries. *Journal of The Electrochemical Society* **2019**, *166*, A89–A97.

(101) Brandt, K. Historical development of secondary lithium batteries. *Solid State Ionics* **1994**, *69*, 173–183.

(102) Lin, D.; Liu, Y.; Liang, Z.; Lee, H. W.; Sun, J.; Wang, H.; Yan, K.; Xie, J.; Cui, Y. Layered reduced graphene oxide with nanoscale interlayer gaps as a stable host for lithium metal anodes. *Nature Nanotechnology* **2016**, *11*, 626–632.

(103) Liang, Z.; Lin, D.; Zhao, J.; Lu, Z.; Liu, Y.; Liu, C.; Lu, Y.; Wang, H.; Yan, K.; Tao, X.; Cui, Y. Composite lithium metal anode by melt infusion of lithium into a 3D conducting scaffold with lithiophilic coating. *Proceedings of the National Academy of Sciences of the United States of America* **2016**, *113*, 2862–2867.

(104) Basile, A.; Bhatt, A. I.; O'Mullane, A. P. Stabilizing lithium metal using ionic liquids for long-lived batteries. *Nature Communications* **2016**, *7*, 1–11.

(105) Love, C. T.; Baturina, O. A.; Swider-Lyons, K. E. Observation of lithium dendrites at ambient temperature and below. *ECS Electrochemistry Letters* **2014**, *4*, A24–A27.

(106) Li, W.; Yao, H.; Yan, K.; Zheng, G.; Liang, Z.; Chiang, Y.-M.; Cui, Y. The synergetic effect of lithium polysulfide and lithium nitrate to prevent lithium dendrite growth. *Nature Communications* **2015**, *6*, 7436.

(107) Choudhury, S.; Mangal, R.; Agrawal, A.; Archer, L. A. A highly reversible room-temperature lithium metal battery based on crosslinked hairy nanoparticles. *Nature Communications* **2015**, *6*, 1–9.

(108) Wu, H.; Zhuo, D.; Kong, D.; Cui, Y. Improving battery safety by early detection of internal shorting with a bifunctional separator. *Nature Communications* **2014**, *5*, 1–6.

(109) Dickinson, E. J. F.; Limon-petersen, J. G.; Rees, N. V.; Compton, R. G. Quantitatively Diffusional? A Theoretical and Experimental Investigation. **2009**, 11157–11171.

(110) Sandifer, J. R.; Buck, R. P. An algorithm for simulation of transient and alternating current electrical properties of conducting membranes, junctions, and one-dimensional, finite galvanic cells. *Journal of Physical Chemistry* **1975**, *79*, 384–392.

(111) Aurbach, D.; Gofer, Y.; Langzam, J. The Correlation Between Surface Chemistry, Surface Morphology, and Cycling Efficiency of Lithium Electrodes in a Few Polar Aprotic Systems. *Journal of The Electrochemical Society* **1989**, *136*, 3198.

(112) Yu, S.; Schmidt, R. D.; Garcia-Mendez, R.; Herbert, E.; Dudney, N. J.; Wolfenstine, J. B.; Sakamoto, J.; Siegel, D. J. Elastic Properties of the Solid Electrolyte Li7La3Zr2O12 (LLZO). *Chemistry of Materials* **2016**, *28*, 197–206.

(113) Murugan, R.; Thangadurai, V.; Weppner, W. Fast lithium ion conduction in garnet-type Li7La 3Zr2O12. *Angewandte Chemie - International Edition* **2007**, *46*, 7778–7781.

(114) Zhang, S. S.; Xu, K.; Jow, T. R. The low temperature performance of Li-ion batteries. *Journal of Power Sources* **2003**, *115*, 137–140.

(115) Sharafi, A.; Meyer, H. M.; Nanda, J.; Wolfenstine, J.; Sakamoto, J. Characterizing the Li-Li7La3Zr2O12 interface stability and kinetics as a function of temperature and current density. *Journal of Power Sources* **2016**, *302*, 135–139.

(116) Cheng, L.; Chen, W.; Kunz, M.; Persson, K.; Tamura, N.; Chen, G.; Doeff, M. Effect of Surface Microstructure on Electrochemical Performance of Garnet Solid Electrolytes. *ACS Applied Materials & Interfaces* **2015**, *7*, 2073–2081.

(117) Tsai, C. L.; Roddatis, V.; Chandran, C. V.; Ma, Q.; Uhlenbruck, S.; Bram, M.; Heitjans, P.; Guillon, O. Li7La3Zr2O12Interface Modification for Li Dendrite Prevention. *ACS Applied Materials and Interfaces* **2016**, *8*, 10617–10626.

(118) Han, X.; Gong, Y.; Fu, K.; He, X.; Hitz, G. T.; Dai, J.; Pearse, A.; Liu, B.; Wang, H.; Rubloff, G.; Mo, Y.; Thangadurai, V.; Wachsman, E. D.; Hu, L. Negating interfacial impedance in garnet-based solid-state Li metal batteries. *Nature Materials* **2017**, *16*, 572–579.

(119) Fu, K. K.; Gong, Y.; Liu, B.; Zhu, Y.; Xu, S.; Yao, Y.; Luo, W.; Wang, C.; Lacey, S. D.; Dai, J.; Chen, Y.; Mo, Y.; Wachsman, E.; Hu, L. Toward garnet electrolyte-based Li metal batteries: An ultrathin, highly effective, artificial solid-state electrolyte/metallic Li interface. *Science Advances* **2017**, *3*, e1601659.

(120) Wang, C.; Gong, Y.; Liu, B.; Fu, K.; Yao, Y.; Hitz, E.; Li, Y.; Dai, J.; Xu, S.; Luo, W.; Wachsman, E. D.; Hu, L. Conformal, Nanoscale ZnO Surface Modification of Garnet-Based Solid-State Electrolyte for Lithium Metal Anodes. *Nano letters* **2017**, *17*, 565–571.

(121) Larraz, G.; Orera, a.; Sanjuán, M. L. Cubic phases of garnet-type Li7La3Zr2O12: the role of hydration. *Journal of Materials Chemistry A* **2013**, *1*, 11419.

(122) Sharafi, A.; Yu, S.; Naguib, M.; Lee, M.; Ma, C.; Meyer, H. M.; Nanda, J.; Chi, M.; Siegel, D. J.; Sakamoto, J. Impact of air exposure and surface chemistry on

Li-Li7La3Zr2O12interfacial resistance. *Journal of Materials Chemistry A* **2017**, *5*, 13475–13487.

(123) Beyer, H.; Meini, S.; Tsiouvaras, N.; Piana, M.; Gasteiger, H. A. Thermal and electrochemical decomposition of lithium peroxide in non-catalyzed carbon cathodes for Li-air batteries. *Physical Chemistry Chemical Physics* **2013**, *15*, 11025.

(124) Luo, W.; Gong, Y.; Zhu, Y.; Li, Y.; Yao, Y.; Zhang, Y.; Fu, K. K.; Pastel, G.; Lin, C. F.; Mo, Y.; Wachsman, E. D.; Hu, L. Reducing Interfacial Resistance between Garnet-Structured Solid-State Electrolyte and Li-Metal Anode by a Germanium Layer. *Advanced Materials* **2017**, *29*, 1–7.

(125) Liu, Z.; Qi, Y.; Lin, Y. X.; Chen, L.; Lu, P.; Chen, L. Q. Interfacial study on solid electrolyte interphase at Li metal anode: Implication for Li dendrite growth. *Journal of the Electrochemical Society* **2016**, *163*, A592–A598.

(126) Kanamura, K.; Tamura, H.; Takehara, Z.-i. XPS analysis of a lithium surface immersed in propylene carbonate solution containing various salts. *Journal of Electroanalytical Chemistry* **1992**, *333*, 127–142.

(127) Irvine, B. J. T. S.; Sinclair, D. C.; West, A. R. Electroceramics Characterisation by impedance sepctroscopy. *Advanced Materials* **1990**, *2*, 132–138.

(128) Cheng, E. J.; Sharafi, A.; Sakamoto, J. Intergranular Li metal propagation through polycrystalline Li6.25Al0.25La3Zr2O12 ceramic electrolyte. *Electrochimica Acta* **2017**, *223*, 85–91.

(129) Buschmann, H. et al. Structure and dynamics of the fast lithium ion conductor Li7La3Zr2O12. *Physical Chemistry Chemical Physics* **2011**, *13*, 19378–19392.

(130) Dupin, J. C.; Gonbeau, D.; Vinatier, P.; Levasseur, A. Systematic XPS studies of metal oxides, hydroxides and peroxides. *Physical Chemistry Chemical Physics* **2000**, *2*, 1319–1324.

(131) Yao, K. P. C.; Kwabi, D. G.; Quinlan, R. A.; Mansour, A. N.; Grimaud, A.; Lee, Y. L. Y.-L. Y.-L.; Lu, Y.-C. C.; Shao-Horn, Y. Thermal Stability of Li2O2 and Li2O for Li-Air Batteries: In Situ XRD and XPS Studies. *Journal of the Electrochemical Society* **2013**, *160*, A824–A831.

(132) Huang, M.; Liu, T.; Deng, Y.; Geng, H.; Shen, Y.; Lin, Y.; Nan, C. W. Effect of sintering temperature on structure and ionic conductivity of Li 7 - XLa 3Zr 2O 12 - 0.5x (x = 0.5 - 0.7) ceramics. *Solid State Ionics* **2011**, *204-205*, 41–45.

(133) Jena, R. K.; Yue, C. Y. Cyclic olefin copolymer based microfluidic devices for biochip applications: Ultraviolet surface grafting using 2-methacryloyloxyethyl phosphorylcholine. *Biomicrofluidics* **2012**, *6*, 012822.

(134) Young, T. III. An essay on the cohesion of fluids. *Philosophical Transactions of the Royal Society of London* **1805**, *95*, 65–87.

(135) Huggins, R. A. Simple method to determine electronic conductivity and ionic components of the conductors in mixed a review. *Ionics* **2002**, *8*, 300–313.

(136) Wang, M.; Wolfenstine, J. B.; Sakamoto, J. Temperature dependent flux balance of the Li/Li7La3Zr2O12 interface. *Electrochimica Acta* **2019**, *296*, 842–847.

(137) Yang, C.; Xie, H.; Ping, W.; Fu, K.; Liu, B.; Rao, J.; Dai, J.; Wang, C.; Pastel, G.; Hu, L. An Electron/Ion Dual-Conductive Alloy Framework for High-Rate and High-Capacity Solid-State Lithium-Metal Batteries. *Advanced Materials* **2019**, *31*, 1–7.

(138) Garcia-Mendez, R.; Mizuno, F.; Zhang, R.; Arthur, T. S.; Sakamoto, J. Effect of Processing Conditions of 75Li2S-25P2S5 Solid Electrolyte on its DC Electrochemical Behavior. *Electrochimica Acta* **2017**, *237*, 144–151.

(139) Swamy, T.; Park, R.; Sheldon, B. W.; Rettenwander, D.; Porz, L.; Berendts, S.; Uecker, R.; Carter, W. C.; Chiang, Y.-M. Lithium Metal Penetration Induced by Electrodeposition through Solid Electrolytes: Example in Single-Crystal Li 6 La

3 ZrTaO 12 Garnet. *Journal of The Electrochemical Society* **2018**, *165*, A3648–A3655.

(140) Han, F.; Westover, A. S.; Yue, J.; Fan, X.; Wang, F.; Chi, M.; Leonard, D. N.; Dudney, N. J.; Wang, H.; Wang, C. High electronic conductivity as the origin of lithium dendrite formation within solid electrolytes. *Nature Energy* **2019**, *4*, 187–196.

(141) Krauskopf, T.; Hartmann, H.; Zeier, W. G.; Janek, J. Toward a Fundamental Understanding of the Lithium Metal Anode in Solid-State Batteries-An Electrochemo-Mechanical Study on the Garnet-Type Solid Electrolyte Li 6.25 Al 0.25 La 3 Zr 2 O 12. *ACS Applied Materials & Interfaces* **2019**, *11*, 14463–14477.

(142) Shen, F.; Dixit, M. B.; Xiao, X.; Hatzell, K. B. Effect of Pore Connectivity on Li Dendrite Propagation within LLZO Electrolytes Observed with Synchrotron X-ray Tomography. *ACS Energy Letters* **2018**, *3*, 1056–1061.

(143) Lewis, J. A.; Tippens, J.; Cortes, F. J. Q.; McDowell, M. T. Chemo-Mechanical Challenges in Solid-State Batteries. *Trends in Chemistry* **2019**, 1–14.

(144) Yu, S.; Siegel, D. J. Grain Boundary Softening: A Potential Mechanism for Lithium Metal Penetration through Stiff Solid Electrolytes. *ACS Applied Materials & Interfaces* **2018**, *10*, 38151–38158.

(145) Krauskopf, T.; Dippel, R.; Hartmann, H.; Peppler, K.; Mogwitz, B.; Richter, F. H.; Zeier, W. G.; Janek, J. Lithium-Metal Growth Kinetics on LLZO Garnet-Type Solid Electrolytes. *Joule* **2019**, *3*, 2030–2049.

(146) Song, Y.; Yang, L.; Zhao, W.; Wang, Z.; Zhao, Y.; Wang, Z.; Zhao, Q.; Liu, H.; Pan, F. Revealing the Short-Circuiting Mechanism of Garnet-Based Solid-State Electrolyte. *Advanced Energy Materials* **2019**, *9*, 1900671.

(147) Wang, M. J.; Choudhury, R.; Sakamoto, J. Characterizing the Li-Solid-Electrolyte Interface Dynamics as a Function of Stack Pressure and Current Density. *Joule* **2019**, *3*, 2165–2178.

(148) Lewis, J. A.; Cortes, F. J. Q.; Boebinger, M. G.; Tippens, J.; Marchese, T. S.; Kondekar, N.; Liu, X.; Chi, M.; McDowell, M. T. Interphase Morphology between a Solid-State Electrolyte and Lithium Controls Cell Failure. *ACS Energy Letters* **2019**, *4*, 591–599.

(149) Fu, J.; Yu, P.; Zhang, N.; Ren, G.; Zheng, S.; Huang, W.; Long, X.; Li, H.; Liu, X. In situ formation of a bifunctional interlayer enabled by a conversion reaction to initiatively prevent lithium dendrites in a garnet solid electrolyte. *Energy and Environmental Science* **2019**, *12*, 1404–1412.

(150) Huang, X.; Lu, Y.; Guo, H.; Song, Z.; Xiu, T.; Badding, M. E.; Wen, Z. None-Mother-Powder Method to Prepare Dense Li-Garnet Solid Electrolytes with High Critical Current Density. *ACS Applied Energy Materials* **2018**, *1*, 5355–5365.

(151) Marbella, L. E.; Zekoll, S.; Kasemchainan, J.; Emge, S. P.; Bruce, P. G.; Grey, C. P. 7 Li NMR Chemical Shift Imaging To Detect Microstructural Growth of Lithium in All-Solid-State Batteries. *Chemistry of Materials* **2019**, *31*, 2762–2769.

(152) Manalastas, W.; Rikarte, J.; Chater, R. J.; Brugge, R.; Aguadero, A.; Buannic, L.; Llordés, A.; Aguesse, F.; Kilner, J. Mechanical failure of garnet electrolytes during Li electrodeposition observed by in-operando microscopy. *Journal of Power Sources* **2019**, *412*, 287–293.

(153) Tippens, J.; Miers, J. C.; Afshar, A.; Lewis, J. A.; Cortes, F. J. Q.; Qiao, H.; Marchese, T. S.; Di Leo, C. V.; Saldana, C.; McDowell, M. T. Visualizing Chemomechanical Degradation of a Solid-State Battery Electrolyte. *ACS Energy Letters* **2019**, *4*, 1475–1483.

(154) Wood, K. N.; Noked, M.; Dasgupta, N. P. Lithium metal anodes: Toward an improved understanding of coupled morphological, electrochemical, and mechanical behavior. *ACS Energy Letters* **2017**, *2*, 664–672.

(155) Sharafi, A.; Haslam, C. G.; Kerns, R. D.; Wolfenstine, J.; Sakamoto, J. Controlling and correlating the effect of grain size with the mechanical and electrochemical properties of Li7La3Zr2O12 solid-state electrolyte. *Journal of Materials Chemistry A* **2017**, *5*, 21491–21504.

(156) Tenhaeff, W. E.; Rangasamy, E.; Wang, Y.; Sokolov, A. P.; Wolfenstine, J.; Sakamoto, J.; Dudney, N. J. Resolving the Grain Boundary and Lattice Impedance of Hot-Pressed Li7La3Zr2O12 Garnet Electrolytes. *ChemElectroChem* **2014**, *1*, 375–378.

(157) Thangadurai, V.; Narayanan, S.; Pinzaru, D. Garnet-type solid-state fast Li ion conductors for Li batteries: Critical review. *Chemical Society Reviews* **2014**, *43*, 4714–4727.

(158) Lu, Y.; Huang, X.; Ruan, Y.; Wang, Q.; Kun, R.; Yang, J.; Wen, Z. An: In situ element permeation constructed high endurance Li-LLZO interface at high current densities. *Journal of Materials Chemistry A* **2018**, *6*, 18853–18858.

(159) Taylor, N. J.; Stangeland-Molo, S.; Haslam, C. G.; Sharafi, A.; Thompson, T.; Wang, M.; Garcia-Mendez, R.; Sakamoto, J. Demonstration of high current densities and extended cycling in the garnet Li7La3Zr2O12 solid electrolyte. *Journal of Power Sources* **2018**, *396*, 314–318.

(160) Trustrum, K.; Jayatilaka, A. D. S. Statistical approach to brittle fracture. *Journal of Materials Science* **1977**, *12*, 1426–1430.

(161) Masias, A.; Felten, N.; Garcia-Mendez, R.; Wolfenstine, J.; Sakamoto, J. Elastic, plastic, and creep mechanical properties of lithium metal. *Journal of Materials Science* **2019**, *54*, 2585–2600.

(162) Xia, Z.; Riester, L.; Curtin, W. A.; Li, H.; Sheldon, B. W.; Liang, J.; Chang, B.; Xu, J. M. Direct observation of toughening mechanisms in carbon nanotube ceramic matrix composites. *Acta Materialia* **2004**, *52*, 931–944.

(163) Chawla, K. K. In *Composite Materials: Science and Engineering*, 3rd; Springer: New York, 2012; Chapter 7, pp 249–290.

(164) Sevener, K. M.; Tracy, J. M.; Chen, Z.; Kiser, J. D.; Daly, S. Crack opening behavior in ceramic matrix composites. *Journal of the American Ceramic Society* **2017**, *100*, 4734–4747.

(165) De Jonghe, L. C.; Feldman, L.; Beuchele, A. Slow degradation and electron conduction in sodium/beta-aluminas. *Journal of Materials Science* **1981**, *16*, 780–786.

(166) Gupta, A.; Kazyak, E.; Craig, N.; Christensen, J.; Dasgupta, N. P.; Sakamoto, J. Evaluating the Effects of Temperature and Pressure on Li/PEO-LiTFSI Interfacial Stability and Kinetics. *Journal of The Electrochemical Society* **2018**, *165*, A2801–A2806.

(167) Wenzel, S.; Randau, S.; Leichtweiß, T.; Weber, D. A.; Sann, J.; Zeier, W. G.; Janek, J. Direct Observation of the Interfacial Instability of the Fast Ionic Conductor Li10GeP2S12 at the Lithium Metal Anode. *Chemistry of Materials* **2016**, *28*, 2400–2407.

(168) Ge, X.; Fu, C.; Chan, S. H. Double layer capacitance of anode/solid-electrolyte interfaces. *Physical Chemistry Chemical Physics* **2011**, *13*, 15134–15142.

(169) Yu, S.; Park, H.; Siegel, D. J. Thermodynamic Assessment of Coating Materials for Solid-State Li, Na, and K Batteries. *ACS Applied Materials and Interfaces* **2019**, *11*, 36607–36615.

(170) Ma, L.; Nuwayhid, R. B.; Wu, T.; Lei, Y.; Amine, K.; Lu, J. Atomic Layer Deposition for Lithium-Based Batteries. *Advanced Materials Interfaces* **2016**, *3*, 1600564.

(171) Lobe, S.; Dellen, C.; Finsterbusch, M.; Gehrke, H. G.; Sebold, D.; Tsai, C. L.; Uhlenbruck, S.; Guillon, O. Radio frequency magnetron sputtering of Li7La3Zr2O12 thin films for solid-state batteries. *Journal of Power Sources* **2016**, *307*, 684–689.

(172) Saccoccio, M.; Yu, J.; Lu, Z.; Kwok, S. C.; Wang, J.; Yeung, K. K.; Yuen, M. M.; Ciucci, F. Low temperature pulsed laser deposition of garnet Li6.4La3Zr1.4Ta0.6O12 films as all solid-state lithium battery electrolytes. *Journal of Power Sources* **2017**, *365*, 43–52.

(173) Loho, C.; Djenadic, R.; Bruns, M.; Clemens, O.; Hahn, H. Garnet-Type Li7La3Zr2O12 solid electrolyte thin films grown by CO2-laser assisted CVD for All-solid-state batteries. *Journal of the Electrochemical Society* **2017**, *164*, A6131–A6139.

(174) Hitz, G. T.; McOwen, D. W.; Zhang, L.; Ma, Z.; Fu, Z.; Wen, Y.; Gong, Y.; Dai, J.; Hamann, T. R.; Hu, L.; Wachsman, E. D. High-rate lithium cycling in a scalable trilayer Li-garnet-electrolyte architecture. *Materials Today* **2018**, *22*, 50–57.

(175) Pearse, A.; Schmitt, T.; Sahadeo, E.; Stewart, D. M.; Kozen, A.; Gerasopoulos, K.; Talin, A. A.; Lee, S. B.; Rubloff, G. W.; Gregorczyk, K. E. Three-Dimensional Solid-State Lithium-Ion Batteries Fabricated by Conformal Vapor-Phase Chemistry. *ACS Nano* **2018**, *12*, 4286–4294.

(176) Oudenhoven, J. F. M.; Baggetto, L.; Notten, P. H. L. All-Solid-State Lithium-Ion Microbatteries: A Review of Various Three-Dimensional Concepts. *Advanced Energy Materials* **2011**, *1*, 10–33.

(177) Kozen, A. C.; Pearse, A. J.; Lin, C.-F.; Noked, M.; Rubloff, G. W. Atomic Layer Deposition of the Solid Electrolyte LiPON. *Chemistry of Materials* **2015**, *27*, 5324–5331.

(178) Lin, C. F.; Noked, M.; Kozen, A. C.; Liu, C.; Zhao, O.; Gregorczyk, K.; Hu, L.; Lee, S. B.; Rubloff, G. W. Solid Electrolyte Lithium Phosphous Oxynitride as a

Protective Nanocladding Layer for 3D High-Capacity Conversion Electrodes. *ACS Nano* **2016**, *10*, 2693–2701.

(179) Nisula, M.; Shindo, Y.; Koga, H.; Karppinen, M. Atomic Layer Deposition of Lithium Phosphorus Oxynitride. *Chemistry of Materials* **2015**, *27*, 6987–6993.

(180) Perng, Y.-C.; Cho, J.; Sun, S. Y.; Membreno, D.; Cirigliano, N.; Dunn, B.; Chang, J. P. Synthesis of ion conducting LixAlySizO thin films by atomic layer deposition. *J. Mater. Chem. A* **2014**, *2*, 9566–9573.

(181) Wang, B.; Liu, J.; Sun, Q.; Li, R.; Sham, T.-K.; Sun, X. Atomic layer deposition of lithium phosphates as solid-state electrolytes for all-solid-state microbatteries. *Nanotechnology* **2014**, *25*, 504007.

(182) Hu, Y.; Ruud, A.; Miikkulainen, V.; Norby, T.; Nilsen, O.; Fjellvåg, H. Electrical characterization of amorphous LiAlO2 thin films deposited by atomic layer deposition. *RSC Adv.* **2016**, *6*, 60479–60486.

(183) Cao, Y.; Meng, X.; Elam, J. W. Atomic Layer Deposition of LixAlyS Solid-State Electrolytes for Stabilizing Lithium-Metal Anodes. *ChemElectroChem* **2016**, *3*, 858–863.

(184) Wang, B.; Zhao, Y.; Banis, M. N.; Sun, Q.; Adair, K. R.; Li, R.; Sham, T.-K.; Sun, X. Atomic Layer Deposition of Lithium Niobium Oxides as Potential Solid-State Electrolytes for Lithium-Ion Batteries. *ACS Applied Materials & Interfaces* **2018**, *10*, 1654–1661.

(185) Liu, J.; Banis, M. N.; Li, X.; Lushington, A.; Cai, M.; Li, R.; Sham, T. K.; Sun, X. Atomic layer deposition of lithium tantalate solid-state electrolytes. *Journal of Physical Chemistry C* **2013**, *117*, 20260–20267.

(186) Xie, J.; Sendek, A. D.; Cubuk, E. D.; Zhang, X.; Lu, Z.; Gong, Y.; Wu, T.; Shi, F.; Liu, W.; Reed, E. J.; Cui, Y. Atomic Layer Deposition of Stable LiAlF4Lithium

Ion Conductive Interfacial Layer for Stable Cathode Cycling. *ACS Nano* **2017**, *11*, 7019–7027.

(187) Comstock, D. J.; Elam, J. W. Mechanistic Study of Lithium Aluminum Oxide Atomic Layer Deposition. *The Journal of Physical Chemistry C* **2013**, *117*, 1677–1683.

(188) Kozen, A. C.; Lin, C. F.; Zhao, O.; Lee, S. B.; Rubloff, G. W.; Noked, M. Stabilization of Lithium Metal Anodes by Hybrid Artificial Solid Electrolyte Interphase. *Chemistry of Materials* **2017**, *29*, 6298–6307.

(189) Shibata, S. Thermal Atomic Layer Deposition of Lithium Phosphorus Oxynitride as a Thin-Film Solid Electrolyte. *Journal of The Electrochemical Society* **2016**, *163*, A2555–A2562.

(190) Wang, B.; Liu, J.; Norouzi Banis, M.; Sun, Q.; Zhao, Y.; Li, R.; Sham, T. K.; Sun, X. Atomic Layer Deposited Lithium Silicates as Solid-State Electrolytes for All-Solid-State Batteries. *ACS Applied Materials and Interfaces* **2017**, *9*, 31786–31793.

(191) Aaltonen, T.; Nilsen, O.; Magraso, A.; Fjellvag, H. Atomic Layer Deposition of Li2O-Al2O3 Thin Films. *Chemistry of Materials* **2011**, *23*, 4669–4675.

(192) Pearse, A. J.; Schmitt, T. E.; Fuller, E. J.; El-Gabaly, F.; Lin, C. F.; Gerasopoulos, K.; Kozen, A. C.; Talin, A. A.; Rubloff, G.; Gregorczyk, K. E. Nanoscale Solid State Batteries Enabled by Thermal Atomic Layer Deposition of a Lithium Polyphosphazene Solid State Electrolyte. *Chemistry of Materials* **2017**, *29*, 3740–3753.

(193) Nowak, S.; Berkemeier, F.; Schmitz, G. Ultra-thin LiPON films - Fundamental properties and application in solid state thin film model batteries. *Journal of Power Sources* **2015**, *275*, 144–150.

(194) Thimsen, E.; Peng, Q.; Martinson, A. B.; Pellin, M. J.; Elam, J. W. Ion exchange in Ultrathin Films of Cu2s and Zns Under Atomic Layer Deposition Conditions. *Chemistry of Materials* **2011**, *23*, 4411–4413.

(195) Elam, J. W.; Routkevitch, D.; George, S. M. Properties of ZnO/Al2O3 Alloy Films Grown Using Atomic Layer Deposition Techniques. *Journal of The Electrochemical Society* **2003**, *150*, G339.

(196) Knoops, H. C.; Elam, J. W.; Libera, J. A.; Kessels, W. M. Surface loss in ozone-based atomic layer deposition processes. *Chemistry of Materials* **2011**, *23*, 2381–2387.

(197) Xia, H.; Lu, L.; Meng, Y. S. Growth of layered LiNi 0 . 5 Mn 0 . 5 O 2 thin films by pulsed laser deposition for application in microbatteries. **2008**, 3–5.

(198) Miikkulainen, V.; Nilsen, O.; Laitinen, M.; Sajavaara, T.; Fjellvåg, H. Atomic layer deposition of LixTiyOz thin films. *RSC Advances* **2013**, *3*, 7537–7542.

(199) Aaltonen, T.; Alnes, M.; Nilsen, O.; Costelle, L.; Fjellvåg, H. Lanthanum titanate and lithium lanthanum titanate thin films grown by atomic layer deposition. *Journal of Materials Chemistry* **2010**, *20*, 2877–2881.

(200) Hämäläinen, J.; Holopainen, J.; Munnik, F.; Hatanpää, T.; Heikkilä, M.; Ritala, M.; Leskelä, M. Lithium phosphate thin films grown by atomic layer deposition. *Journal of the Electrochemical Society* **2012**, *159*, 259–263.

(201) Lee, B.; Park, T. J.; Hande, A.; Kim, M. J.; Wallace, R. M.; Kim, J.; Liu, X.; Yi, J. H.; Li, H.; Rousseau, M.; Shenai, D.; Suydam, J. Electrical properties of atomic-layer-deposited La2O3 films using a novel La formamidinate precursor and ozone. *Microelectronic Engineering* **2009**, *86*, 1658–1661.

(202) Kwon, J.; Dai, M.; Halls, M. D.; Langereis, E.; Chabal, Y. J.; Gordon, R. G. In situ infrared characterization during atomic layer deposition of lanthanum oxide. *Journal of Physical Chemistry C* **2009**, *113*, 654–660.

(203) Kozen, A. C.; Pearse, A. J.; Lin, C.-F.; Schroeder, M. A.; Noked, M.; Lee, S. B.; Rubloff, G. W. Atomic Layer Deposition and in Situ Characterization of Ultraclean Lithium Oxide and Lithium Hydroxide. *The Journal of Physical Chemistry C* **2014**, *118*, 27749–27753.

(204) Malherbe, J.; Hofmann, S.; Sanz, J. Preferential sputtering of oxides: A comparison of model predictions with experimental data. *Applied Surface Science* **1986**, *27*, 355–365.

(205) Bielinski, A. R.; Kazyak, E.; Schlepütz, C. M.; Jung, H. J.; Wood, K. N.; Dasgupta, N. P. Hierarchical ZnO Nanowire Growth with Tunable Orientations on Versatile Substrates Using Atomic Layer Deposition Seeding. *Chemistry of Materials* **2015**, *27*, 4799–4807.

(206) Larraz, G.; Orera, A.; Sanjuán, M. L. Cubic phases of garnet-type Li7La3Zr 2O12: The role of hydration. *Journal of Materials Chemistry A* **2013**, *1*, 11419–11428.

(207) Cao, X. Q.; Vassen, R.; Stoever, D. Ceramic materials for thermal barrier coatings. *Journal of the European Ceramic Society* **2004**, *24*, 1–10.

(208) Vassen, R.; Cao, X.; Tietz, F.; Basu, D.; Stöver, D. Zirconates as New Materials for Thermal Barrier Coatings. *Journal of the American Ceramic Society* **2004**, *83*, 2023–2028.

(209) Nair, J.; Nair, P.; Doesburg, G. B. M.; Ommen, J. G.; Ross, J. R. H.; Burggraaf, A. J.; Mizukami, F. Sintering of Lanthanum Zirconate. *Journal of the American Ceramic Society* **2004**, *82*, 2066–2072.

(210) Digeos, A. A.; Valdez, J. A.; Sickafus, K. E.; Atiq, S.; Grimes, W.; Boccaccini, A. R. Glass matrix/pyrochlore phase composites for nuclear wastes encapsulation. *Journal of Materials Science* **2003**, *38*, 1597–1604.

(211) Kong, L.; Karatchevtseva, I.; Gregg, D. J.; Blackford, M. G.; Holmes, R.; Triani, G. A novel chemical route to prepare La2Zr2O7 pyrochlore. *Journal of the American Ceramic Society* **2013**, *96*, 935–941.

(212) Thompson, T.; Wolfenstine, J.; Allen, J. L.; Johannes, M.; Huq, A.; David, I. N.; Sakamoto, J. Tetragonal vs. cubic phase stability in Al - free Ta doped Li7La3Zr2O12 (LLZO). *Journal of Materials Chemistry A* **2014**, *2*, 13431–13436.

(213) Tan, J.; Tiwari, A. Fabrication and characterization of Li7La3Zr 2O12 thin films for lithium ion battery. *ECS Solid State Letters* **2012**, *1*, 57–60.

(214) Rawlence, M.; Garbayo, I.; Buecheler, S.; Rupp, J. L. On the chemical stability of post-lithiated garnet Al-stabilized Li7La3Zr2O12solid state electrolyte thin films. *Nanoscale* **2016**, *8*, 14746–14753.

(215) Djenadic, R.; Botros, M.; Benel, C.; Clemens, O.; Indris, S.; Choudhary, A.; Bergfeldt, T.; Hahn, H. Nebulized spray pyrolysis of Al-doped Li7La3Zr2O12 solid electrolyte for battery applications. *Solid State Ionics* **2014**, *263*, 49–56.

(216) Chen, Y.; Rangasamy, E.; Dela Cruz, C. R.; Liang, C.; An, K. A study of suppressed formation of low-conductivity phases in doped Li7La3Zr2O12 garnets by in situ neutron diffraction. *Journal of Materials Chemistry A* **2015**, *3*, 22868–22876.

(217) Ma, C.; Cheng, Y.; Yin, K.; Luo, J. J.; Sharafi, A.; Sakamoto, J. J.; Li, J.; More, K. L.; Dudney, N. J.; Chi, M. Interfacial Stability of Li Metal-Solid Electrolyte Elucidated via in Situ Electron Microscopy. *Nano Letters* **2016**, *16*, 7030–7036.

(218) Yu, S.; Siegel, D. J. Grain Boundary Contributions to Li-Ion Transport in the Solid Electrolyte Li7La3Zr2O12(LLZO). *Chemistry of Materials* **2017**, *29*, 9639–9647.

(219) Dawson, J. A.; Canepa, P.; Famprikis, T.; Masquelier, C.; Islam, M. S. Atomic-Scale Influence of Grain Boundaries on Li-Ion Conduction in Solid Electrolytes for All-Solid-State Batteries. *Journal of the American Chemical Society* **2018**, *140*, 362–368.

(220) Shannon, R. D.; Taylor, B. E.; English, A. D.; Berzins, T. New Li solid electrolytes. *Electrochimica Acta* **1977**, *22*, 783–796.

(221) Horopanitis, E. E.; Perentzis, G.; Beck, A.; Guczi, L.; Peto, G.; Papadimitriou, L. Correlation between structural and electrical properties of heavily lithiated boron oxide solid electrolytes. *Journal of Non-Crystalline Solids* **2008**, *354*, 374–379.

(222) Okumura, T.; Takeuchi, T.; Kobayashi, H. All-solid-state lithium-ion battery using Li2.2C0.8B0.2O3electrolyte. *Solid State Ionics* **2016**, *288*, 248–252.

(223) Nagao, K.; Hayashi, A.; Tatsumisago, M. Mechanochemical synthesis and crystallization of Li3BO3-Li2CO3 glass electrolytes. *Journal of the Ceramic Society of Japan* **2016**, *124*, 915–919.

(224) Horopanitis, E. E.; Perentzis, G.; Pavlidou, E.; Papadimitriou, L. Electrical properties of lithiated boron oxide fast-ion conducting glasses. *Ionics* **2003**, *9*, 88–94.

(225) Park, K.; Yu, B. C.; Jung, J. W.; Li, Y.; Zhou, W.; Gao, H.; Son, S.; Goodenough, J. B. Electrochemical Nature of the Cathode Interface for a Solid-State Lithium-Ion Battery: Interface between LiCoO2and Garnet-Li7La3Zr2O12. *Chemistry of Materials* **2016**, *28*, 8051–8059.

(226) Zhang, H.; Hao, S.; Lin, J. Influence of Li2O-B2O3glass on ionic migration and interfacial properties of La2/3-xLi3xTiO3solid electrolyte. *Journal of Alloys and Compounds* **2017**, *704*, 109–116.

(227) Berkemeier, F.; Abouzari, M. R. S.; Schmitz, G. Thickness-dependent dc conductivity of lithium borate glasses. *Physical Review B - Condensed Matter and Materials Physics* **2007**, *76*, 1–9.

(228) Putkonen, M.; Niinistö, L. Atomic layer deposition of B2O3 thin films at room temperature. *Thin Solid Films* **2006**, *514*, 145–149.

(229) Kim, W.-H.; Oh, I.-K.; Kim, M.-K.; Maeng, W. J.; Lee, C.-W.; Lee, G.; Lansalot-Matras, C.; Noh, W.; Thompson, D.; Chu, D.; Kim, H. Atomic layer deposition of B2O3/SiO2 thin films and their application in an efficient diffusion doping process. *Journal of Materials Chemistry C* **2014**, *2*, 5805.

(230) Kalkofen, B.; Mothukuru, V. V. M.; Lisker, M.; Burte, E. P. E. P-type Doping of Silicon Suitable for Structures with High Aspect Ratios by Using a Dopant Source of Boron Oxide Grown by Atomic Layer Deposition. *ECS Transactions* **2012**, *45*, 55–67.

(231) Seidel, T. E.; Elam, J. W.; Current, M. I.; Mane, A. U. ALD Process for Dopant-Rich Films on Si. *Proceedings of the International Conference on Ion Implantation Technology* **2017**, 9–12.

(232) Gatz, H. A.; Koushik, D.; Rath, J. K.; Kessels, W. M.; Schropp, R. E. Atomic Layer Deposited ZnO: B As Transparent Conductive Oxide for Increased Short Circuit Current Density in Silicon Heterojunction Solar Cells. *Energy Procedia* **2016**, *92*, 624–632.

(233) Garcia-Alonso, D.; Potts, S. E.; van Helvoirt, C. A. A.; Verheijen, M. A.; Kessels, W. M. M. Atomic layer deposition of B-doped ZnO using triisopropyl borate as the boron precursor and comparison with Al-doped ZnO. *J. Mater. Chem. C* **2015**, *3*, 3095–3107.

(234) Varsamis, C.-P. E.; Vegiri, A.; Kamitsos, E. I. Molecular dynamics investigation of lithium borate glasses: Local structure and ion dynamics. *Physical Review B* **2002**, *65*, 104203.

(235) Hensley, D. A.; Garofalini, S. H. XPS investigation of lithium borate glass and the Li/LiBO2 interface. *Applied Surface Science* **1994**, *81*, 331–339.

(236) Xu, F.; Dudney, N. J.; Veith, G. M.; Kim, Y.; Erdonmez, C.; Lai, W.; Chiang, Y. M. Properties of lithium phosphorus oxynitride (Lipon) for 3D solid-state lithium batteries. *Journal of Materials Research* **2010**, *25*, 1507–1515.

(237) Liu, J.; Banis, M. N.; Li, X.; Lushington, A.; Cai, M.; Li, R.; Sham, T. K.; Sun, X. Atomic layer deposition of lithium tantalate solid-state electrolytes. *Journal of Physical Chemistry C* **2013**, *117*, 20260–20267.

(238) Jain, A.; Ong, S. P.; Hautier, G.; Chen, W.; Richards, W. D.; Dacek, S.; Cholia, S.; Gunter, D.; Skinner, D.; Ceder, G.; Persson, K. A. Commentary: The Materials Project: A materials genome approach to accelerating materials innovation. *APL Materials* **2013**, *1*, 011002.

(239) Ong, S. P.; Richards, W. D.; Jain, A.; Hautier, G.; Kocher, M.; Cholia, S.; Gunter, D.; Chevrier, V. L.; Persson, K. A.; Ceder, G. Python Materials Genomics (pymatgen): A robust, open-source python library for materials analysis. *Computational Materials Science* **2013**, *68*, 314–319.

(240) Geryl, K. Atomic layer deposition of vanadium oxides for lithium-ion batteries. **2014**.

(241) Chen, K.-H.; Wood, K. N.; Kazyak, E.; LePage, W. S.; Davis, A. L.; Sanchez, A. J.; Dasgupta, N. P. Dead lithium: mass transport effects on voltage, capacity, and failure of lithium metal anodes. *Journal of Materials Chemistry A* **2017**, *5*, 11671–11681.